

**DOCTORAL THESIS**

Study of  $\text{Cu}_2\text{Ge}(\text{S},\text{Se})_3$  and  
 $\text{Cu}_2\text{CdGe}(\text{S},\text{Se})_4$  Monograin  
Powders for Photovoltaic  
Applications

Xiaofeng Li

TALLINN UNIVERSITY OF TECHNOLOGY  
DOCTORAL THESIS  
17/2022

**Study of  $\text{Cu}_2\text{Ge}(\text{S},\text{Se})_3$  and  $\text{Cu}_2\text{CdGe}(\text{S},\text{Se})_4$   
Monograin Powders for Photovoltaic  
Applications**

XIAOFENG LI



TALLINN UNIVERSITY OF TECHNOLOGY

School of Engineering

Department of Materials and Environmental Technology

This dissertation was accepted for the defence of the degree 29/04/2022

**Supervisor:**

Senior Researcher, Dr. Marit Kauk-Kuusik  
School of Engineering  
Tallinn University of Technology  
Tallinn, Estonia

**Co-supervisor:**

Senior Researcher, Dr. Kristi Timmo  
School of Engineering  
Tallinn University of Technology  
Tallinn, Estonia

**Opponents:**

Associated Professor, Dr. Edgardo Saucedo Silva  
Department of Electronic Engineering  
Universitat Politècnica de Catalunya (UPC)  
Barcelona, Spain

Senior Researcher, Dr. Rokas Kondrotas  
Centre for Physical Science and Technology  
Vilnius, Lithuania

**Defence of the thesis:** 03/06/2022, Tallinn

**Declaration:**

Hereby I declare that this doctoral thesis, my original investigation and achievement, submitted for the doctoral degree at Tallinn University of Technology has not been submitted for doctoral or equivalent academic degree.

Xiaofeng Li

-----  
signature



European Union  
European Regional  
Development Fund



Investing  
in your future

Copyright: Xiaofeng Li, 2022

ISSN 2585-6898 (publication)

ISBN 978-9949-83-819-6 (publication)

ISSN 2585-6901 (PDF)

ISBN 978-9949-83-820-2 (PDF)

Printed by Auratrükk

TALLINNA TEHNIKAÜLIKOOL  
DOKTORITÖÖ  
17/2022

**$\text{Cu}_2\text{Ge}(\text{S},\text{Se})_3$  ja  $\text{Cu}_2\text{CdGe}(\text{S},\text{Se})_4$   
monoterapulbrite uurimine ning kasutamine  
päikesepatareides**

XIAOFENG LI





# Contents

List of Publications .....	7
Author's Contribution to the Publications .....	8
Introduction .....	9
Abbreviations .....	11
1 Literature overview and the aim of the study.....	12
1.1 Solar cells based on $\text{Cu}_2\text{-II-IV-VI}_4$ and $\text{Cu}_2\text{-IV-VI}_3$ compounds.....	12
1.2 Structural properties of $\text{Cu}_2\text{Ge(S,Se)}_3$ and $\text{Cu}_2\text{CdGe(S,Se)}_4$ .....	13
1.2.1 Crystal structures of $\text{Cu}_2\text{GeS}_3$ and $\text{Cu}_2\text{GeSe}_3$ .....	13
1.2.2 Crystal structures of $\text{Cu}_2\text{CdGeSe}_4$ and $\text{Cu}_2\text{CdGeS}_4$ .....	14
1.3 Phase diagrams of $\text{Cu}_2\text{Ge(S,Se)}_3$ and $\text{Cu}_2\text{CdGe(S,Se)}_4$ .....	15
1.3.1 Phase diagrams of $\text{Cu}_2\text{GeSe}_3$ and $\text{Cu}_2\text{GeS}_3$ .....	15
1.3.2 Phase diagram of $\text{Cu}_2\text{GeSe}_3\text{-Cu}_2\text{GeS}_3$ system .....	17
1.3.3 Phase diagrams of $\text{Cu}_2\text{CdGeSe}_4$ and $\text{Cu}_2\text{CdGeS}_4$ .....	17
1.3.4 Phase diagram of $\text{Cu}_2\text{CdGeSe}_4\text{-Cu}_2\text{CdGeS}_4$ .....	19
1.4 Optical and electronic properties of $\text{Cu}_2\text{Ge(S,Se)}_3$ and $\text{Cu}_2\text{CdGe(S,Se)}_4$ .....	19
1.4.1 Photoluminescence properties of $\text{Cu}_2\text{Ge(S,Se)}_3$ .....	19
1.4.2 Optical and electronic properties of $\text{Cu}_2\text{CdGe(S,Se)}_4$ .....	20
1.4.3 Band gap engineering.....	21
1.5 Monograin powder technology.....	22
1.5.1 Molten salt synthesis of monograin powder.....	22
1.5.2 Flux materials .....	23
1.5.3 Monograin layer solar cells.....	24
1.6 Absorber surface modification.....	25
1.7 Summary of literature review and the aim of the study.....	26
2 Experimental .....	28
2.1 Preparation of $\text{Cu}_2\text{CdGe(S,Se)}_4$ monograin powders.....	28
2.2 Preparation of $\text{Cu}_2\text{Ge(Se,S)}_3$ monograin powders.....	29
2.3 Post-treatment of $\text{Cu}_2\text{CdGe(Se,S)}_4$ and $\text{Cu}_2\text{Ge(Se,S)}_3$ monograin powders.....	30
2.4 Characterization of monograin powders.....	31
2.4.1 Room temperature micro-Raman spectroscopy .....	31
2.4.2 X-ray photoelectron spectroscopy (XPS) .....	31
2.4.3 Scanning electron microscopy (SEM) .....	31
2.4.4 Energy dispersive X-ray spectroscopy (EDX) .....	31
2.4.5 X-ray powder diffraction (XRD) .....	32
2.4.6 Photoluminescence spectroscopy (PL).....	32
2.5 Solar cell characteristics .....	32
2.5.1 Current-Voltage measurements.....	32
2.5.2 Quantum efficiency measurements .....	32
3 Results and discussion.....	33
3.1 $\text{Cu}_2\text{CdGeSe}_4$ monograin powders .....	33
3.1.1 Morphology of $\text{Cu}_2\text{CdGeSe}_4$ powder crystals .....	33
3.1.2 Particle size distribution .....	34
3.1.3 Elemental bulk composition of $\text{Cu}_2\text{CdGeSe}_4$ powders.....	35
3.1.4 Phase composition and structure.....	36

3.1.5 Cu <sub>2</sub> CdGeSe <sub>4</sub> surface modifications .....	37
3.1.6 Cu <sub>2</sub> CdGeSe <sub>4</sub> monograin layer solar cell .....	39
3.2 Cu <sub>2</sub> CdGe(S <sub>x</sub> Se <sub>1-x</sub> ) <sub>4</sub> monograin powders .....	42
3.2.1 Morphology and composition of Cu <sub>2</sub> CdGe(S <sub>x</sub> Se <sub>1-x</sub> ) <sub>4</sub> monograin powders .....	42
3.2.2 Structural properties of Cu <sub>2</sub> CdGe(S <sub>x</sub> Se <sub>1-x</sub> ) <sub>4</sub> monograin powders .....	43
3.2.3 Raman analysis of Cu <sub>2</sub> CdGe(S <sub>x</sub> Se <sub>1-x</sub> ) <sub>4</sub> monograin powders .....	46
3.2.4 Cu <sub>2</sub> CdGe(S <sub>x</sub> Se <sub>1-x</sub> ) <sub>4</sub> monograin layer solar cells .....	46
3.3 Cu <sub>2</sub> Ge(Se <sub>x</sub> S <sub>1-x</sub> ) <sub>3</sub> monograin powders .....	48
3.3.1 Morphology and composition of Cu <sub>2</sub> Ge(Se <sub>x</sub> S <sub>1-x</sub> ) <sub>3</sub> monograin powders .....	48
3.3.2 Structural analysis of Cu <sub>2</sub> Ge(Se <sub>x</sub> S <sub>1-x</sub> ) <sub>3</sub> monograin powders .....	49
3.3.3 PL analysis of Cu <sub>2</sub> Ge(Se <sub>x</sub> S <sub>1-x</sub> ) <sub>3</sub> monograin powders .....	51
3.3.4 Cu <sub>2</sub> Ge(Se <sub>x</sub> S <sub>1-x</sub> ) <sub>3</sub> monograin layer solar cells .....	52
Conclusions .....	54
References .....	56
Abstract .....	67
Lühikokkuvõte .....	69
Appendix .....	71
Curriculum vitae .....	115
Elulookirjeldus .....	117

## List of Publications

The list of author's publications, on the basis of which the thesis has been prepared:

- I M. Kauk-Kuusik\*, X. Li, M. Pilvet, K. Timmo, M. Grossberg, T. Raadik, M. Danilson, V. Mikli, M. Altosaar, J. Krustok, J. Raudoja. "Study of  $\text{Cu}_2\text{CdGeSe}_4$  monograin powders synthesized by molten salt method for photovoltaic applications", *Thin Solid Films*, Volume 666, 15–19, 2018. <https://doi.org/10.1016/j.tsf.2018.09.025>
- II X. Li\*, M. Pilvet, K. Timmo, M. Grossberg, M. Danilson, V. Mikli, M. Kauk-Kuusik. "Effect of absorber surface modification on the optoelectronic properties of  $\text{Cu}_2\text{CdGeSe}_4$  solar cells", *Thin Solid Films*, Volume 697, 137822, 2020. <https://doi.org/10.1016/j.tsf.2020.137822>
- III X. Li\*, M. Pilvet, K. Timmo, M. Grossberg, V. Mikli, M. Kauk-Kuusik, "The effect of S/Se ratio on the properties of  $\text{Cu}_2\text{CdGe}(\text{S}_x\text{Se}_{1-x})_4$  microcrystalline powders for photovoltaic applications", *Solar Energy*, Volume 209, 646–652, 2020. <https://doi.org/10.1016/j.solener.2020.09.045>
- IV J. Krustok\*, R. Kaupmees, X. Li, M. Kauk-Kuusik, and M. Grossberg. "Detailed photoluminescence study of  $\text{Cu}_2\text{Ge}(\text{SSe})_3$  microcrystals", *AIP Advances* 11, 085105 2021. <https://doi.org/10.1063/5.0053928>
- V X. Li\*, K. Timmo, M. Grossberg, M. Pilvet, R. Kaupmees, J. Krustok, K. Muska, V. Mikli, M. Kauk-Kuusik. "Study of the structure and optoelectronic properties of  $\text{Cu}_2\text{Ge}(\text{Se}_x\text{S}_{1-x})_3$  microcrystalline powders", *Thin Solid Films* 742, 139053, 2022 <https://doi.org/10.1016/j.tsf.2021.139053>

## Author's Contribution to the Publications

Contribution to the papers in this thesis are:

- I Major part of experimental work (preparation of precursors and monograin powders), part of characterization (Raman measurement,  $I-V$  measurement, particle size distribution), analysis of the results, and major part of writing.
- II Major part of experimental work (preparation of precursors and monograin powders, post-treatment of monograin powders), part of characterization (Raman measurement,  $I-V$  measurement), analysis of the results, and major part of writing.
- III Major part of experimental work (preparation of precursors and monograin powders, optimization of powders, post-treatment of monograin powders), part of characterization (Raman measurement,  $I-V$  measurement), analysis of the results, and major part of writing.
- IV Major part of experimental work (preparation of precursors and monograin powders), part of characterization (Raman measurement), analysis of the results.
- V Major part of experimental work (preparation of precursors and monograin powders, optimization of powders, post treatment of monograin powders), part of characterization (Raman measurement,  $I-V$  measurement), analysis of the results, and major part of writing.

## Introduction

The global energy outlook made by International Energy Agency in 2021 shows that a new energy economy is emerging- but not yet fast enough to reach the net zero by 2050 [1]. In 2019, global final electricity consumption reached 22848 TWh [2], almost two-thirds (63.3%) of global electricity came from fossil fuels. Today's energy systems are still heavily dependent on fossil fuels. Therefore, a sustainable and environmentally friendly energy source that meets the growing demand for energy services, including reduction of greenhouse gas emissions is a huge task.

Achieving carbon-neutral processes in the energy domain is the focus as well as the challenge for our generation. In the power markets, renewables have become the technology of the choice, making up almost two-thirds of the global capacity additions to 2040, thanks to the falling costs and supportive government policies [3]. Despite of the COVID-19 pandemic, the total photovoltaic (PV) cumulative installations amounted to 760.4 GWp at the end of year 2020 [4]. PV technology, as one of the renewable energy sources, is growing fast due to the most abundant energy source, reduced cost, high efficiency and environmentally friendly processes while comparing with the conventional energy technologies [5]. The global photovoltaic market is segmented based on the technology, which is mainly classified into mono-crystalline silicon and multi-crystalline silicon and thin films (cadmium telluride (CdTe), copper indium gallium diselenide (Cu(In,Ga)Se<sub>2</sub>). Nowadays, crystalline silicon (c-Si) is one of the most widely used semiconductor material in PV technology to manufacture the solar cells. Crystalline silicon occupies more than 95% of the total photovoltaic market revenue owing to its several benefits such as high efficiency (26.7% for mono-crystalline [6] and 24.4% for multi-crystalline silicon wafer-based technology [7]).

The market share of the highest efficiency thin film technologies, mainly 23.4% for Cu(In,Ga)Se<sub>2</sub> [8] and 22.1% for CdTe [7], accounts for only 5%. According to [9,10], Cu(In,Ga)Se<sub>2</sub> and CdTe thin film technologies may have a big potential to be utilized on a much larger scale, however, there are the limitations considering the usage of the availability of large quantities of the rather rare metals, such as indium or tellurium.

To avoid the above-mentioned limitations, the researchers started to look for new potential candidate absorber materials in quaternary I<sub>2</sub>-II-IV-VI<sub>4</sub> (I = Cu, Ag; II = Zn, Cd; IV = Si, Ge, Sn; VI = S, Se) chalcogenides. The Cu<sub>2</sub>ZnSnS<sub>4</sub> compounds (kesterite) as *p*-type semiconductor materials have many required properties, such as direct bandgap (~1.5 eV) and high absorption coefficient (~10<sup>5</sup> cm<sup>-1</sup>) [11], to replace CdTe or Cu(In,Ga)Se<sub>2</sub> as absorber materials in thin film photovoltaics. The bandgap (*E<sub>g</sub>*) can be tuned from ~1.0 eV for the pure selenide Cu<sub>2</sub>ZnSnSe<sub>4</sub> to ~1.5 eV for the pure sulfide Cu<sub>2</sub>ZnSnS<sub>4</sub> by adjusting the concentration ratio of chalcogenides (S/Se) in the Cu<sub>2</sub>ZnSn(S<sub>*x*</sub>Se<sub>1-*x*</sub>)<sub>4</sub> [12]. It covers the optimum band gap range for single junction solar cell according to Shockley-Queisser limit [13,14]. Currently, the record efficiency of thin film solar cells based on the Cu<sub>2</sub>ZnSnS<sub>4</sub> and Cu<sub>2</sub>ZnSnSe<sub>4</sub> are 11.2% [11] and 12.5% [15], respectively. The highest efficiency of 12.6% for Cu<sub>2</sub>ZnSn(S,Se)<sub>4</sub> based thin-film solar cells has been presented by the IBM group in 2013 [16]. Recently, it was renewed over 13% by Zhou *et al* [12] and Gong *et al* [17]. Additionally, 14% of efficiency was reported by Professor Hao Xin from *Nanjing University of Posts and Telecommunications* in the 12<sup>th</sup> European Kesterite Workshop in 2022.

The highest power conversion efficiency (PCE) of thin film solar cell based on the Cu<sub>2</sub>ZnSn(S,Se)<sub>4</sub> absorber materials is still considerably lower compared to c-Si,

Cu(In,Ga)Se<sub>2</sub> and CdTe devices. According to the reports [18–22], the main culprits of limitations are open circuit voltage deficit, deep defects related to divalent Sn, interface recombination, coexistence of the complex secondary phases, the band tailing issue, short minority lifetime, bulk defects, and undesirable band alignment at *p-n* interfaces. Thus, further research and knowledge is necessary to overcome the present limitations and improve the performance of the kesterite-based technologies. Also, further research on the other ternary and quaternary copper chalcogenide compounds with suitable properties for solar cell absorber is motivated.

Based on literature data, Cu<sub>2</sub>CdGe(S,Se)<sub>4</sub> compounds are less studied. According to the Web of Science, there are 21 publications for Cu<sub>2</sub>CdGeSe<sub>4</sub>, 25 papers for Cu<sub>2</sub>CdGeS<sub>4</sub> and one recently published work about Cu<sub>2</sub>CdGe(S,Se)<sub>4</sub>. In addition, the Cu<sub>2</sub>Ge(S,Se)<sub>3</sub> compounds, which are also not extensively investigated, could be suitable for photovoltaic applications. Cu<sub>2</sub>GeSe<sub>3</sub> is mainly investigated as thermoelectric material [23], and only in few studies as for photovoltaic application [24]. Structural, electronic, and optical properties of Cu<sub>2</sub>GeS<sub>3</sub> compound are presented in several studies [25–28], but only in few works it is studied as an absorber material for solar cell applications.

In this thesis the monograin layer solar cell technology is used. The monograin layer solar cell technology, as one of the cheapest non-vacuum technologies, is applicable for large-scale photovoltaics, helping to reduce the costs of solar cell production. Therefore, the research in this thesis is focused on the synthesis and characterization of ternary Cu<sub>2</sub>Ge(S,Se)<sub>3</sub> and quaternary Cu<sub>2</sub>CdGe(S,Se)<sub>4</sub> monograin powders for photovoltaic applications.

The thesis is divided into three main chapters, a brief overview of the literature and the aim of the study are presented in the Chapter 1. The Chapter 2 presents the experimental details, including sample preparation, describes the techniques used to characterize the properties of the powders and solar cells. The experimental results and discussions based on the Papers I-V are summarized in the Chapter 3.

## Abbreviations

Br <sub>2</sub> -MeOH	Bromine in methanol
CBD	Chemical bath deposition
CIGS	Cu(In <sub>x</sub> Ga <sub>1-x</sub> )Se <sub>2</sub> , copper (indium gallium) diselenide
CIS	CuInSe <sub>2</sub> , copper indium diselenide
c-Si	Crystalline silicon
EDX	Energy dispersive x-ray spectroscopy
$E_g$	Band gap energy
$E_g^*$	Effective band gap energy
EQE	External quantum efficiency
$FF$	Fill factor
HT	High temperature
$I$ - $V$	Current-Voltage
$J_{sc}$	Short circuit current density
LT	Low temperature
MGL	Monograin layer
MGP	Monograin powder
$o$ -Cu <sub>2</sub> CdGeSe <sub>4</sub>	Orthorhombic structure of Cu <sub>2</sub> CdGeSe <sub>4</sub>
PCE	Power conversion efficiency
PL	Photoluminescence
PV	Photovoltaic
QE	Quantum efficiency
RT	Room temperature
SEM	Scanning electron microscopy
$t$ -Cu <sub>2</sub> CdGeSe <sub>4</sub>	Tetragonal structure of Cu <sub>2</sub> CdGeSe <sub>4</sub>
$V_{oc}$	Open circuit voltage
$V_{oc-def}$	Open circuit voltage deficit
XRD	X-ray diffraction
XPS	X-ray photoelectron spectrometry
$\eta$	Efficiency



# 1 Literature overview and the aim of the study

## 1.1 Solar cells based on $\text{Cu}_2\text{-II-IV-VI}_4$ and $\text{Cu}_2\text{-IV-VI}_3$ compounds

The  $\text{Cu}_2\text{-II-IV-VI}_4$  compounds have received considerable attention due to their suitable properties for thin film solar cell absorbers. The predecessor of quaternary copper chalcogenides was chalcopyrite copper indium diselenide (CIS) developed for the thin-film solar cells from the last century [29]. The photovoltaic effect in the heterojunction consisting of a transparent conductive film of cadmium-tin-oxide and a  $\text{Cu}_2\text{ZnSnS}_4$  thin film was recorded for the first time by Ito *et al.* [30]. The same group of researchers established that  $\text{Cu}_2\text{ZnSnS}_4$  materials have the *p*-type conductivity and a high absorption coefficient larger than  $10^4 \text{ cm}^{-1}$  in the visible range of the spectrum. Katagiri *et al.* reported the first fully functional  $\text{Cu}_2\text{ZnSnS}_4$  absorber materials by sulfurization of evaporated precursors and demonstrated the power conversion efficiency of 0.66% [27]. After that, different methods were used for the growth of  $\text{Cu}_2\text{ZnSn(S,Se)}_4$  absorber materials and remarkable progress has been made in solar cell efficiency. By 2003, 5.45% efficiency of  $\text{Cu}_2\text{ZnSnS}_4$  based solar cell was achieved by using electron-beam evaporation technique for fabrication of Cu/Sn/ZnS layers followed by sulfurization in  $\text{N}_2+\text{H}_2\text{S}$  atmosphere [31]. In 2009, the same group reached up to the 6.77% power conversion efficiency by using a three sources radio frequency co-sputtering for the metal film deposition followed by annealing in sulfur containing atmosphere [32]. Mitzi *et al.* reported the efficiency of 10% for spin-coated  $\text{Cu}_2\text{ZnSn(S,Se)}_4$  thin film solar cells in 2010 [33]. Wang *et al.* reported long-standing world's record efficiency of 12.6% for  $\text{Cu}_2\text{ZnSn(S,Se)}_4$  based thin film solar cells fabricated by hydrazine pure-solution method in 2014 [16].  $\text{Cu}_2\text{ZnSnS}_4$  monograin layer solar cells made by same technology used in this thesis have achieved an efficiency of 11.7% [34]. Although the performance of solar cells based on the kesterite materials has been renewed in 2021 [12,17], the efficiency has no great improvement owing to the open circuit voltage deficit ( $V_{oc-def}$ ) (expressed as  $(E_g/q)-V_{oc}$ , where  $E_g$  is the absorber's bandgap value and  $q$  is the elemental charge).

Cation substitution in kesterite materials has proven to be a successful strategy to overcome the limitation of the open circuit voltage deficit. Among the varieties, Sn substitution by Ge in the kesterite materials has been the emerging trend. By considering the most stable oxidation states of these two elements, Ge is more likely to be present in tetravalent state than Sn, thus avoiding the presence of potentially harmful +2 oxidation states [17,20]. A significant increase in the open circuit voltage ( $V_{oc}$ ) values of solar cells based on Ge containing kesterite absorbers have been presented in several papers [35–37]. Among them, Leo *et al.* [36] improved the  $V_{oc}$  by substituting Sn with Ge and achieved 8.5% efficiency for  $\text{Cu}_2\text{ZnGeSe}_4$ -based solar cells, which is a record for Sn-free kesterite devices. Schnabel *et al.* [37] reported efficiencies exceeding 5% for a sulfo-selenide  $\text{Cu}_2\text{ZnGe(S,Se)}_4$  solar cell by using Mo/ $\text{Cu}_2\text{ZnGe(S,Se)}_4$ /Zn(O,S)/ZnO/Ni-Al grid structure. Cation substitution of Zn by Cd in kesterite system has also drawn considerable attention. Although Cd is toxic, it is firmly bound into the form of stable ternary and quaternary semiconductor compounds in the absorber layers used in solar cells and not harmful for people in normal atmospheric conditions [38]. As a positive effect, Cd incorporation into the kesterite structure could reduce or even avoid the formation of harmful antisite defects such as  $\text{Cu}_{\text{Zn}}$  and  $\text{Zn}_{\text{Cu}}$ . Since the ionic radius of  $\text{Cd}^{2+}$  (0.92 Å) is larger than that of  $\text{Cu}^+$  and  $\text{Zn}^{2+}$  (both 0.74 Å), thereby suppressing the Cu-Zn

disorder and band tailing issues in kesterite system [20,39]. Therefore, novel  $\text{Cu}_2\text{CdGe}(\text{S},\text{Se})_4$  compounds are synthesized and studied as the main materials in this thesis.

Ternary compounds,  $\text{Cu}_2\text{GeS}_3$  and  $\text{Cu}_2\text{GeSe}_3$  have shown many promising photo-absorber material properties, such as *p*-type conductivity and a direct band gap energy of 1.5 eV and 0.8 eV, respectively [24,28]. However, there are only few studies presenting the results of solar cells based on  $\text{Cu}_2\text{GeS}_3$  and  $\text{Cu}_2\text{GeSe}_3$  or their solid solutions [40]. The best power conversion efficiency of 2.67% for  $\text{Cu}_2\text{GeS}_3$  thin film solar cell was achieved by sulfurized powders prepared by combustion method [28]. Yang *et al.* [40] reported the efficiency of 0.2% for solar cells based on  $\text{Cu}_2\text{Ge}(\text{Se}_{0.33}\text{S}_{0.67})_3$  colloidal nanocrystals (NCs).

With regard to  $\text{Cu}_2\text{CdGeS}_4$ , different synthesis methods have been used to grow single crystals, such as vertical Bridgman method [41], chemical vapour transport and gradient freezing [42] and some more. As  $\text{Cu}_2\text{CdGeS}_4$  compound has wide band gap ( $\sim 2$  eV) for single junction solar cells, it can be used in many different devices, such as a top cell absorber material in a tandem solar cell structure or as photoelectrode in photo-electrochemical water splitting devices [43]. The top cell has a larger band gap and thus expands the spectral sensitivity range of a multi-junction solar cell toward higher photon energies. As for  $\text{Cu}_2\text{CdGeSe}_4$  compound, there have been published a number of reports on the synthesis of this compound by various methods like the horizontal gradient freezing method [44], directional solidification method [45], Bridgman method [46,47] and solid-state reaction method in sealed evacuated quartz ampoules [48].  $\text{Cu}_2\text{CdGeSe}_4$  has suitable absorber material properties for single junction solar cell such as high absorption coefficient ( $> 10^4 \text{ cm}^{-1}$ ), *p*-type conductivity and direct band gap energy ( $\sim 1.2$  eV) [49], but no reports about solar cells based on this material could be found in the literature.

The following sections focus on the phase diagrams, structural, optical and electrical properties of  $\text{Cu}_2\text{Ge}(\text{S},\text{Se})_3$  and  $\text{Cu}_2\text{CdGe}(\text{S},\text{Se})_4$ .

## 1.2 Structural properties of $\text{Cu}_2\text{Ge}(\text{S},\text{Se})_3$ and $\text{Cu}_2\text{CdGe}(\text{S},\text{Se})_4$

### 1.2.1 Crystal structures of $\text{Cu}_2\text{GeS}_3$ and $\text{Cu}_2\text{GeSe}_3$

$\text{Cu}_2\text{GeS}_3$  can exist in different crystal structures, such as cubic and monoclinic structure, depending on the synthesis temperature [25,26,28,50]. Monoclinic crystal structure (shown in the Figure 1.1a) has been found for  $\text{Cu}_2\text{GeS}_3$  grown at 620 °C [50].

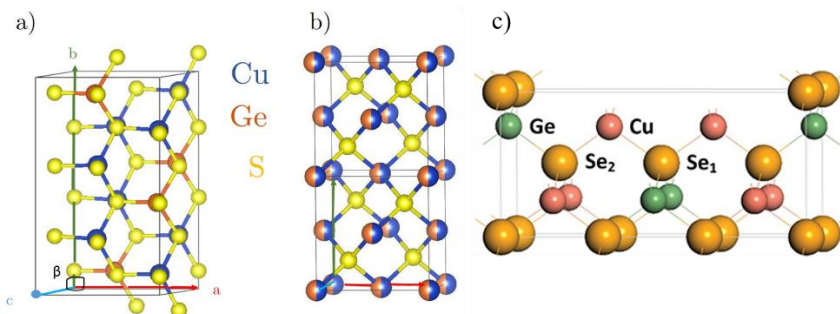


**Figure 1.1.** a) Unit cell of monoclinic  $\text{Cu}_2\text{GeS}_3$ , b) two unit cells of cubic  $\text{Cu}_2\text{GeS}_3$  [50] and c) unit cell of orthorhombic  $\text{Cu}_2\text{GeSe}_3$  [51].

Thin films of  $\text{Cu}_2\text{GeS}_3$  annealed at  $480^\circ\text{C}$  showed cubic crystal structure (Figure 1.1b) and transition to monoclinic polymorph was observed between  $480\text{--}500^\circ\text{C}$  [50].  $\text{Cu}_2\text{GeS}_3$  colloidal NCs produced by a hot-injection method showed cubic structure [52] and by adding Se into the compound, the orthorhombic structure was observed [40]. Although some researchers have found that  $\text{Cu}_2\text{GeSe}_3$  compound crystallizes in the monoclinic structure [24,53,54], mostly it has been observed that pure  $\text{Cu}_2\text{GeSe}_3$  crystallizes in an orthorhombic structure (Figure 1.1c) and has the lattice parameters  $a = 1.1857(1)$ ,  $b = 0.39522(8)$ ,  $c = 0.54865(7)$  nm [51,55].

### 1.2.2 Crystal structures of $\text{Cu}_2\text{CdGeSe}_4$ and $\text{Cu}_2\text{CdGeS}_4$

$\text{Cu}_2\text{CdGeSe}_4$  has two crystal structure modifications such as the tetragonal structure with a  $I-42m$  space group and an orthorhombic structure with a  $Pmn21$  space group (Figure 1.2) [56]. The orthorhombic crystal structure ( $o\text{-Cu}_2\text{CdGeSe}_4$ ) is dominating at higher temperatures ( $T > 605^\circ\text{C}$ ) while the tetragonal crystal structure ( $t\text{-Cu}_2\text{CdGeSe}_4$ ) is obtained at lower temperatures [48].

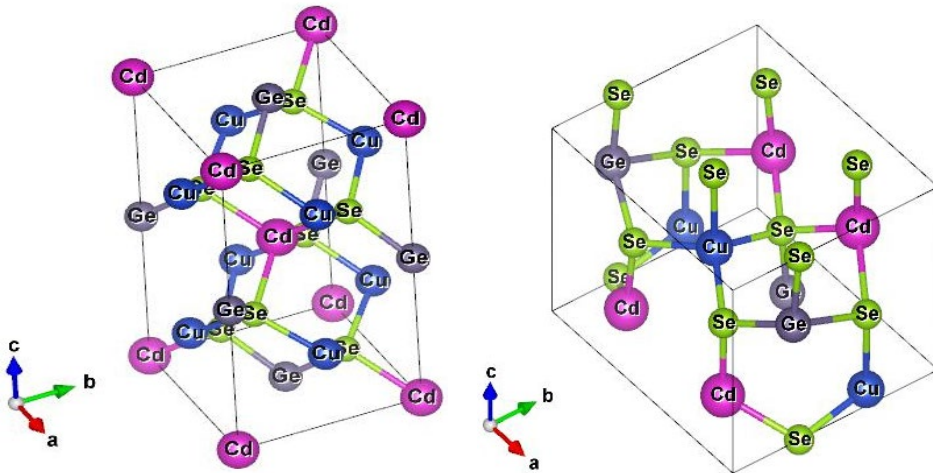


**Figure 1.2** Tetragonal (left) and orthorhombic (right) crystal structure of  $\text{Cu}_2\text{CdGeSe}_4$  (Drawn by author with VESTA).

The crystal structure of  $t\text{-Cu}_2\text{CdGeSe}_4$  and  $o\text{-Cu}_2\text{CdGeSe}_4$  is usually presented as the packing of selenium tetrahedra centred on germanium atoms. Cu and Cd atoms are located in the voids between these tetrahedral [46]. In the  $t\text{-Cu}_2\text{CdGeSe}_4$ , the coordination polyhedral of all cations are tetrahedra formed by four Se atoms. Although all the metal (Me) - Se bond lengths are equal for each cation, the tetrahedra are slightly distorted since the Se-Me-Se valency angles differ from the regular tetrahedral angle  $109.5^\circ$  [56]. In the  $o\text{-Cu}_2\text{CdGeSe}_4$  structure all atoms also have a tetrahedral surrounding, but one crystallographic position is occupied by a statistical mixture ( $M = 0.5 \text{ Cu} + 0.5 \text{ Cd}$ ). The coordination tetrahedra of cations and anions are distorted, which indicates some disordering of the  $o\text{-Cu}_2\text{CdGeSe}_4$  structure [56]. In addition, the Ge-Se bond lengths in  $t\text{-Cu}_2\text{CdGeSe}_4$  are in good agreement with the sum of the ionic radii [ $r(\text{Ge}^{4+}) = 0.053$  nm and  $r(\text{Se}^{2-}) = 0.184$  nm] while the Cu-Se and Cd-Se bond lengths are slightly shorter than the respective sum [ $r(\text{Cu}^+) = 0.074$  nm and  $r(\text{Cd}^{2+}) = 0.092$  nm]. The interatomic distances in  $o\text{-Cu}_2\text{CdGeSe}_4$  are generally longer than those for the tetragonal modification, which leads to a slight increase of the volume cell at the same number of formula units

per unit cell [56]. According to [56], the tetragonal  $\text{Cu}_2\text{CdGeSe}_4$  has lattice parameters  $a = b = 0.5748$  nm and  $c = 1.1053$  nm. The orthorhombic modification has lattice parameters  $a = 0.8088$  nm,  $b = 0.6875$  nm and  $c = 0.6564$  nm.

In addition, some peculiarities of the tetragonal  $\leftrightarrow$  orthorhombic structure transformation has been discussed. It was supposed that there is a similarity with the sphalerite  $\leftrightarrow$  wurtzite transformation while considering that the tetragonal and orthorhombic modifications derive from the zinc blende and wurtzite structures, respectively. As the structure reconstruction demands a break of bonds, the transformations proceed slowly and metastable modifications can be persist for a long time [56]. Quintero *et al.* [57] determined that the phase transition orthorhombic  $\leftrightarrow$  tetragonal takes place at 605 °C. In the present thesis, the method of monograin powder (MGP) synthesis in molten salt has been used. The method allows to use different synthesis temperatures to obtain different crystal structure of  $\text{Cu}_2\text{CdGeSe}_4$ . Additionally, different cooling rates after heat-treatments can also result in different crystal structures [58].

In the  $\text{Cu}_2\text{CdGeS}_4$  system, only orthorhombic structure has been reported. The orthorhombic structure (space group  $Pmn21$ ,  $a = 0.7692$  nm,  $b = 0.6555$  nm,  $c = 0.6299$  nm) of  $\text{Cu}_2\text{CdGeS}_4$  were first established by Parthé *et al.* [59]. The  $\text{Cu}_2\text{CdGeS}_4$  structure can be considered as a wurtzite related superstructure [60]. The findings were confirmed later in studies [41,42]. The crystal structure of  $\text{Cu}_2\text{CdGeS}_4$  is shown in Figure 1.3, there are two formula units per cell and each sulfur atom is surrounded by two Cu atoms, one Cd atom and one Ge atom while every cation atom is tetrahedrally surrounded by sulfur atoms [59].

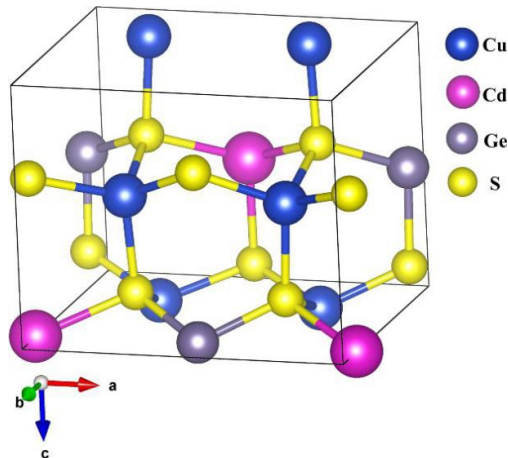


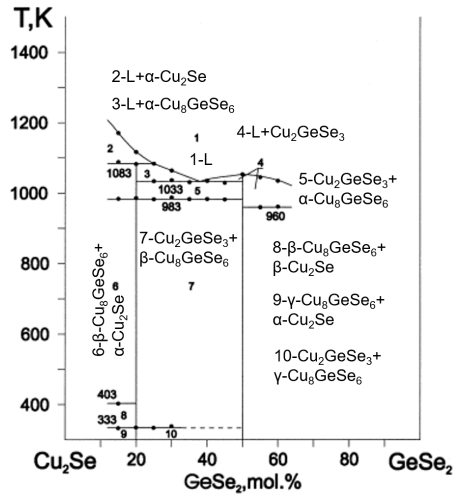
**Figure 1.3.** The orthorhombic crystal structure of  $\text{Cu}_2\text{CdGeS}_4$  [59].

## 1.3 Phase diagrams of $\text{Cu}_2\text{Ge}(\text{S},\text{Se})_3$ and $\text{Cu}_2\text{CdGe}(\text{S},\text{Se})_4$

### 1.3.1 Phase diagrams of $\text{Cu}_2\text{GeSe}_3$ and $\text{Cu}_2\text{GeS}_3$

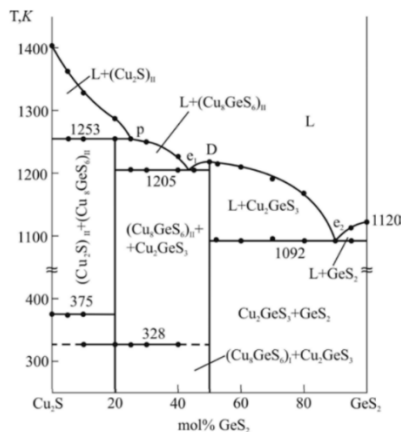
Phase diagrams can be used to predict the phase changes that may occur during the synthesis process of multinary compound. This is important because the properties of a compound depend on the phases present in the material. Figure 1.4 shows the phase diagram of the  $\text{Cu}_2\text{Se}-\text{GeSe}_2$  system [53], which has been investigated in the

concentration interval 15 – 60 mol% GeSe<sub>2</sub>. The existence of the two phases Cu<sub>2</sub>GeSe<sub>3</sub> and Cu<sub>8</sub>GeSe<sub>6</sub> was confirmed. The ternary Cu<sub>2</sub>GeSe<sub>3</sub> compound melts congruently at 780 °C. The peritectic reaction L+Cu<sub>2</sub>Se⇌Cu<sub>8</sub>GeSe<sub>6</sub>, taking place at 810 °C, corresponds to the formation of Cu<sub>8</sub>GeSe<sub>6</sub>. Two polymorphous transformations at 710 and 60 °C were found for this phase. The same value of the phase transition temperature on both sides of the intermediate phase indicates that it has only a small homogeneity region. A further horizontal at 130 °C is interpreted as polymorphous transformation of Cu<sub>2</sub>Se. The interaction between Cu<sub>8</sub>GeSe<sub>6</sub> and Cu<sub>2</sub>GeSe<sub>3</sub> is of the eutectic type. The eutectic point is located at 38 mol% GeSe<sub>2</sub> and at 760 °C [53].



**Figure 1.4.** Phase diagram of the Cu<sub>2</sub>Se–GeSe<sub>2</sub> system [53].

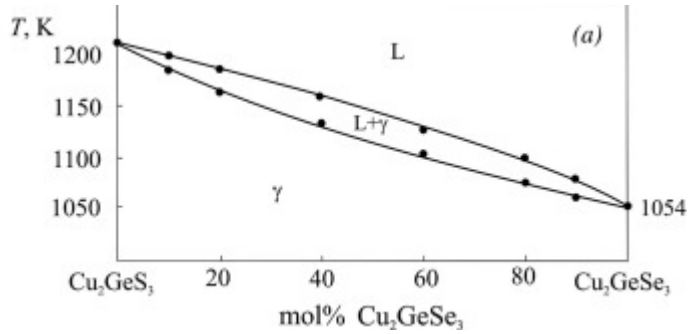
Phase diagram of the Cu<sub>2</sub>S–GeS<sub>2</sub> system is presented in the Figure 1.5 [61], it is seen that two ternary compounds are formed in the system: Cu<sub>8</sub>GeS<sub>6</sub> and Cu<sub>2</sub>GeS<sub>3</sub>. Cu<sub>8</sub>GeS<sub>6</sub> melts incongruently at 980 °C and has a phase transition at 55 °C while Cu<sub>2</sub>GeS<sub>3</sub> melts congruently at 942 °C [61]. The peritectic point (p) has a composition of 25 mol%. There are two eutectics (e1 and e2) in the system that have compositions of 43 and 90 mol% and are crystallized at 932 and 819 °C, respectively [61].



**Figure 1.5.** Phase diagram of the Cu<sub>2</sub>S–GeS<sub>2</sub> system [61].

### 1.3.2 Phase diagram of $\text{Cu}_2\text{GeSe}_3$ - $\text{Cu}_2\text{GeSe}_3$ system

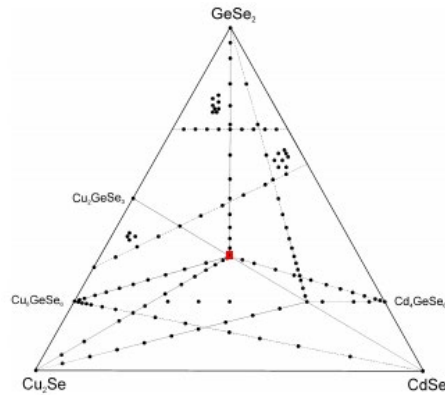
Figure 1.6 presents the phase diagram of the  $\text{Cu}_2\text{GeS}_3$ - $\text{Cu}_2\text{GeSe}_3$  system [62]. In this system, it is characterized by continuous solubility in both, solid and liquid states. From this system, the melting point of  $\text{Cu}_2\text{GeS}_3$  and  $\text{Cu}_2\text{GeSe}_3$  compounds are 940 and 780 °C, respectively.



**Figure 1.6.** Phase diagram of the  $\text{Cu}_2\text{GeSe}_3$ - $\text{Cu}_2\text{GeS}_3$  system [62].

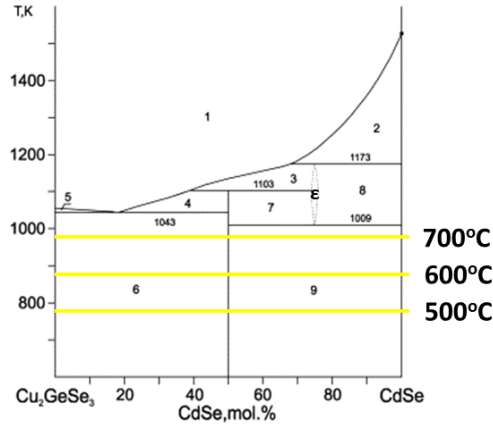
### 1.3.3 Phase diagrams of $\text{Cu}_2\text{CdGeSe}_4$ and $\text{Cu}_2\text{CdGeSe}_4$

$\text{Cu}_2\text{Se}$ - $\text{CdSe}$ - $\text{GeSe}_2$  ternary phase diagram is presented in Figure 1.7. All dots present compositions of different alloys prepared to study this system [58]. The existence region of  $\text{Cu}_2\text{CdGeSe}_4$  is indicated by a small red square in the centre. The binary and ternary compounds, which have revealed semiconductor properties are shown on the edges of triangle.



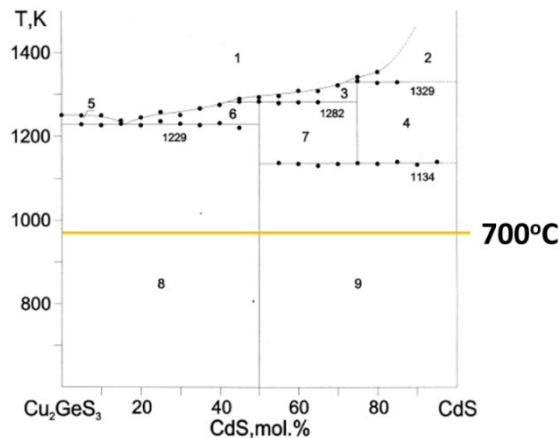
**Figure 1.7.** Phase diagram of the quasi-ternary  $\text{Cu}_2\text{Se}$ - $\text{CdSe}$ - $\text{GeSe}_2$  system [58].

Figure 1.8 presents the phase diagram of the quasi-binary section of the  $\text{Cu}_2\text{GeSe}_3$ - $\text{CdSe}$  [58]. It shows that the quaternary compound  $\text{Cu}_2\text{CdGeSe}_4$  exists in a narrow homogeneity region and melts incongruently at 830 °C in this system [58]. The regions for different phases are bordered with lines. The eutectic mixture of  $\text{Cu}_2\text{CdGeSe}_4$  and  $\text{Cu}_2\text{GeSe}_3$  melts at 770 °C. The sign  $\epsilon$  between the areas 7 and 8 in the Figure 1.8 is another quaternary phase with composition  $\text{Cu}_2\text{Cd}_3\text{GeSe}_6$ , which is formed by a peritectic process  $\text{L} + \text{CdSe} \leftrightarrow \text{Cu}_2\text{Cd}_3\text{GeSe}_6$  at 900 °C and decomposes by the eutectoid reaction  $\text{Cu}_2\text{Cd}_3\text{GeSe}_6 \leftrightarrow \text{Cu}_2\text{CdGeSe}_4 + \text{CdSe}$  at 736 °C [58]. The three yellow horizontal lines represent the temperatures at 500 °C, 600 °C and 700 °C, which are used for  $\text{Cu}_2\text{CdGeSe}_4$  monograin powder synthesis in this thesis.



**Figure 1.8.** Phase diagram of the quasi-binary section  $\text{Cu}_2\text{GeSe}_3\text{-CdSe}$ : (1) L, (2)  $\text{L}+\text{CdSe}$ , (3)  $\text{L}+\epsilon$ , (4)  $\text{L}+\text{Cu}_2\text{CdGeSe}_4$ , (5)  $\text{L}+\text{Cu}_2\text{GeSe}_3$ , (6)  $\text{Cu}_2\text{GeSe}_3+\text{Cu}_2\text{CdGeSe}_4$ , (7)  $\epsilon+\text{Cu}_2\text{CdGeSe}_4$ , (8)  $\epsilon+\text{CdSe}$ , (9)  $\text{Cu}_2\text{CdGeSe}_4+\text{CdSe}$ .

There are several studies about structural properties of pure  $\text{Cu}_2\text{CdGeSe}_4$  [48,56,57,63]. According to these studies, it might become a challenge to produce homogeneous single-phase  $\text{Cu}_2\text{CdGeSe}_4$  absorber material due to the existence of number of elements and secondary phases.



**Figure 1.9.** Phase diagram of the quasi-binary  $\text{Cu}_2\text{GeS}_3\text{-CdS}$  system: (1) L, (2)  $\text{L}+\text{CdS}$ , (3)  $\text{L}+\text{Cu}_2\text{Cd}_3\text{GeS}_6$ , (4)  $\text{CdS}+\text{Cu}_2\text{Cd}_3\text{GeS}_6$ , (5)  $\text{L}+\text{Cu}_2\text{GeS}_3$ , (6)  $\text{L}+\text{Cu}_2\text{Cd}_3\text{GeS}_6$ , (7)  $\text{Cu}_2\text{CdGeS}_4+\text{Cu}_2\text{Cd}_3\text{GeS}_6$ , (8)  $\text{Cu}_2\text{GeS}_3+\text{Cu}_2\text{CdGeS}_4$ , (9)  $\text{Cu}_2\text{CdGeS}_4+\text{CdS}$ .

The phase diagram of the  $\text{Cu}_2\text{GeS}_3\text{-CdS}$  system (Figure 1.9) was investigated by Piskach *et al.* [53].  $\text{Cu}_2\text{CdGeS}_4$  melts incongruently at 1009 °C. The eutectic forms between  $\text{Cu}_2\text{GeS}_3$  and  $\text{Cu}_2\text{CdGeS}_4$  at 956 °C. There are two intermediate quaternary phases with peritectic type of melting in the system. The first one is formed at 1056 °C according to the reaction  $\text{L}+\text{CdS}\rightleftharpoons\text{Cu}_2\text{Cd}_3\text{GeS}_6$ . It is unstable and decomposes at 861 °C. In the case of  $\text{Cu}_2\text{CdGeS}_4$ , the temperature of the peritectic process  $\text{L}+\text{Cu}_2\text{Cd}_3\text{GeS}_6\rightleftharpoons\text{Cu}_2\text{CdGeS}_4$  is 1009 °C. It possesses narrow homogeneity range [53]. The temperature at 700 °C (yellow horizontal line in Figure 1.9) is used for the monograin powder synthesis in this thesis.

### 1.3.4 Phase diagram of $\text{Cu}_2\text{CdGeSe}_4\text{-Cu}_2\text{CdGeSe}_4$

In the Figure 1.10 is shown the phase diagram of the  $\text{Cu}_2\text{CdGeS}_4\text{-Cu}_2\text{CdGeSe}_4$  section. The system is quasi-binary below solidus and contains a continuous  $\gamma$ -solid solution series [63]. The liquidus of the  $\text{Cu}_2\text{CdGeS}_4\text{-Cu}_2\text{CdGeSe}_4$  section is the line of the primary crystallization of  $\zeta$ -solid solutions of the quaternary phases  $\text{Cu}_2\text{Cd}_3\text{GeS}_6$  and  $\text{Cu}_2\text{Cd}_3\text{GeSe}_6$ . These phases take part in the peritectic processes of the formation of the section components ( $\text{L}+\text{Cu}_2\text{Cd}_3\text{GeX}_6\rightleftharpoons\text{Cu}_2\text{CdGeX}_4$ ) [53]. Below the field of the primary crystallization of  $\zeta$ -solid solutions, the field of the co-existence of three phases L,  $\gamma$  and  $\zeta$  appears. This field is a part of the volume of the secondary crystallization of the binary peritectic  $\text{L}+\zeta\rightleftharpoons\gamma$  [63].

As  $\gamma$ -phase is the continuous solid solution series of isostructural compounds  $\text{Cu}_2\text{CdGeS}_4$  and  $o\text{-Cu}_2\text{CdGeSe}_4$ , this explains the absence of a two-phase field between the single-phase and the three-phase fields. Below 600 °C,  $\gamma$ -solid solutions undergo solid-state decomposition into  $\delta$ -solid solution range of  $\text{Cu}_2\text{CdGeS}_4$  and  $t\text{-Cu}_2\text{CdGeSe}_4$ . At 400 °C, the  $\gamma$ -solid solutions range from 0 to 89 mol%  $\text{Cu}_2\text{CdGeS}_4$ , from 90 to 98 mol%  $\text{Cu}_2\text{CdGeSe}_4$  exist both - the orthorhombic symmetry typical of  $\gamma$ -solid solutions and the tetragonal symmetry characteristic of  $\delta$ -solid solution range of  $t\text{-Cu}_2\text{CdGeSe}_4$ . The extent of  $\delta$ -solid solutions was observed in the limited alloy region  $x < 0.02$  in  $\text{Cu}_2\text{CdGe}(\text{S}_x\text{Se}_{1-x})_4$  [63].

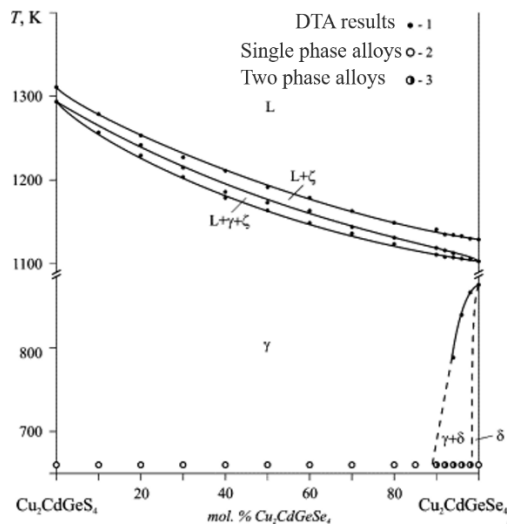


**Figure 1.10.** Phase diagram of the  $\text{Cu}_2\text{CdGeS}_4\text{-Cu}_2\text{CdGeSe}_4$  section [63].

## 1.4 Optical and electrical properties of $\text{Cu}_2\text{Ge}(\text{S,Se})_3$ and $\text{Cu}_2\text{CdGe}(\text{S,Se})_4$

### 1.4.1 Photoluminescence properties of $\text{Cu}_2\text{Ge}(\text{S,Se})_3$

There are only few papers about the defect structure of  $\text{Cu}_2\text{GeS}_3$ ,  $\text{Cu}_2\text{GeSe}_3$  and their solid solutions. Robert *et al.* [50] reported photoluminescence (PL) studies, where only the monoclinic  $\text{Cu}_2\text{GeS}_3$  showed PL emission with peak maximum at 1.57 eV. They assigned it to the band-to-band transition. In the same study, the bandgaps of the cubic phase and monoclinic phase of  $\text{Cu}_2\text{GeS}_3$  were determined from absorption measurements to be 1.23 and 1.55 eV, respectively. They attributed this difference between cubic and monoclinic to the higher quasi fermi level splitting of the monoclinic phase [50].



According to the study [55], for  $\text{Cu}_2\text{GeSe}_3$  compound, three PL bands were detected. The peak positions at 0.637 and 0.753 eV were assigned to free-to-bound recombination from the conduction band to acceptor states and peak position at 0.727 eV was assigned to recombination of an exciton bound to an ionized acceptor.

#### 1.4.2 Optical and electronic properties of $\text{Cu}_2\text{CdGe}(\text{S},\text{Se})_4$

There are few studies reported about optical properties of the  $\text{Cu}_2\text{CdGeSe}_4$  compound. Recently, Grossberg *et al.* [64] presented detailed PL analysis for orthorhombic and tetragonal  $\text{Cu}_2\text{CdGeSe}_4$ , which revealed different dominating radiative recombination mechanisms. The PL spectrum of *t*- $\text{Cu}_2\text{CdGeSe}_4$  included one PL band at 1.053 eV showing different behaviour at low ( $T < 50$  K) and high ( $T > 50$  K) temperatures. The low-temperature process was attributed to the thermal redistribution of electrons between the localized energy levels near the conduction band edge. At higher temperatures was proposed band-to-impurity recombination involving acceptor states. The PL spectrum of *o*- $\text{Cu}_2\text{CdGeSe}_4$  included three PL bands at 1.027 eV, 1.146 eV and 1.218 eV. Strong dependence of the PL band at 1.218 eV was found to originate from tail-to-impurity recombination involving an acceptor defect and electrons localized in potential wells created by clusters of donor defects [64]. Krustok *et al.* [65] reported the excitation power and temperature dependences of the steady-state PL spectra in polycrystalline  $\text{Cu}_2\text{CdGeSe}_4$  containing a mixture of orthorhombic and tetragonal phases. In that study, the low-temperature excitation power dependences of the PL peak shape with a peak position at about 1.17 eV indicated a state filling effect. Reflectivity measurements revealed the band gap energies 1.257 eV and 1.223 eV at 10 K and 300 K, respectively. Additionally, the asymmetric PL band shape analysis indicated the presence of hot carriers having a temperature about 75 K higher than the lattice temperature. It was shown that the low-temperature PL emission is due to recombination of localized electrons with holes captured by the deep acceptor defect  $\text{Cu}_{\text{Cd}}$  with a depth  $E_A = 80$  meV [65].

The electronic properties of the  $\text{Cu}_2\text{CdGeS}_4$  compound were studied based on first-principles density functional theory (DFT) calculations as incorporated in the CASTEP (CAmbridge Serial Total Energy Package) module of the Materials Studio package [66]. The DFT-calculations have established that  $\text{Cu}_2\text{CdGeS}_4$  is a direct gap semiconductor. Additionally, the valence band maximum (VBM) of  $\text{Cu}_2\text{CdGeS}_4$  is formed by the relatively localized Cu 3d states while the unoccupied Ge 4p, 4s states are the dominant contributors to the conduction band maximum (CBM), therefore the d-p charge transfer plays the most important role in this compound [66]. The Ge-S and Cd-S bonds are mainly of covalent type while the Cu-S bonds are more ionic in  $\text{Cu}_2\text{CdGeS}_4$  [66]. Furthermore, the DFT-calculations of dependencies of the lattice parameters upon pressure indicated that all three lattice parameters  $a$ ,  $b$  and  $c$  decrease linearly with pressure and the largest compressibility of the  $\text{Cu}_2\text{CdGeS}_4$  compound is realized along the  $b$  crystallographic axis (Figure 1.3) [66]. Davidyuk *et al.* [67] reported that the  $\text{Cu}_2\text{CdGeS}_4$  are *p*-type, the band gap of  $\text{Cu}_2\text{CdGeS}_4$  evaluated from the position of its fundamental absorption edge is  $E_g \approx 2.05$  eV at room temperature [67]. According to [43], a detailed analysis of radiative recombination in  $\text{Cu}_2\text{CdGeS}_4$  microcrystals was studied by temperature and laser power dependent photoluminescence spectroscopy that revealed the origin for the detected low-temperature ( $T = 10$  K) PL bands as donor-acceptor pair recombination. Three PL bands – 1.919 eV, 1.855 eV and 1.748 eV were detected, where the 1.919 eV and 1.855 eV bands included more distant donor-acceptor pairs with relatively shallow acceptor (probably  $V_{\text{Cu}}$ ) and deep donor

defects. The 1.748 eV PL band resulted from the deep donor—deep acceptor recombination [43]. The manifestation of shallow acceptor defects showed that this material does not have deep potential or band gap fluctuations and could be used in photovoltaic applications.

### 1.4.3 Band gap engineering

The semiconductors can be suitable materials for photovoltaic applications by absorbing the incident photons to create electron-hole pairs. The choice of the absorber material with appropriate bandgap is very important while considering the absorption of the solar radiation. The maximum light to electric power conversion efficiency for AM 1.5G illumination, based on Shockley and Queisser’s detailed balance considerations is around 30% and requires a semiconductor band gap between 1.0 and 1.5 eV (Figure 1.11) [13].

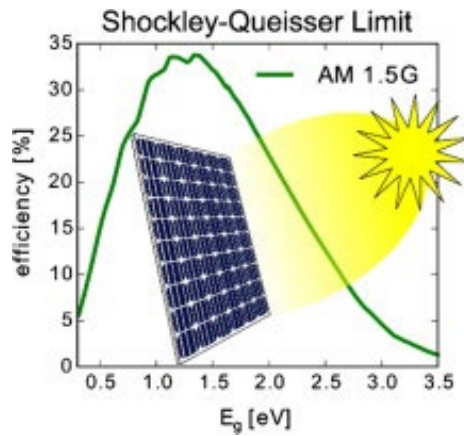


**Figure 1.11.** The maximum light to electric power conversion efficiency (detailed balance limit) as a function of the band gap energy for a solar cell operated at RT and illuminated with the AM 1.5G spectral irradiance in accordance with standard solar test conditions [13].

There are several studies, where  $\text{Cu}_2\text{ZnSn}(\text{S},\text{Se})_4$  solid solutions as solar cell absorber materials with optimum band gap value ( $\sim 1.3$  eV) were produced by modifying the S/Se concentration ratio and thereby increasing the value of  $V_{OC}$  [12,16,21,68–70]. Additionally, cation substitution of Zn by Cd [71–73] in  $\text{Cu}_2\text{ZnSnS}_4$  absorber materials enables to decrease the optical band gap from 1.55 to 1.35 eV [72] and Sn by Ge [44, 74–76] enables to increase from 1.55 to 2.1 eV [44]. Therefore, it offers new opportunities in the development of highly efficient photovoltaic devices based on quaternary compounds. In addition to the change in the defects system, the replacement of Zn by Cd can also facilitate the grain growth and suppress the formation of secondary phase ZnS [71]. Su *et al.* [77] reported that the grain sizes of  $\text{Cu}_2\text{ZnSnS}_4$  thin films are improved significantly due to the effect that Cd (due to the low melting point  $T_M = 321$  °C [78]) acts as a flux which assists in grain growth, and the ZnS secondary phase can be reduced with appropriate ratio of Zn/Cd in  $\text{Cu}_2\text{ZnSnS}_4$  solar cells [77]. Therefore, Cd alloying in kesterite has drawn considerable attention. Su *et al.* reported a significant device performance improvement and achieved 12.6% by Cd-alloyed  $\text{Cu}_2\text{ZnSnS}_4$  thin-film solar cell [71]. As for Sn substitution by Ge, Kim *et al.* [73] reported that over 12% device performance was achieved via an optimized thermal annealing at 500–550°C in  $\text{GeSe}_2$

atmosphere. This optimized thermal annealing led to lower  $V_{oc}$  deficit by reducing band tailing, and reduced carrier recombination at the absorber/buffer interface and/or in the space-charge region. Therefore, band gap engineering is a promising method to get ideal band gap and thereby to obtain close to maximum theoretical efficiency of solar cell.

As noted above, the pure  $Cu_2CdGeSe_4$  have two different crystal structures – an orthorhombic and a tetragonal, which have the band gaps 1.29 eV [58] and 1.2 eV at room temperature, as reported by Marushko *et al.* [63]. The pure  $Cu_2CdGeSe_4$  compound is found to be *p*-type semiconductor with the band gap energy of 2.05 eV at room temperature [63]. This value is close to those ( $E_g = 1.9–2.0$  eV) determined by measuring the spectra of the diffuse reflection of light in  $Cu_2CdGeSe_4$  single crystals [59].

For  $Cu_2GeS_3$ , the band gap values between 1.5–1.6 eV have been reported [25,26,28,50]. It is reasonable to believe, that somewhat different reported  $E_g$  values are related to coexistence of different crystal structures, as  $Cu_2GeS_3$  could exist in both cubic and monoclinic structure. In several papers, it has been observed that pure  $Cu_2GeSe_3$  crystallized in an orthorhombic structure with the band gap around 0.78 eV [51,55].

To sum up, the band gaps of  $Cu_2GeSe_3$  and  $Cu_2CdGeSe_4$  can be modified by adjusting the concentration ratio of chalcogenides (S/Se) in the  $Cu_2Ge(S_xSe_{1-x})_3$  and  $Cu_2CdGe(S_xSe_{1-x})_4$  solid solutions – the band gap changes in the range from 0.78 to 1.6 eV and 1.2 to 2 eV, respectively [50,55,59,63]. In this thesis, the band gap is varied by changing the ratio of chalcogens (S/Se) in  $Cu_2Ge(S_xSe_{1-x})_3$  and  $Cu_2CdGe(S_xSe_{1-x})_4$  solid solutions and the optimal ratios for absorber materials in monograin layer solar cells will be determined.

## 1.5 Monograin powder technology

### 1.5.1 Molten salt synthesis of monograin powder

In order to reduce the energy consumption and to achieve cost reductions during the preparation of solar cell [79], one of alternative approaches is to synthesize absorber materials by using molten salt method [80].

Many studies have been performed on the formation of the multinary chalcogenide compounds by using molten salt synthesis method [81–86]. This method has advantages of the simplicity in the process equipment, versatile and large-scale synthesis, and friendly environment, which provides an approach to synthesize high purity multinary compound powders with controllable compositions and morphologies. Zhang *et al.* [81] reported two phases for binary  $Ga_2S_3$ - cubic and monoclinic were synthesized with and without KI as flux material. This finding demonstrates apparently how a flux can divert the reaction pathway and lead to a different product. In another study, the morphology of  $CoS_2$  compound was adjusted from the irregular to polyhedral particle by using the flux (KCl) for the crystal growth [82]. The same reaction in the absence of the flux resulted in a product with the same composition, however in the form of smaller single crystals. In addition, Huber *et al.* [84] formed successfully single crystals of  $Li_3AsS_3$  in Lil flux at 450 °C, lower than the melting point of Lil (469 °C) [84]. Leinemann *et al.* [87] found a similar phenomenon of lowering the melting point of fluxes (KI,  $CdI_2$ ). It could be explained by different processes taking place in parallel in the molten salt synthesis process – some part of solid precursors (for example binaries CuS, CuSe, CdS, CdSe) being in contact with the used flux begin to dissolve in it and therefore the melting temperature of the flux decreases. In short, the particle size and optical properties of the compound crystals can be adjusted by using different fluxes and reaction temperatures.

In this thesis, the monograin powders were formed by isothermal heating of precursor materials in the presence of liquid phase of a suitable flux. The monograin powder production process has many advantages for the synthesis of ternary and quaternary compounds. The main one is that synthesis in flux has a great potential to obtain high crystallinity of grains and thus potentially good optoelectronic properties [88]. For the monograin powders growth, the melting point of the used flux should be lower than the melting point of desired semiconductor compound [89]. Herein, it is worth noting that in the monograin powder synthesis-growth process, the forming crystals can be doped with constituent elements of flux as impurities at the level of saturation at process temperature [90]. Furthermore, such factors as the synthesis temperature, the nature and amount of a flux are important for the characteristics of monograin powder crystals. The criterion for the growth of single grains is that the amount of flux should be sufficient to fill the whole free space between initial particles.

### 1.5.2 Flux materials

Molten salts have proven to be useful to enhance the rate of solid-state reactions and to allow fast diffusion of constituent elements through liquid phase. The synthesis of multicomponent compounds in the liquid phase of a flux provides uniform composition of produced materials [91]. In addition to exploratory crystal growth, the molten fluxes have been used to recrystallize polycrystalline powders, control crystal morphology and structure [80]. There are many different halide salts suitable as flux materials, but the following conditions should be fulfilled – lower melting point than main material, low vapour pressure at growth temperature and high solubility in water for easy separation of the powder particles from the fluxes after growth process [86]. Several flux materials have been used such as CsBr, NaI, LiI, KCl, KI, CdI<sub>2</sub>, and several mixed fluxes including KCl/KI, NaBr/KBr, NaBr/CsBr, KI/KNO<sub>3</sub> [72,80,83,84,89,92,93].

Before this thesis, the Taltech research group have investigated the synthesis of many different compounds in liquid phase of flux materials including CdTe, Cu<sub>2</sub>ZnSnS<sub>4</sub>, CuInSe<sub>2</sub> and others. Among them, CdTe, CuInSe<sub>2</sub> and Cu<sub>2</sub>ZnSnSe<sub>4</sub> monograin powders were synthesized by using different fluxes – Se, CuSe and CdI<sub>2</sub> [87,88]. Timmo *et al.* [83] presented the influence of CdI<sub>2</sub>, SnCl<sub>2</sub> and KI fluxes on the synthesis of binary SnS monograin powders. Furthermore, ternary Cu(In,Ga)Se<sub>2</sub> and quaternary (Cu,Ag)<sub>2</sub>(Cd,Zn)SnS<sub>4</sub> were grown in KI flux [94,95]. In this thesis, LiI, KI and CdI<sub>2</sub> as flux materials were used.

Lithium iodide (LiI) is a white crystalline solid. The melting point of LiI is 469 °C [78]. LiI has high solubility in water (1670 g/L in H<sub>2</sub>O at 25 °C) [78]. LiI is hygroscopic and readily oxidized in air to discolour the crystals [78]. Therefore, the preparation of synthesis powders requires a dry and inert gas environment (such as glove box).

Melting temperature of potassium iodide (KI) is  $T_M = 681$  °C. It is higher than  $T_M$  of cadmium iodide ( $T_M = 387$  °C) and therefore, the doping of the synthesized material with potassium and iodine is highly probable [93]. Although KI is rather stable in dry air, the decomposition of it can be accelerated when exposed to light and moisture. The aged and impure KI will turn yellow due to the instability of KI in air, which is caused by the slow oxidation of the salt to potassium carbonate and elemental iodine [93]. Although the solubility will be higher with the increasing of the temperature, the solubility of CdI<sub>2</sub> in water at 25 °C is 847 g/L while the solubility of KI is 1400 g/L at the room temperature [78].

### 1.5.3 Monograin layer solar cells

The monograin layer (MGL) solar cell technology has generated a rising interest in reducing the cost of producing the solar cell. The production of absorber materials and fabrication of solar cell by using this technology could be done separately, which indicates the possibility of lowering the producing cost of flexible solar cells [96]. Despite the advantages of MGL solar cells technology, there are some technological limitations for its rapid development. Such as the limitation of the working area of membrane due to the existence of epoxy between the powder crystals, the requirement of almost equal size powder grains and perfect mono-crystalline structure, surface modification of monograins and so on [96].

The structure of typical MGL solar cell (Au/absorber crystals/CdS/*i*-ZnO/ZnO:Al) is presented in Figure 1.12. All synthesized monograin powders require chemical etching and post-annealing at elevated temperatures before using them as absorber materials in monograin layer solar cells. The absorber surface modification processes are discussed in the section 1.6. Then, the formation of heterojunction is processed prior to embedding the crystals into a polymer. Standard process for buffer layer deposition is chemical bath deposition method. After that, the photoactive membranes are formed by using nearly unisize and compact shape crystals embedded in the thin layer of organic resin (epoxy).

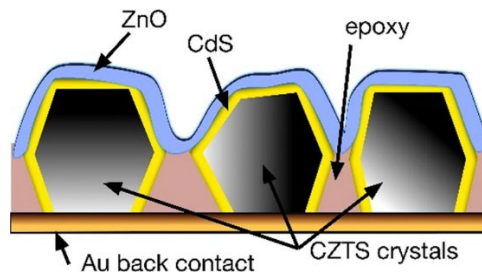


**Figure 1.12.** The device structure of MGL solar cell: gold back contact/absorber crystal/CdS buffer/*i*-ZnO/ZnO:Al window layer [69].

In this step, many issues could be rise, which affect later the performance of monograin layer solar cells. Most important is to ensure that the crystals reach out from polymer almost 50% of grain size and remain uncovered by epoxy (Figure 1.13b and c). Also, the packing density of crystals in polymer layer is important (Figure 1.13a). Calculations have shown that average packing density (active area) is about 75% [95]. Completely polymerized membranes are covered with transparent conductive oxide layer (*i*-ZnO and ZnO:Al) by radio-frequency magnetron sputtering. Finally, the structure is glued onto a durable substrate.

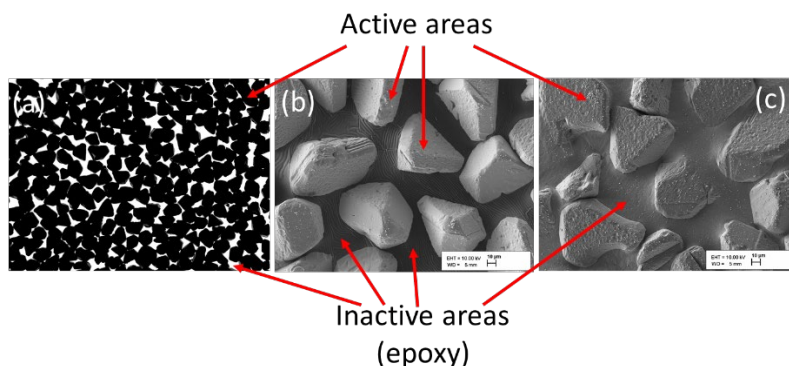


**Figure 1.13.** (a) Planar image of the packing density of crystals in the membrane, (b) Top view of membrane, where crystals are half embedded into the epoxy and (c) more than half inside the epoxy [96].

After removing the supporting plastic foil from the top of the structure, the powder crystals are released from epoxy by concentrated  $\text{H}_2\text{SO}_4$  followed by polishing with ultrafine sandpaper. Back contact is formed by applying contact material (graphite or metal) on the back side of the crystals [97].

## 1.6 Absorber surface modification

The homogeneous active interface of the  $p$ -type absorber plays a key role in solar cell performance. Commonly, Cu-poor and Zn-rich composition of absorber material is used in the kesterite-type solar cells. According to phase diagrams [98,99], the single phase area for CZTS is about 2 mol% and for CZTSe around 7 mol% at 400 °C, which leads often to the formation of undesired secondary or ternary phases in the synthesis process. Under these conditions, several binary or ternary phases could be present. For example, the high series resistance of device is attributed to the  $\text{ZnS}(\text{Se})$  phase in kesterite absorber layer, which will decrease the fill factor and short circuit current of solar cell [100]. Low band gap phases  $\text{Cu}_2\text{SnS}(\text{Se})_3$  ( $E_g \approx 0.8\text{--}1$  eV) may limit the open circuit voltage of the solar cells, due to a lower band gap than that of the kesterites [100]. Additionally,  $\text{Cu}_x\text{S}(\text{Se})$  is considered highly detrimental in kesterite materials, which will severely increase the hole concentration and cause short circuits of the  $p$ - $n$  junction, clearly decreases the efficiency of solar cells [100]. Analogous to the kesterites, the challenges of this study were to synthesize uniform single phase ternary  $\text{Cu}_2\text{Ge}(\text{Se},\text{S})_3$  and quaternary  $\text{Cu}_2\text{CdGe}(\text{Se},\text{S})_4$  monograin powders with off-stoichiometric compositions. As discussed above in section 1.3 (Figure 1.7), in the system of the  $\text{Cu}_2\text{Se}$ - $\text{CdSe}$ - $\text{GeSe}_2$  ternary phase diagram [58] may form some undesired phases, such as  $\text{GeSe}$  phase in Ge-rich region, and in the Cu-rich region, the existence of  $\text{Cu}_2\text{Se}$  phase could appear and in the Cd-rich side could form  $\text{CdSe}$  as secondary phase.

In addition, in the monograin powder growth process, some part of the precursors (for example  $\text{CuS}$ ,  $\text{CuSe}$ ,  $\text{CdS}$ ,  $\text{CdSe}$  and  $\text{Ge}$ ) and the formed absorber materials may partially dissolve in the molten flux salt at growth temperature, and the dissolved part precipitates on the solid crystal surfaces during the cooling period [101]. The surface morphology and the composition of the absorber crystal surface will be changed due to the existence of these precipitations. Usually, these conditions result in the formation of the undesired secondary and ternary phases in addition to main compound. Therefore,

the removal of secondary phases from the surface of the powder crystals synthesized in the present study is one of the main challenges to improve the performance of monograin layer solar cells. Various chemical etchants can be used to remove these undesired secondary phases. KCN chemical etching approach, originally developed for the removal of  $\text{Cu}_x\text{Se}$  phases in  $\text{Cu}(\text{In,Ga})(\text{S,Se})_2$  thin films [102], is now applied also in many kesterite studies [103,104]. HCl etching for the selective removal of Zn-rich secondary phases in kesterite is shown in [105–107] and the effectiveness of bromine in methanol ( $\text{Br}_2\text{-MeOH}$ ) etchant to remove Cu- and Sn-based secondary phases is presented in the several studies [106–108]. It is known that CdSe crystals dissolve in a  $\text{HNO}_3 + \text{HCl}$  mixture [109], in the concentrated HCl and in the  $\text{Br}_2\text{-MeOH}$  solutions [110]. In this study, CdSe secondary phases were removed by using 1% v/v  $\text{Br}_2\text{-MeOH}$  solution or 10% v/v HCl solution, followed by KCN solution to remove Se,  $\text{Cu}_x\text{Se}$  and GeSe phases.

After chemical etching, it is essential to anneal the powders at elevated temperatures before implementing the powder crystals as absorber materials in monograin layer solar cells. Several groups reported that an effective method to improve the quality of the thin-film absorber materials ( $\text{Cu}_2\text{ZnSnS}_4$ ,  $\text{Cu}_2\text{ZnSnSe}_4$  and  $\text{Cu}_2\text{ZnSn}(\text{S,Se})_4$ ) is to do post-annealing around 500–650 °C, thereby improve the solar cell performance [11,17,101,108,111]. Kauk-Kuusik *et al.* [101] emphasized that after the chemical etching, the annealing temperature is crucial to heal the surface of monograin powders for the final performance of  $\text{Cu}_2\text{ZnSnSe}_4$  MGL solar cells. IREC group indicated that the improvement of device performance is partly attributed to the post-annealing treatment of the full solar cells, which resulted more Cu poor and Zn rich absorber surface [111].

In this thesis, the comparative investigations of the influence of different etchants such as  $\text{Br}_2\text{-MeOH}$ , KCN and HCl followed by isothermal annealing at different temperatures on the performance of monograin layer solar cells were carried out.

## 1.7 Summary of literature review and the aim of the study

In the last few years, the interest and research on new inorganic materials for photovoltaic applications have largely increased. Among them, kesterite type semiconductors, including  $\text{Cu}_2\text{ZnSn}(\text{S,Se})_4$  is recognized as one of the most relevant and promising thin film photovoltaic technologies. Although the performance has been renewed up to 14% in 2022, the progress of efficiency is rather slow and several fundamental issues are still unsolved. Therefore, new alternative materials and related technologies should be considered in order to contribute to the predicted and necessary increase in electricity generation by photovoltaics.

Cation replacement in kesterite type materials is one of the most promising methods to tune the optical band gap and offers new opportunities in the development of highly efficient photovoltaic devices. Among them, Sn by Ge and Zn by Cd replacements have been considered and shown a successful strategy to improve the efficiency for solar cell devices. Sn substitution by Ge is considered due to the most stable oxidation states of these two elements, Ge is more likely to present +4 than Sn, thus avoiding the presence of potentially harmful +2 oxidation states [17,20]. Cation substitution of Zn by Cd in kesterite system is expected to reduce the  $\text{Cu}_{\text{Cd}}$  and  $\text{Cd}_{\text{Cu}}$  antisite defects due to the ionic radius of  $\text{Cd}^{2+}$  (0.92 Å) is larger than that of  $\text{Cu}^+$  and  $\text{Zn}^{2+}$  (both 0.74 Å), thereby suppressing the cation disorder, secondary phase formation and band tailing issues in kesterite system [20,39]. In view of the above given, quaternary  $\text{Cu}_2\text{CdGe}(\text{S,Se})_4$  or Cd-free ternary  $\text{Cu}_2\text{Ge}(\text{S,Se})_3$  compounds are considered as alternatives, but have been less studied. Ternaries  $\text{Cu}_2\text{GeS}_3$ ,  $\text{Cu}_2\text{GeSe}_3$  and their solid solutions have many promising

properties for absorber materials, including *p*-type conductivity and a direct band gap energy ( $\sim 0.8\text{--}1.5$  eV depending on the S/Se ratio) [24,28]. The best power conversion efficiencies for  $\text{Cu}_2\text{GeS}_3$  and  $\text{Cu}_2\text{Ge}(\text{Se}_{0.33}\text{S}_{0.67})_3$  thin film solar cells are 2.67% [28] and 0.2% [40], respectively. Quaternary  $\text{Cu}_2\text{CdGeSe}_4$  has also suitable properties for absorber material in the single junction solar cell such as high absorption coefficient ( $> 10^4 \text{ cm}^{-1}$ ), *p*-type conductivity and direct band gap energy ( $\sim 1.2$  eV) [49]. Incorporation of S into the  $\text{Cu}_2\text{CdGeSe}_4$  and the properties of solid solutions are also less discussed. With regard to  $\text{Cu}_2\text{CdGeS}_4$ , which has too wide band gap ( $\sim 2$  eV) for single junction solar cells, it can be used in many different devices, such as a top cell absorber material in a tandem solar cell structure or as a photoelectrode in photo-electrochemical water splitting devices [112]. However, no paper has reported the characteristics of solar cells based on these materials.

In this thesis, monograin powders formed by molten salt synthesis-growth method and monograin layer solar cell technology has been used to evaluate the applicability of  $\text{Cu}_2\text{Ge}(\text{S,Se})_3$  and  $\text{Cu}_2\text{CdGe}(\text{S,Se})_4$  as absorber materials for photovoltaics. Monograin layer solar cell technology has generated a growing interest in reducing solar cell production costs. With this technology, the preparation of the absorber material and the fabrication of solar cells can be completed separately, which makes it possible to produce light-weight, flexible and less expensive solar cells [96].

Based on the literature review and knowledge gap about  $\text{Cu}_2\text{Ge}(\text{S,Se})_3$  and  $\text{Cu}_2\text{CdGe}(\text{S,Se})_4$  as absorber materials for photovoltaics, the objectives of the present doctoral thesis were:

- ❖ to synthesize  $\text{Cu}_2\text{CdGeSe}_4$  monograin powders in the liquid phase of molten salts (KI and  $\text{CdI}_2$ ) with two different crystal structure and to study the compositional and structural properties of  $\text{Cu}_2\text{CdGeSe}_4$  powders and monograin layer solar cells based on these absorber materials;
- ❖ to study the effect of initial Cu and Cd content on the bulk composition of grown orthorhombic  $\text{Cu}_2\text{CdGeSe}_4$  crystals and to modify the crystal surface properties by chemical etching and post-annealing with the aim to improve the performance of orthorhombic  $\text{Cu}_2\text{CdGeSe}_4$  monograin layer solar cells;
- ❖ to investigate the effect of S/Se ratio in  $\text{Cu}_2\text{CdGe}(\text{S}_x\text{Se}_{1-x})_4$  ( $x = 0 - 1$ ) solid solutions of monograin powders synthesised in KI molten salt on the morphology, structural and compositional properties of  $\text{Cu}_2\text{CdGe}(\text{S}_x\text{Se}_{1-x})_4$  monograin powders and photovoltaic properties of monograin layer solar cells based on these powders;
- ❖ to synthesize  $\text{Cu}_2\text{Ge}(\text{Se}_x\text{S}_{1-x})_3$  ( $x = 0 - 1$ ) solid solutions of monograin powders in LiI molten salt and to investigate the effect of S/Se ratio on the morphology, structural, compositional and optical properties of  $\text{Cu}_2\text{Ge}(\text{Se}_x\text{S}_{1-x})_3$  monograin powders and photovoltaic properties of monograin layer solar cells based on these powders.



## 2 Experimental

The main experimental features are summarized in this section. In addition, the experimental procedure is illustrated in Figure 2.1. More details of the experiments are published in Papers I–V.

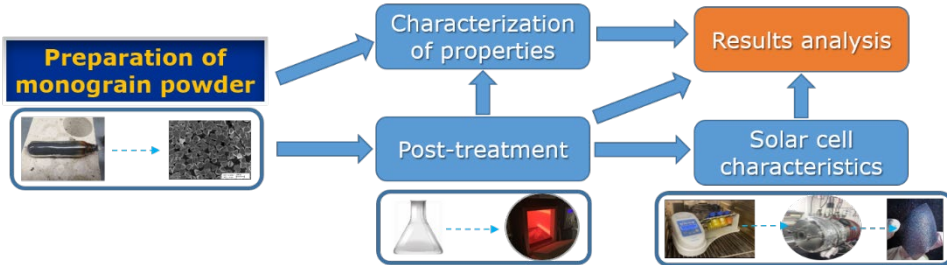


**Figure 2.1** The schematic of experimental procedure.

### 2.1 Preparation of $\text{Cu}_2\text{CdGe}(\text{S,Se})_4$ monograin powders

$\text{Cu}_2\text{CdGe}(\text{Se,S})_4$  monograin powder materials studied in this thesis were synthesized from commercially available CdSe, self-synthesized CuSe, elemental Ge powder, Se shots [published in Paper I, II] and S powder [published in Paper III] in the molten salts. Two different salts – cadmium iodide ( $\text{CdI}_2$ ) and potassium iodide (KI) – were used as fluxes. All used materials and fluxes are purchased from the company of Alfa Aesar. The used flux salt was added with the mass ratio of  $m_{\text{precursors}}/m_{\text{flux}} = 1 : 1$ . In the Paper I, the precursors for synthesis of  $\text{Cu}_2\text{CdGeSe}_4$  were weighted in the molar ratio of elements 2 : 1 : 1 : 4. The preparation conditions of  $\text{Cu}_2\text{CdGeSe}_4$  monograin powders are summarized in Table 2.1.

**Table 2.1** Preparation conditions for the synthesis of  $\text{Cu}_2\text{CdGeSe}_4$  monograin powders.

Sample name	Used flux	$T_{\text{synth}}$ , °C	$t_{\text{synth}}$ , h	Cu, at%	Cd, at%	Ge, at%	Se, at%	[Cu]/([Cd]+[Ge])	[Cd]/[Ge]	Ref.
CCGSe-101	$\text{CdI}_2$	500	120							
CCGSe-102	$\text{CdI}_2$	600	120							
CCGSe-103	$\text{CdI}_2$	700	120	25.0	12.5	12.5	50.0	1.0	1.0	[I]
CCGSe-104	KI	700	60							
CCGSe-105	KI	700	120							

In the Paper II, the chemical composition of  $\text{Cu}_2\text{CdGeSe}_4$  quaternary compound was investigated by varying the Cu and Cd content in  $\text{Cu}_{2-x}\text{Cd}_y\text{GeSe}_4$  ( $x = 0.1; 0.15; 0.2$  and  $y = 1.0; 1.05; 1.1$ ) powder materials. Initial compositions of  $\text{Cu}_{2-x}\text{Cd}_y\text{GeSe}_4$  powders are summarised in Table 2.2. These powders were synthesized from similar precursors as mentioned above in the liquid phase of KI flux material at 700 °C.

**Table 2.2** Initial composition of  $\text{Cu}_{2-x}\text{Cd}_y\text{GeSe}_4$  powders with different Cu and Cd content.

Sample name	x	y	Cu, at%	Cd, at%	Ge, at%	Se, at%	[Cu]/([Cd]+[Ge])	[Cd]/[Ge]	Ref.
CCGSe-201	0.1	1.0	24.4	12.8	12.8	50.0	0.95	1.0	
CCGSe-202	0.1	1.05	24.1	13.3	12.7	50.0	0.93	1.05	
CCGSe-203	0.15	1.02	23.9	13.2	12.9	50.0	0.92	1.02	
CCGSe-204	0.1	1.1	23.8	13.8	12.5	50.0	0.90	1.1	[II]
CCGSe-205	0.15	1.1	23.4	13.9	12.7	50.0	0.88	1.1	
CCGSe-206	0.2	1.1	23.1	14.1	12.8	50.0	0.86	1.1	

According to  $\text{Cu}_2\text{CdGeS}_4\text{--Cu}_2\text{CdGeSe}_4$  phase diagram [66], there exist  $\gamma$ -solid solutions formed at 602 °C between  $\text{Cu}_2\text{CdGeS}_4$  and  $\text{Cu}_2\text{CdGeSe}_4$  with the orthorhombic structure, and a small range of  $\delta$ -solid solution formed between  $\text{Cu}_2\text{CdGeS}_4$  and  $\text{Cu}_2\text{CdGeSe}_4$  with the tetragonal structure. In the Paper III, the  $\gamma$ -phase of  $\text{Cu}_{1.91}\text{Cd}_{1.05}\text{Ge}_{1.03}(\text{S}_x\text{Se}_{1-x})_4$  ( $x = 0; 0.2; 0.4; 0.6; 0.8; 1$ ) monograin powders were synthesized in KI flux at 700 °C. The initial composition of  $\text{Cu}_2\text{CdGe}(\text{S}_x\text{Se}_{1-x})_4$  powders with different S/Se ratio are summarized in Table 2.3.

**Table 2.3** Initial composition of  $\text{Cu}_2\text{CdGe}(\text{S}_x\text{Se}_{1-x})_4$  powders with different S/Se ratio synthesized in KI.

Sample name	Cu, at%	Cd, at%	Ge, at%	Se, at%	S, at%	[Cu]/([Cd]+[Ge])	[Cd]/[Ge]	[S]/([S]+[Se])	Ref.
CCGSe-S0.0				50.0	0			0	
CCGSe-S0.2				40.0	10.0			0.2	
CCGSe-S0.4	23.9	13.2	12.9	30.0	20.0	0.92	1.02	0.4	[III]
CCGSe-S0.6				20.0	30.0			0.6	
CCGSe-S0.8				10.0	40.0			0.8	
CCGSe-S1.0				0	50.0			1.0	

Additionally, four  $\text{Cu}_2\text{CdGe}(\text{S}_x\text{Se}_{1-x})_4$  ( $x = 0; 0.05; 0.1; 0.15$ ) powders without and with small amount of sulfur were synthesized in  $\text{CdI}_2$  molten salt at 500 °C to produce  $\delta$ -solid solutions. Details about initial composition of these materials are presented in Table 2.4.

**Table 2.4** Initial composition of  $\text{Cu}_2\text{CdGe}(\text{S}_x\text{Se}_{1-x})_4$  powders with different S/Se ratio synthesized in  $\text{CdI}_2$ .

Sample name	Cu, at%	Cd, at%	Ge, at%	Se, at%	S, at%	[Cu]/([Cd]+[Ge])	[Cd]/[Ge]	[S]/([S]+[Se])	Ref.
CCGSe-S0				50.0	-			0	
CCGSe-S0.05	25.0	12.5	12.5	45.0	5.0	1.0	1.0	0.05	[III]
CCGSe-S0.1				40.0	10.0			0.1	
CCGSe-S0.15				35.0	15.0			0.15	

The precursor's mixtures with flux (KI or  $\text{CdI}_2$ ) were ground in desired amounts in an agate mortar. All the preparation were completed in glove box. Then the grinded precursor's mixtures were placed in quartz ampoules, which were degassed under dynamic vacuum (continuous vacuum pumping) and sealed by using  $\text{C}_3\text{H}_8/\text{O}_2$  flame. For the synthesis of monograin powders, the temperature of the furnace was increased from room temperature (RT) to 500/600/700 °C (in case of using  $\text{CdI}_2$  flux) and 700 °C (in case of using KI flux) at a rate of 0.5 °C/min and kept at elevated temperature for 120 h. The growth of monograin powder crystals was stopped by cooling the ampoules naturally in the air. The flux was removed by leaching with deionized water in ultrasonic bath and released monograin powders were dried in a Memmert drying oven at 50 °C for at least 10 hours. Dried powders were sieved into granulometric fractions between 38 to 500  $\mu\text{m}$ . The sieving was performed on a vibratory sieve shaker Retsch AS 200. For future technological processes, the grains with diameters of 45–112  $\mu\text{m}$  were selected.

Detailed procedure of monograin powders preparation and synthesis is described in experimental sections in Papers I-III, respectively.

## 2.2 Preparation of $\text{Cu}_2\text{Ge}(\text{Se,S})_3$ monograin powders

In the Paper V, the ternary  $\text{Cu}_2\text{Ge}(\text{Se}_x\text{S}_{1-x})_3$  ( $x = 0; 0.2; 0.4; 0.6; 0.8; 1$ ) monograin powders were synthesized from commercially available elemental powders Cu, Ge, S, and Se in the alkali salt LiI, used as a molten salt medium. LiI was added with the mass ratio of  $m_{\text{precursors}}/m_{\text{flux}} = 1 : 1$ . All the preparation were completed in glove box. Then the material

mixtures were degassed, sealed into quartz ampoules, and heated from room temperature to 700 °C at a rate of ~0.5 °C/min and maintained at 700 °C for 120 h. Ampoules were cooled down to RT in air. Details about initial composition of  $\text{Cu}_2\text{Ge}(\text{Se}_x\text{S}_{1-x})_3$  powders are presented in Table 2.5.

**Table 2.5** Initial composition of  $\text{Cu}_2\text{Ge}(\text{Se}_x\text{S}_{1-x})_3$  powders with different S/Se ratio synthesized in Lil.

Sample name	Composition and element concentration ratios in precursor's mixture						Ref.
	Cu, at%	Ge, at%	S, at%	Se, at%	[Cu]/[Ge]	[Se]/([S]+[Se])	
CGS-Se0.0			50.0	0		0	
CGS-Se0.2			40.0	10.0		0.2	
CGS-Se0.4	33.3	16.7	30.0	20.0	2	0.4	[V]
CGS-Se0.6			20.0	30.0		0.6	
CGS-Se0.8			10.0	40.0		0.8	
CGS-Se1.0			0	50.0		1.0	

### 2.3 Post-treatment of $\text{Cu}_2\text{CdGe}(\text{Se},\text{S})_4$ and $\text{Cu}_2\text{Ge}(\text{Se},\text{S})_3$ monograin powders

In the molten salt growth process, some part of the used precursor's and the formed crystals dissolve in the flux material at growth temperature, and precipitate out on the surface of crystals during the cooling process. These precipitates change the morphology and composition of the absorber crystals' surfaces. Therefore, the removal of secondary phases from the surface of the powder crystals is one of the major challenges to improve the performance of monograin layer solar cells. Different chemical etchants, fresh-made 1% v/v bromine in methanol ( $\text{Br}_2\text{-MeOH}$ ), 10% v/v hydrochloric acid (HCl) and 10% m/m potassium cyanide (KCN) solutions were used to remove selectively undesired phases. Detailed chemical etching conditions for monograin powders are described in experimental sections in Papers I-V, respectively.

After chemical etching, it is essential to anneal the powder crystals before implementing as absorber materials in monograin layer solar cells. In the Paper I, the size of crystals synthesized at 500 °C was too small to use as absorber in monograin layer solar cells. Therefore, the powder crystals synthesized at 700 °C in KI flux was used for the different post-annealing procedures providing both possible structural modifications of  $\text{Cu}_2\text{CdGeSe}_4$  as solar cell absorber materials. To produce *o*- $\text{Cu}_2\text{CdGeSe}_4$ , the powder was post-annealed at 500 °C for 1 h and cooled by quenching into water. *t*- $\text{Cu}_2\text{CdGeSe}_4$  modification was obtained by applying the same annealing condition at 500 °C for 1 h, but powder was cooled slowly to room temperature (~0.5 °C/min).

The effect of post-annealing on the  $\text{Cu}_2\text{CdGeSe}_4$  based solar cells performance was investigated by annealing chemically etched *o*- $\text{Cu}_2\text{CdGeSe}_4$  powders at different temperatures from 300 to 700 °C for 1 h in the closed quartz ampoules and then cooled by quenching in water [Paper II]. Whereas, the S containing powders need higher post-annealing temperature [95], the  $\text{Cu}_2\text{CdGe}(\text{S}_x\text{Se}_{1-x})_4$  solid solution series were isothermally annealed at 740 °C for 30 min in the sealed quartz ampoules [Paper III].  $\text{Cu}_2\text{Ge}(\text{Se}_x\text{S}_{1-x})_3$  powders were treated isothermally at 400 °C for 60 min [presented in Paper V]. Detailed post annealing conditions for different monograin powder materials are presented in Table 2.6.

**Table 2.6** Experimental post annealing conditions for different monograin powder materials.

Monograin powder material	Cu <sub>2</sub> CdGeSe <sub>4</sub> (Paper I)	Cu <sub>2-x</sub> Cd <sub>y</sub> GeSe <sub>4</sub> (Paper II)	Cu <sub>2</sub> CdGe (S <sub>x</sub> Se <sub>1-x</sub> ) <sub>4</sub> (Paper III)	Cu <sub>2</sub> Ge(S <sub>x</sub> Se <sub>1-x</sub> ) <sub>3</sub> (Paper IV, V)
Combined etching conditions before annealing	-	1% v/v Br <sub>2</sub> -MeOH + 10% m/m KCN	1% v/v Br <sub>2</sub> -MeOH + 10% m/m KCN	1% v/v Br <sub>2</sub> -MeOH + 10% m/m KCN
Annealing temperature, °C	500	300, 350, 400, 450, 500, 600, 700	740	400
Annealing time, min	60	60	30	60
Cooling	In water	In oven	In air	In air

## 2.4 Characterization of monograin powders

This section presents the analytical techniques used to characterize the monograin powder materials. Detailed information about the instruments and measurements is given in the experimental sections in Papers I–V.

### 2.4.1 Room temperature micro-Raman spectroscopy

The phase composition of the powders [Papers I–V] was studied by room temperature micro-Raman spectroscopy using a Horiba LabRAM HR800 system equipped with a cooled multichannel CCD detection system in the backscattering configuration with a spectral resolution better than 1 cm<sup>-1</sup>. A YAG: Nd laser (wavelength  $\lambda = 532$  nm) was used for excitation. The laser spot size was about 2  $\mu$ m in diameter. The same equipment was used for room temperature photoluminescence measurements.

### 2.4.2 X-ray photoelectron spectroscopy (XPS)

XPS measurements were used to study the information about elemental composition of the crystals surface [Paper II]. Kratos Analytical Axis Ultra DLD spectrometer fitted with monochromatic Al K $\alpha$  X-ray source. The achromatic Mg K $\alpha$ /Al K $\alpha$  dual anode X-ray source was used to collect secondary Survey spectra to distinguish the core level and Auger peaks in XPS spectra. The XPS measurements were carried out by Dr. Mati Danilson at Tallinn University of Technology.

### 2.4.3 Scanning electron microscopy (SEM)

The morphology of synthesized powder crystals was studied by high-resolution scanning electron microscope (HR-SEM) Zeiss ULTRA 55 and Zeiss Merlin [Papers I–V]. The SEM images were made by Dr. Valdek Mikli at Tallinn University of Technology.

### 2.4.4 Energy dispersive X-ray spectroscopy (EDX)

The bulk composition [Papers I–V] of the synthesized powder crystals were analyzed by energy dispersive X-ray spectroscopy (EDX) by using the Bruker EDX- XFlash6/30 detector with an accelerating voltage of 20 kV. Compositional analysis and elemental mapping of crystals` bulk were made from polished cross-section of individual crystals by selecting 8–10 crystals and then average composition was calculated. The measurement error for elemental analysis is about 0.5 at%. The EDX measurements were carried out by Dr. Valdek Mikli at Tallinn University of Technology.

### 2.4.5 X-ray powder diffraction (XRD)

The crystalline structure of monograin powders [Papers I-V] was characterized by X-ray diffraction using a Rigaku Ultima IV diffractometer with monochromatic Cu K $\alpha$  radiation  $\lambda = 1.54056 \text{ \AA}$  at 40 kV and 40 mA, using a D/teX Ultra silicon strip detector. All samples were studied in the  $2\theta$  range of 20–60 deg. with the scan step of 0.02 deg. The phase analysis and lattice parameters calculations were made by using software on the Rigaku's system PDXL2. The XRD measurements of monograin powders were carried out by Dr. Arvo Mere at Tallinn University of Technology.

### 2.4.6 Photoluminescence spectroscopy (PL)

For low temperature (20 K) and room temperature PL measurements [Papers IV–V], a 0.64 m focal length single grating ( $600 \text{ mm}^{-1}$ ) monochromator and the 442 nm line of a He-Cd laser with different power were used. For PL signal detection a Hamamatsu InGaAs photomultiplier tube or the cooled CCD detector were used. A closed-cycle helium cryostat was employed to measure the PL spectra at temperature from 20 K to 300 K. The laser spot size for these measurements was 200  $\mu\text{m}$  in diameter. The measurement error in the values of the PL peak position is 0.005 eV. The PL measurements were carried out by Prof. Maarja Grossberg-Kuusk and Dr. Reelika Kaupmees. PL spectra fittings and analysis were done by Prof. Jüri Krustok at Tallinn University of Technology.

## 2.5 Solar cell characteristics

Completed solar cell structures were characterized by dark and light current-voltage ( $I$ – $V$ ) and quantum efficiency ( $QE$ ) measurements [Paper I–III, V].

### 2.5.1 Current-Voltage measurements

Several parameters were used to characterize the efficiency of the solar cells.  $I$ – $V$  curves were measured to evaluate the open-circuit voltage ( $V_{oc}$ ), short-circuit current density ( $J_{sc}$ ), fill factor ( $FF$ ) and efficiency ( $\eta$ ) of the monograin layer solar cells. Measurements were performed using Keithley 2400 source meter in dark and under standard test conditions light with illumination intensity of  $100 \text{ mW/cm}^2$  (AM 1.5) with a Newport Oriel Class A 91195A solar simulator [Paper I–III, V].

### 2.5.2 Quantum efficiency measurements

Quantum efficiency analysis is an alternative method that can be used to estimate the effective bandgap energy  $E_g^*$  of the synthesized absorber materials [113]. From the linear segment of the low-energy side of the construction  $(E^*QE)^2$  vs.  $E$  curves, the  $E_g^*$  can be evaluated. Spectral response measurements [Paper I–III, V] were performed in the spectral region of 350–1235 nm using a computer controlled SPM-2 prism monochromator. The generated photocurrent was detected at 0 V bias voltage at RT by using a 250 W halogen lamp. The QE measurements were carried out by Dr. Mati Danilson at Tallinn University of Technology.

## 3 Results and discussion

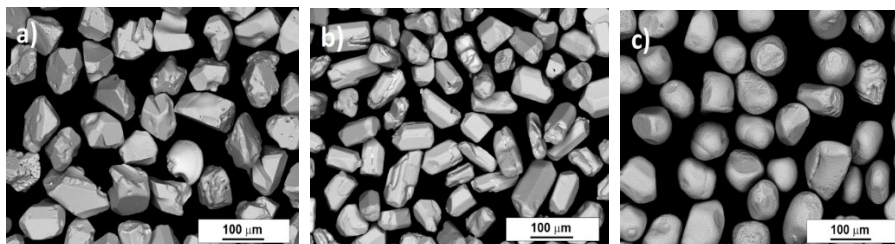
### 3.1 $\text{Cu}_2\text{CdGeSe}_4$ monograin powders

#### 3.1.1 Morphology of $\text{Cu}_2\text{CdGeSe}_4$ powder crystals

At first, the effect of synthesis temperature on the morphology, structural and compositional properties was investigated [Paper I].

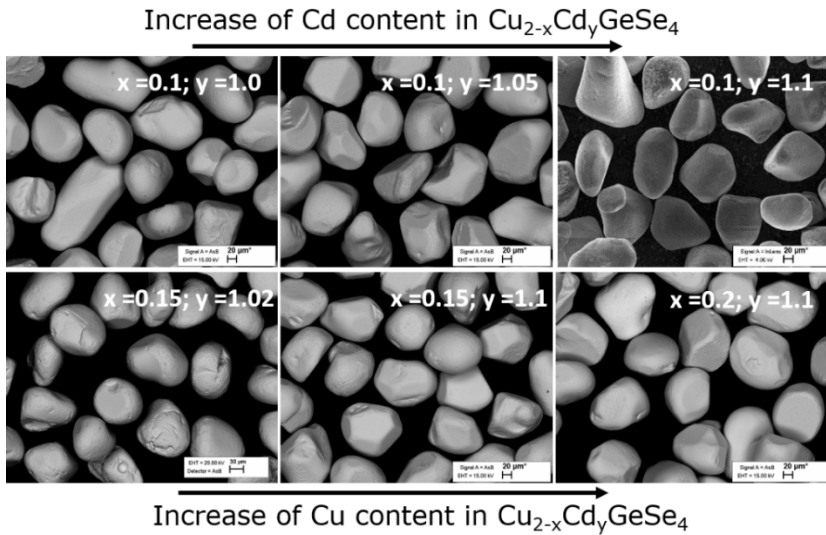
In the molten salt synthesis, a large amount (typically almost equal to the precursor's weight) of a flux salt is used to provide liquid medium between solid particles that conduces to recrystallization and avoids sintering of formed crystals. In addition, molten medium enhances the rate of solid-state reactions and controls the characteristics (size, shape, etc.) of the forming powder crystals. During the heating up of the mixture of  $\text{CuSe-Ge-Se-CdSe-CdI}_2$  to the synthesis-growth temperature, the firstly formed liquid phase is elemental Se ( $T_{\text{melt}} = 221\text{ }^\circ\text{C}$  [94]). It means that liquid Se can act as a flux at this temperature, but the volume of this flux is not enough to repel separate solid particles from each other, and they start to sinter together. This sintering process arises in the heating step of the material below the melting point of the main flux material  $\text{CdI}_2$  and continues until  $\text{CdI}_2$  melts at  $387\text{ }^\circ\text{C}$ . Then the volume of the liquid phase exceeds the volume of voids between precursor particles and repelling forces between solid particles arise [114]. In this case, the formed liquid phase is sufficient to repel both, the solid precursor particles and the formed  $\text{Cu}_2\text{CdGeSe}_4$  particles from each other and to avoid sintering caused by the contracting capillary forces arising in the solid-liquid phase boundaries.

Figure 3.1a and Figure 3.1b show the sintered particles with sharp edges synthesized at  $500\text{ }^\circ\text{C}$  and  $600\text{ }^\circ\text{C}$  in  $\text{CdI}_2$  flux. The shape of the particles indicates to the crystal formation mechanism by sintering process and to the insufficient recrystallization of crystals in conditions of low solubility of  $\text{Cu}_2\text{CdGeSe}_4$  in  $\text{CdI}_2$ . By increasing the temperature, the solubility of synthesized material in flux increases and results in spherical grains as seen in Figure 3.1c. Rounded grains are synthesized at  $700\text{ }^\circ\text{C}$  irrespective of the used flux material.



**Figure 3.1.** SEM images of  $\text{Cu}_2\text{CdGeSe}_4$  powder crystals (fraction size  $63\text{--}75\text{ }\mu\text{m}$ ) synthesized at a)  $500\text{ }^\circ\text{C}$ ; b)  $600\text{ }^\circ\text{C}$  and c)  $700\text{ }^\circ\text{C}$  for 120 h in the  $\text{CdI}_2$  flux.

The effect of initial composition on the morphology of  $\text{Cu}_2\text{CdGeSe}_4$  crystals was also investigated [Paper II]. Figure 3.2 shows the SEM images of  $\text{Cu}_{2-x}\text{Cd}_y\text{GeSe}_4$  powder crystals in the fraction size  $100\text{--}112\text{ }\mu\text{m}$  with different compositions synthesised in KI flux. The compositional deviations in precursor mixture have no direct influence on the morphology of crystals. Formed crystals have round shape with some well-defined plains.



**Figure 3.2.** SEM images of  $\text{Cu}_{2-x}\text{Cd}_y\text{GeSe}_4$  powder crystals with different compositions ( $x = 0.1; 0.15; 0.2$  and  $y = 1.0; 1.05; 1.1$ ).

### 3.1.2 Particle size distribution

Figure 3.3 shows the lognormal plot of the accumulative weight percentage of the particles under a specific particle size versus the particle size for the powder samples synthesized at different temperatures in  $\text{CdI}_2$  flux and for the powders grown in KI flux for different times at  $700\text{ }^\circ\text{C}$  [Paper I]. The black solid horizontal line marking 50% shows the powder median grain size values ( $D_{50}$ ) calculated from weight percentage. The  $D_{50}$  is the size in micrometers that splits the distribution in half above and half below this diameter.

The sieving analysis revealed that median particle size of produced powder crystals increased with increasing synthesis temperature and duration [Paper II]. By increasing the synthesis temperature from  $500$  to  $700\text{ }^\circ\text{C}$  the median size of particles grown in  $\text{CdI}_2$  increases from  $25$  to  $139\text{ }\mu\text{m}$ . Median size of particles for powders synthesized in KI flux at  $700\text{ }^\circ\text{C}$  increased from  $112$  to  $132\text{ }\mu\text{m}$  by increasing the synthesis time from  $60$  to  $120\text{ h}$ . Results show that the median size of particles grown at  $700\text{ }^\circ\text{C}$  does not depend much on the flux material. The most applicable fractions of crystals for monograin membrane preparation in lab conditions are between  $45$  and  $112\text{ }\mu\text{m}$ , the highest yield in this range was gained by synthesizing the  $\text{Cu}_2\text{CdGeSe}_4$  monograin powder in  $\text{CdI}_2$  flux at  $600\text{ }^\circ\text{C}$  for  $120\text{ h}$ , which resulted in the needle like crystals (see Figure 3.1b). Therefore, the synthesis temperature  $700\text{ }^\circ\text{C}$  was selected to synthesize monograin powders in this study. Besides, to get the more suitable fraction size of powder crystals for monograin membrane preparation, shorter synthesis time and the usage of smaller size of initial precursors should be considered.

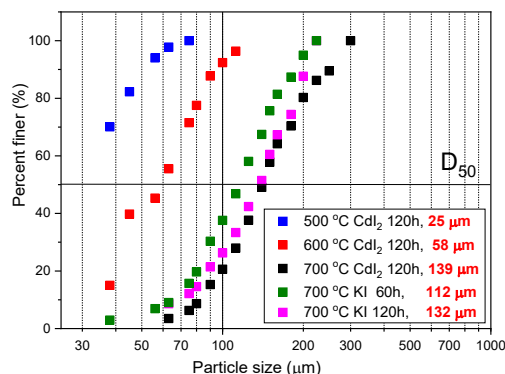


**Figure 3.3.** Particle size distribution obtained from sieving analysis for all powders.

The effect of  $\text{Cu}_2\text{CdGeSe}_4$  composition on the particle size distribution was also examined [Paper II]. Table 3.1 presents the powder median grain size values calculated from weight percentage average size of the powder crystals. The sieving analysis showed that median size of the crystals increased with lower Cu-content and higher Cd-content in precursors (amount of crystals with diameter > 100  $\mu\text{m}$  increased from 72 to 88% of total weight).

**Table 3.1** The initial composition of  $\text{Cu}_{2-x}\text{Cd}_y\text{GeSe}_4$  and the powder median grain size values ( $D_{50}$ ) calculated from the weight percentage of average size of the powder crystals.

Sample name	x in $\text{Cu}_{2-x}\text{Cd}_y\text{GeSe}_4$	y in $\text{Cu}_{2-x}\text{Cd}_y\text{GeSe}_4$	$D_{50}$ ( $\mu\text{m}$ )
CCGSe-201	0.1	1.0	115
CCGSe-202	0.1	1.05	131
CCGSe-203	0.15	1.02	146
CCGSe-204	0.1	1.1	154
CCGSe-205	0.15	1.1	164
CCGSe-206	0.2	1.1	188

### 3.1.3 Elemental bulk composition of $\text{Cu}_2\text{CdGeSe}_4$ powders

Bulk composition of  $\text{Cu}_2\text{CdGeSe}_4$  monograin powders were measured by EDX from polished crystals (example of cross-sectional SEM image is presented in Figure 3.4) [Paper I and II]. EDX analysis showed that the atomic concentrations of Cu and Se remained almost the same with increasing synthesis temperature of  $\text{Cu}_2\text{CdGeSe}_4$  in  $\text{CdI}_2$  flux while the atomic concentrations of Cd increased and Ge decreased probably due to that  $\text{CdI}_2$  is not passive in the synthesis and Cd from  $\text{CdI}_2$  incorporates into the crystal lattice of  $\text{Cu}_2\text{CdGeSe}_4$  [115].

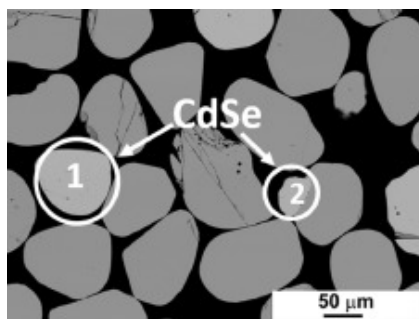


**Figure 3.4.** SEM images of cross section of  $\text{Cu}_2\text{CdGeSe}_4$  powder crystal.



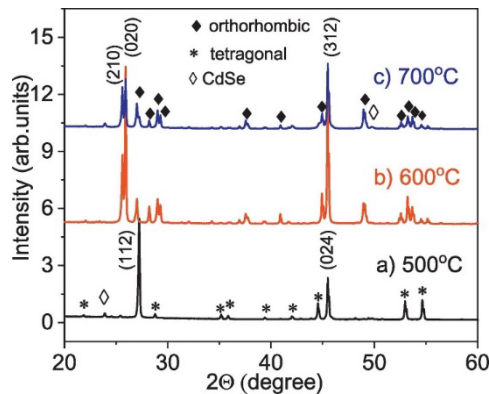
By increasing the synthesis temperature from 500 °C to 700 °C, the ratio of [Cd]/[Ge] increased from 0.99 to 1.07. The ratio of [Cu]/([Cd]+[Ge]) was ~1.0 for Cu<sub>2</sub>CdGeSe<sub>4</sub> powders synthesized in CdI<sub>2</sub> at 500 °C and 700 °C, but powders synthesized at 600 °C had Cu-poor (the ratio of [Cu]/([Cd]+[Ge]) = 0.93) composition.

Bulk composition of the Cu<sub>2</sub>CdGeSe<sub>4</sub> powders synthesized in KI flux for different synthesis times was also slightly Cd-rich (the ratio of [Cd]/[Ge] = 1.03) and did not depend on synthesis time. But the ratio of [Cu]/([Cd]+[Ge]) decreased from 1.0 to 0.96 by increasing the synthesis time.

Change in initial composition of Cu<sub>2-x</sub>Cd<sub>y</sub>GeSe<sub>4</sub> monograin powders showed that Cu-poor (x = 0.15) and [Cd]/[Ge] = 1.0 input composition resulted in powder with nearly stoichiometric composition – Cu<sub>2</sub>Cd<sub>1.03</sub>Ge<sub>1.02</sub>Se<sub>4</sub>. If the precursors composition was Cu-poor (x > 0) and Cd-rich ([Cd]/[Ge] > 1.0), the average bulk composition of all powders was slightly Cu-poor (([Cu]/([Cd]+[Ge]) = 0.96)) and Cd-rich ([Cd]/[Ge] = 1.09) – Cu<sub>1.95</sub>Cd<sub>1.06</sub>Ge<sub>0.97</sub>Se<sub>4</sub>. In the Figure 3.4 is presented cross-sectional image of Cu-poor and Cd-rich powder crystals. It is seen that powder contains some lighter crystals (point 1), which are comparable size of the main material crystals. According to EDX analysis, the light crystal contained mainly Cd and Se (50.4 at% : 48.1 at%). The existence of CdSe secondary phase in the powder was also confirmed by XRD (Figure 3.5). CdSe is *n*-type semiconductor material with direct band gap ~1.74 eV [116]. This phenomenon is not a problem if the CdSe crystal is detached and has high resistance. In this case, it will be just as a filler of the polymer in the monograin membrane. More harmful is the case, when secondary phase is in connection with main material grain (point 2) or segregated on the surface of grains. In that case, it needs to be removed by selective chemical etchings.

### 3.1.4 Phase composition and structure

The Cu<sub>2</sub>CdGeSe<sub>4</sub> powders synthesized in CdI<sub>2</sub> flux at different temperatures were investigated by XRD as shown in Figure 3.5 [Paper I]. The XRD pattern of the powder synthesized at 500 °C showed peaks corresponding to the tetragonal crystal structure (ICCD PDF-2-2013, 01-070-9042) with the space group *I*-42*m* of the main phase and the presence of CdSe secondary phase. The main peak is attributed to (112) plane of Cu<sub>2</sub>CdGeSe<sub>4</sub>. The powders synthesized at 600 °C and 700 °C revealed the presence of the orthorhombic phase (ICCD PDF-2-2013, 01-074-3115). Calculated lattice parameters *a*, *b* and *c* of all the samples are presented in the Table 3.2.

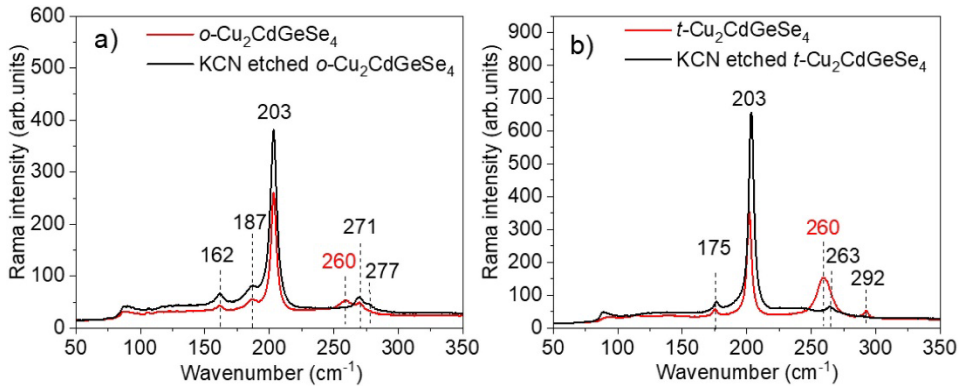


**Figure 3.5.** XRD patterns of Cu<sub>2</sub>CdGeSe<sub>4</sub> powder synthesized at a) 500 °C; b) 600 °C and c) 700 °C in CdI<sub>2</sub> flux.

**Table 3.2** Lattice parameters of  $\text{Cu}_2\text{CdGeSe}_4$  powders synthesized in  $\text{CdI}_2$  flux.

Material	Space group	$a$ , Å	$b$ , Å	$c$ , Å
CCGSe-101 (500 °C)	<i>I</i> -42 <i>m</i> -tetragonal	5.7476	5.7476	11.0511
CCGSe-102 (600 °C)	<i>Pmn</i> 21-orthorhombic	8.0726	6.8855	6.6118
CCGSe-103 (700 °C)	<i>Pmn</i> 21-orthorhombic	8.0634	6.8793	6.6035

Raman spectroscopy was used to analyse the phase composition of the  $\text{Cu}_2\text{CdGeSe}_4$  monograin powders synthesized at different temperatures [Paper I]. There was no Raman data published in the literature for this compound before this study. Figure 3.6a and 3.6b show Raman spectra of *o*- $\text{Cu}_2\text{CdGeSe}_4$  and *t*- $\text{Cu}_2\text{CdGeSe}_4$  powders, respectively. The most intensive peak in the spectra of  $\text{Cu}_2\text{CdGeSe}_4$  is observed at  $203\text{ cm}^{-1}$  and it is not dependent on the phase structure. The additional characteristic Raman modes for the *o*- $\text{Cu}_2\text{CdGeSe}_4$  phase were detected at 162, 187, 271 and  $277\text{ cm}^{-1}$  (Figure 3.6a) and for *t*- $\text{Cu}_2\text{CdGeSe}_4$  phase at 175, 263 and  $292\text{ cm}^{-1}$  (Figure 3.6b). All the as-grown powders had an additional peak in Raman spectra at  $260\text{ cm}^{-1}$ , which has been assigned to  $\text{Cu}_{2-x}\text{Se}$  phase [117]. In order to remove selectively the  $\text{Cu}_{2-x}\text{Se}$  phase from the surface of as-grown  $\text{Cu}_2\text{CdGeSe}_4$  powders, the chemical etching with 10% m/m KCN + 1% m/m KOH solution for 30 min was performed. The  $\text{Cu}_{2-x}\text{Se}$  Raman scattering peak at  $260\text{ cm}^{-1}$  disappeared completely after the KCN etching while no change was observed in the  $\text{Cu}_2\text{CdGeSe}_4$  peaks. No CdSe phase was detected by Raman measurement because Raman analysis was performed on the different single grains. While XRD measurements require tenths of a gram of ground material, which means that amount of material used for these analyses was totally different and detection of secondary phases is different.

**Figure 3.6.** RT-Raman spectra of a) *o*- $\text{Cu}_2\text{CdGeSe}_4$  and b) *t*- $\text{Cu}_2\text{CdGeSe}_4$  powders before and after KCN etching.

### 3.1.5 $\text{Cu}_2\text{CdGeSe}_4$ surface modifications

Detailed chemical etching investigations were performed on the Cd-rich  $\text{Cu}_{1.95}\text{Cd}_{1.06}\text{Ge}_{0.97}\text{Se}_4$  (CCGSe-202) powder [Paper II]. Two different combinational etching processes were applied – 1% v/v  $\text{Br}_2$ -MeOH etching followed by 10% m/m KCN etching and a 10% v/v HCl etching followed by 10% m/m KCN etching to remove the secondary phases from the surface of the absorber layer. EDX and XPS were used to investigate the surface composition of etched crystals and Raman spectroscopy was used to analyze the change in phase composition on the surface of  $\text{Cu}_{1.95}\text{Cd}_{1.06}\text{Ge}_{0.97}\text{Se}_4$  crystals.

Figure 3.7a shows the SEM image of crystal surface after  $\text{Br}_2$ -MeOH etching for 5 min at RT. According to EDX analysis, the surface of crystals was covered by amorphous

selenium. The surface became more Cu-rich and Cd-poor, as the ratio of  $[Cu]/([Cd]+[Ge])$  increased from 0.96 to 1.02 and the ratio of  $[Cd]/[Ge]$  decreased from 1.1 to 1.0. KCN etching restored the Cu-poor and Cd-rich surface and removed selenium from the surface. Additional annealing at 400 °C did not change the surface composition within the detection limits.

In Figure 3.7b is shown the SEM image of crystal surface after 10 v/v% HCl etching for 10 min. After HCl etching, the surface of crystals was slightly Cu-rich ( $[Cu]/([Cd]+[Ge]) = 1.03$ ) and Cd-rich ( $[Cd]/[Ge] = 1.07$ ). Subsequent etching with KCN removed Cu-rich surface and restored original composition –  $Cu_{1.97}Cd_{1.06}Ge_{0.98}Se_4$ .

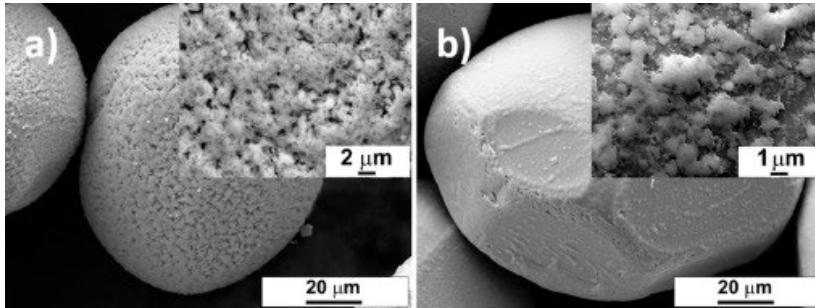


**Figure 3.7.** SEM images of  $Cu_{1.95}Cd_{1.06}Ge_{0.97}Se_4$  crystals after a) 1%  $Br_2$ -MeOH etching for 5 min and b) 10% HCl etching for 10 min.

Raman spectroscopy has emerged as a promising and feasible technique for the advanced characterization of the secondary phases at the surface [Paper II]. The most intensive peak in the Raman spectra of orthorhombic  $Cu_{1.97}Cd_{1.06}Ge_{0.98}Se_4$  is observed at  $203\text{ cm}^{-1}$  and it is not dependent on the applied chemical etchant. The additional characteristic Raman modes for the  $o$ - $Cu_2CdGeSe_4$  phase were detected at 163, 182, 187, 271 and  $278\text{ cm}^{-1}$  [Paper I and II] (see Figure 3.8a and 3.8b).

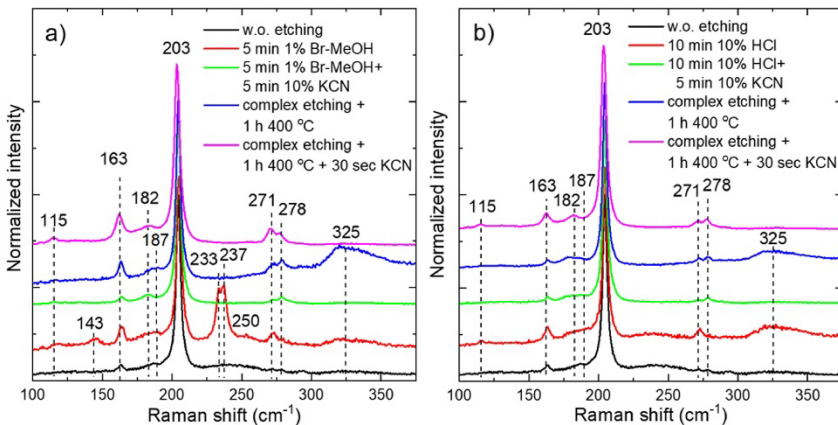


**Figure 3.8.** RT Raman spectra of  $o$ - $Cu_{1.95}Cd_{1.06}Ge_{0.97}Se_4$  powders: a) without etching and after different combinations of bromine and KCN etchings and annealing at 400 °C, b) without etching and after different combinations of HCl and KCN etchings and annealing at 400 °C.

After bromine etching additional peaks appeared at 143, 233, 237  $\text{cm}^{-1}$  and 250  $\text{cm}^{-1}$ . Raman peaks at 143, 233 and 237  $\text{cm}^{-1}$  correspond to the trigonal Se ( $t$ -Se); peak at 233  $\text{cm}^{-1}$  is attributed to bond-stretching E mode and at 237  $\text{cm}^{-1}$  to symmetric

bond-stretching A1 mode [118]. Weak band at  $250\text{ cm}^{-1}$  corresponds to the A1 mode of amorphous selenium [118]. After bromine and also after HCl etching wide band appeared around at  $300\text{--}350\text{ cm}^{-1}$ . The latter band was even stronger after annealing at  $400\text{ }^{\circ}\text{C}$ . This could be assigned to GeSe or GeSe<sub>2</sub> phase. XPS analysis was used to confirm this assumption. Figure 3.9 shows the Ge 3d and Se 3d core-level spectra for Cu<sub>2</sub>CdGeSe<sub>4</sub> after annealing at  $400\text{ }^{\circ}\text{C}$  and after additional KCN etching. All measured XPS spectra were charge corrected based on the standard reference signal from C 1s ( $284.6\text{ eV}$ ). The Ge 3d core-level spectrum exhibited two doublet peaks with main peak ( $3d_{5/2}$ ) centred at  $30.3\text{ eV}$  belonging to Ge<sup>IV</sup> (possible in Cu<sub>2</sub>CdGeSe<sub>4</sub> or GeSe<sub>2</sub> phase) and at  $30.8\text{ eV}$  belong to Ge<sup>II</sup> (possible GeSe phase) both with duplet separation set to  $0.58\text{ eV}$  [46,119,120]. The Se 3d core-level spectrum of the surface of annealed Cu<sub>2</sub>CdGeSe<sub>4</sub> also exhibited two doublets with main peak ( $3d_{5/2}$ ) binding energies centred at  $53.8\text{ eV}$  and  $54.7\text{ eV}$ . The first one belongs to Se<sup>II</sup> in Cu<sub>2</sub>CdGeSe<sub>4</sub> and the second belongs to Ge<sub>x</sub>Se<sub>1-x</sub> [121]. After KCN etching in the Ge 3d core-level spectrum only one doublet with main peak located at the same energy  $30.3\text{ eV}$  remained. The second doublet at higher binding energy was considerably suppressed. The reduction of GeSe signal accompanied also in the Se 3d core-level spectrum, where the intense doublet with main peak located at  $53.9\text{ eV}$  was remained.

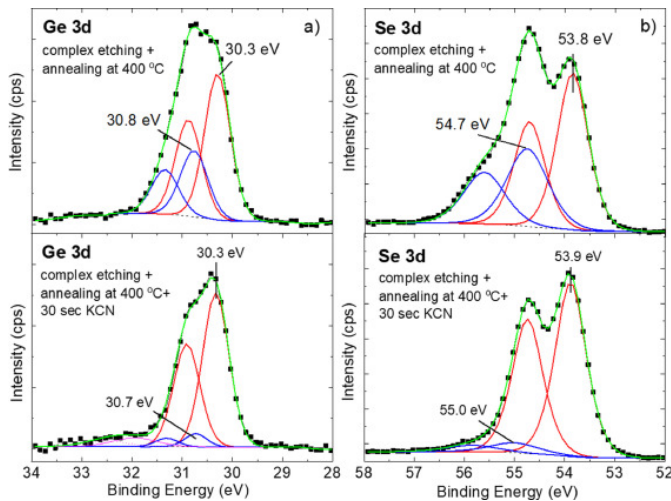


**Figure 3.9.** XPS spectra of a) Ge 3d and b) Se 3d for surface of Cu<sub>2</sub>CdGeSe<sub>4</sub> after annealing at  $400\text{ }^{\circ}\text{C}$  and after additional KCN etching.

### 3.1.6 Cu<sub>2</sub>CdGeSe<sub>4</sub> monograin layer solar cell

Sieving analysis showed that the yield of the applicable size of the crystals synthesized at  $500\text{ }^{\circ}\text{C}$  for monograin layer solar cell preparation was very small. Therefore, to produce MGL solar cells, the powder synthesized at  $700\text{ }^{\circ}\text{C}$  in KI flux was used for the different post-annealing procedures providing both possible structural modifications of Cu<sub>2</sub>CdGeSe<sub>4</sub> as solar cell absorber materials. To produce *o*-Cu<sub>2</sub>CdGeSe<sub>4</sub>, the powder was post-annealed at  $500\text{ }^{\circ}\text{C}$  for 1 h and cooled by quenching into water; *t*-Cu<sub>2</sub>CdGeSe<sub>4</sub> modification was obtained by annealing at  $500\text{ }^{\circ}\text{C}$  for 1 h and cooling slowly to room temperature ( $\sim 0.5\text{ }^{\circ}\text{C}/\text{min}$ ). XRD patterns of these powders confirmed the formation of different respective modifications (not presented).

To investigate the effect of the crystalline structure of  $\text{Cu}_2\text{CdGeSe}_4$  on device performance,  $J$ - $V$  curves of the solar cell devices were measured under AM1.5 illumination, as shown in Figure 3.10a [Paper I]. For the device based on  $t\text{-Cu}_2\text{CdGeSe}_4$  absorber, the highest obtained power conversion efficiency was 2.16% with  $V_{oc}$  of 315 mV,  $J_{sc}$  of 14.7 mA/cm<sup>2</sup>, and  $FF$  of 35% while for the  $o\text{-Cu}_2\text{CdGeSe}_4$  solar cell, PCE of 4.21% was achieved with a  $V_{oc}$  of 464 mV,  $J_{sc}$  of 17.5 mA/cm<sup>2</sup> and  $FF$  of 39%. These initial results indicated that both –  $t\text{-Cu}_2\text{CdGeSe}_4$  and  $o\text{-Cu}_2\text{CdGeSe}_4$  materials are potential candidates for absorber material in photovoltaic devices.

EQE analysis was used to estimate the effective bandgap energy ( $E_g^*$ ) of the synthesized absorber materials [113] since the evaluation of  $E_g$  from the optical absorption or reflectance spectra of the monograins is rather challenging. The  $E_g^*$  values obtained (Figure 3.10b) from EQE measurements was found to be 1.14 eV for  $t\text{-Cu}_2\text{CdGeSe}_4$  powders and 1.27 eV for  $o\text{-Cu}_2\text{CdGeSe}_4$  powders.

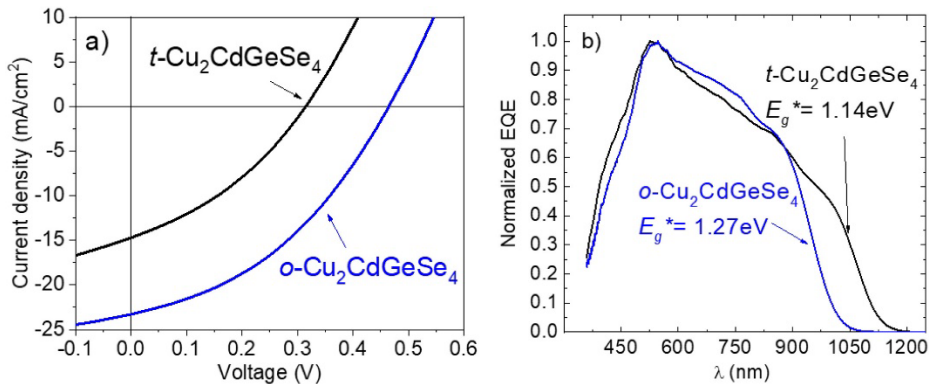


**Figure 3.10.** a)  $J$ - $V$  characteristics and b) EQE spectra of MGL solar cell prepared from  $t\text{-Cu}_2\text{CdGeSe}_4$  and  $o\text{-Cu}_2\text{CdGeSe}_4$  powders.

The influence of the surface chemical etching and the annealing conditions on the optoelectronic properties of solar cells were investigated [Paper II]. In Figure 3.11, the output parameters of monograin layer solar cells fabricated from  $o\text{-Cu}_{1.95}\text{Cd}_{1.06}\text{Ge}_{0.97}\text{Se}_4$  powder that was etched with different chemical solutions followed by annealing at 400 °C for 1 hour are displayed as box plots. Results showed that all used chemical etchants are beneficial to improve solar cell performance. All etchants improved the values of open circuit voltage about 150 mV. The largest improvement on the optoelectronic parameters was achieved by HCl etching followed by KCN-etching, giving conversion efficiency of 3.82%. The efficiency improvement was mainly due to increased values of current density from 11.5 to 21.3 mA/cm<sup>2</sup>.

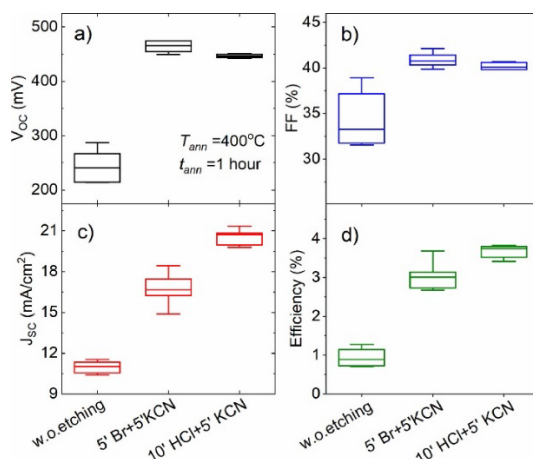


**Figure 3.11.** Box plot of a) open circuit voltage; b) fill factor; c) current density and d) efficiency of monograin layer solar cells fabricated from  $\text{Cu}_{1.95}\text{Cd}_{1.06}\text{Ge}_{0.97}\text{Se}_4$  powder that was etched with different chemical solutions followed by annealing at  $400^\circ\text{C}$  for 1 h.

For the investigation of the effect of post-annealing temperature, 1% v/v  $\text{Br}_2$ -MeOH and 10% m/m KCN combinational etching was used for nearly stoichiometric  $o\text{-Cu}_2\text{Cd}_{1.03}\text{Ge}_{1.02}\text{Se}_4$  (CCGSe-203) powder and subsequently the powder was annealed at different temperatures for 1 h in closed ampoules.

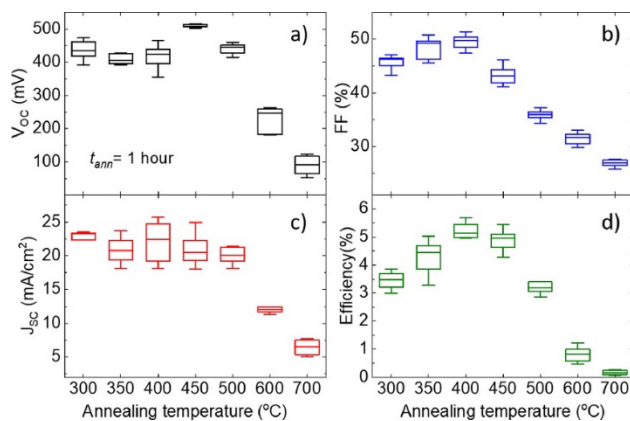


**Figure 3.12.** Box plot of a) open circuit voltage; b) fill factor; c) current density and d) efficiency of monograin layer solar cells fabricated from  $o\text{-Cu}_2\text{Cd}_{1.03}\text{Ge}_{1.02}\text{Se}_4$  powder that was etched with methanol and KCN solutions followed by annealing at temperatures from 300 to  $700^\circ\text{C}$  for 1 h.

The output parameters of monograin layer solar cells based on differently annealed powders are presented as box plot in Figure 3.12. Note that these parameters were obtained with an additional short time (30 sec) chemical etching with KCN solution prior to CdS buffer layer deposition. It was applied due to the formation of GeSe phase on the crystals surface after annealing and as Raman and XPS analysis confirmed, this phase was removed by short time KCN etching. The values of  $V_{oc}$  increased from 473 to 515 mV by increasing the annealing temperature from 300 to  $450^\circ\text{C}$ . The value of FF reached its maximum (51%) at  $400^\circ\text{C}$  and decreased again at higher annealing temperatures. The similar trend was observed for  $J_{sc}$ , the values were increased up to  $400^\circ\text{C}$  and then

started to decrease. After annealing the powder over 450 °C, the decrease in the output parameters could be caused by decomposition of absorber material surface. The largest improvement on the optoelectronic parameters was achieved by annealing  $\alpha$ - $\text{Cu}_2\text{Cd}_{1.03}\text{Ge}_{1.02}\text{Se}_4$  powder at 400 °C for 1 hour, giving conversion efficiency of 5.69% with the following parameters:  $V_{OC} = 459$  mV;  $J_{SC} = 25.6$  mA/cm<sup>2</sup> and  $FF = 48\%$ .

### Summary of the study of $\text{Cu}_2\text{CdGeSe}_4$ monograin powder properties and solar cells

$\text{Cu}_2\text{CdGeSe}_4$  powders were synthesized by molten salt method in  $\text{CdI}_2$  and KI for photovoltaic applications. Phase analysis by Raman spectroscopy and X-ray diffraction showed that  $\text{Cu}_2\text{CdGeSe}_4$  powder synthesized at 500 °C had tetragonal structure and powders synthesized at temperatures 600 °C and 700 °C had orthorhombic structure regardless of the used molten salt. The results of compositional analysis indicated that Cu-poor and Cd-rich powders were synthesized at 700 °C in KI flux and at 600 °C in  $\text{CdI}_2$  flux. The band gap values determined from EQE measurements were found to be 1.27 eV for orthorhombic  $\text{Cu}_2\text{CdGeSe}_4$  and 1.14 eV for tetragonal  $\text{Cu}_2\text{CdGeSe}_4$  material. The best power conversion efficiency of 4.21% was achieved by using the orthorhombic structured  $\text{Cu}_2\text{CdGeSe}_4$  powder as absorber material, which were annealed at 500 °C for 1 hour.

A comparative investigation of the influence of different etchants such as  $\text{Br}_2$ -MeOH, KCN and HCl followed by isothermal annealing at different temperatures on the performance of  $\alpha$ - $\text{Cu}_2\text{CdGeSe}_4$  monograin layer solar cells was carried out. Results showed that all used chemical etchants are beneficial to improve  $\text{Cu}_2\text{CdGeSe}_4$  solar cell efficiencies. After chemical etching of crystal surfaces, the powder needed additional annealing at 400 °C to improve the performance of  $\text{Cu}_2\text{CdGeSe}_4$  solar cells. It was found that after post-annealing the etching with KCN solution is necessary to remove  $\text{Ge}_x\text{Se}_{1-x}$  phase on the surface of  $\text{Cu}_2\text{CdGeSe}_4$  powder crystal.

The highest conversion efficiency of 5.69% was gained by using  $\alpha$ - $\text{Cu}_2\text{CdGeSe}_4$  with nearly stoichiometric composition, which was etched with 1% v/v  $\text{Br}_2$ -MeOH and 10% m/m KCN solutions for 5 minutes and post-annealed at 400 °C for 1 hour.

## 3.2 $\text{Cu}_2\text{CdGe}(\text{S}_x\text{Se}_{1-x})_4$ monograin powders

### 3.2.1 Morphology and composition of $\text{Cu}_2\text{CdGe}(\text{S}_x\text{Se}_{1-x})_4$ monograin powders

In the Paper III, the  $\gamma$ -phase of  $\text{Cu}_2\text{CdGe}(\text{S}_x\text{Se}_{1-x})_4$  ( $x = 0; 0.2; 0.4; 0.6; 0.8; 1$ ) monograin powders were synthesized at 700 °C for 120 hours by using KI as a molten salt medium. Additionally, four  $\text{Cu}_2\text{CdGe}(\text{S}_x\text{Se}_{1-x})_4$  ( $x = 0; 0.05; 0.1; 0.15$ ) powders without and with small amount of sulfur were synthesized in  $\text{CdI}_2$  molten salt to produce  $\delta$ -solid solutions. SEM images of  $\text{Cu}_2\text{CdGeSe}_4$  and  $\text{Cu}_2\text{CdGeS}_4$  powder crystals are shown in Figure 3.13a and 3.13b [Paper III]. With the increasing S content in the  $\text{Cu}_2\text{CdGe}(\text{S}_x\text{Se}_{1-x})_4$  solid solutions, the formed crystals with round shape and smooth surface planes changed to more irregular and oblong shape. The median grain size of the powders decreased with the increasing S content in the  $\text{Cu}_2\text{CdGe}(\text{S}_x\text{Se}_{1-x})_4$  powder, being  $D_{50} = 143$   $\mu\text{m}$  for the  $\text{Cu}_2\text{CdGeSe}_4$  powder and  $D_{50} = 85$   $\mu\text{m}$  for  $\text{Cu}_2\text{CdGeS}_4$ .



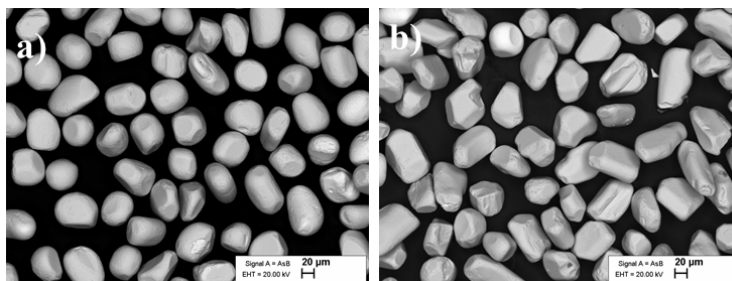


**Figure 3.13.** SEM images of monograin powders of  $\text{Cu}_2\text{CdGeSe}_4$  (left) and  $\text{Cu}_2\text{CdGeS}_4$  (right) (fraction size 45–56  $\mu\text{m}$ ).

Therefore, it was found that selenide powder crystals grow almost two times larger than sulfide powder crystals under the same synthesis conditions [Paper III]. This could be attributed to the existence of elemental selenium in the precursor mixture at temperature below melting point of salt that could act as sintering agent. For example, at low temperatures ( $\sim 221^\circ\text{C}$ ) forms  $\text{CuSe}_2$ , which decomposes into  $\text{CuSe}$  and  $\text{Se}$  at  $\sim 330^\circ\text{C}$ . At  $380^\circ\text{C}$ ,  $\text{CuSe}$  decomposes into  $\text{Cu}_{2-x}\text{Se}$  and liquid  $\text{Se}$ . In the sulfide system, all metals precursors react with sulfur at much lower temperature ( $\sim 250^\circ\text{C}$ ) and do not release free sulfur at higher temperatures. Similar phenomenon about crystal sizes is also observed for thin films with different ratio of S/Se [122].

The elemental composition of the bulk of the  $\text{Cu}_2\text{CdGe}(\text{S}_x\text{Se}_{1-x})_4$  microcrystals was determined by EDX analysis and is presented in Table 3.3 [Paper III]. It was found that the increasing S content in the precursor's mixture increased the Cu content in the powder from 24.6 at% ( $x = 0$ ) to 25.6 at% ( $x = 1$ ). The powders synthesized at  $700^\circ\text{C}$  in KI, the ratio of  $[\text{S}]/([\text{S}]+[\text{Se}])$  and  $[\text{Cd}]/[\text{Ge}]$  in precursor's mixture was nearly the same in all powders. While the powders synthesized at  $500^\circ\text{C}$  in  $\text{CdI}_2$  with  $x = 0 - 0.15$  had Cd-rich composition ( $[\text{Cd}]/[\text{Ge}] > 1.1$ ) and the ratio of  $[\text{S}]/([\text{S}]+[\text{Se}])$  in the powders was slightly higher than in precursor's mixture.

**Table 3.3** Bulk composition of  $\text{Cu}_2\text{CdGe}(\text{S}_x\text{Se}_{1-x})_4$  microcrystalline powders by EDX analysis

$x = [\text{S}]/([\text{S}]+[\text{Se}])$ in precursor	$T_{\text{synth}}$ , $^\circ\text{C}$	Bulk composition of powders by EDX								
		$[\text{S}]/([\text{S}]+[\text{Se}])$	Cu, at%	Cd, at%	Ge, at%	Se, at%	S, at%	$[\text{Cu}]/[\text{Ge}]$	$[\text{Cd}]/[\text{Ge}]$	$[\text{Cu}]/([\text{Cd}]+[\text{Ge}])$
0	700	0	24.6	13.5	11.7	50.0	-	2.10	1.15	0.98
0.2		0.21	24.4	12.4	11.8	39.4	10.6	2.07	1.05	1.0
0.4		0.39	24.8	12.7	12.0	30.3	19.7	2.07	1.06	1.0
0.6		0.60	25.2	12.2	12.0	19.9	30.1	2.10	1.02	1.04
0.8		0.80	25.2	12.6	12.1	10.0	40.0	2.08	1.04	1.02
1		1	25.6	12.5	11.9	-	50.0	2.15	1.05	1.04
0	500	0	24.9	13.0	12.6	50.0	-	1.98	1.03	0.97
0.05		0.07	25.1	13.8	11.6	46.6	3.4	2.16	1.19	0.95
0.1		0.12	25.5	13.2	11.7	44.0	6.0	2.18	1.13	1.02
0.15		0.23	25.3	13.2	11.7	38.6	11.3	2.16	1.13	1.02

### 3.2.2 Structural properties of $\text{Cu}_2\text{CdGe}(\text{S}_x\text{Se}_{1-x})_4$ monograin powders

The crystal structure and phase composition of the synthesized  $\text{Cu}_2\text{CdGe}(\text{S}_x\text{Se}_{1-x})_4$  powders with different S/Se ratios was investigated by XRD [Paper III]. Figure 3.14a shows the XRD patterns of monograin powders of  $\text{Cu}_2\text{CdGe}(\text{S}_x\text{Se}_{1-x})_4$  solid solutions synthesized at  $700^\circ\text{C}$  in KI flux. The major diffraction peaks are indexed as corresponding



to the (210), (020), (002), (211), (203), (213) and (040) planes of orthorhombic phase of  $\text{Cu}_2\text{CdGeS}_4$  (ICDD PDF-2 Release 2019 RDB, 00-043-1387) and  $\text{Cu}_2\text{CdGeSe}_4$  (ICDD PDF-2 Release 2019 RDB, 01-074-3115). The position of most intensive diffraction peak (020) shifted from 25.88 deg (for  $\text{Cu}_2\text{CdGeS}_4$ ) to 27.19 deg (for  $\text{Cu}_2\text{CdGeSe}_4$ ) as shown in Figure 3.14b. Minor amount of secondary phases like CdS, CdSe or Cd(S,Se) were detected in the all solid solutions.

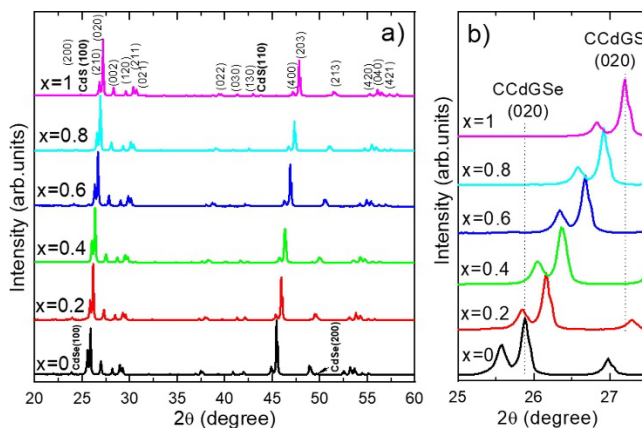


**Figure 3.14.** a) XRD patterns of monograin powders of  $\text{Cu}_2\text{CdGe}(\text{S,Se})_4$  solid solutions synthesized at 700 °C in KI; b) magnified view of (020) diffraction peak.

Using the XRD patterns, the values of lattice parameters  $a$ ,  $b$  and  $c$  for all the powders were calculated. A linear decrease of the lattice parameters values ( $a$  from 8.064 Å to 7.705 Å;  $b$  from 6.882 Å to 6.556 Å and  $c$  from 6.604 Å to 6.301 Å) was observed upon replacement of selenium with sulfur due to the smaller atom radius of S compared to Se. The structural linearity is shown in Figure 3.15. This behaviour strictly follows Vegard's empirical heuristic law, which states that at the same temperature the lattice parameter of a solid solution of two materials with the same crystal structure can be approximated by an equation of the two constituents' lattice parameters [123].

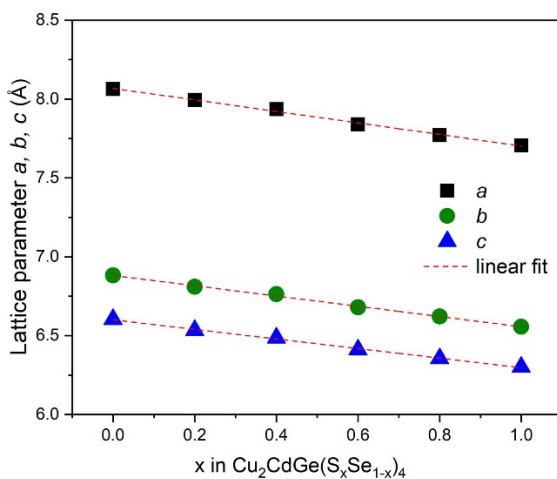


**Figure 3.15.** Lattice parameters  $a$ ,  $b$  and  $c$  as a function of S content in the orthorhombic  $\text{Cu}_2\text{CdGe}(\text{S}_x\text{Se}_{1-x})_4$  solid solutions synthesized at 700 °C.

In order to confirm the existent limits of a tetragonal structure in  $\text{Cu}_2\text{CdGe}(\text{S}_x\text{Se}_{1-x})_4$  with low concentration of sulfur, as reported in [66], the monograin powders of  $\text{Cu}_2\text{CdGe}(\text{S}_x\text{Se}_{1-x})_4$  solid solutions ( $x = 0$  to  $x = 0.15$ ) synthesized at  $500^\circ\text{C}$  were analysed by XRD (Figure 3.16). According to this study,  $\text{Cu}_2\text{CdGeSe}_4$  ( $x = 0$ ) and  $\text{Cu}_2\text{CdGe}(\text{S}_x\text{Se}_{1-x})_4$  solid solutions ( $x = 0.05 - 0.1$ ) had a tetragonal structure ( $I-42m$ ) with lattice parameters presented in Table 3.4.  $\text{Cu}_2\text{CdGe}(\text{S}_x\text{Se}_{1-x})_4$  powder with  $x = 0.15$  contains about 79% of crystal with an orthorhombic structure ( $Pmn21$ ) with lattice parameters  $a = 7.994 \text{ \AA}$ ,  $b = 6.809 \text{ \AA}$ ,  $c = 6.534 \text{ \AA}$ , and about 18% of crystal with a tetragonal structure ( $I-42m$ ) with lattice parameters  $a = b = 5.697 \text{ \AA}$ ,  $c = 10.943 \text{ \AA}$ .  $\text{Cu}_2\text{CdGe}(\text{S}_x\text{Se}_{1-x})_4$  solid solutions with  $x = 0.2$  crystallize in the orthorhombic structure regardless of the synthesis temperature.

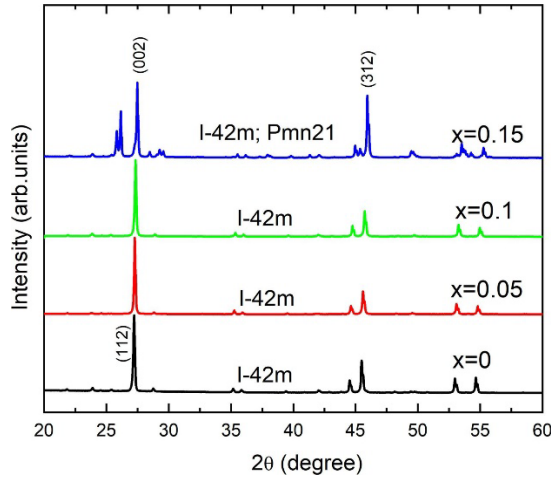


**Figure 3.16.** XRD patterns of the monograin powders of  $\text{Cu}_2\text{CdGe}(\text{S}_x\text{Se}_{1-x})_4$  solid solutions synthesized at  $500^\circ\text{C}$ .

The substitution of Se with the smaller S atoms leads to the contraction of the unit cell (see Table 3.4). Since not only the size but also the electronic structures of S and Se are different, therefore, it is expected that the lattice parameters and electronic structure will be changed.

**Table 3.4** The lattice parameters of the monograin powders of  $\text{Cu}_2\text{CdGe}(\text{S}_x\text{Se}_{1-x})_4$  solid solutions.

$x$ in $\text{Cu}_2\text{CdGe}(\text{S}_x\text{Se}_{1-x})_4$	$T_{\text{synth}}$ , $^\circ\text{C}$	$a$ , $\text{Å}$	$b$ , $\text{Å}$	$c$ , $\text{Å}$	$V$ , $\text{Å}^3$	Space group
0	700	8.064	6.882	6.604	366.47	$Pmn21$
0.2		7.994	6.810	6.534	355.77	$Pmn21$
0.4		7.935	6.762	6.486	348.06	$Pmn21$
0.6		7.839	6.680	6.410	335.67	$Pmn21$
0.8		7.772	6.622	6.355	327.07	$Pmn21$
1		7.705	6.556	6.301	318.33	$Pmn21$
0	500	5.747	5.747	11.051	365.08	$I-42m$
0.05		5.739	5.739	11.033	363.38	$I-42m$
0.1		5.721	5.721	10.994	359.81	$I-42m$
0.15		5.697	5.697	10.943	355.17 (18%)	$I-42m$
		7.994	6.809	6.534	355.72 (79%)	$Pmn21$

### 3.2.3 Raman analysis of $\text{Cu}_2\text{CdGe}(\text{S}_x\text{Se}_{1-x})_4$ monograin powders

The dependence of the Raman spectra on the anion composition of the orthorhombic structured  $\text{Cu}_2\text{CdGe}(\text{S}_x\text{Se}_{1-x})_4$  monograin powders is presented in Figure 3.17a [Paper III]. Figure 3.17b shows the Raman spectra of  $\text{Cu}_2\text{CdGe}(\text{S}_x\text{Se}_{1-x})_4$  monograin powders with tetragonal structure. The A1 Raman peak of pure  $\text{Cu}_2\text{CdGeSe}_4$  is at  $203\text{ cm}^{-1}$  and it is not depending on the crystal structure. The additional characteristic Raman modes for orthorhombic  $\text{Cu}_2\text{CdGeSe}_4$  were detected at  $162$ ,  $185$ ,  $270$  and  $277\text{ cm}^{-1}$ .  $\text{Cu}_2\text{CdGeSe}_4$  with tetragonal structure has additional characteristic Raman modes at  $175$  and  $261\text{ cm}^{-1}$ .

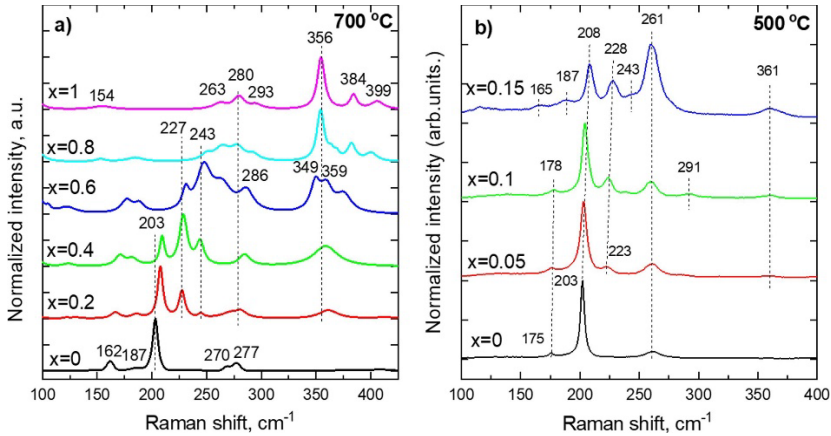


**Figure 3.17.** Raman spectra of  $\text{Cu}_2\text{CdGe}(\text{S}_x\text{Se}_{1-x})_4$  monograin powders synthesized a) at  $700\text{ °C}$  and b) at  $500\text{ °C}$ .

The main Raman mode A1 for pure  $\text{Cu}_2\text{CdGeSe}_4$  is at  $356\text{ cm}^{-1}$  [59]. Other Raman peaks of  $\text{Cu}_2\text{CdGeSe}_4$  were detected at  $154$ ,  $263$ ,  $280$ ,  $293$ ,  $337$ ,  $384$  and  $388\text{ cm}^{-1}$ , which are in good correlation with previously reported vibrational modes in  $\text{Cu}_2\text{CdGeSe}_4$  [59,112]. The spectra of  $\text{Cu}_2\text{CdGe}(\text{S}_x\text{Se}_{1-x})_4$  monograin powders with S content values ( $x = 0.2$ ,  $0.4$ ,  $0.6$  and  $0.8$ ) showed the peaks of two A1 mode because of the co-existence of S and Se atoms in powders.

The spectra of  $\text{Cu}_2\text{CdGe}(\text{S}_x\text{Se}_{1-x})_4$  monograin powders (synthesized at  $500\text{ °C}$ ) with low S content values ( $x = 0.05$ ,  $0.1$  and  $0.15$ ) showed clear shift of A1 mode toward the higher frequency region (from  $203$  to  $208\text{ cm}^{-1}$ ) proportionally to the increase in S content (Figure 3.17b). Additional peaks at  $223$  and  $361\text{ cm}^{-1}$  were detected already for  $\text{Cu}_2\text{CdGe}(\text{S}_x\text{Se}_{1-x})_4$  monograin powders with  $x = 0.05$ . The Raman mode at  $223\text{ cm}^{-1}$  shifted to the high frequency at  $228\text{ cm}^{-1}$ . The same peak exists in orthorhombic structured  $\text{Cu}_2\text{CdGe}(\text{S}_x\text{Se}_{1-x})_4$  monograin powders (synthesized at  $700\text{ °C}$ ).

### 3.2.4 $\text{Cu}_2\text{CdGe}(\text{S}_x\text{Se}_{1-x})_4$ monograin layer solar cells

All orthorhombic structured  $\text{Cu}_2\text{CdGe}(\text{S}_x\text{Se}_{1-x})_4$  powders with different S/Se ratio were also used as absorber materials in the monograin layer solar cells [Paper III]. Photovoltaic properties of the monograin layer solar cells were characterized by  $J$ - $V$  measurements (Figure 3.19a).

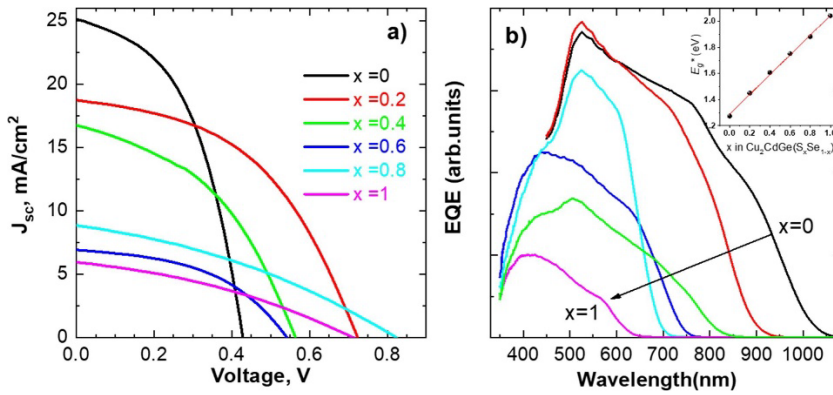


**Figure 3.19.** a) J-V curves and b) EQE curves of  $\text{Cu}_2\text{CdGe}(\text{S}_x\text{Se}_{1-x})_4$  device with different S/Se ratios.

The open circuit voltage of  $\text{Cu}_2\text{CdGe}(\text{S}_x\text{Se}_{1-x})_4$  monograin layer solar cells increased with increasing the sulfur content in the  $\text{Cu}_2\text{CdGe}(\text{S}_x\text{Se}_{1-x})_4$  powders. An increase in the open circuit voltage values indicated to the widening of the band gap of  $\text{Cu}_2\text{CdGe}(\text{S}_x\text{Se}_{1-x})_4$ . The external quantum efficiency spectrum was used to study the spectral response of the  $\text{Cu}_2\text{CdGe}(\text{S}_x\text{Se}_{1-x})_4$  monograin layer solar cells. Figure 3.19b shows the EQE spectra of  $\text{Cu}_2\text{CdGe}(\text{S}_x\text{Se}_{1-x})_4$  monograin layer solar cells. The absorption edge shifted to shorter wavelengths and the change of spectral response in the short wavelengths was visible with increase in S content in the absorber material. Inset graph in Figure 3.19 shows the  $E_g^*$  values of  $\text{Cu}_2\text{CdGe}(\text{S}_x\text{Se}_{1-x})_4$  solid solutions depending on the ratios of S/Se. An increase of  $E_g^*$  from 1.27 eV to 2.04 eV by increasing S content in  $\text{Cu}_2\text{CdGe}(\text{S}_x\text{Se}_{1-x})_4$  monograin powder materials was observed (Table 3.5). However, the values of  $V_{oc}$  were not increasing at the level as expected due to increased band gap values. There are several reasons why real values were not achieved: either the recombination in the bulk increases with a higher S/Se ratio or the band alignment with the CdS buffer becomes worse, increasing detrimental interface recombination. The short circuit current density of  $\text{Cu}_2\text{CdGe}(\text{S}_x\text{Se}_{1-x})_4$  MGL solar cells decreased from 24.9  $\text{mA}/\text{cm}^2$  ( $x = 0$ ) to 5.7  $\text{mA}/\text{cm}^2$  ( $x = 1$ ), going from low to high S-content. As confirmed by EQE measurements, the increased S-content resulted in an increase of the band gap, thus the  $J_{sc}$  decrease was the result of less absorption. The  $\text{Cu}_2\text{CdGe}(\text{S}_x\text{Se}_{1-x})_4$  monograin powders with  $x = 0.2$  gave the best solar cell with parameters:  $V_{oc} = 724$  mV,  $J_{sc} = 18.8$   $\text{mA}/\text{cm}^2$ ,  $FF = 46.9\%$ ,  $\eta = 6.4\%$  (active area) (Table. 3.5).

**Table 3.5** Summary of device parameters for the best performing  $\text{Cu}_2\text{CdGe}(\text{S}_x\text{Se}_{1-x})_4$  MGL solar cells depending on Se replacement with S in absorber materials.

$x = [\text{S}] / ([\text{Se}] + [\text{S}])$ in precursors	$V_{oc}$ (mV)	FF (%)	$J_{sc}$ ( $\text{mA}/\text{cm}^2$ )	Eff. (%) (active area)	$E_g^*$ (eV)
0	429	48.2	24.9	5.2	1.27
0.2	724	46.9	18.8	6.4	1.45
0.4	564	42.9	16.8	4.0	1.61
0.6	542	46.3	6.7	1.7	1.75
0.8	823	34.4	8.5	2.4	1.88
1	712	34.8	5.7	1.5	2.04

The preparation of monograin layer solar cells contain many steps, which need to be optimized for each composition of  $\text{Cu}_2\text{CdGe}(\text{S}_x\text{Se}_{1-x})_4$  absorber material: chemical etching and post-annealing of absorber material, selection of buffer layer etc. Therefore, all these steps need further study to improve the performance of  $\text{Cu}_2\text{CdGe}(\text{S}_x\text{Se}_{1-x})_4$  solar cells with different S/Se ratio.

### **Summary of the effect of the S/Se concentration ratio on the properties of $\text{Cu}_2\text{CdGe}(\text{S}_x\text{Se}_{1-x})_4$ monograin powders for photovoltaic application.**

A continuous series of  $\text{Cu}_2\text{CdGe}(\text{S}_x\text{Se}_{1-x})_4$  monograin powders were synthesized by molten salt method for photovoltaic applications. Structural study by Raman and X-ray diffraction showed that all  $\text{Cu}_2\text{CdGe}(\text{S}_x\text{Se}_{1-x})_4$  monograin powders synthesized at 700 °C crystallize in orthorhombic structure and solid solutions synthesized at 500 °C have only tetragonal structure in the range  $x = 0$  to  $x = 0.1$ .  $\text{Cu}_2\text{CdGe}(\text{S}_x\text{Se}_{1-x})_4$  monograin powders with  $x = 0.15$  synthesized at 500 °C contain mixture of orthorhombic and tetragonal phases. Lattice parameters decreased linearly by increasing the S content in the  $\text{Cu}_2\text{CdGe}(\text{S}_x\text{Se}_{1-x})_4$  monograin powders. The median crystal size decreased almost two times with the increasing S content in the  $\text{Cu}_2\text{CdGe}(\text{S}_x\text{Se}_{1-x})_4$  powders.

The increasing sulfur content in the orthorhombic  $\text{Cu}_2\text{CdGe}(\text{S}_x\text{Se}_{1-x})_4$  monograin powders led to an increase in the effective band gap energy from 1.27 eV to 2.04 eV. Therefore  $\text{Cu}_2\text{CdGe}(\text{S}_x\text{Se}_{1-x})_4$  monograin powders with  $x = 0 - 0.2$  could be used as absorber materials for single junction solar cells and compounds with  $x > 0.2$  could be used as top cell absorber materials in a tandem solar cell structure due to suitable wide band gap ( $E_g > 1.6$  eV).

The highest power conversion efficiency of 6.4% for monograin layer solar cells have been achieved by  $\text{Cu}_2\text{CdGe}(\text{S}_x\text{Se}_{1-x})_4$  monograin powders with  $x = 0.2$  showing the parameters:  $V_{OC} = 724$  mV,  $J_{SC} = 18.8$  mA/cm<sup>2</sup> and  $FF = 46.9\%$ .

## **3.3 $\text{Cu}_2\text{Ge}(\text{Se}_x\text{S}_{1-x})_3$ monograin powders**

### **3.3.1 Morphology and composition of $\text{Cu}_2\text{Ge}(\text{Se}_x\text{S}_{1-x})_3$ monograin powders**

$\text{Cu}_2\text{GeSe}_3$  and  $\text{Cu}_2\text{GeS}_3$  have many promising properties for absorber material, such as *p*-type conductivity, high absorption coefficient ( $10^4$  cm<sup>-1</sup>) and a direct band gap energy (0.8 – 1.5 eV) [24,28], there are only few studies presenting the results about  $\text{Cu}_2\text{GeSe}_3$ ,  $\text{Cu}_2\text{GeS}_3$  or their solid solution based solar cells [40]. Therefore, solid solutions  $\text{Cu}_2\text{Ge}(\text{Se}_x\text{S}_{1-x})_3$  needed investigation in order to modify the bandgap energy and find the optimal S/Se ratio for absorber material. Figure 3.20 shows the SEM images of  $\text{Cu}_2\text{Ge}(\text{Se}_x\text{S}_{1-x})_3$  ( $x = 0, 0.2, 0.4, 0.6, 0.8, 1$ ) powder crystals (with fraction size 63–75 μm) synthesized in Lil flux. All formed powders consist of non-aggregated, well-formed single crystals with round edges independent of the S/Se ratio [Paper V]. The median grain size of the powders increased with increasing the selenium content in the  $\text{Cu}_2\text{Ge}(\text{Se}_x\text{S}_{1-x})_3$  powders. This is also common in quaternary systems, where S/Se ratio is varied [Paper III].

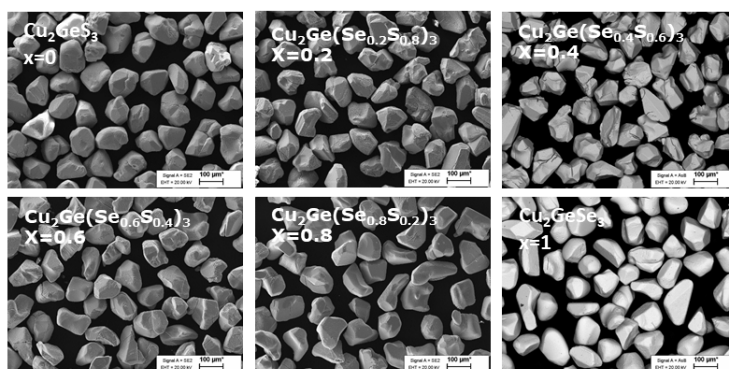


**Figure 3.20.** SEM images of  $\text{Cu}_2\text{Ge}(\text{Se}_x\text{S}_{1-x})_3$  ( $x = 0, 0.2, 0.4, 0.6, 0.8, 1$ ) monograin powders.

EDX analyses were carried out to confirm the bulk composition of monograin powders [Paper V]. Table 3.6 shows the average bulk composition of the  $\text{Cu}_2\text{Ge}(\text{Se}_x\text{S}_{1-x})_3$  monograin powders. It was found that bulk composition of all powders was slightly Cu-rich and Ge-poor ( $[\text{Cu}]/[\text{Ge}] > 2$ ), the ratio of  $[\text{Se}]/([\text{S}]+[\text{Se}])$  in synthesized  $\text{Cu}_2\text{Ge}(\text{Se}_x\text{S}_{1-x})_3$  solid solutions followed the input composition. The ratio of  $([\text{S}]+[\text{Se}])/([\text{Cu}]+[\text{Ge}])$  was approximately 1.0 regardless of the S/Se ratio in material.

**Table 3.6** Bulk composition of  $\text{Cu}_2\text{Ge}(\text{Se}_x\text{S}_{1-x})_3$  ( $x=0, 0.2, 0.4, 0.6, 0.8, 1$ ) monograin powders by EDX.

$x=[\text{Se}]/([\text{S}]+[\text{Se}])$ in precursors	Bulk composition of powder crystals by EDX (at%)				Compositional ratios		
	Cu	Ge	S	Se	$[\text{Se}]/([\text{S}]+[\text{Se}])$	$[\text{Cu}]/[\text{Ge}]$	$([\text{S}]+[\text{Se}])/([\text{Cu}]+[\text{Ge}])$
0.0	33.62	16.28	50.10	-	0.00	2.06	1.00
0.2	33.75	16.51	40.21	9.53	0.19	2.04	0.99
0.4	33.48	16.49	30.01	20.02	0.40	2.03	1.00
0.6	33.48	16.57	19.99	29.96	0.60	2.01	1.00
0.8	33.55	16.24	10.08	40.13	0.80	2.06	1.01
1.0	33.73	16.25	-	50.02	1.00	2.07	1.00

### 3.3.2 Structural analysis of $\text{Cu}_2\text{Ge}(\text{Se}_x\text{S}_{1-x})_3$ monograin powders

Figure 3.21a shows the XRD patterns and Figure 3.21c shows corresponding lattice parameters of  $\text{Cu}_2\text{Ge}(\text{Se}_x\text{S}_{1-x})_3$  monograin powders [Paper V]. The major diffraction peaks for pure  $\text{Cu}_2\text{GeSe}_3$  correspond to monoclinic phase (space group *Cc*) (ICDD PDF-2, 01–088–0827) and for pure  $\text{Cu}_2\text{GeSe}_3$ , the characteristic peaks correspond to orthorhombic phase (space group *Imm2*) (ICDD PDF-2, 01–076–7578). The crystal structure of  $\text{Cu}_2\text{Ge}(\text{Se}_x\text{S}_{1-x})_3$  transformation from monoclinic to orthorhombic was found to range from  $x = 0.2$  to  $x = 0.4$  because the  $\text{Cu}_2\text{Ge}(\text{Se}_x\text{S}_{1-x})_3$  ( $x = 0.2$ ) showed monoclinic structure, but further addition of Se in the  $\text{Cu}_2\text{Ge}(\text{Se}_x\text{S}_{1-x})_3$  ( $x = 0.4$ ) showed already orthorhombic structure. The position of most intensive diffraction peak shifted from 27.8 deg (for  $\text{Cu}_2\text{GeSe}_3$ ) to 29.2 deg (for  $\text{Cu}_2\text{GeS}_3$ ) as shown in enlarged view in Figure 3.21b.

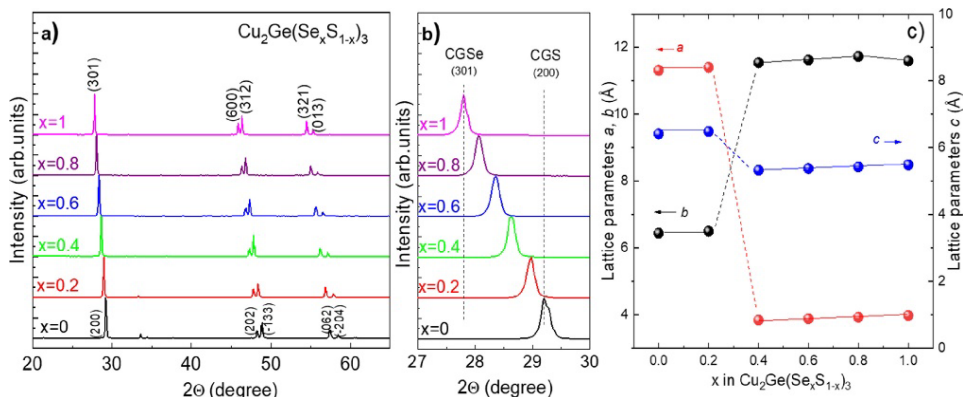


**Figure 3.21.** (a) XRD patterns of  $\text{Cu}_2\text{Ge}(\text{Se}_x\text{S}_{1-x})_3$  monograin powders ( $x = 0, 0.2, 0.4, 0.6, 0.8, 1$ ), b) enlarged view of XRD patterns to show the shift of main peak position and c) lattice parameters  $a$ ,  $b$  and  $c$  as a function of Se content.

Using the X-ray diffraction patterns, the values of lattice parameters ( $a$ ,  $b$  and  $c$ ) for all powders were calculated by Rietveld refinement and presented in Table 3.7 and Figure 3.21c. Monoclinic  $\text{Cu}_2\text{GeS}_3$  had lattice parameters  $a = 6.439 \text{ \AA}$ ,  $b = 11.316 \text{ \AA}$  and  $c = 6.416 \text{ \AA}$ . Small amount of Se in the  $\text{Cu}_2\text{Ge}(\text{Se}_x\text{S}_{1-x})_3$  ( $x = 0.2$ ) increased all the lattice parameters values. Additional S replacement by Se in  $\text{Cu}_2\text{Ge}(\text{Se}_x\text{S}_{1-x})_3$  ( $x = 0.4 - 1$ ) changed the crystal structure from monoclinic to orthorhombic together with enlargement in the lattice parameter values ( $a$  from  $11.541 \text{ \AA}$  to  $11.863 \text{ \AA}$ ;  $b$  from  $3.839 \text{ \AA}$  to  $3.954 \text{ \AA}$  and  $c$  from  $5.326 \text{ \AA}$  to  $5.485 \text{ \AA}$ ). This phenomenon is observed upon replacement of sulfur with selenium due to the smaller atom radius of S compared to Se.

**Table 3.7** Lattice parameters of  $\text{Cu}_2\text{Ge}(\text{Se}_x\text{S}_{1-x})_3$  ( $x = 0, 0.2, 0.4, 0.6, 0.8, 1$ ) monograin powders.

$x = [\text{Se}] / ([\text{S}] + [\text{Se}])$ in precursors	$a, \text{ \AA}$	$b, \text{ \AA}$	$c, \text{ \AA}$	$V, \text{ \AA}^3$	Space group
0.0	6.439	11.316	6.416	443.97	$Cc$ [No. 9]-monoclinic
0.2	6.497	11.402	6.486	456.31	$Cc$ [No. 9]-monoclinic
0.4	11.541	3.839	5.326	236.32	$Imm2$ [No. 44]-orthorhombic
0.6	11.626	3.883	5.376	242.70	$Imm2$ [No. 44]-orthorhombic
0.8	11.729	3.925	5.428	249.90	$Imm2$ [No. 44]-orthorhombic
1.0	11.863	3.954	5.485	257.28	$Imm2$ [No. 44]-orthorhombic

Figure 3.22 shows the Raman spectra obtained for  $\text{Cu}_2\text{Ge}(\text{Se}_x\text{S}_{1-x})_3$  monograin powders with different  $x$  value [Paper V]. The pure  $\text{Cu}_2\text{GeS}_3$  crystals show main Raman mode frequencies at  $337$  and  $390 \text{ cm}^{-1}$  and minor peaks at  $241, 268, 313$  and  $418 \text{ cm}^{-1}$ . All these peaks are assigned to monoclinic  $\text{Cu}_2\text{GeS}_3$  phase and are in good correlation to single crystal study [25]. Pure  $\text{Cu}_2\text{GeSe}_3$  powder crystals showed main Raman peak at  $191 \text{ cm}^{-1}$  and the additional Raman modes were detected at  $184, 220, 268$  and  $296 \text{ cm}^{-1}$ . All these peaks are assigned to orthorhombic  $\text{Cu}_2\text{GeSe}_3$  phase [54]. In the powders, all sulfide related peaks tend to shift toward smaller wavenumbers and the relative intensity of these peaks decreased. At the same time selenide related peaks shifted toward higher wavenumbers. As the  $x$  value in the  $\text{Cu}_2\text{Ge}(\text{Se}_x\text{S}_{1-x})_3$  monograin powders increased, the Raman spectra of  $\text{Cu}_2\text{Ge}(\text{Se}_x\text{S}_{1-x})_3$  exhibited the two-mode characteristic due to the coexistence of S and Se atoms in powders. This trend is correlated with the

increasing structural disorder due to the random distribution of S and Se atoms in the lattice that leads to fluctuations in the masses and force constants in the neighbourhood [68]. All peaks belong to the  $\text{Cu}_2\text{Ge}(\text{Se}_x\text{S}_{1-x})_3$  monograin powders, no other phases were detected.

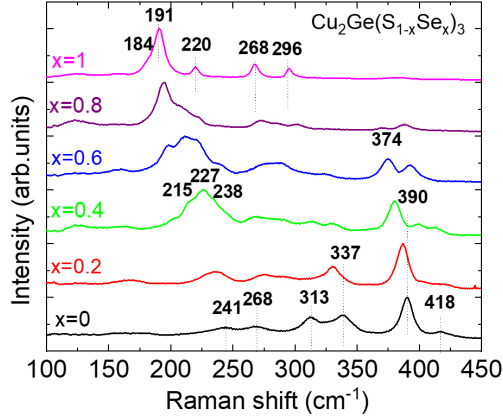


**Figure 3.22.** RT-Raman spectra of  $\text{Cu}_2\text{Ge}(\text{Se}_x\text{S}_{1-x})_3$  ( $x = 0, 0.2, 0.4, 0.6, 0.8, 1$ ) monograin powders.

### 3.3.3 PL analysis of $\text{Cu}_2\text{Ge}(\text{Se}_x\text{S}_{1-x})_3$ monograin powders

Figure 3.23a shows the normalized PL spectra of the  $\text{Cu}_2\text{Ge}(\text{Se}_x\text{S}_{1-x})_3$  monograin powders with different Se/S concentration ratios measured at  $T = 20$  K [Paper V]. All spectra are composed of 2 asymmetric PL peaks. Spectral fitting results with a split-Pearson VII function are shown as coloured bands. Peak positions of these bands (#1 and #2) as a function of Se/S concentration ratio showed nearly linear dependence with a slope about  $-0.8$  eV. Almost the same slope can be detected for  $E_g$  values determined from room temperature EQE measurements, see Figure 3.23b black dashed line. Therefore, the peak position shifted with  $x$  was related to  $E_g$  shift for both PL peaks. A detailed study of these peaks for  $x = 0.6$  was published in Paper IV. It was shown that both peaks are related to donor-acceptor pair recombination and therefore it is quite likely that the same model holds for the whole range of  $x$  values.

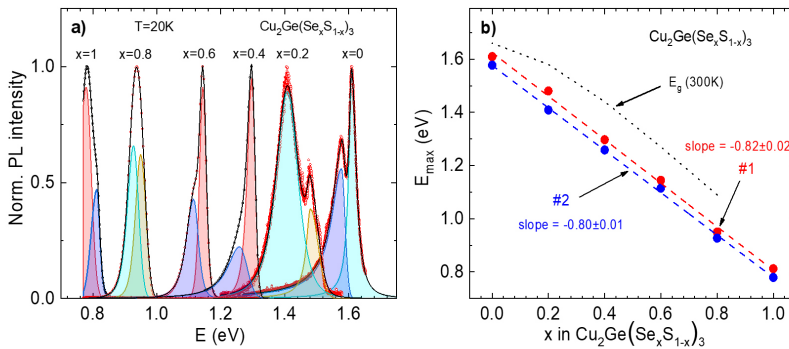


**Figure 3.23.** (a) Normalized low temperature photoluminescence spectra of  $\text{Cu}_2\text{Ge}(\text{Se}_x\text{S}_{1-x})_3$  monograin powders with different Se/S ratios with fitting using an asymmetric double sigmoidal function, (b) Peak positions of two PL bands as a function of  $x$ . Results of linear fitting are shown as dashed lines. Room temperature bandgap energy  $E_g$  determined from EQE measurements is given as a dotted line.



### 3.3.4 $\text{Cu}_2\text{Ge}(\text{Se}_x\text{S}_{1-x})_3$ monograin layer solar cells

The applicability of the  $\text{Cu}_2\text{Ge}(\text{Se}_x\text{S}_{1-x})_3$  powders as absorber materials were tested in monograin layer solar cell structure. Figure 3.24a shows illuminated  $J-V$  characteristics and Figure 3.24b shows corresponding EQE curves for all studied  $\text{Cu}_2\text{Ge}(\text{Se}_x\text{S}_{1-x})_3$  monograin powder based devices [Paper V]. The basic characteristics of solar cells and band gap energy values are presented in Table 3.8.  $\text{Cu}_2\text{GeSe}_3$  based solar cell characteristics were excluded because devices did not show any photoresponse.

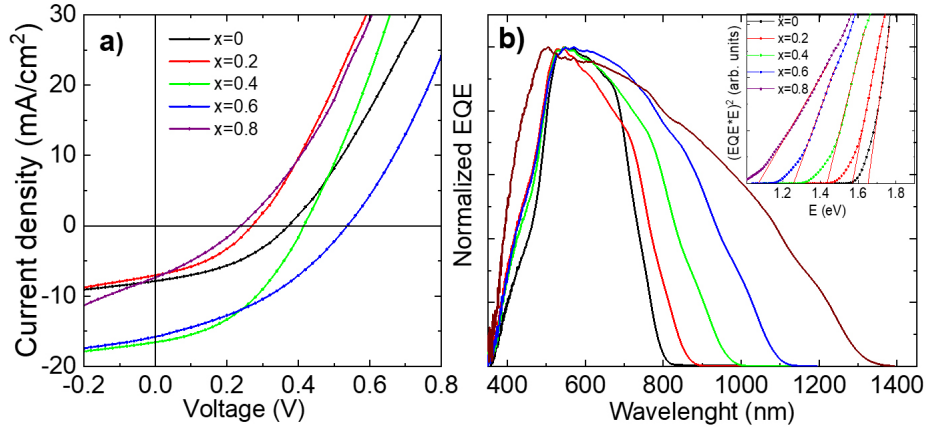


**Figure 3.24.** (a) Light  $J-V$  characteristics and (b) EQE of  $\text{Cu}_2\text{Ge}(\text{Se}_x\text{S}_{1-x})_3$  ( $x = 0, 0.2, 0.4, 0.6, 0.8, 1$ ) monograin layer solar cells. Inset graph shows bandgap extraction by plotting  $[(EQE \cdot E)^2]$  vs.  $E$ .

Open circuit voltage of monograin layer solar cells increased from 372 mV to 537 mV by increasing the selenium content in the  $\text{Cu}_2\text{Ge}(\text{Se}_x\text{S}_{1-x})_3$  from  $x = 0$  to  $x = 0.6$ . Also, current density values increased from 5.9  $\text{mA}/\text{cm}^2$  to 16.5  $\text{mA}/\text{cm}^2$ . In this study, the highest conversion efficiency of monograin layer solar cell were fabricated from  $\text{Cu}_2\text{Ge}(\text{Se}_x\text{S}_{1-x})_3$  ( $x = 0.6$ ), and demonstrated  $V_{oc} = 537$  mV,  $J_{sc} = 15.8$   $\text{mA}/\text{cm}^2$ ,  $FF = 37.2\%$ , and  $\eta = 3.16\%$ . According to EQE spectra in Figure 3.24b, by increasing the selenium content in monograin powders, the absorption edge shifted to longer wavelengths and the change of spectral response in the long wavelengths was seen. The effective band gap ( $E_g^*$ ) of  $\text{Cu}_2\text{Ge}(\text{Se}_x\text{S}_{1-x})_3$  monograin powders was showed in Figure 3.24b (inset graph). A decrease in  $E_g^*$  values from 1.65 eV to 1.07 eV by increasing Se content in  $\text{Cu}_2\text{Ge}(\text{Se}_x\text{S}_{1-x})_3$  ( $x = 0 - 0.8$ ) powder materials was (Table 3.8).

**Table 3.8** Summary of the main characteristics of  $\text{Cu}_2\text{Ge}(\text{Se}_x\text{S}_{1-x})_3$  monograin layer solar cells depending on S replacement with Se in absorber materials.

$x = [\text{Se}] / ([\text{S}] + [\text{Se}])$ in precursors	$V_{oc}$ (mV)	FF (%)	$J_{sc}$ ( $\text{mA}/\text{cm}^2$ )	Eff. (%)	$E_g^*$ (eV)
0	372	39.9	5.9	1.16	1.65
0.2	270	38.1	5.3	0.72	1.57
0.4	415	42.2	16.5	2.90	1.43
0.6	537	37.2	15.8	3.16	1.26
0.8	239	30.6	7.3	0.54	1.07
1	91	25.4	0.7	0.02	-

Results showed that  $\text{Cu}_2\text{Ge}(\text{Se}_x\text{S}_{1-x})_3$  ( $x = 0.4 - 0.6$ ) materials have potential as absorber materials in solar cells. Monograin layer solar cells preparation process contain many technological steps, which need to be optimized for example the optimization of absorber materials composition, selection of the buffer layer etc. Therefore, further research is needed to improve the performance of  $\text{Cu}_2\text{Ge}(\text{Se}_x\text{S}_{1-x})_3$  solar cells.

### **Summary of the study of $\text{Cu}_2\text{Ge}(\text{Se}_x\text{S}_{1-x})_3$ monograin powder properties and solar cells**

$\text{Cu}_2\text{Ge}(\text{Se}_x\text{S}_{1-x})_3$  ( $0 \leq x \leq 1$ ) monograin powders were successfully synthesized in Lil flux by molten salt synthesis–growth method. According to EDX analysis, complete series of solid solutions was formed by changing the S/Se ratio in  $\text{Cu}_2\text{Ge}(\text{Se}_x\text{S}_{1-x})_3$ . All synthesized  $\text{Cu}_2\text{Ge}(\text{Se}_x\text{S}_{1-x})_3$  powders were slightly Cu-rich and Ge-poor and consisted of well-formed crystals independent of the S/Se ratio. Structural studies by X-ray diffraction showed that  $\text{Cu}_2\text{GeS}_3$  crystallize in monoclinic and  $\text{Cu}_2\text{GeSe}_3$  crystallize in orthorhombic structure. The crystal structure of  $\text{Cu}_2\text{Ge}(\text{Se}_x\text{S}_{1-x})_3$  transformation from monoclinic to orthorhombic was detected between  $x = 0.2$  and  $x = 0.4$ . Raman and PL studies also confirmed the formation of the whole series of  $\text{Cu}_2\text{Ge}(\text{Se}_x\text{S}_{1-x})_3$ . Raman modes of solid solutions followed the bimodal behaviour. PL spectra of CGSSe were composed of two asymmetric PL peaks. Peak positions of these bands as a function of Se/S concentration show nearly linear dependence with a slope about  $-0.8$  eV. Almost the same slope was detected for band gap values determined from room temperature EQE measurements. Therefore, the peak position shift with increasing selenium content in powders is related to  $E_g$  shift for both PL peaks. Both peaks are related to donor-acceptor pair recombination.

Most promising compounds for solar cell application are  $\text{Cu}_2\text{Ge}(\text{Se}_x\text{S}_{1-x})_3$  monograin powders with  $x = 0.4 - 0.6$ . A best performing solar cell was fabricated by using  $\text{Cu}_2\text{Ge}(\text{Se}_x\text{S}_{1-x})_3$   $x = 0.6$  powder crystals as absorber material, exhibiting an open-circuit voltage of 537 mV, current density of 15.8 mA/cm<sup>2</sup>, fill factor of 37.2% and a conversion efficiency of 3.16%.

## Conclusions

This thesis focuses on the synthesis of  $\text{Cu}_2\text{Ge}(\text{S},\text{Se})_3$  and  $\text{Cu}_2\text{CdGe}(\text{S},\text{Se})_4$  monograin powders by using molten salt method and characterization of different properties of the synthesized monograin powders. All investigated monograin powders were implemented as absorber materials in monograin layer solar cells. On the base of information gathered via different analytical methods, the following findings can be listed, and conclusions can be made.

### $\text{Cu}_2\text{CdGeSe}_4$

- ❖ According to XRD analysis, the  $\text{Cu}_2\text{CdGeSe}_4$  monograin powders of both possible crystal structures were successfully synthesized by using different synthesis temperatures: at 500 °C tetragonal structure and at temperatures 600 °C and 700 °C orthorhombic structure had gained regardless of the used flux.
- ❖ Raman analysis was found to be very effective method to distinguish both crystal modifications of  $\text{Cu}_2\text{CdGeSe}_4$ . The most intensive peak in the spectra of  $\text{Cu}_2\text{CdGeSe}_4$  was observed at 203  $\text{cm}^{-1}$  regardless on the crystal structure. The additional characteristic Raman modes for the orthorhombic  $\text{Cu}_2\text{CdGeSe}_4$  phase were detected at 162, 187, 271 and 277  $\text{cm}^{-1}$  and for tetragonal  $\text{Cu}_2\text{CdGeSe}_4$  phase, the characteristic peaks were at 175, 263 and 292  $\text{cm}^{-1}$ .
- ❖ Two different band gap values were confirmed by EQE measurements – for orthorhombic  $\text{Cu}_2\text{CdGeSe}_4$  1.27 eV and for tetragonal  $\text{Cu}_2\text{CdGeSe}_4$  1.14 eV.
- ❖ For the first time, the effect of the crystalline structure of  $\text{Cu}_2\text{CdGeSe}_4$  on device performance was studied by  $J-V$  measurements under standard conditions. The highest power conversion efficiency of 2.16% was obtained with tetragonal  $\text{Cu}_2\text{CdGeSe}_4$  based devices with following parameters:  $V_{OC} = 315$  mV,  $J_{SC} = 14.7$   $\text{mA}/\text{cm}^2$ , and  $FF = 35\%$ . Devices based on orthorhombic  $\text{Cu}_2\text{CdGeSe}_4$  absorbers showed efficiency of 4.21% with a  $V_{OC} = 464$  mV,  $J_{SC} = 17.5$   $\text{mA}/\text{cm}^2$  and  $FF = 39\%$ . Devices based on orthorhombic  $\text{Cu}_2\text{CdGeSe}_4$  powders were improved by surface post-treatments by combined chemical etching followed by annealing at elevated temperature. The highest conversion efficiency of 5.69% was gained with nearly stoichiometric composition of  $\text{Cu}_2\text{CdGeSe}_4$ , which was etched with  $\text{Br}_2\text{-MeOH/KCN}$  solutions and post-annealed at 400 °C, with the following parameters:  $V_{OC} = 459$  mV;  $J_{SC} = 25.6$   $\text{mA}/\text{cm}^2$  and  $FF = 48\%$ .

### $\text{Cu}_2\text{CdGe}(\text{S}_x\text{Se}_{1-x})_4$ solid solutions

- ❖ According to XRD analysis, full range of  $\text{Cu}_2\text{CdGe}(\text{S}_x\text{Se}_{1-x})_4$  solid solutions synthesized at 700 °C crystallized in orthorhombic structure and solid solutions synthesized at 500 °C had tetragonal structure in the range  $x = 0$  to  $x = 0.1$ .  $\text{Cu}_2\text{CdGe}(\text{S}_x\text{Se}_{1-x})_4$  solid solutions with  $x = 0.15$  synthesized at 500 °C contain already mixture of orthorhombic and tetragonal phases. Lattice parameters decreased linearly by increasing the S content in the  $\text{Cu}_2\text{CdGe}(\text{S}_x\text{Se}_{1-x})_4$  solid solutions.
- ❖ According to EQE measurements, the effective band gap energy increased from 1.27 eV to 2.04 eV by increasing the sulfur content in the orthorhombic  $\text{Cu}_2\text{CdGe}(\text{S}_x\text{Se}_{1-x})_4$  solid solutions. Therefore, the orthorhombic  $\text{Cu}_2\text{CdGe}(\text{S}_x\text{Se}_{1-x})_4$  solid solutions with  $x = 0 - 0.2$  could be used as absorber materials for single junction solar cells and compounds with  $x > 0.2$  could be used as top cell absorber materials in a tandem solar cell structure due to the wide band gap ( $E_g > 1.6$  eV).

- ❖ The highest power conversion efficiency of 6.4% for  $\text{Cu}_2\text{CdGe}(\text{S}_x\text{Se}_{1-x})_4$  monograin layer solar cells was achieved with  $x = 0.2$  showing the parameters:  $V_{OC} = 724$  mV,  $J_{SC} = 18.8$  mA/cm<sup>2</sup> and  $FF = 46.9\%$ .

### **$\text{Cu}_2\text{Ge}(\text{Se}_x\text{S}_{1-x})_3$ solid solutions**

- ❖ Structural studies by XRD showed that  $\text{Cu}_2\text{GeS}_3$  crystallized in monoclinic and  $\text{Cu}_2\text{GeSe}_3$  crystallized in orthorhombic structure. Transformation from monoclinic to orthorhombic crystal structure in  $\text{Cu}_2\text{Ge}(\text{Se}_x\text{S}_{1-x})_3$  solid solutions was detected between  $x = 0.2$  to  $x = 0.4$ .
- ❖ The effective band gap values of  $\text{Cu}_2\text{Ge}(\text{Se}_x\text{S}_{1-x})_3$  determined from EQE measurements were found to shift nearly linearly to lower energy values from 1.65 eV to 1.07 eV by decreasing the S content from  $x = 0$  to  $x = 0.8$  in  $\text{Cu}_2\text{Ge}(\text{Se}_x\text{S}_{1-x})_3$ .
- ❖ Radiative recombination processes in  $\text{Cu}_2\text{Ge}(\text{Se}_x\text{S}_{1-x})_3$  monograin powders were studied by using photoluminescence spectroscopy. All PL spectra of  $\text{Cu}_2\text{Ge}(\text{Se}_x\text{S}_{1-x})_3$  consisted of two asymmetric PL peaks. Both PL peaks were related to donor-acceptor pair recombination. Peak positions of the PL bands shifted nearly linearly to lower energy values by decreasing the S content in  $\text{Cu}_2\text{Ge}(\text{Se}_x\text{S}_{1-x})_3$ .
- ❖ The highest efficiency of 3.16% was demonstrated by using  $\text{Cu}_2\text{Ge}(\text{Se}_{0.6}\text{S}_{0.4})_3$  powder crystals as absorber material in monograin layer solar cells with following parameters:  $V_{OC} = 537$  mV,  $J_{SC} = 15.8$  mA/cm<sup>2</sup> and  $FF = 37.2\%$ .

In conclusions, it is possible to synthesize  $\text{Cu}_2\text{CdGe}(\text{S}_x\text{Se}_{1-x})_4$  and  $\text{Cu}_2\text{Ge}(\text{Se}_x\text{S}_{1-x})_3$  absorber materials via the monograin powder synthesis-growth method in molten salt medium. As preliminary results indicate, both type of materials are applicable as absorber materials in monograin layer solar cells. The novelty of this thesis is the first time to present solar cell parameters based on these materials and the record efficiency of 6.4% and 3.16% were gained by using  $\text{Cu}_2\text{CdGe}(\text{S}_{0.2}\text{Se}_{0.8})_4$  and  $\text{Cu}_2\text{Ge}(\text{Se}_{0.6}\text{S}_{0.4})_3$  as absorbers. However, the defect composition of powders, crystal surface modifications and band alignments need to be further optimized.

## References

- [1] Key World Energy Statistics, (2021). <https://www.iea.org/reports/key-world-energy-statistics-2021>.
- [2] World total Electricity Consumption Data, (2019). <https://www.iea.org/reports/electricity-information-overview/electricity-consumption>.
- [3] 2018 World Energy Outlook, (2018). <https://www.iea.org/reports/world-energy-outlook-2018>.
- [4] Snapshot of Global PV Markets, (2020). <https://iea-pvps.org/snapshot-reports/snapshot-2021/>.
- [5] N.T. Mbungu, R.M. Naidoo, R.C. Bansal, M.W. Siti, D.H. Tungadio, An overview of renewable energy resources and grid integration for commercial building applications, *J. Energy Storage*. 29 (2020) 101385. <https://doi.org/10.1016/j.est.2020.101385>.
- [6] K. Yoshikawa, H. Kawasaki, W. Yoshida, T. Irie, K. Konishi, K. Nakano, T. Uto, D. Adachi, M. Kanematsu, H. Uzu, K. Yamamoto, Silicon heterojunction solar cell with interdigitated back contacts for a photoconversion efficiency over 26%, *Nat. Energy*. 2 (2017). <https://doi.org/10.1038/nenergy.2017.32>.
- [7] M. Green, E. Dunlop, J. Hohl-Ebinger, M. Yoshita, N. Kopidakis, X. Hao, Solar cell efficiency tables (version 57), *Prog. Photovoltaics Res. Appl.* 29 (2021) 3–15. <https://doi.org/10.1002/pip.3371>.
- [8] M. Nakamura, K. Yamaguchi, Y. Kimoto, Y. Yasaki, T. Kato, H. Sugimoto, Cd-Free  $\text{Cu}(\text{In,Ga})(\text{Se,S})_2$  Thin-Film Solar Cell With Record Efficiency of 23.35%, *IEEE J. Photovoltaics*. 9 (2019) 1863–1867. <https://doi.org/10.1109/JPHOTOV.2019.2937218>.
- [9] C. Maltman, V. Yurkov, Extreme environments and high-level bacterial tellurite resistance, *Microorganisms*. 7 (2019) 1–24. <https://doi.org/10.3390/microorganisms7120601>.
- [10] L. Grandell, M. Höök, Assessing rare metal availability challenges for solar energy technologies, *Sustain*. 7 (2015) 11818–11837. <https://doi.org/10.3390/su70911818>.
- [11] C. Yan, J. Huang, K. Sun, S. Johnston, Y. Zhang, H. Sun, A. Pu, M. He, F. Liu, K. Eder, L. Yang, J.M. Cairney, N.J. Ekins-Daukes, Z. Hameiri, J.A. Stride, S. Chen, M.A. Green, X. Hao,  $\text{Cu}_2\text{ZnSnS}_4$  solar cells with over 10% power conversion efficiency enabled by heterojunction heat treatment, *Nat. Energy*. 3 (2018) 764–772. <https://doi.org/10.1038/s41560-018-0206-0>.
- [12] J. Zhou, X. Xu, B. Duan, H. Wu, J. Shi, Y. Luo, D. Li, Q. Meng, Regulating crystal growth via organic lithium salt additive for efficient Kesterite solar cells, *Nano Energy*. 89 (2021) 106405. <https://doi.org/10.1016/j.nanoen.2021.106405>.
- [13] S. Rühle, Tabulated values of the Shockley-Queisser limit for single junction solar cells, *Sol. Energy*. 130 (2016) 139–147. <https://doi.org/10.1016/j.solener.2016.02.015>.
- [14] J.F. Guillemoles, T. Kirchartz, D. Cahen, U. Rau, Guide for the perplexed to the Shockley–Queisser model for solar cells, *Nat. Photonics*. 13 (2019) 501–505. <https://doi.org/10.1038/s41566-019-0479-2>.

- [15] J. Li, Y. Huang, J. Huang, G. Liang, Y. Zhang, G. Rey, F. Guo, Z. Su, H. Zhu, L. Cai, K. Sun, Y. Sun, F. Liu, S. Chen, X. Hao, Y. Mai, M.A. Green, Defect Control for 12.5% Efficiency  $\text{Cu}_2\text{ZnSnSe}_4$  Kesterite Thin-Film Solar Cells by Engineering of Local Chemical Environment, *Adv. Mater.* 32 (2020) 1–9. <https://doi.org/10.1002/adma.202005268>.
- [16] W. Wang, M.T. Winkler, O. Gunawan, T. Gokmen, T.K. Todorov, Y. Zhu, D.B. Mitzi, Device characteristics of CZTSSe thin-film solar cells with 12.6% efficiency, *Adv. Energy Mater.* 4 (2014) 1–5. <https://doi.org/10.1002/aenm.201301465>.
- [17] Y. Gong, Y. Zhang, Q. Zhu, Y. Zhou, R. Qiu, C. Niu, W. Yan, W. Huang, H. Xin, Identifying the origin of the Voc deficit of kesterite solar cells from the two grain growth mechanisms induced by Sn 2+ and Sn 4+ precursors in DMSO solution, *Energy Environ. Sci.* 14 (2021) 2369–2380. <https://doi.org/10.1039/D0EE03702H>.
- [18] T. Gokmen, O. Gunawan, T.K. Todorov, D.B. Mitzi, Band tailing and efficiency limitation in kesterite solar cells, *Appl. Phys. Lett.* 103 (2013). <https://doi.org/10.1063/1.4820250>.
- [19] K. Fai, T. Solar, C. Solar, C. View, K.F. Tai, Investigating the Open-Circuit Voltage Deficit in CZTSSe Solar Cells, (2016). <https://doi.org/10.13140/RG.2.2.20153.98404>.
- [20] Y.E. Romanyuk, S.G. Haass, S. Giraldo, M. Placidi, D. Tiwari, D.J. Fermin, X. Hao, H. Xin, T. Schnabel, M. Kauk-Kuusik, P. Pistor, S. Lie, L.H. Wong, Doping and alloying of kesterites, *JPhys Energy.* 1 (2019). <https://doi.org/10.1088/2515-7655/ab23bc>.
- [21] K.J. Yang, S. Kim, S.Y. Kim, K. Ahn, D.H. Son, S.H. Kim, S.J. Lee, Y.I. Kim, S.N. Park, S.J. Sung, D.H. Kim, T. Enkhbat, J.H. Kim, C.W. Jeon, J.K. Kang, Flexible  $\text{Cu}_2\text{ZnSn}(\text{S},\text{Se})_4$  solar cells with over 10% efficiency and methods of enlarging the cell area, *Nat. Commun.* 10 (2019) 1–10. <https://doi.org/10.1038/s41467-019-10890-x>.
- [22] M.H. Sharif, T. Enkhbat, E. Enkhbayar, J. Kim, Control of Defect States of Kesterite Solar Cells to Achieve More Than 11% Power Conversion Efficiency, *ACS Appl. Energy Mater.* 3 (2020) 8500–8508. <https://doi.org/10.1021/acsaem.0c01141>.
- [23] J. Yang, B. Lu, R. Song, H. Hou, L. Zhao, X. Zhang, G. Liu, G. Qiao, Realizing enhanced thermoelectric properties in  $\text{Cu}_2\text{GeSe}_3$  via a synergistic effect of In and Ag dual-doping, *J. Eur. Ceram. Soc.* 42 (2022) 169–174. <https://doi.org/10.1016/j.jeurceramsoc.2021.10.009>.
- [24] A. Dugarte-Dugarte, N.R. Pineda, L. Nieves, J.A. Henao, G.D. De Delgado, J.M. Delgado, The crystal structure of  $\text{Cu}_2\text{GeSe}_3$  and the structure-types of the  $\text{I}_2\text{-IV-VI}_3$  family of semiconducting compounds, *Acta Crystallogr. Sect. B Struct. Sci. Cryst. Eng. Mater.* 77 (2021) 158–167. <https://doi.org/10.1107/S2052520620016571>.
- [25] Y. Matsumoto, N. Aihara, N. Saito, K. Tanaka, Growth of  $\text{Cu}_2\text{GeS}_3$  bulk single crystals by chemical vapor transport with iodine, *Mater. Lett.* 194 (2017) 16–19. <https://doi.org/10.1016/j.matlet.2017.02.009>.
- [26] H. Araki, K. Chino, K. Kimura, N. Aihara, K. Jimbo, H. Katagiri, Fabrication of  $\text{Cu}_2\text{GeS}_3$ -based thin film solar cells by sulfurization of Cu/Ge stacked precursors, *Jpn. J. Appl. Phys.* 53 (2014) 2–6. <https://doi.org/10.7567/JJAP.53.05FW10>.

- [27] Q. Chen, T. Maeda, T. Wada, Optical properties and electronic structures of  $\text{Cu}_2\text{SnS}_3$ ,  $\text{Cu}_2\text{GeS}_3$ , and their solid solution  $\text{Cu}_2(\text{Ge,Sn})\text{S}_3$ , *Jpn. J. Appl. Phys.* 57 (2018) 08RC20. <https://doi.org/10.7567/JJAP.57.08RC20>.
- [28] X. Jin, L. Zhang, G. Jiang, W. Liu, C. Zhu, High open-circuit voltage of ternary  $\text{Cu}_2\text{GeS}_3$  thin film solar cells from combustion synthesized Cu-Ge alloy, *Sol. Energy Mater. Sol. Cells.* 160 (2017) 319–327. <https://doi.org/10.1016/j.solmat.2016.11.001>.
- [29] K. Pal, P. Singh, A. Bhaduri, K.B. Thapa, Current challenges and future prospects for a highly efficient (>20%) kesterite CZTS solar cell: A review, *Sol. Energy Mater. Sol. Cells.* 196 (2019) 138–156. <https://doi.org/10.1016/j.solmat.2019.03.001>.
- [30] K. Ito, T. Nakazawa, Electrical and optical properties of stannite-type quaternary semiconductor thin films, *Jpn. J. Appl. Phys.* 27 (1988) 2094–2097. <https://doi.org/10.1143/JJAP.27.2094>.
- [31] K.T. H. Katagiri, K. Jimbo, K. Moriya, Solar cell without environmental pollution by using CZTS thin film, *Energy Convers.* (2003) 2874–2879. 3rd World Conference on Photovoltaic Energy Conversion.
- [32] H. Katagiri, K. Jimbo, W.S. Maw, K. Oishi, M. Yamazaki, H. Araki, A. Takeuchi, Development of CZTS-based thin film solar cells, *Thin Solid Films.* 517 (2009) 2455–2460. <https://doi.org/10.1016/j.tsf.2008.11.002>.
- [33] T.K. Todorov, K.B. Reuter, D.B. Mitzi, High-efficiency solar cell with earth-abundant liquid-processed absorber, *Adv. Mater.* 22 (2010) 156–159. <https://doi.org/10.1002/adma.200904155>.
- [34] M. Kauk-Kuusik, K. Timmo, K. Muska, M. Pilvet, J. Krustok, M. Danilson, V. Mikli, R. Josepson, M. Grossberg, Reduced recombination through the CZTS/CdS interface engineering in monograin layer solar cells, *J. Phys. Energy.* 2 (2022) 0–31. <https://doi.org/10.1088/2515-7655/ac618d>.
- [35] A. Ruiz-Perona, G. Gurieva, M. Sun, T. Kodalle, Y. Sánchez, M. Grossberg, J.M. Merino, S. Schorr, M. León, R. Caballero, Routes to develop a  $\text{S}/([\text{S}]+[\text{Se}])$  gradient in wide band-gap  $\text{Cu}_2\text{ZnGe}(\text{S,Se})_4$  thin-film solar cells, *J. Alloys Compd.* 868 (2021) 159253. <https://doi.org/10.1016/j.jallcom.2021.159253>.
- [36] L. Choubrac, M. Bär, X. Kozina, R. Félix, R.G. Wilks, G. Brammertz, S. Levchenko, L. Arzel, N. Barreau, S. Harel, M. Meuris, B. Vermang, Sn Substitution by Ge: Strategies to Overcome the Open-Circuit Voltage Deficit of Kesterite Solar Cells, *ACS Appl. Energy Mater.* 3 (2020) 5830–5839. <https://doi.org/10.1021/acsaem.0c00763>.
- [37] E.A. T. Schnabel, M. Seboui, A. Bauer, L. Choubrac, L. Arzel, S. Harel, N. Barreaub, Evaluation of different buffer materials for solar cells with wide-gap  $\text{Cu}_2\text{ZnGeS}_x\text{Se}_{4-x}$  absorbers, *RSC Adv.* 7 (2017) 40105–40110. <https://doi.org/10.1039/c7ra06438a>.
- [38] A. Tombak, T. Kilicoglu, Y.S. Ocak, Solar cells fabricated by spray pyrolysis deposited  $\text{Cu}_2\text{CdSnS}_4$  thin films, *Renew. Energy.* 146 (2020) 1465–1470. <https://doi.org/10.1016/j.renene.2019.07.057>.
- [39] W. Zhao, G. Wang, Q. Tian, L. Huang, S. Gao, D. Pan, Solution-processed  $\text{Cu}_2\text{CdSn}(\text{S,Se})_4$  thin film solar cells, *Sol. Energy Mater. Sol. Cells.* 133 (2015) 15–20. <https://doi.org/10.1016/j.solmat.2014.10.040>.
- [40] C. Yang, B. Zhou, S. Miao, C. Yang, B. Cai, W. Zhang, X. Xu,  $\text{Cu}_2\text{Ge}(\text{S}_{3-x}\text{Se}_x)$  Colloidal Nanocrystals: Synthesis, Characterization, and Composition-Dependent Band Gap Engineering, (2013). <https://doi.org/10.1021/ja400452t>.

- [41] O. V. Parasyuk, Y.E. Romanyuk, I.D. Olekseyuk, Single-crystal growth of  $\text{Cu}_2\text{CdGeS}_4$ , *J. Cryst. Growth.* 275 (2005) 2–5. <https://doi.org/10.1016/j.jcrysgro.2004.10.133>.
- [42] G.Y. Davydyuk, O. V. Parasyuk, Y.E. Romanyuk, S.A. Semenyuk, V.I. Zaremba, L.V. Piskach, J.J. Koziol, V.O. Halka, Single crystal growth and physical properties of the  $\text{Cu}_2\text{CdGeS}_4$  compound, *J. Alloys Compd.* 339 (2002) 40–45. [https://doi.org/10.1016/S0925-8388\(01\)01987-9](https://doi.org/10.1016/S0925-8388(01)01987-9).
- [43] J. Krustok, T. Raadik, X. Li, M. Kauk-Kuusik, K. Timmo, S. Oueslati, M. Grossberg, Study of point defects in wide-bandgap  $\text{Cu}_2\text{CdGeS}_4$  microcrystals by temperature and laser power dependent photoluminescence spectroscopy, *J. Phys. D: Appl. Phys.* 53 (2020) 275102. <https://doi.org/10.1088/1361-6463/ab83c1>.
- [44] H. Matsushita, T. Ichikawa, A. Katsui, Structural, thermodynamical and optical properties of  $\text{Cu}_2\text{-II-IV-VI}_4$  quaternary compounds, *J. Mater. Sci.* 40 (2005) 2003–2005. <https://doi.org/10.1007/s10853-005-1223-5>.
- [45] M.A. Konstantinova, N. N., Medvedkin, G. A., Polyshina, I. K., Rud, Y. V., Smirnova, A. D., Sokolova, V. I., Tairov, Optical and electric properties of  $\text{Cu}_2\text{CdSnSe}_4$  and  $\text{Cu}_2\text{CdGeSe}_4$  crystals, *Inorg. Mater.* 25 (1989) 1223–1226.
- [46] V.A. Ocheretova, O. V. Parasyuk, A.O. Fedorchuk, O.Y. Khyzhun, Electronic structure of  $\text{Cu}_2\text{CdGeSe}_4$  single crystal as determined from X-ray spectroscopy data, *Mater. Chem. Phys.* 160 (2015) 345–351. <https://doi.org/10.1016/j.matchemphys.2015.04.049>.
- [47] M.G. Brik, O. V. Parasyuk, G.L. Myronchuk, I. V. Kityk, Specific features of band structure and optical anisotropy of  $\text{Cu}_2\text{CdGeSe}_4$  quaternary compounds, *Mater. Chem. Phys.* 147 (2014) 155–161. <https://doi.org/10.1016/j.matchemphys.2014.04.022>.
- [48] R. Chetty, J. Dadda, J. De Boor, E. Müller, R.C. Mallik, The effect of Cu addition on the thermoelectric properties of  $\text{Cu}_2\text{CdGeSe}_4$ , *Intermetallics.* 57 (2015) 156–162. <https://doi.org/10.1016/j.intermet.2014.10.015>.
- [49] D. Li, F. Ling, Z. Zhu, X. Zhang, Theoretical studies on the structural, electronic, and optical properties of  $\text{Cu}_2\text{CdGeSe}_4$ , *Phys. B Condens. Matter.* 406 (2011) 3299–3302. <https://doi.org/10.1016/j.physb.2011.05.044>.
- [50] E.V.C. Robert, J. de Wild, D. Colombara, P.J. Dale, Crystallographic and optoelectronic properties of the novel thin film absorber  $\text{Cu}_2\text{GeS}_3$ , *Thin Film. Sol. Energy Technol.* VIII. 9936 (2016) 993607. <https://doi.org/10.1117/12.2236621>.
- [51] H. Shao, X. Tan, T. Hu, G.Q. Liu, J. Jiang, H. Jiang, First-principles study on the lattice dynamics and thermodynamic properties of  $\text{Cu}_2\text{GeSe}_3$ , *Epl.* 109 (2015). <https://doi.org/10.1209/0295-5075/109/47004>.
- [52] L.M. De Chalbaud, G.D. De Delgado, J.M. Delgado, A.E. Mora, V. Sagredo, Synthesis and single-crystal structural study of  $\text{Cu}_2\text{GeS}_3$ , *Mater. Res. Bull.* 32 (1997) 1371–1376. [https://doi.org/10.1016/S0025-5408\(97\)00115-3](https://doi.org/10.1016/S0025-5408(97)00115-3).
- [53] L. Piskach, O. Parasyuk, Y. Romanyuk, The phase equilibria in the quasi-binary  $\text{Cu}_2\text{GeS}_3/\text{Se}_3\text{-CdS/Se}$  systems, *J. Alloys Compd.* 299 (2000) 227–231. [https://doi.org/10.1016/S0925-8388\(99\)00797-5](https://doi.org/10.1016/S0925-8388(99)00797-5).
- [54] M. Morihama, T. Maeda, I. Yamauchi, T. Wada, Crystallographic and optical properties of narrow band gap  $\text{Cu}_2\text{GeSe}_3$  and  $\text{Cu}_2(\text{Sn}_{1-x}\text{Ge}_x)\text{Se}_3$  solid solution, in: *Jpn. J. Appl. Phys., Japan Society of Applied Physics*, 2014. <https://doi.org/10.7567/JJAP.53.05FW06>.



- [55] G. Marcano, G.S. Pérez, C. Rincón, Photoluminescence Spectra of  $\text{Cu}_2\text{GeSe}_3$  Orthorhombic Semiconductor Compound, *Phys. Status Solidi Basic Res.* 254 (2017) 2–4. <https://doi.org/10.1002/pssb.201700332>.
- [56] L.D. Gulay, Y.E. Romanyuk, O. V. Parasyuk, Crystal structures of low- and high-temperature modifications of  $\text{Cu}_2\text{CdGeSe}_4$ , *J. Alloys Compd.* 347 (2002) 193–197. [https://doi.org/10.1016/S0925-8388\(02\)00790-9](https://doi.org/10.1016/S0925-8388(02)00790-9).
- [57] E. Quintero, R. Tovar, M. Quintero, G.E. Delgado, M. Morocoima, D. Caldera, J. Ruiz, A.E. Mora, M. Briceño, J.L. Fernandez, Lattice parameter values and phase transitions for the  $\text{Cu}_2\text{Cd}_{1-z}\text{Mn}_z\text{GeSe}_4$  and  $\text{Cu}_2\text{Cd}_{1-z}\text{Fe}_z\text{GeSe}_4$  alloys, *J. Alloys Compd.* 432 (2007) 142–148. <https://doi.org/10.1016/j.jallcom.2006.05.126>.
- [58] I.D. Olekseyuk, L. V Piskach, O. V Parasyuk, T. Mel'nyk, T.A. Lyskovetz, The  $\text{Cu}_2\text{Se}-\text{CdSe}-\text{GeSe}_2$  system, *J. Alloys Compd.* 298 (2000) 203–212.
- [59] A.A. Lavrentyev, B.V. Gabrelian, V.T. Vu, P.N. Shkumat, V.A. Ocheretova, O.V. Parasyuk, O.Y. Khyzhun, Electronic structure and optical properties of  $\text{Cu}_2\text{CdGeS}_4$ : DFT calculations and X-ray spectroscopy measurements, *Opt. Mater. (Amst.)* 47 (2015) 435–444. <https://doi.org/10.1016/j.optmat.2015.06.017>.
- [60] E. Parthé, K. Yvon, R.H. Deitch, The crystal structure of  $\text{Cu}_2\text{CdGeS}_4$  and other quaternary normal tetrahedral structure compounds, *Acta Crystallogr. Sect. B Struct. Crystallogr. Cryst. Chem.* 25 (1969) 1164–1174. <https://doi.org/10.1107/S0567740869003670>.
- [61] I.J. Alverdiyev, REFINEMENT OF PHASE DIAGRAM IN THE  $\text{Cu}_2\text{S}-\text{GeS}_2$  SYSTEM, *Chem. Probl.* 17 (2019) 423–428. <https://doi.org/10.32737/2221-8688-2019-3-423-428>.
- [62] S.M. Bagheri, I.J. Alverdiyev, Z.S. Aliev, Y.A. Yusibov, M.B. Babanly, Phase relationships in the  $1.5\text{GeS}_2 + \text{Cu}_2\text{GeSe}_3 \leftrightarrow 1.5\text{GeSe}_2 + \text{Cu}_2\text{GeS}_3$  reciprocal system, *J. Alloys Compd.* 625 (2015) 131–137. <https://doi.org/10.1016/j.jallcom.2014.11.118>.
- [63] L.P. Marushko, L.V. Piskach, O.V. Parasyuk, I.D. Olekseyuk, S.V. Volkov, V.I. Pekhnyo, The reciprocal system  $\text{Cu}_2\text{GeS}_3 + 3\text{CdSe} \leftrightarrow \text{Cu}_2\text{GeSe}_3 + 3\text{CdS}$ , *J. Alloys Compd.* 473 (2009) 94–99. <https://doi.org/10.1016/j.jallcom.2008.05.073>.
- [64] M. Grossberg, T. Raadik, J. Krustok, M. Kauk-Kuusik, K. Timmo, R. Kaupmees, V. Mikli, A. Mere, Optical and structural properties of orthorhombic and tetragonal polymorphs of  $\text{Cu}_2\text{CdGeSe}_4$ , *Thin Solid Films.* 666 (2018) 44–47. <https://doi.org/10.1016/j.tsf.2018.09.031>.
- [65] J. Krustok, T. Raadik, R. Kaupmees, M. Grossberg, M. Kauk-Kuusik, K. Timmo, A. Mere, Observation of band gap fluctuations and carrier localization in  $\text{Cu}_2\text{CdGeSe}_4$ , *J. Phys. D. Appl. Phys.* 52 (2019). <https://doi.org/10.1088/1361-6463/ab1afd>.
- [66] M.G. Brik, I. V. Kityk, O. V. Parasyuk, G.L. Myronchuk, Photoinduced features of energy bandgap in quaternary  $\text{Cu}_2\text{CdGeS}_4$  crystals, *J. Phys. Condens. Matter.* 25 (2013). <https://doi.org/10.1088/0953-8984/25/50/505802>.
- [67] G.E. Davidyuk, O. V. Parasyuk, S.A. Semenyuk, Y.E. Romanyuk, Electrical and optical properties of  $\text{Cu}_2\text{CdGeS}_4$  single crystals, *Inorg. Mater.* 39 (2003) 919–923. <https://doi.org/10.1023/A:1025596903080>.

- [68] M. Grossberg, J. Krustok, J. Raudoja, K. Timmo, M. Altosaar, T. Raadik, Photoluminescence and Raman study of  $\text{Cu}_2\text{ZnSn}(\text{Se}_x\text{S}_{1-x})_4$  monograins for photovoltaic applications, *Thin Solid Films*. 519 (2011) 7403–7406. <https://doi.org/10.1016/j.tsf.2010.12.099>.
- [69] M. Kauk-Kuusik, X. Li, M. Pilvet, K. Timmo, V. Mikli, R. Kaupmees, M. Danilson, M. Grossberg, Nano-scale sulfurization of the  $\text{Cu}_2\text{ZnSnSe}_4$  crystal surface for photovoltaic applications, *J. Mater. Chem. A*. 7 (2019) 24884–24890. <https://doi.org/10.1039/c9ta08020a>.
- [70] K. Timmo, M. Altosaar, J. Raudoja, K. Muska, M. Pilvet, M. Kauk, T. Varema, M. Danilson, O. Volobujeva, E. Mellikov, Sulfur-containing  $\text{Cu}_2\text{ZnSnSe}_4$  monograin powders for solar cells, *Sol. Energy Mater. Sol. Cells*. 94 (2010) 1889–1892. <https://doi.org/10.1016/j.solmat.2010.06.046>.
- [71] Z. Su, G. Liang, P. Fan, J. Luo, Z. Zheng, Z. Xie, W. Wang, S. Chen, J. Hu, Y. Wei, C. Yan, J. Huang, X. Hao, F. Liu, Device Postannealing Enabling over 12% Efficient Solution-Processed  $\text{Cu}_2\text{ZnSnS}_4$  Solar Cells with  $\text{Cd}^{2+}$  Substitution, *Adv. Mater.* 32 (2020). <https://doi.org/10.1002/adma.202000121>.
- [72] M. Pilvet, Study of  $\text{Cu}_2(\text{Zn,Cd})\text{SnS}_4$  Absorber Materials for Monograin Layer Solar Cells, 2017. <https://digikogu.taltech.ee/et/Item/06aca692-ae00-4856-9312-46bc6ca7b2ad>.
- [73] F.S. Liu, J.X. Zheng, M.J. Huang, L.P. He, W.Q. Ao, F. Pan, J.Q. Li, Enhanced Thermoelectric Performance of  $\text{Cu}_2\text{CdSnSe}_4$  by Mn Doping: Experimental and First Principles Studies, *Sci. Rep.* 4 (2015) 5774. <https://doi.org/10.1038/srep05774>.
- [74] S. Kim, K.M. Kim, H. Tampo, H. Shibata, S. Niki, Improvement of voltage deficit of Ge-incorporated kesterite solar cell with 12.3% conversion efficiency, *Appl. Phys. Express*. 9 (2016). <https://doi.org/10.7567/APEX.9.102301>.
- [75] T. Nagai, T. Shimamura, K. Tanigawa, Y. Iwamoto, H. Hamada, N. Ohta, S. Kim, H. Tampo, H. Shibata, K. Matsubara, S. Niki, N. Terada, Band Alignment of the  $\text{CdS}/\text{Cu}_2\text{Zn}(\text{Sn}_{1-x}\text{Ge}_x)\text{Se}_4$  Heterointerface and Electronic Properties at the  $\text{Cu}_2\text{Zn}(\text{Sn}_{1-x}\text{Ge}_x)\text{Se}_4$  Surface:  $x = 0, 0.2, \text{ and } 0.4$ , *ACS Appl. Mater. Interfaces*. 11 (2019) 4637–4648. <https://doi.org/10.1021/acsami.8b19200>.
- [76] K. Timmo, M. Kauk-Kuusik, M. Altosaar, J. Raudoja, T. Raadik, M. Grossberg, T. Varema, M. Pilvet, I. Leinemann, O. Volobujeva, E. Mellikov, Novel  $\text{Cu}_2\text{CdSnS}_4$  and  $\text{Cu}_2\text{ZnGeSe}_4$  Absorber Materials for Monograin Layer Solar Cell Application, 28th Eur. Photovolt. Sol. Energy Conf. Exhib. (2013) 2385–2388. <https://doi.org/10.4229/28thEUPVSEC2013-3BV.6.14>.
- [77] Z. Su, J.M.R. Tan, X. Li, X. Zeng, S.K. Batabyal, L.H. Wong, Cation Substitution of Solution-Processed  $\text{Cu}_2\text{ZnSnS}_4$  Thin Film Solar Cell with over 9% Efficiency, *Adv. Energy Mater.* 5 (2015). <https://doi.org/10.1002/aenm.201500682>.
- [78] D.R. Lide, *CRC Handbook of Chemistry and Physics*, 2003.
- [79] R. Goswami, Three Generations of Solar Cells, *Adv. Mater. Res.* 1165 (2021) 113–130. <https://doi.org/10.4028/www.scientific.net/AMR.1165.113>.
- [80] V.V. Klepov, C.A. Juillerat, K.A. Pace, G. Morrison, H.C. zur Loye, “Soft” Alkali Bromide and Iodide Fluxes for Crystal Growth, *Front. Chem.* 8 (2020) 1–18. <https://doi.org/10.3389/fchem.2020.00518>.
- [81] M.J. Zhang, X.M. Jiang, L.J. Zhou, G.C. Guo, Two phases of  $\text{Ga}_2\text{S}_3$ : Promising infrared second-order nonlinear optical materials with very high laser induced damage thresholds, *J. Mater. Chem. C*. 1 (2013) 4754–4760. <https://doi.org/10.1039/c3tc30808a>.

- [82] Y. Wang, J. Wu, Y. Tang, X. Lü, C. Yang, M. Qin, F. Huang, X. Li, X. Zhang, Phase-controlled synthesis of cobalt sulfides for lithium ion batteries, *ACS Appl. Mater. Interfaces*. 4 (2012) 4246–4250. <https://doi.org/10.1021/am300951f>.
- [83] K. Timmo, M. Kauk-Kuusik, M. Pilvet, V. Mikli, E. Kärber, T. Raadik, I. Leinemann, M. Altosaar, J. Raudoja, Comparative study of SnS recrystallization in molten CdI<sub>2</sub>, SnCl<sub>2</sub> and KI, *Phys. Status Solidi*. 13 (2016) 8–12. <https://doi.org/10.1002/pssc.201510082>.
- [84] S. Huber, C. Preitschaft, R. Wehrich, A. Pfitzner, Preparation, crystal structure, electronic structure, impedance spectroscopy, and Raman spectroscopy of Li<sub>3</sub>SbS<sub>3</sub> and Li<sub>3</sub>AsS<sub>3</sub>, *Zeitschrift Fur Anorg. Und Allg. Chemie*. 638 (2012) 2542–2548. <https://doi.org/10.1002/zaac.201200277>.
- [85] H. Lin, Y.Y. Li, M.Y. Li, Z. Ma, L.M. Wu, X.T. Wu, Q.L. Zhu, Centric-to-acentric structure transformation induced by a stereochemically active lone pair: A new insight for design of IR nonlinear optical materials, *J. Mater. Chem. C*. 7 (2019) 4638–4643. <https://doi.org/10.1039/c9tc00647h>.
- [86] Y.-Y. Li, H. Wang, B.-W. Sun, Q.-Q. Ruan, Y.-L. Geng, P.-F. Liu, L. Wang, L.-M. Wu, Ba<sub>10</sub>Zn<sub>7</sub>M<sub>6</sub>Q<sub>26</sub>: Two New Mid-infrared Nonlinear Optical Crystals with T2 Supertetrahedron 3D Framework, *Cryst. Growth Des.* 19 (2019) 1190–1197. <https://doi.org/10.1021/acs.cgd.8b01644>.
- [87] I. Leinemann, J. Raudoja, M. Altosaar, E. Mellikov, CZTS (Cu<sub>2</sub>ZnSnSe<sub>4</sub>) Crystal growth for use in monograin membrane solar cells, (2010).
- [88] M. Altosaar, A. Jagomägi, M. Kauk, M. Krunks, J. Krustok, E. Mellikov, J. Raudoja, T. Varema, Monograin layer solar cells, *Thin Solid Films*. 431–432 (2003) 466–469. [https://doi.org/10.1016/S0040-6090\(03\)00167-6](https://doi.org/10.1016/S0040-6090(03)00167-6).
- [89] E. Mellikov, M. Altosaar, M. Kauk-Kuusik, K. Timmo, D. Meissner, M. Grossberg, J. Krustok, O. Volobujeva, Growth of CZTS-Based Monograins and Their Application to Membrane Solar Cells, *Copp. Zinc Tin Sulfide-Based Thin-Film Sol. Cells*. (2015) 289–309. <https://doi.org/10.1002/9781118437865.ch13>.
- [90] K. Timmo, Formation of Properties of CuInSe<sub>2</sub> and Cu<sub>2</sub>ZnSn(S,Se)<sub>4</sub> Monograin Powders Synthesized in Molten KI, 2011. <https://digikogu.taltech.ee/et/Item/c1409977-56e5-4ef2-8ed5-5f529683b45e>.
- [91] W. Gao, T. Zhou, Y. Gao, B. Louis, D. O’Hare, Q. Wang, Molten salts-modified MgO-based adsorbents for intermediate-temperature CO<sub>2</sub> capture: A review, *J. Energy Chem.* 26 (2017) 830–838. <https://doi.org/10.1016/j.jechem.2017.06.005>.
- [92] K. Timmo, M. Kauk-kuusik, M. Altosaar, J. Raudoja, NOVEL Cu<sub>2</sub>CdSnS<sub>4</sub> AND Cu<sub>2</sub>ZnGeSe<sub>4</sub> ABSORBER MATERIALS FOR MONOGRAIN LAYER SOLAR CELL APPLICATION, (2013) 1–5. <https://doi.org/10.4229/28thEUPVSEC2013-3BV.6.14>.
- [93] I. Klavina, T. Kaljuvee, K. Timmo, J. Raudoja, R. Traksmäa, M. Altosaar, D. Meissner, Study of Cu<sub>2</sub>ZnSnSe<sub>4</sub> monograin formation in molten KI starting from binary chalcogenides, *Thin Solid Films*. 519 (2011) 7399–7402. <https://doi.org/10.1016/j.tsf.2011.01.365>.
- [94] K. Timmo, M. Kauk-Kuusik, M. Pilvet, M. Altosaar, M. Grossberg, M. Danilson, R. Kaupmees, V. Mikli, J. Raudoja, T. Varema, Cu(In,Ga)Se<sub>2</sub> monograin powders with different Ga content for solar cells, *Sol. Energy*. 176 (2018) 648–655. <https://doi.org/10.1016/j.solener.2018.10.078>.

- [95] K. Timmo, M. Altosaar, M. Pilvet, V. Mikli, M. Grossberg, M. Danilson, T. Raadik, R. Josepson, J. Krustok, M. Kauk-Kuusik, The effect of Ag alloying of  $\text{Cu}_2(\text{Zn,Cd})\text{SnS}_4$  on the monograin powder properties and solar cell performance, *J. Mater. Chem. A.* 7 (2019) 24281–24291. <https://doi.org/10.1039/c9ta07768e>.
- [96] E. Mellikov, D. Meissner, T. Varema, M. Altosaar, M. Kauk, O. Volobujeva, J. Raudoja, K. Timmo, M. Danilson, Monograin materials for solar cells, *Sol. Energy Mater. Sol. Cells.* 93 (2009) 65–68. <https://doi.org/10.1016/j.solmat.2008.04.018>.
- [97] M. Kauk-Kuusik, K. Timmo, K. Muska, M. Pilvet, J. Krustok, R. Josepson, G. Brammertz, B. Vermang, M. Danilson, M. Grossberg, Detailed Insight into the CZTS/CdS Interface Modification by Air Annealing in Monograin Layer Solar Cells, *ACS Appl. Energy Mater.* 4 (2021) 12374–12382. <https://doi.org/10.1021/acsaem.1c02186>.
- [98] I.D. Olekseyuk, I.V. Dudchak, L.V. Piskach, Phase equilibria in the  $\text{Cu}_2\text{S}$ – $\text{ZnS}$ – $\text{SnS}_2$  system, *J. Alloys Compd.* 368 (2004) 135–143. <https://doi.org/10.1016/j.jallcom.2003.08.084>.
- [99] I.V. Dudchak, L.V. Piskach, Phase equilibria in the  $\text{Cu}_2\text{SnSe}_3$ – $\text{SnSe}_2$ – $\text{ZnSe}$  system, *J. Alloys Compd.* 351 (2003) 145–150. [https://doi.org/10.1016/S0925-8388\(02\)01024-1](https://doi.org/10.1016/S0925-8388(02)01024-1).
- [100] H. Xie, M. Dimitrievska, X. Fontané, Y. Sánchez, S. López-Marino, V. Izquierdo-Roca, V. Bermúdez, A. Pérez-Rodríguez, E. Saucedo, Formation and impact of secondary phases in Cu-poor Zn-rich  $\text{Cu}_2\text{ZnSn}(\text{S}_{1-y}\text{Se}_y)_4$  ( $0 \leq y \leq 1$ ) based solar cells, *Sol. Energy Mater. Sol. Cells.* 140 (2015) 289–298. <https://doi.org/10.1016/j.solmat.2015.04.023>.
- [101] M. Kauk-Kuusik, M. Altosaar, K. Muska, M. Pilvet, J. Raudoja, K. Timmo, T. Varema, M. Grossberg, E. Mellikov, O. Volobujeva, Post-growth annealing effect on the performance of  $\text{Cu}_2\text{ZnSnSe}_4$  monograin layer solar cells, *Thin Solid Films.* 535 (2013) 18–21. <https://doi.org/10.1016/j.tsf.2012.11.075>.
- [102] N. Kohara, T. Negami, S. Nishiwaki, T. Satoh, Z. Li, H. Qing, Related content Surface Characterization of Chemically Treated  $\text{Cu}(\text{In,Ga})\text{Se}_2$  Thin Films, (1996).
- [103] M. Buffière, G. Brammertz, S. Sahayaraj, M. Batuk, S. Khelifi, D. Mangin, A.A. El Mel, L. Arzel, J. Hadermann, M. Meuris, J. Poortmans, KCN Chemical Etch for Interface Engineering in  $\text{Cu}_2\text{ZnSnSe}_4$  Solar Cells, *ACS Appl. Mater. Interfaces.* 7 (2015) 14690–14698. <https://doi.org/10.1021/acsaami.5b02122>.
- [104] M. Bär, B.A. Schubert, B. Marsen, S. Krause, S. Pookpanratana, T. Unold, L. Weinhardt, C. Heske, H.W. Schock, Impact of KCN etching on the chemical and electronic surface structure of  $\text{Cu}_2\text{ZnSnS}_4$  thin-film solar cell absorbers, *Appl. Phys. Lett.* 99 (2011) 97–100. <https://doi.org/10.1063/1.3650717>.
- [105] A. Fairbrother, E. García-Hemme, V. Izquierdo-Roca, X. Fontané, F.A. Pulgarín-Agudelo, O. Vigil-Galán, A. Pérez-Rodríguez, E. Saucedo, Development of a Selective Chemical Etch To Improve the Conversion Efficiency of Zn-Rich  $\text{Cu}_2\text{ZnSnS}_4$  Solar Cells, *J. Am. Chem. Soc.* 134 (2012) 8018–8021. <https://doi.org/10.1021/ja301373e>.

- [106] M. Mousel, A. Redinger, R. Djemour, M. Arasimowicz, N. Valle, P. Dale, S. Siebentritt, HCl and Br<sub>2</sub>-MeOH etching of Cu<sub>2</sub>ZnSnSe<sub>4</sub> polycrystalline absorbers, *Thin Solid Films*. 535 (2013) 83–87. <https://doi.org/10.1016/j.tsf.2012.12.095>.
- [107] K. Timmo, M. Altosaar, J. Raudoja, M. Grossberg, M. Danilson, O. Volobujeva, E. Mellikov, Chemical etching of Cu<sub>2</sub>ZnSn(S,Se)<sub>4</sub> monograin powder, in: 2010 35th IEEE Photovolt. Spec. Conf., IEEE, 2010: pp. 001982–001985. <https://doi.org/10.1109/PVSC.2010.5616411>.
- [108] M. Kauk-Kuusik, K. Timmo, M. Danilson, M. Altosaar, M. Grossberg, K. Ernits, p–n junction improvements of Cu<sub>2</sub>ZnSnS<sub>4</sub>/CdS monograin layer solar cells, *Appl. Surf. Sci.* 357 (2015) 795–798. <https://doi.org/10.1016/j.apsusc.2015.09.094>.
- [109] B. Tuck, The chemical polishing of semiconductors, *J. Mater. Sci.* 10 (1975) 321–339. <https://doi.org/10.1007/BF00540357>.
- [110] W.H. Strehlow, Chemical Polishing of II-VI Compounds, *J. Appl. Phys.* 40 (1969) 2928–2932. <https://doi.org/10.1063/1.1658103>.
- [111] M. Dimitrievska, S. Giraldo, P. Pistor, E. Saucedo, A. Pérez-Rodríguez, V. Izquierdo-Roca, Raman scattering analysis of the surface chemistry of kesterites: Impact of post-deposition annealing and Cu/Zn reordering on solar cell performance, *Sol. Energy Mater. Sol. Cells*. 157 (2016) 462–467. <https://doi.org/10.1016/j.solmat.2016.07.009>.
- [112] A.P. Litvinchuk, V.M. Dzhagan, V.O. Yukhymchuk, M.Y. Valakh, I.S. Babichuk, O. V. Parasyuk, L. V. Piskach, O.D. Gordan, D.R.T. Zahn, Electronic structure, optical properties, and lattice dynamics of orthorhombic Cu<sub>2</sub>CdGeS<sub>4</sub> and Cu<sub>2</sub>CdSiS<sub>4</sub> semiconductors, *Phys. Rev. B - Condens. Matter Mater. Phys.* 90 (2014) 1–9. <https://doi.org/10.1103/PhysRevB.90.165201>.
- [113] J. Krustok, R. Josepson, T. Raadik, M. Danilson, Potential fluctuations in Cu<sub>2</sub>ZnSnSe<sub>4</sub> solar cells studied by temperature dependence of quantum efficiency curves, *Phys. B Condens. Matter*. 405 (2010) 3186–3189. <https://doi.org/10.1016/j.physb.2010.04.041>.
- [114] S.J. L. Kang, Sintering, Densification, Grain Growth, and Microstructure, 2015. <https://doi.org/10.1016/B978-0-7506-6385-4.X5000-6>.
- [115] I. Leinemann, G.C. Nkwusi, K. Timmo, O. Volobujeva, M. Danilson, J. Raudoja, T. Kaljuvee, R. Traksmaa, M. Altosaar, D. Meissner, Reaction pathway to Cu<sub>2</sub>ZnSnSe<sub>4</sub> formation in CdI<sub>2</sub>, *J. Therm. Anal. Calorim.* 134 (2018) 409–421. <https://doi.org/10.1007/s10973-018-7102-5>.
- [116] F.G. I. A. Kariper, O. Bağlayan, Fabrication and optical characterization of CdSe thin films grown by chemical bath deposition, *Acta Phys. Pol. A*. 128 (2015). <https://doi.org/10.12693/aphyspola.128.b-219>.
- [117] T. Tanaka, T. Sueishi, K. Saito, Q. Guo, M. Nishio, K.M. Yu, W. Walukiewicz, Existence and removal of Cu<sub>2</sub>Se second phase in coevaporated Cu<sub>2</sub>ZnSnSe<sub>4</sub> thin films, *J. Appl. Phys.* 111 (2012) 053522. <https://doi.org/10.1063/1.3691964>.
- [118] V. V. Poborchii, A. V. Kolobov, K. Tanaka, An in situ Raman study of polarization-dependent photocrystallization in amorphous selenium films, *Appl. Phys. Lett.* 72 (1998) 1167–1169. <https://doi.org/10.1063/1.121002>.
- [119] D. Briggs, X-ray photoelectron spectroscopy (XPS), *Handb. Adhes. Second Ed.* (2005) 621–622. <https://doi.org/10.1002/0470014229.ch22>.

- [120] R.B. Shalvoy, G.B. Fisher, P.J. Stiles, Bond ionicity and structural stability of some average-valence-five materials studied by x-ray photoemission, *Phys. Rev. B.* 15 (1977) 1680–1697. <https://doi.org/10.1103/PhysRevB.15.1680>.
- [121] D. Jana, S. Chakrabarti, S.Z. Rahaman, S. Maikap, Resistive and New Optical Switching Memory Characteristics Using Thermally Grown  $\text{Ge}_{0.2}\text{Se}_{0.8}$  Film in  $\text{Cu}/\text{GeSe}_x/\text{W}$  Structure, *Nanoscale Res. Lett.* 10 (2015) 1–8. <https://doi.org/10.1186/s11671-015-1090-1>.
- [122] D.-H. Son, Y.-I. Kim, S.-H. Kim, D. Nam, H. Cheong, J.-K. Kang, K.-J. Yang, D.-H. Kim, Effects of S and Se contents on the physical and photovoltaic properties of  $\text{Cu}_2\text{ZnSn}(\text{S}_x\text{Se}_{1-x})_4$  thin films: achieving a PCE of 9.47%, *J. Mater. Chem. A.* 7 (2019) 22986–22995. <https://doi.org/10.1039/C9TA08319G>.
- [123] A.R. Denton, N.W. Ashcroft, Vegard's law, *Phys. Rev. A.* 43 (1991) 3161–3164. <https://doi.org/10.1103/PhysRevA.43.3161>.

## Acknowledgements

I would like to show my biggest thanks to my supervisors Senior Researcher Marit Kauk-Kuusik, PhD, and Senior Researcher Kristi Timmo, PhD, for their help, guidance, support, advice and encouragement over the whole study period.

I would also like to thank Head of the Department Prof. Maarja Grossberg-Kuusk for giving me the opportunity to carry out my studies in the Department of Materials and Environmental Technology at Tallinn University of Technology.

I appreciate all colleagues who working in the Lab. of Photovoltaic Materials. I am grateful to Prof. Juri Krustok for help and discussion on PL results, Dr. Maris Pilvet for help in fabrication of monograin layer solar cell, Dr. Jaan Raudoja and Dr. Katri Muska for preparation of ampoules, Dr. Mati Danilson for assistance in XPS and EQE measurement, Dr. Reelika Kaupmees for help and discussion in Raman and PL measurement, Dr. Valdek Mikli for SEM and EDX measurements, Dr. Mare Altsaar for help in revising the doctoral thesis. I am thankful to Dr. Arvo Mere for help in XRD measurement, Prof. Malle Krunks for the review of doctoral thesis.

I would like to thank the following funding sources for financial support during the PhD period: the Estonian Ministry of Education and Research project IUT19-28, the Estonian Research Council grant PRG1023, the European Regional Development Fund project TK141 “Advanced materials and high-technology devices for sustainable energetics, sensorics and nanoelectronics”, the ERDF project “Center of nanomaterials technologies and research (NAMUR+)” (1.01.2017–30.06.2022) and the EU Horizon 2020 Project CUSTOM-ART, Grant No. 952982. The research in this thesis was also partially supported by ASTRA “TUT Institutional Development Programme for 2018–2022” Graduate School of Functional Materials and Technologies. DoRa+ 1.1 travel scholarships to international conferences were financed by the Archimedes Foundation.

Finally, I offer my sincerest gratitude to my family whose support throughout the progression of this thesis was paramount. Special thanks to my brothers Li Xiangfeng, Li Weibin for their help and encouragement, my girlfriend Bi Yanyan for her understanding and support.

This thesis is dedicated to my mom Guirong Cui.

## Abstract

### Study of $\text{Cu}_2\text{Ge}(\text{S},\text{Se})_3$ and $\text{Cu}_2\text{CdGe}(\text{S},\text{Se})_4$ Monograin Powders for Photovoltaic Applications

Photovoltaic technology as one of the renewable energy sources is an effective way to achieve carbon-neutral processes in the energy domain. Among the emerging materials for photovoltaics, so-called kesterites as absorber materials have gained a lot of attention due to their promising properties. Although the highest efficiency of  $\sim 13\%$  for  $\text{Cu}_2\text{ZnSn}(\text{S},\text{Se})_4$  based thin-film solar cells has been presented for several years, there is no significant improvement. The main culprits of limitations are open circuit voltage deficit, deep defects related to multivalent Sn, interface recombination, coexistence of complex secondary phases, the band tailing issue, short minority lifetime, bulk defects, and undesirable band alignment at  $p$ - $n$  interfaces. Thus, further research and knowledge is necessary to overcome the present limitations and improve the performance of the kesterite-based technologies. It has also motivated research on the other ternary and quaternary copper chalcogenide compounds with suitable properties for solar cell absorber.

One successful strategy is cation substitution (Zn and Sn substitution by Cd and Ge) in  $\text{Cu}_2\text{ZnSn}(\text{S},\text{Se})_4$ , which has shown promising results and improved performance of solar cells. Additionally, ternary compounds,  $\text{Cu}_2\text{GeS}_3$  and  $\text{Cu}_2\text{GeSe}_3$  have shown many promising photo-absorber material properties, such as  $p$ -type conductivity and a direct band gap energy of 1.5 eV and 0.8 eV, respectively. However, there are only few studies presenting the results about solar cells based on  $\text{Cu}_2\text{GeS}_3$ ,  $\text{Cu}_2\text{GeSe}_3$  or their solid solutions. Therefore, this study was focused on the formation of ternary  $\text{Cu}_2\text{Ge}(\text{S},\text{Se})_3$  and quaternary  $\text{Cu}_2\text{CdGe}(\text{S},\text{Se})_4$  monograin powders in liquid phase of flux materials ( $\text{CdI}_2$ ,  $\text{KI}$  and  $\text{LiI}$ ) as well as characterization of monograin layer solar cells based on the synthesized monograin powders.

$\text{Cu}_2\text{CdGeSe}_4$  has two crystal structure modifications. The monograin powder synthesis by molten salt method allows to use different synthesis temperatures to obtain both crystal structures. Structural studies by XRD showed that powder synthesized at 500 °C had tetragonal structure and powders synthesized at temperatures 600 °C and 700 °C had orthorhombic structure regardless of the used molten salt. According to Raman analysis, the most intensive peak in the spectra of  $\text{Cu}_2\text{CdGeSe}_4$  was observed at 203  $\text{cm}^{-1}$  regardless on the crystal structure. The results showed that Raman analysis is very good additional method to distinguish both crystal structure. The characteristic Raman modes for the  $o$ - $\text{Cu}_2\text{CdGeSe}_4$  phase were detected at 162, 187, 271 and 277  $\text{cm}^{-1}$  and for  $t$ - $\text{Cu}_2\text{CdGeSe}_4$  phase, the characteristic peaks were at 175, 263 and 292  $\text{cm}^{-1}$ . According to EQE measurements, the orthorhombic  $\text{Cu}_2\text{CdGeSe}_4$  had band gap of 1.27 eV and tetragonal  $\text{Cu}_2\text{CdGeSe}_4$  had 1.14 eV. Monograin powders with both crystal structures were implemented as absorber layers in monograin layer solar cells. Preliminary results of this work showed that devices based on  $o$ - $\text{Cu}_2\text{CdGeSe}_4$  had higher performance than  $t$ - $\text{Cu}_2\text{CdGeSe}_4$  based solar cells. The further optimisation of  $o$ - $\text{Cu}_2\text{CdGeSe}_4$  crystal surfaces by the chemical etching with  $\text{Br}_2$ - $\text{MeOH}/\text{KCN}$  solutions and post-annealed at 400 °C for 1 hour resulted in monograin layer solar cell efficiency of 5.69% with the following parameters:  $V_{OC} = 459$  mV;  $J_{SC} = 25.6$   $\text{mA}/\text{cm}^2$  and  $FF = 48\%$ . It was first time reported that  $\text{Cu}_2\text{CdGeSe}_4$  could be successfully used as absorber material in photovoltaics.



Theoretical calculations show that the efficiency for single junction solar cells has a direct bandgap of ~1.4 eV. In this thesis, the solar cell efficiency improvement and band gap optimization was achieved by adjusting the ratio of chalcogens (S/Se) in the  $\text{Cu}_2\text{CdGe}(\text{S}_x\text{Se}_{1-x})_4$  ( $0 \leq x \leq 1$ ) solid solutions. Structural study by XRD and Raman showed that all  $\text{Cu}_2\text{CdGe}(\text{S}_x\text{Se}_{1-x})_4$  solid solutions synthesized at 700 °C crystallize in orthorhombic structure and solid solutions synthesized at 500 °C had tetragonal structure in the range  $x = 0$  to  $x = 0.1$ .  $\text{Cu}_2\text{CdGe}(\text{S}_x\text{Se}_{1-x})_4$  solid solution with  $x = 0.15$  synthesized at 500 °C contain mixture of orthorhombic and tetragonal phases. According to EQE measurements, the band gap energy increased from 1.27 eV to 2.04 eV by increasing the S content in the  $\text{Cu}_2\text{CdGe}(\text{S}_x\text{Se}_{1-x})_4$  solid solutions. The highest power conversion efficiency of 6.4% for monograin layer solar cells was achieved by  $\text{Cu}_2\text{CdGe}(\text{S}_x\text{Se}_{1-x})_4$  solid solution with  $x = 0.2$  showing the parameters:  $V_{OC} = 724$  mV,  $J_{SC} = 18.8$  mA/cm<sup>2</sup> and  $FF = 46.9\%$ .

Regarding the toxicity issue with Cd, which may rise in the future, ternary  $\text{Cu}_2\text{Ge}(\text{Se}_x\text{S}_{1-x})_3$  ( $0 \leq x \leq 1$ ) solid solutions, which are not extensively investigated as absorber materials for solar cell application, were studied. The complete series of  $\text{Cu}_2\text{Ge}(\text{Se}_x\text{S}_{1-x})_3$  ( $0 \leq x \leq 1$ ) monograin powders were synthesized in Lil flux. Structural studies by XRD and Raman showed that  $\text{Cu}_2\text{GeS}_3$  crystallize in monoclinic and  $\text{Cu}_2\text{GeSe}_3$  crystallize in orthorhombic structure. Transformation from monoclinic to orthorhombic crystal structure in  $\text{Cu}_2\text{Ge}(\text{Se}_x\text{S}_{1-x})_3$  solid solutions was detected between  $x = 0.2$  to  $x = 0.4$ . Radiative recombination processes in  $\text{Cu}_2\text{Ge}(\text{Se}_x\text{S}_{1-x})_3$  monograin powders were studied by using photoluminescence spectroscopy. All spectra of  $\text{Cu}_2\text{Ge}(\text{Se}_x\text{S}_{1-x})_3$  consisted of two asymmetric PL peaks. Peak positions of these bands shifted nearly linearly to lower energy values by decreasing the S content in  $\text{Cu}_2\text{Ge}(\text{Se}_x\text{S}_{1-x})_3$ . Almost the same trend was detected for band gap values determined from room temperature EQE measurements. Both PL peaks were related to donor-acceptor pair recombination. The highest efficiency of 3.16% was demonstrated by using  $\text{Cu}_2\text{Ge}(\text{Se}_x\text{S}_{1-x})_3$  with  $x = 0.6$  powder crystals as absorber material in monograin layer solar cells.

Preliminary results indicate that both  $\text{Cu}_2\text{CdGe}(\text{S}_x\text{Se}_{1-x})_4$  and  $\text{Cu}_2\text{Ge}(\text{Se}_x\text{S}_{1-x})_3$  monograin powders are applicable as absorber materials in monograin layer solar cells. However, the defect composition of powders, crystal surface modifications and band alignments need to be further optimized.

## Lühikokkuvõte

### $\text{Cu}_2\text{Ge}(\text{S},\text{Se})_3$ ja $\text{Cu}_2\text{CdGe}(\text{S},\text{Se})_4$ monoterapulbrite uurimine ning kasutamine päikesepatareides

Majanduse areng ja üldine tarbimiskasv suurendab nõudlust ka keskkonnasäästliku ning samas odavama energiatootmise järele. Selleks otsitakse kogu maailmas võimalusi eelkõige taastuvenergeetikast. Päikeseenergiast elektrienergia tootmine on üks tõhusamaid viise süsinikuneutraalse energiamajanduse saavutamiseks. Selleks on vaja järjepidevalt arendada uusi keskkonnasõbralikke ja ressursisäästlikke tehnoloogiaid ja materjale, mis koosneksid maapõues laialt levinud koostiselementidest. Nendele kriteeriumitele vastavad näiteks laialdast tähelepanu pälvinud  $\text{Cu}_2\text{ZnSn}(\text{S},\text{Se})_4$ -tüüpi mitmikühendid, nn kesteriidid. Selliste absorbermaterjalide baasil valmistatud õhukesekilelised päikesepatareid on näidanud kasutegurit ~13%, mis on püsinud juba mitmeid aastaid. Nende nn. kesteriitsete päikesepatareide peamiseks probleemiks on avatud ahela pinge ( $V_{oc}$ ) puudujääk võrreldes  $V_{oc}$  väärtustega, mida nende materjalide keelutsoonid võimaldaksid saada.  $V_{oc}$  puudujääk võib olla tingitud erinevatest põhjustest, milleks peetakse mitmevalentse tinaga seotud sügavaid defekte, pinnarekombinatsiooni, kergesti tekkida võivaid vöörfaase, lühikest laengukandjate eluiga ja ebasobivat energiatasemete paiknemist  $p$ - $n$  siirde alas. Seega on sellist tüüpi materjalide fundamentaalsete probleemide lahendamiseks vaja täiendavaid uuringuid ja teadmisi, mis on ajendanud ka käesoleva töö autorit otsima uusi alternatiivseid, varieeruvate omadustega vaskkalkogeniid-mitmikühendeid, mis sobivad omaduste poolest päikesepatarei absorbermaterjalideks.

Üheks võimalikuks ja lootustandvaid tulemusi näidanud strateegiaks on kesteriitsetes ühendites katioonasendamine (näiteks Zn ja Sn asendamine vastavalt Cd-i ja Ge-ga). Samuti sobivad absorbermaterjalideks paljulubavate omadustega kolmikühendid –  $\text{Cu}_2\text{GeS}_3$  and  $\text{Cu}_2\text{GeSe}_3$ , mis on  $p$ -tüüpi juhtivusega ja otsese keelutsooniga, mille väärtused on vastavalt 1.5 eV ja 0.8 eV. Senini on olnud vähe uuringuid  $\text{Cu}_2\text{GeS}_3$ ,  $\text{Cu}_2\text{GeSe}_3$  või nende tahkete lahuste kohta raskendustest päikeseenergeetikas.

Käesoleva doktoritöö eesmärgiks oli sünteesida  $\text{Cu}_2\text{Ge}(\text{S},\text{Se})_3$  ja  $\text{Cu}_2\text{CdGe}(\text{S},\text{Se})_4$  monoterapulbrid sulade soolade ( $\text{CdI}_2$ ,  $\text{KI}$  ja  $\text{LiI}$ ) keskkonnas, iseloomustada nende materjalide koostist, struktuurseid ja optilisi omadusi ning valmistada neist materjalidest monoterakiht-päikesepatareid ja hinnata nende materjalide rakendatavust päikesepatareides.

Kirjandusest on teada, et  $\text{Cu}_2\text{CdGeSe}_4$  võib omada kahte kristallstruktuuri modifikatsiooni. Käesolevas töös kasutati erineva kristallstruktuuri saamiseks erinevaid sünteesitemperatuure. Struktuuriuuringud XRD-ga näitasid, et 500 °C juures sünteesitud  $\text{Cu}_2\text{CdGeSe}_4$  pulber omas tetragonaalset struktuuri ning temperatuuridel 600 °C ja 700 °C sünteesitud pulbrid omasid ortorombilist struktuuri sõltumata kasutatud sula soola keskkonnast. Esmakordselt näidati, et Raman spektroskoopiline analüüs on väga hea lisameetod mõlema kristallstruktuuri eristamiseks. Raman spektrite kõige intensiivsem piik asus 203  $\text{cm}^{-1}$  juures, sõltumata  $\text{Cu}_2\text{CdGeSe}_4$  kristallstruktuurist, kuid teised Ramani piigid asusid sõltuvalt kristallstruktuurist erinevatel asukohtadel. Ortorombilisele  $\text{Cu}_2\text{CdGeSe}_4$  faasile iseloomulikud Ramani piigid asusid 162, 187, 271 ja 277  $\text{cm}^{-1}$  ning tetragonaalsele  $\text{Cu}_2\text{CdGeSe}_4$  faasile iseloomulikud piigid 175, 263 ja 292  $\text{cm}^{-1}$  juures. Spektraalanalüüsi abil määrati mõlema kristallstruktuuriga  $\text{Cu}_2\text{CdGeSe}_4$ -le keelutsoonid – 1,27 eV ortorombilisele ja 1,14 eV tetragonaalsele. Mõlema kristallstruktuuriga kristallide

pulbreid kasutati absorbermaterjalidena monoterakiht-päikesepatareides. Töö saadud esialgsed tulemused näitasid, et ortorombilise struktuuriga  $\text{Cu}_2\text{CdGeSe}_4$  baasil valmistatud päikesepatareid olid suurema efektiivusega kui tetragonaalse struktuuriga  $\text{Cu}_2\text{CdGeSe}_4$ -i baasil valmistatud päikesepatareid. Seetõttu kasutati keemiliste ja termiliste pinnatötluste optimeerimiseks ortorombilise struktuuriga  $\text{Cu}_2\text{CdGeSe}_4$  monoterapulbreid. Parim päikesepatarei kasuteguri väärtus 5,69% saavutati absorbermaterjaliga, mille pinda oli söövitatud järjestikku broom-metanooli lahuse ja KCN vesilahusega ning seejärel lõõmutatud 400 °C juures. Päikesepatarei väljundparameetrid olid järgnevad:  $V_{OC} = 459$  mV ;  $J_{SC} = 25,6$  mA/cm<sup>2</sup> ja  $FF = 48\%$ . Selle töö tulemused näitasid esmakordselt, et  $\text{Cu}_2\text{CdGeSe}_4$  saab edukalt kasutada absorbermaterjalina päikesepatareides.

Teoreetiliste arvutustega on näidatud, et ühesiirdelise päikesepatarei teoreetiline maksimaalne kasutegur on võimalik saavutada absorbermaterjaliga, mille keelutsoon on ~1.4 eV. Käesolevas doktoritöös saavutati päikesepatareide efektiivsuse tõus ja keelutsooni optimeerimine kalkogeenide (S/Se) kontsentratsiooni suhte varieerimisega  $\text{Cu}_2\text{CdGe}(\text{S}_x\text{Se}_{1-x})_4$  ( $0 \leq x \leq 1$ ). Struktuuriuuringud kinnitasid, et 700 °C juures sünteesitud  $\text{Cu}_2\text{CdGe}(\text{S}_x\text{Se}_{1-x})_4$  tahked lahused kristalliseerusid ortorombilises struktuuris sõltumata S/Se suhtest.  $\text{Cu}_2\text{CdGe}(\text{S}_x\text{Se}_{1-x})_4$  tahked lahused, mis sünteesiti 500 °C juures, olid omandanud tetragonaalse kristallstruktuuri koostiste vahemikus  $x = 0$  kuni  $x = 0,1$ .  $\text{Cu}_2\text{CdGe}(\text{S}_x\text{Se}_{1-x})_4$  koostisega  $x=0,15$  sisaldas juba mõlemat, nii ortorombilist kui ka tetragonaalset kristallmodifikatsiooni. Suurendades väavli sisaldust  $x = 0$  kuni  $x = 1$   $\text{Cu}_2\text{CdGe}(\text{S}_x\text{Se}_{1-x})_4$ -s materjalide keelutsoon laienes 1,27 eV kuni 2,04 eV. Kõrgeim päikesepatarei kasutegur 6,4% saadi  $\text{Cu}_2\text{CdGe}(\text{S}_x\text{Se}_{1-x})_4$  tahke lahusega, kus  $x = 0,2$  ning keelutsooni väärtus oli 1,45 eV. Sellise seadise väljundparameetrid olid järgmised:  $V_{OC} = 724$  mV,  $J_{SC} = 18,8$  mA/cm<sup>2</sup> ja  $FF = 46,9\%$ .

Kaadmiumi kui elemendi toksilisuse aspekti silmas pidades ja ka kolmikühendite kohta teada oleva informatsiooni vähesuse tõttu uuriti doktoritöös lisaks Cd sisaldavatele ühenditele ka  $\text{Cu}_2\text{Ge}(\text{Se}_x\text{S}_{1-x})_3$  ( $0 \leq x \leq 1$ ) tahkete lahuste kasutusvõimalust absorbermaterjalina päikesepatareides. Struktuuriuuringud näitasid, et  $\text{Cu}_2\text{GeS}_3$  kristalliseerub monokliinses ja  $\text{Cu}_2\text{GeSe}_3$  ortorombilises struktuuris. Üleminek monokliinilisest ortorombiliseks kristallstruktuuriks  $\text{Cu}_2\text{Ge}(\text{Se}_x\text{S}_{1-x})_3$  tahketes lahustes toimus vahemikus  $x = 0,2$  kuni  $x = 0,4$ . Kiirguslike rekombinatsiooni-protsesside uurimiseks  $\text{Cu}_2\text{Ge}(\text{Se}_x\text{S}_{1-x})_3$  tahketes lahustes kasutati fotoluminestsentsanalüüsi. Leiti, et kõikide materjalide PL spektrid koosnesid kahest asümmeetrilisest ribast, mis nihkusid lineaarselt väiksemate energiaväärtuste poole S sisalduse vähenemisega  $\text{Cu}_2\text{Ge}(\text{Se}_x\text{S}_{1-x})_3$  tahketes lahustes. Mõlemad PL ribad leiti olevat seotud doonor-aktseptor-paari rekombinatsiooniga. Samasugust lineaarset trendi näitas ka keelutsooni väärtuste muutus spektraalmõõtmiste alusel, keelutsoon vähenes 1,65 eV kuni 1,07 eV seleeni sisalduse suurenemisega ( $x = 0$  kuni  $x = 0,8$ ). Kõrgeim kasuteguri väärtus 3,16%, saadi  $\text{Cu}_2\text{Ge}(\text{Se}_{0,4}\text{S}_{0,6})_3$  monoterapulbri baasil valmistatud päikesepatareiga.

Antud doktoritöö tulemused näitasid, et nii  $\text{Cu}_2\text{CdGe}(\text{S}_x\text{Se}_{1-x})_4$  kui ka  $\text{Cu}_2\text{Ge}(\text{Se}_x\text{S}_{1-x})_3$  monoterapulbrid sobivad absorbermaterjalideks monoterakiht-päikesepatareides, kuid pulbrite defektikoostis, kristallide pinna modifitseerimine ja siirdeala optimeerimine vajavad edasist arendamist.

## Appendix

### Publication I

M. Kauk-Kuusik, X. Li, M. Pilvet, K. Timmo, M. Grossberg, T. Raadik, M. Danilson, V. Mikli, M. Altosaar, J. Krustok, J. Raudoja. "Study of  $\text{Cu}_2\text{CdGeSe}_4$  monograin powders synthesized by molten salt method for photovoltaic applications", *Thin Solid Films*, Volume 666, 15–19, 2018.

<https://doi.org/10.1016/j.tsf.2018.09.025>





## Study of $\text{Cu}_2\text{CdGeSe}_4$ monograin powders synthesized by molten salt method for photovoltaic applications



M. Kauk-Kuusik<sup>a,\*</sup>, X. Li<sup>a</sup>, M. Pilvet<sup>a</sup>, K. Timmo<sup>a</sup>, M. Grossberg<sup>a</sup>, T. Raadik<sup>a</sup>, M. Danilson<sup>a</sup>, V. Mikli<sup>a</sup>, M. Altsaar<sup>a</sup>, J. Krustok<sup>a,b</sup>, J. Raudoja<sup>a</sup>

<sup>a</sup> Department of Materials and Environmental Technology, Tallinn University of Technology, Ehitajate tee 5, 19086 Tallinn, Estonia

<sup>b</sup> Division of Physics, Tallinn University of Technology, Ehitajate tee 5, 19086 Tallinn, Estonia

### ARTICLE INFO

#### Keywords:

Molten salt synthesis-growth  
Crystal structure  
Solar cells  
Copper cadmium germanium selenide

### ABSTRACT

$\text{Cu}_2\text{CdGeSe}_4$  monograin powders were synthesized by molten salt method for photovoltaic applications. The effects of salt material ( $\text{CdI}_2$  and  $\text{KI}$ ), synthesis temperature and time on the structural, morphological, compositional and optoelectronic properties were investigated. Phase analysis by Raman spectroscopy and X-ray diffraction methods showed that the  $\text{Cu}_2\text{CdGeSe}_4$  powder crystals synthesized at  $500^\circ\text{C}$  had tetragonal structure and those synthesized at  $600^\circ\text{C}$  and  $700^\circ\text{C}$  had orthorhombic structure. The band gap values determined from external quantum efficiency measurements were 1.27 eV for orthorhombic  $\text{Cu}_2\text{CdGeSe}_4$  and 1.14 eV for tetragonal  $\text{Cu}_2\text{CdGeSe}_4$  powder crystals. The monograin layer solar cell on the base of orthorhombic  $\text{Cu}_2\text{CdGeSe}_4$  powder showed the best conversion efficiency of 4.21% (active area), with an open-circuit voltage of 0.46 V, a short-circuit current density of  $23.3\text{ mA/cm}^2$  and fill factor of 39%.

### 1. Introduction

There is a large group of ternary and quaternary copper chalcogenide compounds that have attracted considerable attention due to their suitable properties for thin film solar cell absorbers. Among them  $\text{Cu}(\text{In,Ga})\text{Se}_2$  (CIGSe) based thin film solar cells have been studied for several decades and resulted in power conversion efficiency (PCE) of 22.9% [1]. Another semiconductor material which responds to the requests of using only low-cost, non-toxic and earth-abundant elements is the kesterite  $\text{Cu}_2\text{ZnSn}(\text{S,Se})_4$ . The PCE of the kesterite-based devices has stagnated at a level lower than 13% [2–4] in the last few years, which is much lower than the predicted value from the Shockley-Queisser limit. This difference between CIGSe and kesterite-based solar cell devices has also motivated research on the other quaternary copper chalcogenide compounds with suitable band gap energy for solar cell absorber. Among them the  $\text{Cu}_2\text{CdGeSe}_4$  compound is less studied, although it has *p*-type conductivity and the band gap energy about 1.20–1.29 eV [5].

There have been number of reports on the synthesis of the  $\text{Cu}_2\text{CdGeSe}_4$  compound by various methods like the horizontal gradient freezing method [6,7]; directional solidification method [8]; Bridgman method [9,10] and solid-state reaction method in sealed evacuated quartz ampoules [5,11,12].

$\text{Cu}_2\text{CdGeSe}_4$  exists in two modifications of crystal structure such as a

tetragonal structure with an *I*-42m space group and an orthorhombic structure with a *Pmn*2<sub>1</sub> space group [5]. According to [5], the tetragonal structure appears at temperatures lower than  $400^\circ\text{C}$  and/or cooling the samples after synthesis very slowly ( $\sim 5\text{--}10^\circ\text{C/h}$ ) to room temperature (RT). In the earlier studies [13], the optical band gap for tetragonal (*t*- $\text{Cu}_2\text{CdGeSe}_4$ ) was found to be 1.29 eV, but later in the study [9], there was experimentally shown that band gap of  $\text{Cu}_2\text{CdGeSe}_4$  at RT is 1.20 eV. Orthorhombic structure (*o*- $\text{Cu}_2\text{CdGeSe}_4$ ) has been obtained by cooling the material from  $900^\circ\text{C}$  to  $400^\circ\text{C}$  followed by quenching in cold water [5,11]. The optical absorption measurements showed the band gap of synthesized *o*- $\text{Cu}_2\text{CdGeSe}_4$  compound  $\sim 1.2$  eV [6].

The transformation from tetragonal to orthorhombic structure in  $\text{Cu}_2\text{CdGeSe}_4$  was studied in [5]. It was shown that the transformation proceeded slowly and metastable modifications could be persistent for a long time. The *t*- $\text{Cu}_2\text{CdGeSe}_4$  modification with a tetragonal unit cell has the lattice parameters  $a = b = 0.57482(2)$  nm and  $c = 1.10533(3)$  nm. The *o*- $\text{Cu}_2\text{CdGeSe}_4$  modification has lattice parameters  $a = 0.80968(9)$ ,  $b = 0.68929(6)$  and  $c = 0.66264(6)$  nm [5].

So, there have been made several studies about preparation of two polymorphous modifications of the  $\text{Cu}_2\text{CdGeSe}_4$  compound, but the transformation temperature is not exactly determined and different band gap values have been reported, also these materials have not been

\* Corresponding author.

E-mail address: [marit.kauk-kuusik@ttu.ee](mailto:marit.kauk-kuusik@ttu.ee) (M. Kauk-Kuusik).

<https://doi.org/10.1016/j.tsf.2018.09.025>

Received 13 June 2018; Received in revised form 16 August 2018; Accepted 12 September 2018

Available online 13 September 2018

0040-6090/© 2018 Elsevier B.V. All rights reserved.

used as absorber materials in solar cells.

The aim of this study was to synthesize  $\text{Cu}_2\text{CdGeSe}_4$  with two different crystal structure modifications in the monograin powder form in the liquid phase of molten salts and apply these powders as absorber materials in monograin layer (MGL) solar cells.

## 2. Experimental

In this study  $\text{Cu}_2\text{CdGeSe}_4$  powder materials were synthesized from commercially available CdSe, self-synthesized CuSe, elemental Ge powder and Se shots in the liquid phase of flux materials in evacuated quartz ampoules. Two different salts – cadmium iodide ( $\text{CdI}_2$ ) and potassium iodide (KI) – were used as fluxes. A major technological advantage of the usage of these salts as flux materials is the possibility to remove them after the growth process very easily by a simple dissolution process in water. An additional advantage of the usage of  $\text{CdI}_2$  is the low melting temperature of it ( $T_{\text{melt}} = 387^\circ\text{C}$  [14]) that allows to synthesize of  $\text{Cu}_2\text{CdGeSe}_4$  monograin powders in  $\text{CdI}_2$  flux at lower temperatures. In the present study we performed synthesis-growth process in  $\text{CdI}_2$  at 500, 600 and  $700^\circ\text{C}$  for 120 h. As the melting temperature of KI is  $T_{\text{melt}} = 681^\circ\text{C}$  [14], the synthesis-growth of  $\text{Cu}_2\text{CdGeSe}_4$  monograin powders in KI flux was performed at  $700^\circ\text{C}$ , varying synthesis time- 60 and 120 h.

The precursors for synthesis of  $\text{Cu}_2\text{CdGeSe}_4$  were weighted in the molar ratio of elements 2:1:1:4, after that the used flux salt was added with the mass ratio of  $m_{\text{precursors}}/m_{\text{flux}} = 1:1$ . The mixture was degassed and sealed into quartz ampoules and heated at different synthesis temperatures. After cooling down and opening the ampoules the salt was removed from solid powder particles by leaching with deionized  $\text{H}_2\text{O}$ . Then, the powder was dried in thermostat at  $50^\circ\text{C}$  and sieved into narrow size fractions by sieving system Retsch AS 200.

The morphology of synthesized powder crystals was studied by high-resolution scanning electron microscope (HR-SEM Zeiss Merlin). The bulk composition of the synthesized powder crystals was analyzed by energy dispersive X-ray spectroscopy (EDX) on HR-SEM Zeiss Merlin equipped with Bruker EDX-XFlash6/30 detector with an accelerating voltage of 20 kV. Compositional analysis was made from polished individual crystals.

The crystalline structure was studied by X-ray diffraction (XRD) with a Rigaku Ultima IV diffractometer with monochromatic Cu K $\alpha$  radiation  $\lambda = 1.54056 \text{ \AA}$  at 40 kV and 40 mA, using a D/teX Ultra silicon strip detector.

$\text{Cu}_2\text{CdGeSe}_4$  powders were also analyzed by RT micro-Raman spectroscopy using Horiba's LabRam HR 800 spectrometer equipped with a multichannel CCD detection system in the backscattering configuration using a 532 nm laser line with a spot size of 5  $\mu\text{m}$ .

As the MGL technology [15] requires powder grains of nearly equal size, the sieve analysis was used to determine the particle size distribution. The particle size distribution helps to determine the suitable growth conditions for the synthesis process of  $\text{Cu}_2\text{CdGeSe}_4$  monograin powders in different fluxes. The most valuable fractions for making MGLs manually in the lab conditions are between 45 and 112  $\mu\text{m}$ . Sieve analysis is used to divide the particulate material into size fractions and then to determine the weight of these fractions. In this way a relatively broad particle size spectrum can be analyzed quickly and reliably.  $\text{Cu}_2\text{CdGeSe}_4$  powders were implemented as absorber materials in MGL solar cells, the scheme of device is shown in Fig. 1.  $\text{Cu}_2\text{CdGeSe}_4$  powder crystals were covered by CdS buffer layer (~45 nm) deposited by the chemical bath deposition method to form the heterojunction and embedded into a thin epoxy layer. *i*-ZnO and conductive ZnO:Al layers were deposited by RF sputtering. The formed structure was glued onto a glass plate. Conductive graphite paste was used to make back contacts and Ag-paste was used to make front collector.

Device current–voltage (*J–V*) characteristics were measured under AM 1.5G (100 mW/cm $^2$ ) using a Newport Class AAA solar simulator system. *J–V* characteristics were recorded by a Keithley 2400 source

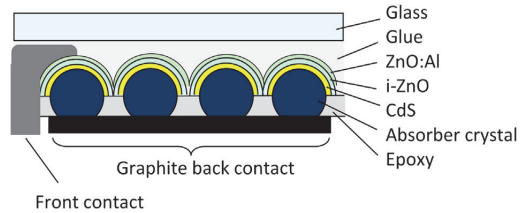


Fig. 1. Scheme of monograin layer solar cell.

meter. A typical solar cell had an active area of approximately 4 mm $^2$ . External quantum efficiency (EQE) was measured in the spectral region of 350–1235 nm using a computer controlled SPM-2 prism monochromator. The generated photocurrent was detected at 0 V bias voltage at room temperature, a 250 W standard halogen lamp was used as a light source.

## 3. Results and discussion

### 3.1. Morphology and particle size distribution

In the molten salt synthesis, a large amount (typically almost equal to the precursor's weight of precursors) of a flux salt is used to provide liquid medium between solid particles that conduces to recrystallization and avoids sintering of solid particles. This liquid phase as solvent controls the characteristics (size, shape, etc.) of the forming powder crystals. Molten medium enhances the rate of solid-state reactions. During the heating up of the mixture of  $\text{CuSe-Ge-Se-CdSe-CdI}_2$  to the synthesis-growth temperature, the firstly formed liquid phase is elemental Se ( $T_{\text{melt}} = 221^\circ\text{C}$  [14]). It means that liquid Se can act as a flux at this temperature, but the volume of this flux is not enough to repel separate solid particles from each other and they start to sinter together. This sintering process arises in heating material below the melting point of the main flux material  $\text{CdI}_2$  and continues until  $\text{CdI}_2$  melts at  $387^\circ\text{C}$ . Then the volume of the liquid phase exceeds the volume of voids between precursor particles and repelling forces [16] between solid particles arise. In this case, the formed liquid phase is sufficient to repel both, the solid precursor particles and the formed  $\text{Cu}_2\text{CdGeSe}_4$  particles from each other and to avoid sintering caused by the contracting capillary forces arising in the solid–liquid phase boundaries. The sintered together particles are seen in Fig. 2a and Fig. 2b. The sharp edges of the crystals synthesized at  $500^\circ\text{C}$  and  $600^\circ\text{C}$  indicate to the crystal formation mechanism by sintering process and to insufficient recrystallization of crystals in conditions of low solubility of  $\text{Cu}_2\text{CdGeSe}_4$  in  $\text{CdI}_2$ .

The growth of crystals by Ostwald ripening is characterized by a normal (Gaussian) distribution of grain sizes (see Fig. 3a). The transport of material occurs from smaller to larger grains because of the difference in surface energy and in solubility between the grains of different size. Therefore, small grains dissolve, large grains grow and average grain size increases. High solubility of synthesized material in flux results in spherical grains as seen in Fig. 2c. Rounded grains are synthesized at  $700^\circ\text{C}$  irrespective of the used flux material due to the higher solubility at higher temperatures.

Fig. 3b shows the lognormal plot of the accumulative weight percentage of the particles under a specific particle size versus the particle size for the powder samples synthesized at different temperatures in  $\text{CdI}_2$  flux and powders grown in KI flux for different times at  $700^\circ\text{C}$ . The black solid horizontal line marking 50% shows the powder median grain size values ( $D_{50}$ ) calculated from weight percentage. The  $D_{50}$  is the size in micrometers that splits the distribution in half above and half below this diameter. The sieving analysis revealed that median particle size of produced powder crystals increased with increasing synthesis temperature and duration. By increasing the synthesis temperature

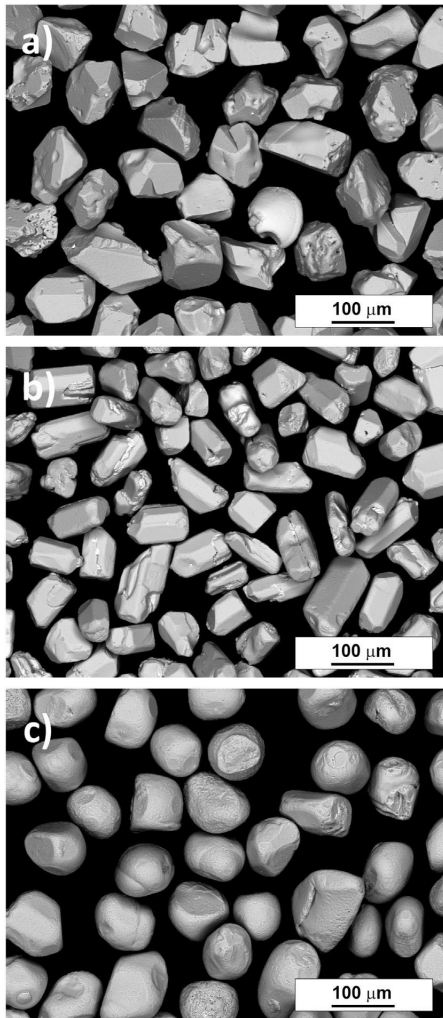


Fig. 2. SEM images of  $\text{Cu}_2\text{CdGeSe}_4$  powder crystals (fraction size 63–75 μm) synthesized at a) 500 °C; b) 600 °C and c) 700 °C for 120 h in the  $\text{CdI}_2$  flux.

from 500 to 700 °C the median size of particles grown in  $\text{CdI}_2$  increases from 25 to 139 μm. Median size of particles for powders synthesized in KI flux at 700 °C increased from 112 to 132 μm by increasing the

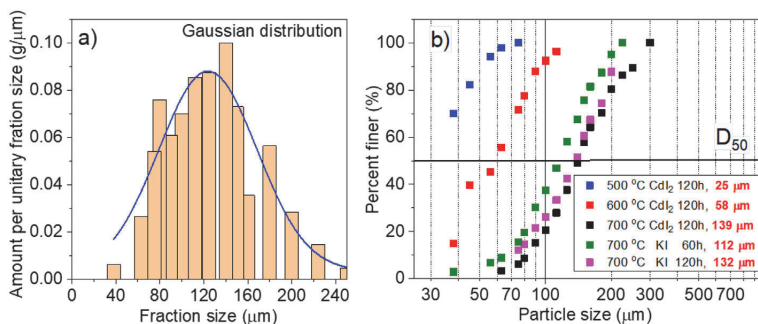


Fig. 3. a) A normal distribution of grain sizes for powder synthesized in KI at 700 °C for 120 h; b) Particle size distribution curves for powders synthesized in  $\text{CdI}_2$  and KI at different temperatures for different times.  $D_{50}$  marks the median size of particles – written in red (at the peak of Gaussian distribution). (For interpretation of the references to colour in this figure legend, the reader is referred to the web version of this article.)

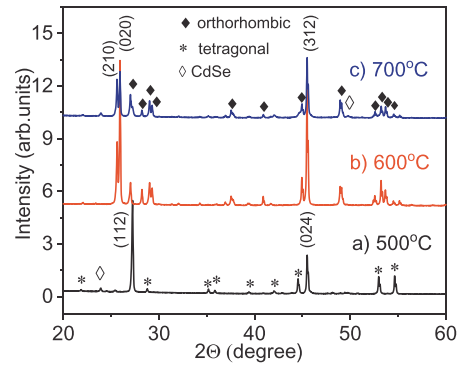


Fig. 4. XRD patterns of  $\text{Cu}_2\text{CdGeSe}_4$  powder synthesized at a) 500 °C; b) 600 °C and c) 700 °C in  $\text{CdI}_2$  flux.

Table 1  
Lattice parameters of  $\text{Cu}_2\text{CdGeSe}_4$  powders.

Samples	Space group	a, Å	b, Å	c, Å
Powder 1 (500 °C)	<i>I</i> -42 <i>m</i> - tetragonal	5.7476	5.7476	11.0511
Powder 2 (600 °C)	<i>Pmm</i> 21-orthorhombic	8.0726	6.8855	6.6118
Powder 3 (700 °C)	<i>Pmm</i> 21- orthorhombic	8.0634	6.8793	6.6035

synthesis time from 60 to 120 h. Results show that the median size of particles grown at 700 °C does not depend much on the flux material. The most applicable fractions of crystals for monograin membrane preparation in lab conditions are between 45 and 112 μm, the highest yield in this range was gained by synthesizing the  $\text{Cu}_2\text{CdGeSe}_4$  monograin powder in  $\text{CdI}_2$  flux at 600 °C for 120 h.

### 3.2. Composition

Bulk composition of the  $\text{Cu}_2\text{CdGeSe}_4$  powders synthesized in  $\text{CdI}_2$  flux at different temperatures was characterized by EDX. The atomic concentrations of Cu and Se remained almost the same with increasing synthesis temperature, while the atomic concentrations of Cd increased and that of the Ge decreased probably by the reason that  $\text{CdI}_2$  is not inactive in the synthesis [18]. By increasing the synthesis temperature from 500 °C to 700 °C, the bulk composition became Cd-rich (the ratio of  $[\text{Cd}]/[\text{Ge}]$  increases from 0.99 to 1.07). The ratio of  $[\text{Cu}]/([\text{Cd}] + [\text{Ge}]) \sim 1.0$  for  $\text{Cu}_2\text{CdGeSe}_4$  powders synthesized in  $\text{CdI}_2$  at 500 °C and 700 °C, but powders synthesized at 600 °C have Cu-poor (the ratio of  $[\text{Cu}]/([\text{Cd}] + [\text{Ge}]) = 0.93$ ) composition probably due to the shape of single phase area of the phase diagram [12]. Bulk composition of the  $\text{Cu}_2\text{CdGeSe}_4$  powders synthesized in KI flux for different times



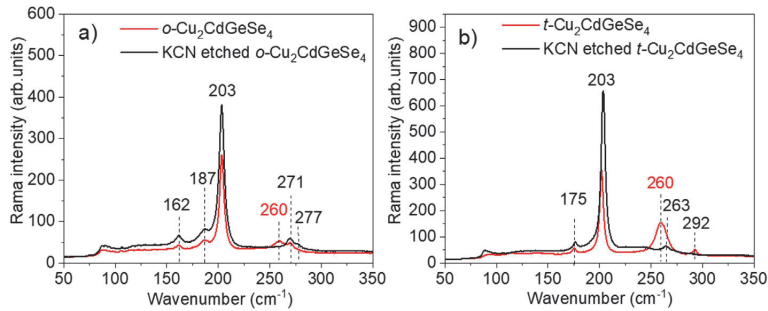


Fig. 5. RT-Raman spectra of  $\text{Cu}_2\text{CdGeSe}_4$  before and after KCN etching - a) with orthorhombic structure and b) with tetragonal structure.

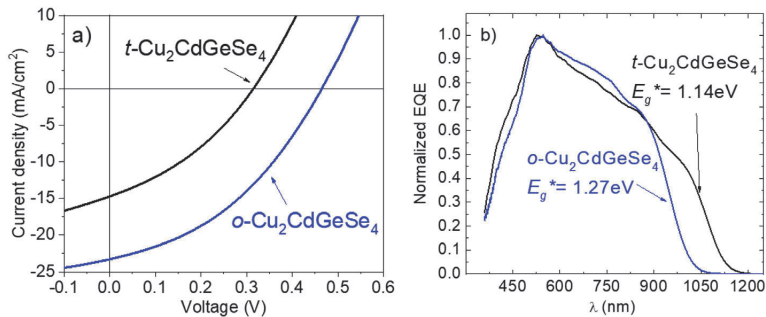


Fig. 6. a)  $J$ - $V$  characteristics and b) EQE spectra of MGL solar cell prepared from  $t\text{-Cu}_2\text{CdGeSe}_4$  and  $o\text{-Cu}_2\text{CdGeSe}_4$  powders.

was also Cd-rich (the ratio of  $[\text{Cd}]/[\text{Ge}] = 1.03$ ) and did not depend on synthesis time. But the ratio of  $[\text{Cu}]/([\text{Cd}] + [\text{Ge}])$  decreased from 1.0 to 0.96 by increasing the synthesis time.

### 3.3. XRD analysis

The  $\text{Cu}_2\text{CdGeSe}_4$  powders synthesized in  $\text{CdI}_2$  flux at different temperatures were investigated by XRD as shown in Fig. 4. The XRD pattern of the powder synthesized at  $500^\circ\text{C}$  showed peaks corresponding to the tetragonal crystal structure (01-070-9042) with the space group  $I-42m$  of the main phase and the presence of CdSe secondary phase. The main peak is attributed to (112) plane of  $\text{Cu}_2\text{CdGeSe}_4$ . The powders synthesized at  $600^\circ\text{C}$  and  $700^\circ\text{C}$  revealed the presence of the orthorhombic phase (01-074-3115). Calculated lattice parameters  $a$ ,  $b$ ,  $c$  of all the samples are presented in the Table 1.

### 3.4. Raman analysis

Raman spectroscopy was used to analyze the phase composition of all the synthesized  $\text{Cu}_2\text{CdGeSe}_4$  monograin batches. Unfortunately there is no Raman data published for this compound in the literature. The most intensive peak in the spectra of  $\text{Cu}_2\text{CdGeSe}_4$  is observed at  $203\text{ cm}^{-1}$  and it is not depending on the phase structure. The additional characteristic Raman modes for the  $o\text{-Cu}_2\text{CdGeSe}_4$  phase were detected at  $162$ ,  $187$ ,  $271$  and  $277\text{ cm}^{-1}$  (see Fig. 5a) and for  $t\text{-Cu}_2\text{CdGeSe}_4$  phase, the characteristic peaks were at  $175$ ,  $263$  and  $292\text{ cm}^{-1}$  (Fig. 5b).

All the as-grown powders had an additional peak in Raman spectra at  $260\text{ cm}^{-1}$ , which has been assigned to  $\text{Cu}_{2-x}\text{Se}$  phase [20]. In order to remove selectively the  $\text{Cu}_{2-x}\text{Se}$  phase from the surface of as-grown  $\text{Cu}_2\text{CdGeSe}_4$  powders, chemical etching with 10% KCN + 1% KOH solution for 30 min was performed. The  $\text{Cu}_{2-x}\text{Se}$  Raman scattering peak at  $260\text{ cm}^{-1}$  disappeared completely after the KCN etching while no

change was observed in the  $\text{Cu}_2\text{CdGeSe}_4$  peaks.

### 3.5. MGL solar cell device properties

Sieving analysis showed that the yield of the applicable size of the crystals synthesized at  $500^\circ\text{C}$  for monograin layer solar cell preparation was very small. So, to produce MGL solar cells, the powder synthesized at  $700^\circ\text{C}$  in KI flux was used for the different post-annealing procedures providing the both possible structural modifications of  $\text{Cu}_2\text{CdGeSe}_4$  as solar cell absorber materials. In order to produce  $o\text{-Cu}_2\text{CdGeSe}_4$ , the powder was post-annealed at  $500^\circ\text{C}$  for 1 h and cooled by quenching into water.  $t\text{-Cu}_2\text{CdGeSe}_4$  modification was obtained by applying the same annealing conditions at  $500^\circ\text{C}$  for 1 h, but powder was cooled slowly to room temperature ( $\sim 0.5^\circ\text{C}/\text{min}$ ). XRD patterns of these powders confirmed the formation of different respective modifications.

To investigate the effect of the crystalline structure of  $\text{Cu}_2\text{CdGeSe}_4$  on device performance,  $J$ - $V$  curves of the solar cell devices were measured under AM1.5 illumination, as shown in Fig. 6a. For the device based on  $t\text{-Cu}_2\text{CdGeSe}_4$  absorber, the highest obtained power conversion efficiency (PCE) was 2.16% with  $V_{oc}$  of 315 mV,  $J_{sc}$  of  $14.7\text{ mA}/\text{cm}^2$ , and  $FF$  of 35%, while for the  $o\text{-Cu}_2\text{CdGeSe}_4$  solar cell, a PCE of 4.21% was achieved, with a  $V_{oc}$  of 464 mV,  $J_{sc}$  of  $17.5\text{ mA}/\text{cm}^2$  and  $FF$  of 39%. These initial results indicate that both  $t\text{-Cu}_2\text{CdGeSe}_4$  and  $o\text{-Cu}_2\text{CdGeSe}_4$  materials are potential candidates for absorber material in photovoltaic devices. However, more information on the dependence of the optoelectronic properties as well as the structural properties on the composition and material preparation conditions is needed in order to optimize the technology.

EQE analysis was used to estimate the effective bandgap energy ( $E_g^*$ ) of the synthesized absorber materials [21] since the evaluation of  $E_g^*$  from the optical absorption or reflectance spectra of the monograins is rather challenging. The EQE of  $\text{Cu}_2\text{CdGeSe}_4$  solar cells was measured as a function of the wavelength of the incident light at room

temperature (see Fig. 6b). From the linear segment of the low-energy side of the construction  $(E^*QE)^2$  vs.  $E$  curves, the  $E_g^*$  can be evaluated. The  $E_g^*$  values obtained from EQE measurements was found to be 1.27 eV for orthorhombic  $\text{Cu}_2\text{CdGeSe}_4$  powders and 1.14 eV for tetragonal  $\text{Cu}_2\text{CdGeSe}_4$  powders.

#### 4. Conclusions

$\text{Cu}_2\text{CdGeSe}_4$  powders for photovoltaic applications were synthesized by molten salt method in  $\text{CdI}_2$  and KI. Phase analysis by Raman spectroscopy and X-ray diffraction showed that  $\text{Cu}_2\text{CdGeSe}_4$  powder synthesized at 500 °C had tetragonal structure and powders synthesized at temperatures 600 °C and 700 °C had orthorhombic structure regardless of the used molten salt. The results of compositional analysis indicated that Cu-poor and Cd-rich powders were synthesized in KI flux at 700 °C and in  $\text{CdI}_2$  flux at 600 °C. The band gap values determined from EQE measurements were found to be 1.27 eV for orthorhombic  $\text{Cu}_2\text{CdGeSe}_4$  and 1.14 eV for tetragonal  $\text{Cu}_2\text{CdGeSe}_4$  material. The best PCE of 4.21% was achieved by using the orthorhombic structured  $\text{Cu}_2\text{CdGeSe}_4$  powder as absorber material.

#### Acknowledgements

The authors acknowledge Dr. A. Mere for recording the XRD patterns. This work was supported by the Estonian Research Council under the contract IUT19-28 and the Estonian Centre of Excellence in Research project “Advanced materials and high-technology devices for sustainable energetics, sensorics and nanoelectronics”(TK141).

#### References

- [1] Solar Frontier press release dated, [http://www.solar-frontier.com/eng/news/2017/1220\\_press.html](http://www.solar-frontier.com/eng/news/2017/1220_press.html), (December 8, 2017).
- [2] W. Wang, M.T. Winkler, O. Gunawan, T. Gokmen, T.K. Todorov, Y. Zhu, D.B. Mitzi, Device Characteristics of CZTSSe Thin-Film Solar Cells with 12.6% Efficiency, *Adv. Energy Mater.* 4 (2014) 1301465, <https://doi.org/10.1002/aenm.201301465>.
- [3] T. Taskesen, J. Neerken, J. Schoneberg, D. Pareek, V. Steininger, J. Parisi, L. Güta, *Adv. Energy Mater.* 8 (16) (2018) 1703295, <https://doi.org/10.1002/aenm.201703295>.
- [4] Y.S. Lee, T. Gershon, O. Gunawan, T.K. Todorov, T. Gokmen, Y. Virgus, S. Guha,  $\text{Cu}_2\text{ZnSnSe}_4$  Thin-Film Solar Cells by thermal Co-evaporation with 11.6% Efficiency and improved Minority carrier Diffusion Length, *Adv. Energy Mater.* 5 (2015) 1401372, <https://doi.org/10.1002/aenm.201401372>.
- [5] L.D. Gulay, Ya.E. Romanyuk, O.V. Parasyuk, Crystal structures of low- and high-temperature modifications of  $\text{Cu}_2\text{CdGeSe}_4$ , *J. Alloys Compd.* 347 (2002) 193–197, [https://doi.org/10.1016/S0925-8388\(02\)00790-9](https://doi.org/10.1016/S0925-8388(02)00790-9).
- [6] H. Matsushita, T. Maeda, A. Katsui, T. Takizawa, Thermal analysis and synthesis from the melts of Cu-based quaternary compounds Cu–III–IV–VI<sub>4</sub> and Cu<sub>2</sub>–II–IV–VI<sub>4</sub> (II = Zn, Cd; III = Ga, In; IV = Ge, Sn; VI = Se), *J. Cryst. Growth* 208 (2000) 416–422, [https://doi.org/10.1016/S0022-0248\(99\)00468-6](https://doi.org/10.1016/S0022-0248(99)00468-6).
- [7] H. Matsushita, T. Ichikawa, A. Katsui, Structural, thermodynamical and optical properties of Cu<sub>2</sub>–II–IV–VI<sub>4</sub> quaternary compounds, *J. Mater. Sci.* 40 (2005) 2003–2005, <https://doi.org/10.1007/s10853-005-1223-5>.
- [8] N.N. Konstantinova, G.A. Medvedkin, I.K. Polushina, Yu.V. Rud, A.D. Smirnova, V.I. Sokolova, M.A. Tairov, Optical and electric properties of  $\text{Cu}_2\text{CdSnSe}_4$  and  $\text{Cu}_2\text{CdGeSe}_4$ , *Izv. Akad. Nauk SSSR Neorgan. Mater. (rus)* 25 (1989) 1445–1448.
- [9] M.G. Brik, O.V. Parasyuk, G.L. Myronchuk, I.V. Kityk, Specific features of band structure and optical anisotropy of  $\text{Cu}_2\text{CdGeSe}_4$  quaternary compounds, *Mater. Chem. Phys.* 147 (2014) 155–161, <https://doi.org/10.1016/j.matchemphys.2014.04.022>.
- [10] V.A. Ocheretova, O.V. Parasyuk, A.O. Fedorchuk, O.Y. Khyzhun, Electronic structure of  $\text{Cu}_2\text{CdGeSe}_4$  single crystal as determined from X-ray spectroscopy data, *Mater. Chem. Phys.* 160 (2015) 345–351, <https://doi.org/10.1016/j.matchemphys.2015.04.049>.
- [11] R. Chetty, J. Dadda, J. de Boer, E. Müller, R.C. Mallik, The effect of Cu addition on the thermoelectric properties of  $\text{Cu}_2\text{CdGeSe}_4$ , *Intermetallics* 57 (2015) 156–162, <https://doi.org/10.1016/j.intermet.2014.10.015>.
- [12] L.V. Piskach, O.V. Parasyuk, Ya.E. Romanyuk, The phase equilibria in the quasi-binary  $\text{Cu}_2\text{GeS}_3/\text{Se}_2$ – $\text{CdS}/\text{Se}$  systems, *J. Alloys Compd.* 299 (2000) 227–231, [https://doi.org/10.1016/S0925-8388\(99\)00797-5](https://doi.org/10.1016/S0925-8388(99)00797-5).
- [13] S.A. Mkrtchyan, K. Dovletov, E.G. Zhukov, A.G. Melikdzhanyan, S. Nuryev, Electrical properties of  $\text{Cu}_2\text{A}^2\text{B}^4\text{Se}_4$  compounds ( $\text{A}^2$ –Cd, Hg;  $\text{B}^4$ –Ge, Sn), *Izv. Akad. Nauk SSSR Neorgan. Mater. (rus)* 24 (7) (1988) 1094–1096.
- [14] CRC Handbook of Chemistry and Physics 84<sup>th</sup> Edition by David R. Lide, CRC Press LLC (2003).
- [15] E. Mellikov, M. Altosaar, M. Kauk-Kuusik, K. Timmo, D. Meissner, M. Grossberg, J. Krustok, O. Volobujeva, Growth of CZTS-based monograins and their application to membrane solar cells, in: K. Ito (Ed.), *Copper Zinc Tin Sulfide-Based Thin-Film Solar Cells*, John Wiley & Sons Ltd, 2015, pp. 289–309, <https://doi.org/10.1002/9781118437865.ch13>.
- [16] Suk-Joong L. Kang, Sintering, Densification, Grain Growth, and Microstructure, Elsevier Ltd, 2015, <https://doi.org/10.1016/B978-0-7506-6385-4.X5000-6>.
- [17] I. Leinemann, G.C. Nkwusi, K. Timmo, O. Volobujeva, M. Danilson, J. Raudoja, T. Kaljueve, R. Traksmaa, M. Altosaar, D. Meissner, Reaction pathway to  $\text{Cu}_2\text{ZnSnSe}_4$  formation in  $\text{CdI}_2$ , Part I. Chemical reactions and enthalpies in mixtures of  $\text{CdI}_2$ – $\text{ZnSe}$ ,  $\text{CdI}_2$ – $\text{SnSe}$ , and  $\text{CdI}_2$ – $\text{CuSe}$ , *J. Therm. Anal. Calorim.* (2018) 1–13, <https://doi.org/10.1007/s10973-018-7102-5>.
- [18] T. Tanaka, T. Sueishi, K. Saito, Q. Guo, M. Nishio, K.M. Yu, W. Walukiewicz, Existence and removal of  $\text{Cu}_2\text{Se}$  second phase in coevaporated  $\text{Cu}_2\text{ZnSnSe}_4$  thin films, *J. Appl. Phys.* 111 (2012) 053522, <https://doi.org/10.1063/1.3691964>.
- [19] J. Krustok, R. Josepson, T. Raadik, M. Danilson, Potential fluctuations in  $\text{Cu}_2\text{ZnSnSe}_4$  solar cells studied by temperature dependence of quantum efficiency curves, *Physica B* 405 (15) (2010) 3186–3189, <https://doi.org/10.1016/j.physb.2010.04.041>.



**Publication II**

X. Li, M. Pilvet, K. Timmo, M. Grossberg, M. Danilson, V. Mikli, M. Kauk-Kuusik. "Effect of absorber surface modification on the optoelectronic properties of  $\text{Cu}_2\text{CdGeSe}_4$  solar cells", *Thin Solid Films*, Volume 697, 137822, 2020.

<https://doi.org/10.1016/j.tsf.2020.137822>





# Effect of absorber surface modification on the optoelectronic properties of $\text{Cu}_2\text{CdGeSe}_4$ solar cells.

X. Li<sup>\*</sup>, M. Pilvet, K. Timmo, M. Grossberg, M. Danilson, V. Mikli, M. Kauk-Kuusik

Department of Materials and Environmental Technology, Tallinn University of Technology, Ehitajate tee 5, 19086 Tallinn, Estonia

## ARTICLE INFO

### Keywords:

Copper cadmium germanium selenide  
Flux method  
Thermal treatment  
Chemical etching  
Solar cells

## ABSTRACT

High quality  $\text{Cu}_2\text{CdGeSe}_4$  micro-crystalline powder has been synthesized by molten salt method at 700 °C in closed quartz ampoules using elemental Ge, binary CdSe and CuSe as precursor materials and KI as flux material. The effect of initial Cu and Cd content on the bulk composition of grown crystals was investigated. According to energy dispersive X-ray spectroscopy results, the two types of  $\text{Cu}_2\text{CdGeSe}_4$  powders, with nearly stoichiometric and with Cd-rich composition were synthesized. X-ray diffraction and Raman analyses confirmed that all studied  $\text{Cu}_2\text{CdGeSe}_4$  crystals had orthorhombic crystal structure. It was essential to chemically and thermally modify the surface of crystals before implementing the powder crystals as absorber materials in monograin layer solar cells. Results showed that both  $\text{Br}_2\text{-MeOH}$  and HCl combined with KCN etching were effective to remove secondary phases on the crystal surface. Raman and X-ray photoelectron spectroscopy analyses revealed that after annealing at 400 °C the crystal surface is covered by  $\text{Ge}_x\text{Se}_{1-x}$  phase, which was effectively removed by KCN etching. Using this approach, we achieved  $\text{Cu}_2\text{CdGeSe}_4$  monograin layer device conversion efficiency of 5.7%.

## 1. Introduction

The large group of quaternary copper chalcogenides has attracted considerable attention due to their suitable properties for photovoltaics. From this group of compounds the record power conversion efficiency of 12.6% is obtained for kesterite  $\text{Cu}_2\text{ZnSn}(\text{S,Se})_4$  (CZTSSe) [1]. This is still far behind the 23.35% efficiency of  $\text{Cu}(\text{In,Ga})\text{Se}_2$ -based solar cells [2] and the theoretical efficiencies of quaternary chalcogenide semiconductors (~ 32%), which is expected from the Shockley–Queisser radiative limit [3]. The current bottleneck that kesterite solar cell encounters is the large open circuit voltage ( $V_{OC}$ ) deficit (expressed as  $E_g/q-V_{OC}$ , where  $E_g$  is absorber bandgap and  $q$  the elemental charge) reported unanimously by various literature. The losses in kesterite devices can be attributed to various reasons such as coexistence of complex secondary phases, the band tailing issue, short minority lifetime, bulk defects, and undesirable band alignment at  $p$ - $n$  interfaces [4].

One promising method to reduce  $V_{OC}$  deficit is cation substitution. Cation substitution of Zn by Cd [4–6] or Sn by Ge [7–10] enables to tune the optical band gap and offers new opportunities in the development of highly efficient kesterite based photovoltaic devices. The ionic radius of  $\text{Cd}^{2+}$  is larger than that of  $\text{Cu}^+$  and  $\text{Zn}^{2+}$ , so Cd is expected to increase the formation energy of  $\text{Cu}_{Cd}$  and  $\text{Cd}_{Cu}$  antisite defects, thereby suppressing the disorder and band tailing issues in

kesterite system. In addition to the change in the defects system, replacing Zn by Cd can also facilitate the grain growth and suppress the secondary phase formation [4,5]. Therefore, Cd alloying in kesterite has drawn considerable attention. Yan et al. reported significant device performance improvement an over 11% by Cd-alloyed  $\text{Cu}_2\text{ZnSnS}_4$  solar cell [4]. The other beneficial cation substitution to reduce  $V_{OC}$  deficit is replacing Sn by Ge. In the study [10], the device performance was improved up to 12.3% by Ge incorporation in the  $\text{Cu}_2\text{ZnSnSe}_4$ . The best efficiency was achieved through the optimization of a thermal annealing containing  $\text{GeSe}_2$  leading to an improvement of the  $V_{OC}$  deficit by reducing band tailing, and a reduced carrier recombination at the absorber/buffer interface and/or in the space-charge region.

There are also some reports about pure  $\text{Cu}_2\text{CdSnS}_4$  ( $E_g \sim 1.4$  eV) [11–13] and  $\text{Cu}_2\text{ZnGeSe}_4$  ( $E_g \sim 1.4$  eV) materials as potential candidates for absorber material [14–17]. The highest power conversion efficiency reported so far using  $\text{Cu}_2\text{CdSnS}_4$  as absorber layer is 4.2% [11] and using  $\text{Cu}_2\text{ZnGeSe}_4$  as absorber layer is 7.6% [15].

$\text{Cu}_2\text{CdSnS}_4$  has stannite type structure [11] and  $\text{Cu}_2\text{ZnGeSe}_4$  has kesterite type structure based on neutron diffraction data presented by Gunder et al. [18]. Recently, less investigated compound  $\text{Cu}_2\text{CdGeSe}_4$ , where Zn is totally replaced by Cd and Sn is replaced by Ge, has attracted also more scientific interest. This compound exists in two types of the crystal structure: the orthorhombic  $\text{Cu}_2\text{CdGeSe}_4$  (o-CCGSe) with

<sup>\*</sup> Corresponding author.

E-mail address: [xiaofeng.li@taltech.ee](mailto:xiaofeng.li@taltech.ee) (X. Li).

band gap of 1.27 eV and tetragonal (*t*-CCGSe) with band gap of 1.14 eV [19]. In our previous study the efficiency of 4.2% for monograin layer solar cell based on the *o*-Cu<sub>2</sub>CdGeSe<sub>4</sub> absorber material was reported [19]. Grossberg et al. made detailed analysis of the photoluminescence (PL) emission of *t*-CCGSe and *o*-CCGSe, which showed significant difference in the radiative recombination processes in comparison to most studied multinary kesterite compound Cu<sub>2</sub>ZnSn(S,Se)<sub>4</sub> giving the less studied material CCGSe an opportunity to overcome the factors limiting the efficiency of the CZTSSe based solar cells [20].

Usually in kesterite solar cells, Cu-poor and Zn-rich composition of absorber material is used. Analogous to the kesterite, the challenges of this study were to synthesize uniform single phase CCGSe monograin powder with off-stoichiometric compositions. Considering the phase diagram of the Cu<sub>2</sub>GeSe<sub>3</sub>-CdSe system [21,22], the quaternary Cu<sub>2</sub>CdGeSe<sub>4</sub> compound exist in a narrow homogeneity region. The Gerich compound, which contains more than 2% GeSe<sub>2</sub>, is two-phase. In the Cu-rich region, beside the Cu<sub>2</sub>Se phase exists Cu<sub>2</sub>GeSe<sub>3</sub> ternary phase and in the Cd-rich side appears CdSe secondary phase.

In the monograin powder growth process, some part of the precursors and the formed CCGSe may partially dissolve in the molten flux salt at growth temperature, and the dissolved part precipitates on the solid crystal surfaces during the cooling period [23]. The surface morphology and the composition of the absorber crystal surface will be changed due to the existence of these precipitations. Usually, these conditions result in the formation of the undesired secondary and ternary phases in addition to main compound. Therefore, the removal of secondary phases from the surface of the Cu<sub>2</sub>CdGeSe<sub>4</sub> crystals is one of the major challenges to improve the performances of solar cells. KCN chemical etching approach, originally developed for the removal of Cu<sub>2</sub>Se phases in Cu(In,Ga)(S,Se)<sub>2</sub> thin films [24], is now applied also in many kesterite studies [25–27]. HCl etching for the selective removal of Zn-rich secondary phases in kesterite is shown in [26,28,29] and the effectiveness of bromine in methanol (Br<sub>2</sub>-MeOH) etchant to remove Cu- and Sn-based secondary phases is presented in the several studies [26,28,30]. It is known that CdSe crystals dissolve in a HNO<sub>3</sub> + HCl mixture [31], in the concentrated HCl and in the Br<sub>2</sub>-MeOH solutions [32].

After chemical etching, it is essential to anneal the powders at elevated temperatures before implementing the powder crystals as absorber materials in monograin layer (MGL) solar cells.

In this study a comparative investigation of the influence of different etchants such as Br<sub>2</sub>-MeOH, KCN and HCl followed by isothermal annealing at different temperatures on the performance of *o*-Cu<sub>2</sub>CdGeSe<sub>4</sub> monograin layer solar cells was carried out.

## 2. Experimental

The quaternary compound Cu<sub>2-x</sub>Cd<sub>y</sub>GeSe<sub>4</sub> ( $x = 0.1; 0.15; 0.2$  and  $y = 1.0; 1.05; 1.1$ ) powder materials were synthesized from commercially available CdSe, self-synthesized CuSe, elemental Ge powder and Se shots in the liquid phase of KI flux material in evacuated quartz ampoules. As the melting temperature of KI is  $T_{melt} = 681$  °C [33], the synthesis-growth of Cu<sub>2-x</sub>Cd<sub>y</sub>GeSe<sub>4</sub> monograin powders in KI flux was performed at 700 °C. The ratio of the precursors were weighted in the desired molar ratio of elements, after that the used flux salt was added with the mass ratio of  $m_{precursors}/m_{flux} = 1: 1$ . The mixture was degassed and sealed into quartz ampoules and heated slowly to the synthesis temperature (0.5 deg/min). The powders were grown at 700 °C for 120 h and then naturally cooled to room-temperature (RT). After opening the ampoules, the salt was removed from solid powder particles by leaching with deionized H<sub>2</sub>O. Then, the powder was dried in thermostat at 50 °C and sieved into narrow size fractions by sieving system Retsch AS 200.

Before implementing the powders as absorber materials in monograin layer solar cells, different surface treatments were applied. Prior to heat-treatment of powders, the chemical etching by 1% Br<sub>2</sub>-MeOH,

10% KCN and 10% HCl solutions or combination of these etchants were applied. The first two etchings processes were performed at 50 °C and last mentioned at 70 °C in ultra-sonic bath. After chemical etching, the powders were annealed in quartz ampoules at different temperatures for 1 hour.

The morphology of synthesized powder crystals was studied by high-resolution scanning electron microscope (HR-SEM Zeiss Merlin). The bulk composition of the synthesized powder crystals was analyzed by energy dispersive X-ray spectroscopy (EDX) on HR-SEM Zeiss Merlin equipped with Bruker EDX-XFlash6/30 detector with an accelerating voltage of 20 kV. Compositional analysis was made from polished individual crystals. The information about elemental composition of the crystals surface were studied by X-ray photoelectron spectroscopy (XPS) method using a Kratos Analytical Axis Ultra DLD spectrometer fitted with monochromatic Al K $\alpha$  X-ray source and achromatic Mg K $\alpha$ /Al K $\alpha$  dual anode X-ray source. The achromatic Mg K $\alpha$ /Al K $\alpha$  dual anode X-ray source was used to collect secondary Survey spectra in order to help to distinguish the core level and Auger peaks in XPS spectra.

Phase composition of Cu<sub>2-x</sub>Cd<sub>y</sub>GeSe<sub>4</sub> powders were analyzed by RT micro-Raman spectroscopy using Horiba's LabRam HR 800 spectrometer equipped with a multichannel CCD detector in the backscattering configuration using a 532 nm laser line with a spot size of 5 micrometers.

Narrow granulometric fractions of chemically and thermally treated powders were used as absorber layer in the MGL solar cell structure: graphite/CCGSe/CdS/ZnO/Ag. Cu<sub>2-x</sub>Cd<sub>y</sub>GeSe<sub>4</sub> powder crystals were covered with CdS buffer layer deposited by the chemical bath deposition method to form the *p-n* junction and then embedded into a thin epoxy layer (called monograin membrane). After polymerization of this epoxy, *i*-ZnO and conductive ZnO:Al were deposited by Radio Frequency sputtering onto the surface of the membrane. Conductive graphite paste was used to make back contacts and Ag-paste was used to make front collector.

Photovoltaic properties of monograin layer solar cells were characterized by current-voltage (*I-V*) measurements under AM 1.5 G (100 mW/cm<sup>2</sup>) using a Newport Class AAA solar simulator system. *I-V* characteristics were recorded by a Keithley 2400 source meter. A typical solar cell had an active area of approximately 4 mm<sup>2</sup>.

## 3. Results and discussion

### 3.1. Morphology and size of Cu<sub>2</sub>CdGeSe<sub>4</sub> monograin powders

In the Fig. 1, it is shown the SEM images of Cu<sub>2-x</sub>Cd<sub>y</sub>GeSe<sub>4</sub> powder crystals in size 100–112  $\mu$ m with different compositions. The compositional deviations in precursor mixture have no direct influence on the morphology of crystals. Formed crystals have round shape with some well-defined plains. Table 1 presents the powder median grain size values ( $D_{50}$ ) calculated from weight percentage average size of the powder crystals. The sieving analysis showed that median size of the crystals increased with lower Cu-content and higher Cd-content in precursors (amount of crystals with diameter > 100  $\mu$ m increased from 72 to 88% of total weight). More detailed explanation about the method how to calculate median particle size is presented in [19].

### 3.2. Elemental and phase composition

Bulk composition of Cu<sub>2-x</sub>Cd<sub>y</sub>GeSe<sub>4</sub> ( $x = 0.1; 0.15; 0.2$  and  $y = 1.0; 1.05; 1.1$ ) monograin powders were measured by EDX from polished crystals. According to EDX results, Cu-poor ( $x = 0.15$ ) and  $y = [Cd]/[Ge] = 1.0$  input composition resulted in powder with nearly stoichiometric composition- Cu<sub>2</sub>Cd<sub>1.03</sub>Ge<sub>1.02</sub>Se<sub>4</sub>. If the precursors composition was Cu-poor ( $x > 0$ ) and Cd-rich ( $[Cd]/[Ge] > 1.0$ ), the average bulk composition of all powders was slightly Cu-poor ( $([Cu]/([Cd] + [Ge]) = 0.96)$ ) and Cd-rich ( $[Cd]/[Ge] = 1.09$ )



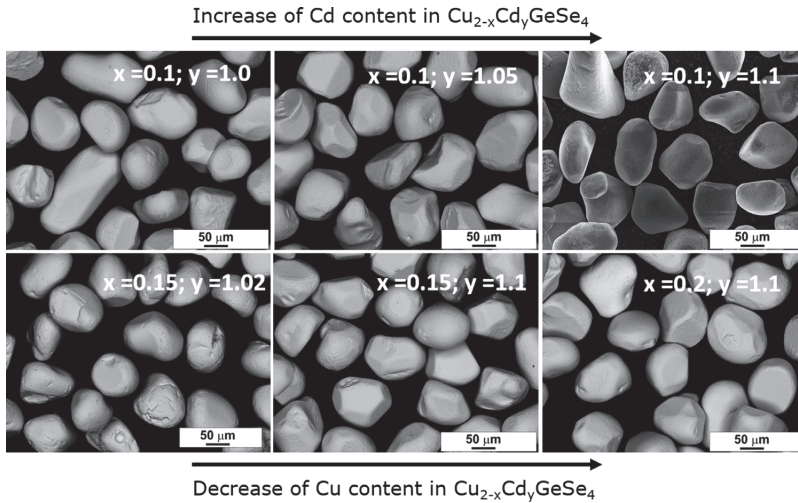


Fig. 1. SEM images of  $\text{Cu}_{2-x}\text{Cd}_y\text{GeSe}_4$  powder crystals with different compositions.

–  $\text{Cu}_{1.95}\text{Cd}_{1.06}\text{Ge}_{0.97}\text{Se}_4$ . The XRD patterns (not presented) of all synthesized  $\text{Cu}_{2-x}\text{Cd}_y\text{GeSe}_4$  powders showed peaks corresponding to the orthorhombic structure (JCPDS 01–074–3115) with the space group  $Pmn21$  of the main phase.

Cross-sectional SEM images and EDX mappings of the  $\text{Cu}_{2-x}\text{Cd}_y\text{GeSe}_4$  powders have been investigated by scanning electron microscopy. In the Fig. 2, the polished  $\text{Cu}_{1.95}\text{Cd}_{1.06}\text{Ge}_{0.97}\text{Se}_4$  powder crystals are presented. It is seen from the SEM image that powder material contain some lighter crystals (point 1) which are comparable size of the main material crystals. According to EDX analysis, the light crystal contains mainly Cd and Se (50.4 at%: 48.1 at%). The existence of CdSe secondary phase in the powder was also confirmed by XRD. CdSe is *n*-type semiconductor material with direct band gap  $\sim 1.74$  eV [34]. This phenomenon is not a problem if the CdSe crystal is detached and has high resistance. In that case it will be just as a filler of the polymer in the monograin membrane. More harmful is the case, when secondary phase is in connection with main material grain (point 2) or segregated on the surface of grains. In that case it needs to be removed by selective etchant.

In this study, the detailed chemical etching investigations were performed on the Cd-rich  $\text{Cu}_{1.95}\text{Cd}_{1.06}\text{Ge}_{0.97}\text{Se}_4$  powder. Two different combinational etching processes were applied - 1% v/v  $\text{Br}_2$ –MeOH etching followed by 10% m/m KCN etching and a 10% v/v HCl etching followed by 10% m/m KCN etching to remove the secondary phases from the surface of the absorber layer. EDX and XPS were used to investigate the surface composition of etched crystals and Raman spectroscopy was used to analyze the change in phase composition on the surface of  $\text{Cu}_{1.95}\text{Cd}_{1.06}\text{Ge}_{0.97}\text{Se}_4$  crystals.

Fig. 3a shows the SEM image of crystal surface after  $\text{Br}_2$ –MeOH etching for 5 min at RT. According to EDX analysis, the surface of crystals was covered by amorphous selenium. The surface became more

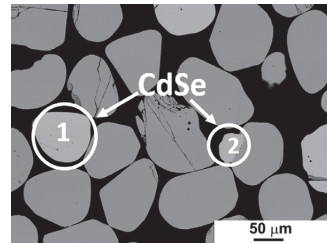


Fig. 2. SEM image of cross section of  $\text{Cu}_{2-x}\text{Cd}_y\text{GeSe}_4$  powder crystals.

Cu-rich and Cd-poor, as the ratio of  $[\text{Cu}]/([\text{Cd}] + [\text{Ge}])$  increased from 0.96 to 1.02 and the ratio of  $[\text{Cd}]/[\text{Ge}]$  decreased from 1.1 to 1.0. KCN etching restored the Cu-poor and Cd-rich surface and removed selenium from the surface. Additional annealing at 400 °C did not change the surface composition within the detection limits. In Fig. 3b is shown the SEM image of crystal surface after HCl etching for 10 min. After HCl etching, the surface of crystals was slightly Cu-rich ( $[\text{Cu}]/([\text{Cd}] + [\text{Ge}]) = 1.03$ ) and Cd-rich ( $[\text{Cd}]/[\text{Ge}] = 1.07$ ). Subsequent etching with KCN removed Cu-rich surface and restored original composition- $\text{Cu}_{1.97}\text{Cd}_{1.06}\text{Ge}_{0.98}\text{Se}_4$ .

Raman spectroscopy has emerged as a promising and feasible technique for the advanced characterization of the secondary phases at the surface. The most intensive peak in the Raman spectra of orthorhombic  $\text{Cu}_{1.95}\text{Cd}_{1.06}\text{Ge}_{0.97}\text{Se}_4$  is observed at  $203\text{ cm}^{-1}$  [19] and it is not depending on the applied chemical etchant. The additional characteristic Raman modes for the *o*- $\text{Cu}_2\text{CdGeSe}_4$  phase were detected at 163, 182, 187, 271 and  $278\text{ cm}^{-1}$  [19] (see Fig. 4a and b).

After bromine etching additional peaks appeared at 143, 233,

Table 1

The initial composition of  $\text{Cu}_{2-x}\text{Cd}_y\text{GeSe}_4$  and the powder median grain size values ( $D_{50}$ ) calculated from the weight percentage of average size of the powder crystals.

$\text{Cu}_{2-x}\text{Cd}_y\text{GeSe}_4$	$[\text{Cu}]/([\text{Cd}] + [\text{Ge}])$ in precursors	$[\text{Cd}]/[\text{Ge}]$ in precursors	$D_{50}$ ( $\mu\text{m}$ )
Powder 1: $x = 0.1; y = 1.0$	0.95	1.0	115
Powder 2: $x = 0.1; y = 1.05$	0.93	1.05	131
Powder 3: $x = 0.15; y = 1.02$	0.92	1.02	146
Powder 4: $x = 0.1; y = 1.1$	0.90	1.1	154
Powder 5: $x = 0.15; y = 1.1$	0.88	1.1	164
Powder 6: $x = 0.2; y = 1.1$	0.86	1.1	188



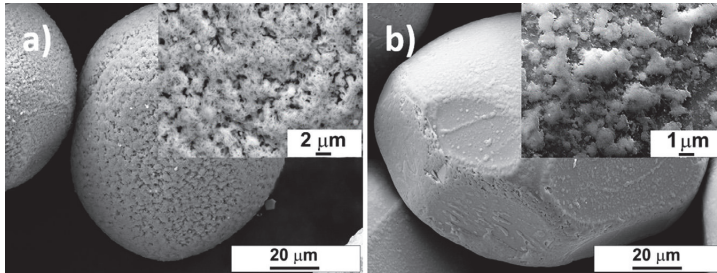


Fig. 3. SEM images of  $\text{Cu}_{1.95}\text{Cd}_{1.06}\text{Ge}_{0.97}\text{Se}_4$  crystals after a) 1%  $\text{Br}_2$ -MeOH etching for 5 min and b) 10% HCl etching for 10 min.

$237\text{ cm}^{-1}$  and  $250\text{ cm}^{-1}$ . Raman peaks at  $143$ ,  $233$  and  $237\text{ cm}^{-1}$  correspond to the trigonal Se (*t*-Se), peak at  $233\text{ cm}^{-1}$  is attributed to bond-stretching E mode and at  $237\text{ cm}^{-1}$  to symmetric bond-stretching A1 mode [35]. Weak band at  $250\text{ cm}^{-1}$  corresponds to the A1 mode of amorphous selenium [35]. After bromine etching and also after HCl etching wide band appeared around at  $300$ – $350\text{ cm}^{-1}$ . The latter band was even stronger after annealing at  $400\text{ }^\circ\text{C}$ . This could be assigned to GeSe or  $\text{GeSe}_2$  phase. XPS analysis was used to confirm this assumption. Fig. 5 shows the Ge 3d and Se 3d core-level spectra for  $\text{Cu}_2\text{CdGeSe}_4$  after annealing at  $400\text{ }^\circ\text{C}$  and after additional KCN etching. All measured XPS spectra were charge corrected based on the standard reference signal from C 1 s ( $284.6\text{ eV}$ ). The Ge 3d core-level spectrum exhibits two doublet peaks with main peak ( $3d_{5/2}$ ) centered at  $30.3\text{ eV}$  belonging to  $\text{Ge}^{\text{IV}}$  (possible  $\text{Cu}_2\text{CdGeSe}_4$  phase) and at  $30.8\text{ eV}$  belong to  $\text{Ge}^{\text{II}}$  (possible GeSe phase) both with duplet separation set to  $0.58\text{ eV}$  [36–38]. The Se 3d core-level spectrum of the surface of annealed  $\text{Cu}_2\text{CdGeSe}_4$  exhibit also two doublets with main peak ( $3d_{5/2}$ ) binding energies centered at  $53.8\text{ eV}$  and  $54.7\text{ eV}$ . The first one belongs to  $\text{Se}^{\text{II}}$  in  $\text{Cu}_2\text{CdGeSe}_4$  and the second belongs to  $\text{Ge}_3\text{Se}_{1-x}$  [39]. After KCN etching, in the Ge 3d core-level spectrum only one doublet with main peak located at the same energy  $30.3\text{ eV}$  remains. The second doublet at higher binding energy is considerably suppressed. The reduction of GeSe signal accompanies also in the Se 3d core-level spectrum, where the intense doublet with main peak located at  $53.9\text{ eV}$  is remained.

### 3.3. Impacts of the chemical etchings and annealing conditions on the solar cells performances

The influence of the surface chemical etching and the annealing conditions on the optoelectronic properties of solar cells were investigated. In Fig. 6, the output parameters of monograin layer solar cells fabricated from *o*- $\text{Cu}_{1.95}\text{Cd}_{1.06}\text{Ge}_{0.97}\text{Se}_4$  powder that was etched with different chemical solutions followed by annealing at  $400\text{ }^\circ\text{C}$  for 1 hour are displayed as box plots. Results show that all used chemical etchants are beneficial to improve solar cell performance. All etchants improved the values of open circuit voltage about  $150\text{ mV}$ . The largest improvement on the optoelectronic parameters is achieved by HCl-etching followed by KCN-etching, giving conversion efficiency of  $3.82\%$ . The efficiency improvement is mainly due to increased values of current density ( $J_{\text{SC}}$ ) from  $11.5$  to  $21.3\text{ mA/cm}^2$ .

For the investigation of the effect of post-annealing temperature,  $\text{Br}_2$ -MeOH/KCN complex etching was used for nearly stoichiometric  $\text{Cu}_2\text{Cd}_{1.03}\text{Ge}_{1.02}\text{Se}_4$  powder and subsequently the powder was annealed at different temperatures for 1 h in closed ampoules. The output parameters of monograin layer solar cells based on differently annealed powders are presented as box plot in Fig. 7. Note that these parameters were obtained with an additional short time (30 s) chemical etching with KCN solution prior to CdS buffer layer deposition. It was applied due to the formation of GeSe phase on the crystals surface after annealing. As Raman and XPS analysis confirmed, this phase was removed

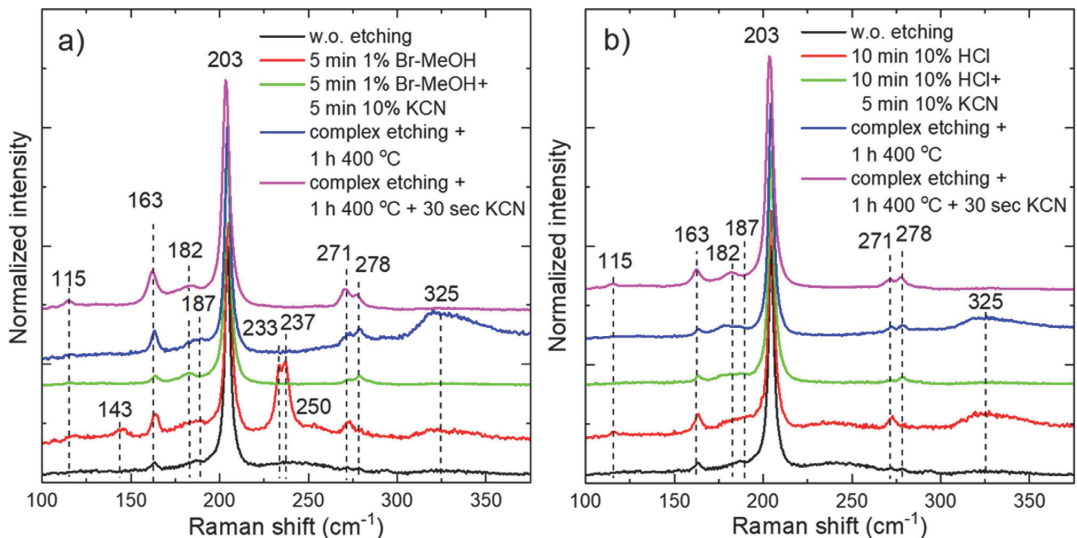


Fig. 4. RT Raman spectra of *o*- $\text{Cu}_{1.95}\text{Cd}_{1.06}\text{Ge}_{0.97}\text{Se}_4$  powders a) without etching and after different combinations of bromine and KCN etchings and annealing at  $400\text{ }^\circ\text{C}$  and b) without etching and after different combinations of HCl and KCN etchings and annealing at  $400\text{ }^\circ\text{C}$ .

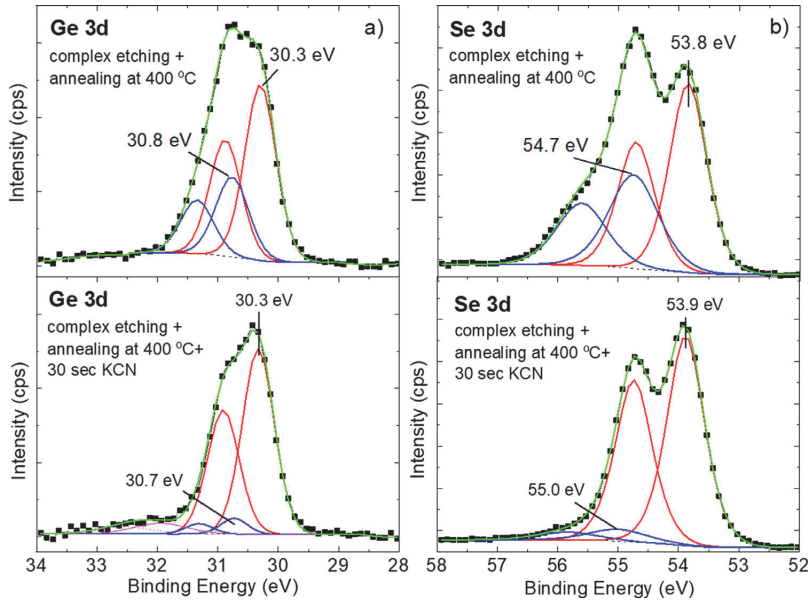


Fig. 5. XPS spectra of a) Ge 3d and b) Se 3d for surface of  $\text{Cu}_2\text{CdGeSe}_4$  after annealing at 400 °C and after additional KCN etching.

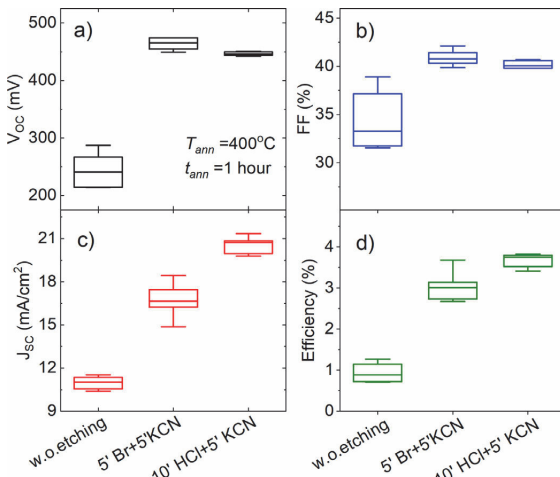


Fig. 6. Box plot of a) open circuit voltage; b) fill factor; c) current density and d) efficiency of monograin layer solar cells fabricated from  $\text{Cu}_{1.95}\text{Cd}_{1.06}\text{Ge}_{0.97}\text{Se}_4$  powder that was etched with different chemical solutions followed by annealing at 400 °C for 1 h.

by short time KCN etching. The values of  $V_{OC}$  increased from 473 to 515 mV by increasing the annealing temperature from 300 to 450 °C. The value of fill factor ( $FF$ ) reaches its maximum (51%) at 400 °C and decreases again at higher annealing temperatures. The similar trend was observed for  $J_{SC}$  values, the values were increased up to 400 °C and then started to decrease. After annealing the powder over 450 °C, the decrease in the values of output parameters could be caused by decomposition of absorber material surface. The largest improvement on the optoelectronic parameters is achieved by annealing absorber powder at 400 °C for 1 hour, giving conversion efficiency of 5.69% with the following parameters:  $V_{OC} = 459$  mV;  $J_{SC} = 25.6$  mA/cm<sup>2</sup> and

$FF = 48\%$ .

#### 4. Conclusions

High quality  $\text{Cu}_2\text{CdGeSe}_4$  micro-crystalline powder have been synthesized by molten salt method and implemented as absorber material in monograin layer solar cells. A comparative investigation of the influence of different etchants such as  $\text{Br}_2 - \text{MeOH}$ , KCN and HCl followed by isothermal annealing at different temperatures on the performance of  $o\text{-Cu}_2\text{CdGeSe}_4$  monograin layer solar cells was carried out. Results showed that all used chemical etchants are beneficial to improve  $\text{Cu}_2\text{CdGeSe}_4$  solar cell efficiencies. After chemical etching of crystal surfaces, the powder needed additional annealing at 400 °C to improve the performance of  $\text{Cu}_2\text{CdGeSe}_4$  solar cells. After post-annealing is necessary to remove  $\text{Ge}_x\text{Se}_{1-x}$  phase on the surface of  $\text{Cu}_2\text{CdGeSe}_4$  by KCN solution.

The highest conversion efficiency of 5.69% was gained by using  $\text{Cu}_2\text{CdGeSe}_4$  with nearly stoichiometric composition, which was etched with  $\text{Br}_2 - \text{MeOH}/\text{KCN}$  solutions and post-annealed at 400 °C for 1 hour.

#### CRedit authorship contribution statement

X. Li: Investigation, Validation, Writing - original draft. M. Pilvet: Investigation. K. Timmo: Supervision, Writing - review & editing. M. Grossberg: Writing - review & editing, Funding acquisition. M. Danilson: Investigation, Writing - review & editing. V. Mikli: Investigation, Writing - review & editing. M. Kauk-Kuusik: Conceptualization, Supervision, Writing - review & editing, Project administration.

#### Declaration of Competing Interest

The authors declare that they have no known competing financial interests or personal relationships that could have appeared to influence the work reported in this paper.

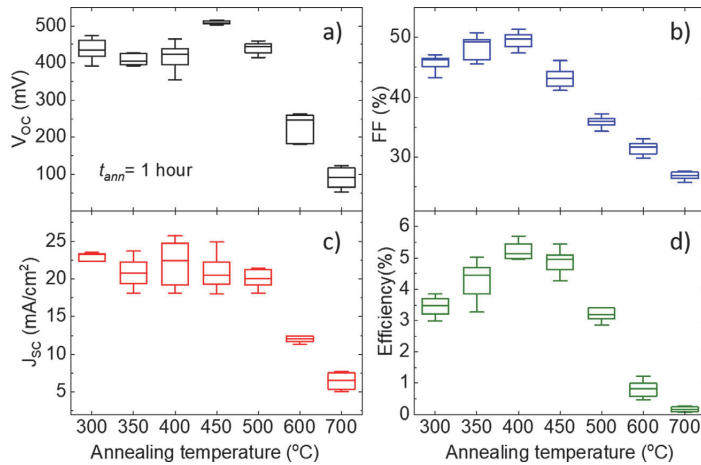


Fig. 7. Box plot of a) open circuit voltage; b) fill factor; c) current density and d) efficiency of monograin layer solar cells fabricated from  $\text{Cu}_2\text{Cd}_{1.03}\text{Ge}_{1.02}\text{Se}_4$  powder that was etched with bromine in methanol and KCN solutions followed by annealing at temperatures from 300 to 700 °C for 1 h.

## Acknowledgements

This work was supported by institutional research funding IUT19-28 of the Estonian Ministry of Education and Research, and by the European Union through the European Regional Development Fund, Project TK141.

## References

- W. Wang, M.T. Winkler, O. Gunawan, T. Gokmen, T.K. Todorov, Y. Zhu, D.B. Mitzi, Device characteristics of CZTSSe thin-film solar cells with 12.6% efficiency, *Adv. Energy Mater.* 4 (2014) 1301465, <https://doi.org/10.1002/aenm.201301465>.
- Solar Frontier, Solar frontier achieves world record thin-film solar cell efficiency of 23.35%, (2019). [http://www.solar-frontier.com/eng/news/2019/0117\\_press.html](http://www.solar-frontier.com/eng/news/2019/0117_press.html).
- W. Shockley, H.J. Queisser, Detailed balance limit of efficiency of p-n junction solar cells, *J. Appl. Phys.* 32 (1961) 510–519, <https://doi.org/10.1063/1.1736034>.
- C. Yan, K. Sun, J. Huang, S. Johnston, F. Liu, B.P. Veettil, K. Sun, A. Pu, F. Zhou, J.A. Stride, M.A. Green, X. Hao, Beyond 11% Efficient Sulfide Kesterite  $\text{Cu}_2\text{Zn}_x\text{Cd}_{1-x}\text{SnS}_4$  Solar Cell: Effects of Cadmium alloying, *ACS Energy Lett.* 2 (2017) 930–936, <https://doi.org/10.1021/acsenergylett.7b00129>.
- Z. Su, J.M.R. Tan, X. Li, X. Zeng, S.K. Batabyal, L.H. Wong, Cation substitution of solution-processed  $\text{Cu}_2\text{ZnSnS}_4$  thin film solar cell with over 9% efficiency, *Adv. Energy Mater.* 5 (2015) 1500682, <https://doi.org/10.1002/aenm.201500682>.
- M. Pilvet, M. Kauk-Kuusik, M. Altoasaar, M. Grossberg, M. Danilson, K. Timmo, A. Mere, V. Mikli, Compositionally tunable structure and optical properties of  $\text{Cu}_{1.85}(\text{Cd},\text{Zn}_{1-x})_{0.15}\text{SnS}_{4.1}$  ( $0 \leq x \leq 1$ ) monograin powders, *Thin Solid Films* 582 (2015) 180–183, <https://doi.org/10.1016/j.tsf.2014.10.091>.
- M. Grossberg, K. Timmo, T. Raadik, E. Kärber, V. Mikli, J. Krustok, Study of structural and optoelectronic properties of  $\text{Cu}_2\text{Zn}(\text{Sn}_{1-x}\text{Ge}_x)\text{Se}_4$  ( $x = 0$  to 1) alloy compounds, *Thin Solid Films* 582 (2015) 176–179, <https://doi.org/10.1016/j.tsf.2014.10.055>.
- T. Nagai, T. Shimamura, K. Tanigawa, Y. Iwamoto, H. Hamada, N. Ohta, S. Kim, H. Tampo, H. Shibata, K. Matsubara, S. Niki, N. Terada, Band alignment of the  $\text{CdS}/\text{Cu}_2\text{Zn}(\text{Sn}_{1-x}\text{Ge}_x)\text{Se}_4$  heterointerface and electronic properties at the  $\text{Cu}_2\text{Zn}(\text{Sn}_{1-x}\text{Ge}_x)\text{Se}_4$  surface:  $x = 0, 0.2, \text{ and } 0.4$ , *ACS Appl. Mater. Interfaces* 11 (2019) 4637–4648, <https://doi.org/10.1021/acami.8b19200>.
- S. Giraldo, E. Saucedo, M. Neuschitzer, F. Oliva, M. Placidi, X. Alcobé, V. Izquierdo-Roca, S. Kim, H. Tampo, H. Shibata, A. Pérez-Rodríguez, P. Pistor, How small amounts of Ge modify the formation pathways and crystallization of kesterites, *Energy Environ. Sci.* 11 (2018) 582–593, <https://doi.org/10.1039/C7EE02318A>.
- S. Kim, K.M. Kim, H. Tampo, H. Shibata, S. Niki, Improvement of voltage deficit of Ge-incorporated kesterite solar cell with 12.3% conversion efficiency, *Appl. Phys. Express* 9 (2016) 102301, <https://doi.org/10.7567/APEX.9.102301>.
- M. Pilvet, M. Kauk-Kuusik, M. Grossberg, T. Raadik, V. Mikli, R. Traksmaa, J. Raudoja, K. Timmo, J. Krustok, Modification of the optoelectronic properties of  $\text{Cu}_2\text{CdSnS}_4$  through low-temperature annealing, *J. Alloys Compd.* 723 (2017) 820–825, <https://doi.org/10.1016/j.jallcom.2017.06.307>.
- L. Nie, S. Liu, Y. Chai, R. Yuan, Spray pyrolysis deposition and photoresponse of  $\text{Cu}_2\text{CdSnS}_4$  thin films, *J. Anal. Appl. Pyrolysis* 112 (2015) 363–368, <https://doi.org/10.1016/j.jaap.2014.12.020>.
- Q. Zhang, H. Deng, L. Chen, J. Tao, J. Yu, P. Yang, J. Chu, Effects of sulfurization temperature on the structural and optical properties of  $\text{Cu}_2\text{CdSnS}_4$  thin films prepared by direct liquid method, *Mater. Lett.* 193 (2017) 206–209, <https://doi.org/10.1016/j.matlet.2017.02.002>.
- S. Sahayaraj, G. Brammertz, B. Vermang, T. Schnabel, E. Ahlswede, Z. Huang, S. Ranjbar, M. Meuris, J. Vleugels, J. Poortmans, Optoelectronic properties of thin film  $\text{Cu}_2\text{ZnGeSe}_4$  solar cells, *Sol. Energy Mater. Sol. Cells* 171 (2017) 136–141, <https://doi.org/10.1016/j.solmat.2017.06.050>.
- L. Choubrac, G. Brammertz, N. Barreau, L. Arzel, S. Harel, M. Meuris, B. Vermang, 7.6% CZGSe solar cells thanks to optimized cds chemical bath deposition, *Phys. Status Solidi* 215 (2018) 1800043, <https://doi.org/10.1002/pssa.201800043>.
- K. Nagaya, S. Fujimoto, H. Tampo, S. Kim, M. Nishiwaki, Y. Nishigaki, M. Kato, H. Shibata, H. Fujiwara, Very small tail state formation in  $\text{Cu}_2\text{ZnGeSe}_4$ , *Appl. Phys. Lett.* 113 (2018) 093901, <https://doi.org/10.1063/1.5031799>.
- K. Timmo, M. Kauk-Kuusik, M. Altoasaar, J. Raudoja, T. Raadik, M. Grossberg, T. Varema, M. Pilvet, I. Leinemann, O. Volobujeva, E. Mellikov, Novel  $\text{Cu}_2\text{CdSnS}_4$  and  $\text{Cu}_2\text{ZnGeSe}_4$  absorber materials for monograin layer solar cell application, *Proceeding of 28th EUPVSEC*, 2013, pp. 2385–2388, <https://doi.org/10.4229/28thEUPVSEC2013-3BV.6.14>.
- R. Gunder, J.A. Márquez-Prieto, G. Gurieva, T. Unold, S. Schorr, Structural characterization of off-stoichiometric kesterite-type  $\text{Cu}_2\text{ZnGeSe}_4$  compound semiconductors: from cation distribution to intrinsic point defect density, *CrystEngComm* 20 (2018) 1491–1498, <https://doi.org/10.1039/C7CE02090B>.
- M. Kauk-Kuusik, X. Li, M. Pilvet, K. Timmo, M. Grossberg, T. Raadik, M. Danilson, V. Mikli, M. Altoasaar, J. Krustok, J. Raudoja, Study of  $\text{Cu}_2\text{CdGeSe}_4$  monograin powders synthesized by molten salt method for photovoltaic applications, *Thin Solid Films* 666 (2018) 15–19, <https://doi.org/10.1016/j.tsf.2018.09.025>.
- M. Grossberg, T. Raadik, J. Krustok, M. Kauk-Kuusik, K. Timmo, R. Kaupmees, V. Mikli, A. Mere, Optical and structural properties of orthorhombic and tetragonal polymorphs of  $\text{Cu}_2\text{CdGeSe}_4$ , *Thin Solid Films* 666 (2018) 44–47, <https://doi.org/10.1016/j.tsf.2018.09.031>.
- I. Olekseyuk, L. Piskach, O. Parasyuk, O. Mel'nyk, T. Lyskovetz, The  $\text{Cu}_2\text{Se}-\text{CdSe}-\text{GeSe}_2$  system, *J. Alloys Compd.* 298 (2000) 203–212, [https://doi.org/10.1016/S0925-8388\(99\)00669-6](https://doi.org/10.1016/S0925-8388(99)00669-6).
- L. Piskach, O. Parasyuk, Y. Romanyuk, The phase equilibria in the quasi-binary  $\text{Cu}_2\text{GeSe}_3/\text{Se}_3-\text{CdS}/\text{Se}$  systems, *J. Alloys Compd.* 299 (2000) 227–231, [https://doi.org/10.1016/S0925-8388\(99\)00797-5](https://doi.org/10.1016/S0925-8388(99)00797-5).
- M. Kauk-Kuusik, M. Altoasaar, K. Muska, M. Pilvet, J. Raudoja, K. Timmo, T. Varema, M. Grossberg, E. Mellikov, O. Volobujeva, Post-growth annealing effect on the performance of  $\text{Cu}_2\text{ZnSnSe}_4$  monograin layer solar cells, *Thin Solid Films* 535 (2013) 18–21, <https://doi.org/10.1016/j.tsf.2012.11.075>.
- Y. Hashimoto, N. Kohara, T. Negami, M. Nishitani, T. Wada, Surface characterization of chemically treated  $\text{Cu}(\text{In,Ga})\text{Se}_2$  thin films, *Jpn. J. Appl. Phys.* 35 (1996) 4760–4764, <https://doi.org/10.1143/JJAP.35.4760>.
- M. Buffière, G. Brammertz, S. Sahayaraj, M. Batuk, S. Khelifi, D. Mangin, A.-A. El Mel, L. Arzel, J. Hadermann, M. Meuris, J. Poortmans, KCN chemical etch for interface engineering in  $\text{Cu}_2\text{ZnSnSe}_4$  solar cells, *ACS Appl. Mater. Interfaces* 7 (2015) 14690–14698, <https://doi.org/10.1021/acami.5b02122>.
- K. Timmo, M. Altoasaar, J. Raudoja, M. Grossberg, M. Danilson, O. Volobujeva, E. Mellikov, Chemical etching of  $\text{Cu}_2\text{ZnSn}(\text{S,Se})_4$  monograin powder, 2010 35th IEEE Photovolt. Spec. Conf. IEEE, 2010, pp. 001982–001985, <https://doi.org/10.1109/PVSC.2010.5616411>.
- M. Bär, B.-A. Schubert, B. Marsen, S. Krause, S. Pookpanratana, T. Unold, L. Weinhardt, C. Heske, H.-W. Schock, Impact of KCN etching on the chemical and electronic surface structure of  $\text{Cu}_2\text{ZnSnS}_4$  thin-film solar cell absorbers, *Appl. Phys. Lett.* 99 (2011) 152111, <https://doi.org/10.1063/1.3650717>.
- M. Mousel, A. Redinger, R. Djemour, M. Arasimowicz, N. Valle, P. Dale, S. Siebentritt, HCl and  $\text{Br}_2$ -MeOH etching of  $\text{Cu}_2\text{ZnSnSe}_4$  polycrystalline absorbers,

- Thin Solid Films 535 (2013) 83–87, <https://doi.org/10.1016/j.tsf.2012.12.095>.
- [29] A. Fairbrother, E. García-Hemme, V. Izquierdo-Roca, X. Fontané, F.A. Pulgarín-Agudelo, O. Vigil-Galán, A. Pérez-Rodríguez, E. Saucedo, Development of a selective chemical etch to improve the conversion efficiency of Zn-Rich  $\text{Cu}_2\text{ZnSnS}_4$  solar cells, *J. Am. Chem. Soc.* 134 (2012) 8018–8021, <https://doi.org/10.1021/ja301373e>.
- [30] M. Kauk-Kuusik, K. Timmo, M. Danilson, M. Altsaar, M. Grossberg, K. Ernits, p-n junction improvements of  $\text{Cu}_2\text{ZnSnS}_4/\text{CdS}$  monograin layer solar cells, *Appl. Surf. Sci.* 357 (2015) 795–798, <https://doi.org/10.1016/j.apsusc.2015.09.094>.
- [31] B. Tuck, The chemical polishing of semiconductors, *J. Mater. Sci.* 10 (1975) 321–339, <https://doi.org/10.1007/BF00540357>.
- [32] W.H. Strehlow, Chemical polishing of II-VI compounds, *J. Appl. Phys.* 40 (1969) 2928–2932, <https://doi.org/10.1063/1.1658103>.
- [33] D.R. Lide, *CRC Handbook of Chemistry and Physics*, 84th Ed., (2003).
- [34] C. Kittel, *Introduction to Solid State Physics*, eighth Ed., (2004).
- [35] V.V. Poborchii, A.V. Kolobov, K. Tanaka, An in situ Raman study of polarization-dependent photocrystallization in amorphous selenium films, *Appl. Phys. Lett.* 72 (1998) 1167–1169, <https://doi.org/10.1063/1.121002>.
- [36] J. Moulder, W. Stickle, P. Sobol, K. Bomben, *Handbook of X-ray Photoelectron Spectroscopy*, (1995), <https://doi.org/10.1002/sia.740030412>.
- [37] R.B. Shalvoy, G.B. Fisher, P.J. Stiles, Bond ionicity and structural stability of some average-valence-five materials studied by X-ray photoemission, *Phys. Rev. B.* 15 (1977) 1680–1697, <https://doi.org/10.1103/PhysRevB.15.1680>.
- [38] V.A. Ocheretova, O.V. Parasyuk, A.O. Fedorchuk, O.Y. Khyzhun, Electronic structure of  $\text{Cu}_3\text{CdGeSe}_4$  single crystal as determined from X-ray spectroscopy data, *Mater. Chem. Phys.* 160 (2015) 345–351, <https://doi.org/10.1016/j.matchemphys.2015.04.049>.
- [39] D. Jana, S. Chakrabarti, S.Z. Rahaman, S. Maikap, Resistive and new optical switching memory characteristics using thermally grown  $\text{Ge}_{0.2}\text{Se}_{0.8}$  film in Cu/GeSe<sub>x</sub>/W structure, *Nanoscale Res. Lett.* 10 (2015) 392, <https://doi.org/10.1186/s11671-015-1090-1>.



**Publication III**

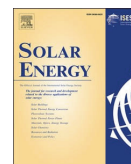
X. Li, M. Pilvet, K. Timmo, M. Grossberg, V. Mikli, M. Kauk-Kuusik, "The effect of S/Se ratio on the properties of  $\text{Cu}_2\text{CdGe}(\text{S}_x\text{Se}_{1-x})_4$  microcrystalline powders for photovoltaic applications", *Solar Energy*, Volume 209, 646–652, 2020.  
<https://doi.org/10.1016/j.solener.2020.09.045>





Contents lists available at ScienceDirect

Solar Energy

journal homepage: [www.elsevier.com/locate/solener](http://www.elsevier.com/locate/solener)

# The effect of S/Se ratio on the properties of $\text{Cu}_2\text{CdGe}(\text{S}_x\text{Se}_{1-x})_4$ microcrystalline powders for photovoltaic applications

X. Li<sup>\*</sup>, M. Pilvet, Ph.D, K. Timmo, Ph.D, M. Grossberg, Professor, V. Mikli, Ph.D, M. Kauk-Kuusik, Ph.D

Department of Materials and Environmental Technology, Tallinn University of Technology, Ehitajate tee 5, 19086 Tallinn, Estonia

## ARTICLE INFO

### Keywords:

$\text{Cu}_2\text{CdGe}(\text{S}_x\text{Se}_{1-x})_4$   
Crystal structure  
S/Se ratio  
Microcrystalline powder  
Solar cells

## ABSTRACT

The morphology, structural and compositional properties of  $\text{Cu}_2\text{CdGe}(\text{S}_x\text{Se}_{1-x})_4$  ( $x = 0; 0.05; 0.1; 0.15; 0.2; 0.4; 0.6; 0.8; 1$ ) microcrystalline powders and solar cells based on these powders are investigated by X-ray diffraction (XRD), Raman spectroscopy, scanning electron microscopy, energy dispersive X-ray spectroscopy as well as current-voltage and external quantum efficiency (EQE) methods. XRD analysis showed that all  $\text{Cu}_2\text{CdGe}(\text{S}_x\text{Se}_{1-x})_4$  solid solutions synthesized at 700 °C crystallize in orthorhombic structure (*Pmn21*) regardless of S/Se ratio.  $\text{Cu}_2\text{CdGe}(\text{S}_x\text{Se}_{1-x})_4$  solid solutions ( $x = 0; 0.05; 0.1$ ) synthesized at 500 °C have a tetragonal structure (*I-42m*).  $\text{Cu}_2\text{CdGe}(\text{S}_x\text{Se}_{1-x})_4$  solid solution with  $x = 0.15$  has a mixture of two crystal structures. Lattice parameters decrease by increasing the S-content in the solid solutions. The median crystal size decreased with the increasing S content in the  $\text{Cu}_2\text{CdGe}(\text{S}_x\text{Se}_{1-x})_4$  powders about two times.

According to EQE measurements of the solar cells, the band gap of the  $\text{Cu}_2\text{CdGe}(\text{S}_x\text{Se}_{1-x})_4$  absorber material shifted towards shorter wavelengths with increasing S content, growing from 1.27 eV for  $x = 0$  to 2.04 eV for  $x = 1$ . In this study,  $\text{Cu}_2\text{CdGe}(\text{S}_x\text{Se}_{1-x})_4$  solid solution with  $x = 0.2$  enabled the highest power conversion efficiency of 6.4% for monograin layer solar cells with parameters  $V_{OC} = 724$  mV,  $J_{SC} = 18.8$  mA/cm<sup>2</sup> and FF = 46.9%.

## 1. Introduction

The  $\text{Cu}_2\text{-II-IV-VI}_4$  compounds reveal useful properties and have been proposed as potential candidates for absorber materials in photovoltaic cells. Among quaternary chalcogenides  $\text{Cu}_2\text{ZnSn}(\text{S}_x\text{Se}_{1-x})_4$  are explored as the promising alternate absorber material to  $\text{CuIn}_x\text{Ga}_{1-x}\text{Se}_2$ . However, there are several limitations, which have been keeping the efficiencies below the level of 13% almost 6 years. For example power conversion efficiency (PCE) of devices based on pure  $\text{Cu}_2\text{ZnSnSe}_4$  have reached to 11.95% (Li et al., 2019), based on  $\text{Cu}_2\text{ZnSn}(\text{S}_x\text{Se}_{1-x})_4$  12.6% (Wang et al., 2014), based on pure sulfide  $\text{Cu}_2\text{ZnSnS}_4$  11% (Yan et al., 2018) and by Cd-alloyed CZTS solar cells have been achieved 11.73% (Sharif et al., 2020). Thus, the search for alternative materials with promising properties in the chalcogenide systems is needed. In the search for a trade-off between high performances and low processing cost,  $\text{Cu}_2\text{CdGe}(\text{S}_x\text{Se}_{1-x})_4$  has recently driven the attention of the scientific community.

Our previous studies (Grossberg et al., 2018; Kauk-Kuusik et al.,

2018) have shown that  $\text{Cu}_2\text{CdGeSe}_4$  (CCdGSe) has potential properties for single junction solar cell applications, the first monograin layer solar cells with the device structure of  $\text{ZnO}/\text{CdS}/o\text{-Cu}_2\text{CdGeSe}_4/\text{graphite}$  showed the power conversion efficiency of 5.7%. Up to now, 7.67% efficiency of the  $\text{Cu}_2\text{CdGeS}_4$  (CCdGS) solar cell has been reported (Huang et al., 2016). In their study, the highest efficiency has been achieved by manufacturing the dye-sensitized solar cells based on  $\text{Cu}_2\text{CdGeS}_4$  nanocrystals. As  $\text{Cu}_2\text{CdGeS}_4$  compound has too wide band gap for single junction solar cells, it could be used as top cell absorber material in a tandem solar cell structure. The top cell has a larger band gap and thus expands the spectral sensitivity range of a multi-junction solar cell toward higher photon energies. The band gap of  $\text{Cu}_2\text{CdGeSe}_4$  can be modified by several ways. One possibility to vary is through adjusting the chalcogenides ratio (S/Se) in the  $\text{Cu}_2\text{CdGe}(\text{S}_x\text{Se}_{1-x})_4$  solid solutions, the band gap changes in the range from 1.27 to 2.05 eV (Kauk-Kuusik et al., 2018; Krustok et al., 2020; Marushko et al., 2009). Another approach for band gap engineering would be the replacement of cations - Cd by Zn or Ge by Sn in the  $\text{Cu}_2(\text{Cd}_x\text{Zn}_{1-x})(\text{Sn}_x\text{Ge}_{1-x})\text{Se}_4$  leading to the

<sup>\*</sup> Corresponding author.

E-mail addresses: [xiaofeng.li@taltech.ee](mailto:xiaofeng.li@taltech.ee) (X. Li), [maris.pilvet@taltech.ee](mailto:maris.pilvet@taltech.ee) (M. Pilvet), [kristi.timmo@taltech.ee](mailto:kristi.timmo@taltech.ee) (K. Timmo), [maarja.grossberg@taltech.ee](mailto:maarja.grossberg@taltech.ee) (M. Grossberg), [valdek.mikli@taltech.ee](mailto:valdek.mikli@taltech.ee) (V. Mikli), [marit.kauk-kuusik@taltech.ee](mailto:marit.kauk-kuusik@taltech.ee) (M. Kauk-Kuusik).

<https://doi.org/10.1016/j.solener.2020.09.045>

Received 2 July 2020; Received in revised form 11 September 2020; Accepted 14 September 2020

Available online 24 September 2020

0038-092X/© 2020 International Solar Energy Society. Published by Elsevier Ltd. All rights reserved.



band gap energy values from 1.27 to 1.35 eV (Timmo et al., 2013) or from 1.27 to 0.96 eV (Liu et al., 2014), respectively.

The structural properties of  $\text{Cu}_2\text{CdGe}(\text{S}_x\text{Se}_{1-x})_4$  polycrystals have been investigated by (Marushko et al., 2009). There are several studies about structural properties of pure  $\text{Cu}_2\text{CdGeSe}_4$ . It was confirmed that the pure  $\text{Cu}_2\text{CdGeSe}_4$  exists in two polymorphous modifications- an orthorhombic high-temperature (HT) one with the band gap 1.27 eV and a tetragonal low-temperature (LT) modification with the band gap 1.14 eV (Gulay et al., 2002; Kauk-Kuusik et al., 2018). Transition from orthorhombic (wurtzite-stannite structure with space group  $Pmn21$ ) to tetragonal structure (stannite with space group  $I-42m$ ) in monograin powders was obtained by controlling the synthesis temperature (below 500 °C tetragonal, above 500 °C orthorhombic) or by changing the cooling rate after post-annealing process (Kauk-Kuusik et al., 2018). The pure  $\text{Cu}_2\text{CdGeSe}_4$  compound was found to crystallize only in the wurtzite-stannite structure (orthorhombic symmetry, with space group  $Pmn21$ ), with band gap  $\sim 2.0$  eV (Huang et al., 2016). According to phase diagram of the system  $\text{Cu}_2\text{CdGeS}_4\text{-Cu}_2\text{CdGeSe}_4$  (Marushko et al., 2009), it is quasi-binary below solidus and contains a continuous  $\gamma$ -solid solution series.  $\gamma$ -phase is the continuous solid solution series of isostructural compounds  $\text{Cu}_2\text{CdGeS}_4$  and HT- $\text{Cu}_2\text{CdGeSe}_4$ . Below 600 °C,  $\gamma$ -solid solutions undergo solid-state decomposition into  $\delta$ -solid solution range of  $\text{Cu}_2\text{CdGeS}_4$  and LT- $\text{Cu}_2\text{CdGeSe}_4$ . At 400 °C, the  $\gamma$ -solid solutions range from 0 to 89 mol%  $\text{Cu}_2\text{CdGeSe}_4$ , from 90 to 98 mol%  $\text{Cu}_2\text{CdGeSe}_4$  exist both - the orthorhombic symmetry typical of  $\gamma$ -solid solutions and the tetragonal symmetry characteristic of  $\delta$ -solid solution range of LT- $\text{Cu}_2\text{CdGeSe}_4$ . The extent of  $\delta$ -solid solutions was observed in the limited alloy region  $x < 0.02$  in  $\text{Cu}_2\text{CdGe}(\text{S}_x\text{Se}_{1-x})_4$ .

In the present paper we report an advanced study on the properties of solid solutions of  $\text{Cu}_2\text{CdGe}(\text{S}_x\text{Se}_{1-x})_4$  in the form of microcrystalline powders. The  $\text{Cu}_2\text{CdGe}(\text{S}_x\text{Se}_{1-x})_4$  solid solutions were synthesized by molten salt method. The effect of S/Se ratio on the crystal and phase structure, morphology and compositional properties of  $\text{Cu}_2\text{CdGe}(\text{S}_x\text{Se}_{1-x})_4$  microcrystalline powders and photovoltaic properties of  $\text{Cu}_2\text{CdGe}(\text{S}_x\text{Se}_{1-x})_4$  monograin layer solar cells is investigated.

## 2. Experimental

The commercially available CdS and CdSe powders (99.999%, Alfa Aesar), Ge powder (99.999%, Alfa Aesar), S powder (99.999%, Alfa Aesar), Se shots (99.999%, Alfa Aesar) and self-synthesized CuSe and CuS powders (made from Cu shots 99.999%, Alfa Aesar and S powder 99.999%, Alfa Aesar) were used to synthesize the  $\gamma$ -phase of  $\text{Cu}_2\text{CdGe}(\text{S}_x\text{Se}_{1-x})_4$  ( $x = 0; 0.2; 0.4; 0.6; 0.8; 1$ ) microcrystalline powders by molten salt method. The initial compositional ratios of precursor mixtures were following:  $[\text{Cu}]/([\text{Cd}] + [\text{Ge}]) = 0.92$  and  $[\text{Cd}]/[\text{Ge}] = 1.02$ . KI (99.5%, Merck) was used as a molten salt medium. Additionally, four  $\text{Cu}_2\text{CdGe}(\text{S}_x\text{Se}_{1-x})_4$  ( $x = 0; 0.05; 0.1; 0.15$ ) powders without and with small amount of sulfur were synthesized in  $\text{CdI}_2$  molten salt to produce  $\delta$ -solid solutions. These powders had stoichiometric initial composition  $-\text{[Cu]}/([\text{Cd}] + [\text{Ge}]) = 1.0$  and  $[\text{Cd}]/[\text{Ge}] = 1.0$ . Powders synthesized in  $\text{CdI}_2$  flux were used only for structural studies. The powder crystals with homogeneous composition can be obtained at temperatures higher than the melting point of the used flux salts and at temperatures lower than the melting point of the semiconductor itself (Mellikov et al., 2015). Molten salt enhances the rate of solid-state reactions. The melting temperature of KI is  $T_{\text{melt}} = 681$  °C (Lide, 2003), which makes it suitable for synthesis of  $\gamma$ -phase of  $\text{Cu}_2\text{CdGe}(\text{S}_x\text{Se}_{1-x})_4$ . The melting temperature of  $\text{CdI}_2$  is  $T_{\text{melt}} = 387$  °C (Lide, 2003) that allows to synthesize of  $\delta$ -phase of  $\text{Cu}_2\text{CdGe}(\text{S}_x\text{Se}_{1-x})_4$ .

Details of the synthesis of solid solutions are described as follows: The desired amounts and ratio of the precursors and flux material were weighted, mixed and grinded in an agate mortar using an agate pestle. The mass ratio  $m_{\text{precursors}}/m_{\text{flux}} = 1:1$  was kept throughout the series. The homogenized mixture was loaded into the quartz ampoules. The ampoules were degassed under dynamic vacuum, sealed and then placed

into a chamber furnace. Afterwards, the furnace was heated slowly at a rate of  $2^\circ/\text{min}$  to the desired temperatures of 700 °C for synthesis in KI and 500 °C for synthesis in  $\text{CdI}_2$  and then maintained for 120 h. For cooling, the ampoules were taken out from furnace into air. After opening the ampoules, the water-soluble flux salt was removed from solid powder particles by leaching with deionized  $\text{H}_2\text{O}$ . Then, the powder was dried in a hot-air thermostat at 50 °C and sieved into narrow size fractions by sieving system Retsch AS 200.

In this study, all monograin membranes were prepared from powder crystals, which were synthesized in KI at 700 °C. Before implementing the powders as absorber materials in monograin layer solar cells (MGL), combined chemical etching (remove the undesired secondary and ternary compounds in the surface of the main powder) and post annealing treatment (heal the surface imperfections generated by chemical etching) were applied. For combined chemical etching of crystal surface, the 1% v/v  $\text{Br}_2\text{-MeOH}$  and 10% m/m KCN solutions were used for 1 min. The etchings processes were performed at room temperature. After chemical etching, the powders were isothermally annealed in the sealed quartz ampoules at 740 °C for 30 min.

According to our previous research (Kauk-Kuusik et al., 2018; Li et al., 2020), the devices based on orthorhombic structured  $\text{Cu}_2\text{CdGeSe}_4$  showed better performance than devices based on tetragonal structured  $\text{Cu}_2\text{CdGeSe}_4$ . Therefore, in this study only of  $\text{Cu}_2\text{CdGe}(\text{S}_x\text{Se}_{1-x})_4$  microcrystalline powders with orthorhombic structure were used in the monograin layer solar cell structure: graphite/ $\text{Cu}_2\text{CdGe}(\text{S}_x\text{Se}_{1-x})_4/\text{CdS}/\text{ZnO}/\text{Ag-NW}$ . The absorber layer is a layer of same fraction size crystals embedded into a polymer matrix so that the upper part of the crystals remains uncovered. Prior to embedding the crystals into a polymer, the crystals are covered with a CdS buffer layer by the chemical bath deposition method. Bi-layer (*i*-ZnO and ZnO:Al) transparent front contact is deposited by RF-sputtering process. Finally, highly conductive Ag-nanowires (Ag-NWs) are applied on top of the ZnO layer. This combination benefits from the improved mechanical stability of Ag-NWs compared with brittle TCOs, which is an important aspect for flexible PVs. Finally, the structure is glued onto a durable transparent substrate. For back contacting, the bottom side of the MGL is polished to remove polymer from powder crystals and to form a  $p^+$  layer before applying graphite back contact. This type of back contact uses a  $p^+$  layer in order to facilitate hole tunneling from absorber bulk into conductive graphite.

The morphology of synthesized powder crystals was studied by high-resolution scanning electron microscope (HR-SEM Zeiss Merlin). The bulk composition of the synthesized powder crystals was analyzed by energy dispersive X-ray spectroscopy (EDX) by using the Bruker EDX-XFlash6/30 detector. Compositional analysis was made from polished individual crystals. The crystal structure of studied  $\text{Cu}_2\text{CdGe}(\text{S}_x\text{Se}_{1-x})_4$  microcrystalline powders was characterized by X-ray powder diffraction (XRD) by using a Rigaku Ultima IV diffractometer with monochromatic Cu  $K\alpha 1$  radiation ( $\lambda = 1.5406$  Å) at 40 kV and 40 mA operating with the silicon strip detector D/teX Ultra. All samples were studied in the 2 $\theta$  range of 20–60 deg. with the scan step of 0.02 deg. The phase analysis and lattice parameters calculations were made by using software on the Rigaku's system PDXL2. Phase composition of powders was analyzed by room temperature micro-Raman spectroscopy. Raman measurements were carried out using a Horiba LabRAM HR800 micro-Raman system equipped with a cooled multichannel CCD detection system in the backscattering configuration with a spectral resolution better than  $1\text{ cm}^{-1}$ . A YAG: Nd laser (wavelength  $\lambda = 532$  nm) was used for excitation. The laser spot size was about 2  $\mu\text{m}$  in diameter.

Photovoltaic properties of monograin layer solar cells were characterized by *J-V* measurements under AM 1.5G (100  $\text{mW}/\text{cm}^2$ ) using a Newport Class AAA solar simulator system. *J-V* characteristics were recorded by a Keithley 2400 source meter. A typical solar cell had an active area around 75% of the total area (Neubauer et al., 2017; Timmo et al., 2019), the MGL solar cell efficiency values were re-calculated for the active area. External quantum efficiency (EQE) measurements were performed in the spectral region of 350–1235 nm using a computer

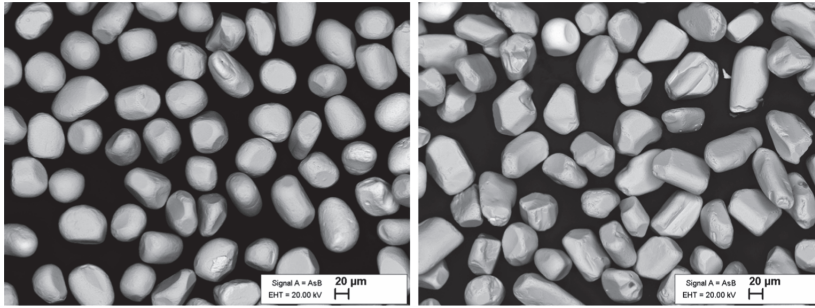


Fig. 1. SEM images of monograin powders of  $\text{Cu}_2\text{CdGeSe}_4$  (left) and  $\text{Cu}_2\text{CdGeS}_4$  (right) (fraction size 45–56  $\mu\text{m}$ ).

controlled SPM-2 prism monochromator. The generated photocurrent was detected at 0 V bias voltage at RT by using a 250 W halogen lamp.

### 3. Results

#### 3.1. Morphology and composition of $\text{Cu}_2\text{CdGe}(\text{S}_x\text{Se}_{1-x})_4$ monograin powders

In the Fig. 1 the SEM images of  $\text{Cu}_2\text{CdGeSe}_4$  and  $\text{Cu}_2\text{CdGeS}_4$  powder crystals are shown. With the increasing S content in the  $\text{Cu}_2\text{CdGe}(\text{S}_x\text{Se}_{1-x})_4$  solid solutions, the formed crystals with round shape and smooth surface planes changed to more irregular shape. The median grain size ( $D_{50}$ ) of the powders decreased with the increasing S content in the  $\text{Cu}_2\text{CdGe}(\text{S}_x\text{Se}_{1-x})_4$  powder, being  $D_{50} = 143 \mu\text{m}$  for the  $\text{Cu}_2\text{CdGeSe}_4$  powder and  $D_{50} = 85 \mu\text{m}$  for  $\text{Cu}_2\text{CdGeS}_4$ . Therefore, it was found that selenide powder crystals grow almost two times larger than sulfide powder crystals under the same synthesis conditions. This could be attributed to the existence of elemental selenium in the precursor mixture at temperature below melting point of salt that could act as sintering agent. For example, at low temperatures forms  $\text{CuSe}_2$ , which decomposes into CuSe and Se at  $\sim 330^\circ\text{C}$ . At  $380^\circ\text{C}$ , CuSe decomposes into  $\text{Cu}_{2-x}\text{Se}$  and liquid Se. In the sulfide system, all metals precursors react with sulfur much lower temperature and do not release free sulfur at higher temperature. Similar phenomenon about crystal sizes is also observed for thin films with different ratio of S/Se (Son et al., 2019). More detailed description of the median particle size calculation method is presented in (Kauk-Kuusik et al., 2018).

The elemental composition of the bulk of the  $\text{Cu}_2\text{CdGe}(\text{S}_x\text{Se}_{1-x})_4$  microcrystals was determined by EDX analysis and is presented in Table 1. It was found that the increasing S content in the precursor's mixture increased the Cu content in the powder from 24.6 at% ( $x = 0$ ) to 25.6 at% ( $x = 1$ ). The ratio of  $[\text{S}]/([\text{S}] + [\text{Se}])$  and slightly Cd-rich composition ( $\text{Cd}/\text{Ge} \geq 1.02$ ) in precursor's mixture was nearly the same in all powders, which were synthesized in KI at  $700^\circ\text{C}$ . The

powders synthesized in  $\text{CdI}_2$  at  $500^\circ\text{C}$  with  $x = 0$ –0.15 had Cd-rich composition ( $[\text{Cd}]/[\text{Ge}] > 1.1$ ) and the ratio of  $[\text{S}]/([\text{S}] + [\text{Se}])$  in the powders was slightly higher than in precursor's mixture.

#### 3.2. Structural properties of $\text{Cu}_2\text{CdGe}(\text{S}_x\text{Se}_{1-x})_4$ solid solutions

The crystal structure and phase composition of the synthesized  $\text{Cu}_2\text{CdGe}(\text{S}_x\text{Se}_{1-x})_4$  powders with different S/Se ratios was investigated by XRD. Fig. 2a shows the XRD patterns of microcrystalline powders of  $\text{Cu}_2\text{CdGe}(\text{S}_x\text{Se}_{1-x})_4$  solid solutions synthesized in KI at  $700^\circ\text{C}$ . The major diffraction peaks are indexed as corresponding to the (210), (020), (002), (211), (203), (213) and (040) planes of orthorhombic phase of  $\text{Cu}_2\text{CdGeS}_4$  (ICDD (PDF-2 Release 2019 RDB), 00-043-1387) and  $\text{Cu}_2\text{CdGeSe}_4$  (ICDD (PDF-2 Release 2019 RDB), 01-074-3115). The position of most intensive diffraction peak (020) shifts from  $25.88^\circ$  deg (for  $\text{Cu}_2\text{CdGeSe}_4$ ) to  $27.19^\circ$  deg (for  $\text{Cu}_2\text{CdGeS}_4$ ) as shown in Fig. 2b.

Minor amount of secondary phases like CdS, CdSe or Cd(S,Se) with additional diffraction peaks were detected in the all solid solutions. Using the XRD patterns, the values of lattice parameters ( $a$ ,  $b$  and  $c$ ) for all the powders were calculated. A linear decrease of the lattice parameter values ( $a$  from  $8.064 \text{ \AA}$  to  $7.705 \text{ \AA}$ ;  $b$  from  $6.882 \text{ \AA}$  to  $6.556 \text{ \AA}$  and  $c$  from  $6.604 \text{ \AA}$  to  $6.301 \text{ \AA}$ ) was observed upon replacement of selenium with sulfur due to the smaller atom radius of S compared to Se. This structural linearity is shown in Fig. 3. This behavior strictly follows Vegard's empirical heuristic law, which states that at the same temperature the lattice parameter of a solid solution of two materials with the same crystal structure can be approximated by an equation of the two constituents' lattice parameters (Denton and Ashcroft, 1991).

In order to confirm the existent limits of a tetragonal structure in  $\text{Cu}_2\text{CdGe}(\text{S}_x\text{Se}_{1-x})_4$  with low concentration of sulphur, as reported in (Marushko et al., 2009), the microcrystalline powders of  $\text{Cu}_2\text{CdGe}(\text{S}_x\text{Se}_{1-x})_4$  solid solutions ( $x = 0$  to  $x = 0.15$ ) synthesized at  $500^\circ\text{C}$  were analyzed by XRD (Fig. 4). According to this study,  $\text{Cu}_2\text{CdGeSe}_4$  ( $x = 0$ ) and  $\text{Cu}_2\text{CdGe}(\text{S}_x\text{Se}_{1-x})_4$  solid solutions ( $x = 0.05$ ;  $0.1$ ) had a tetragonal

Table 1  
Bulk composition of  $\text{Cu}_2\text{CdGe}(\text{S}_x\text{Se}_{1-x})_4$  microcrystalline powders by EDX analysis.

$x = [\text{S}]/([\text{S}] + [\text{Se}])$ in precursor	$T_{\text{synth}}$ , $^\circ\text{C}$	Bulk composition of powders by EDX								
		$[\text{S}]/([\text{S}] + [\text{Se}])$	Cu, at %	Cd, at %	Ge, at %	Se, at %	S, at %	$[\text{Cu}]/[\text{Ge}]$	$[\text{Cd}]/[\text{Ge}]$	$[\text{Cu}]/([\text{Cd}] + [\text{Ge}])$
0	700	0	24.6	13.5	11.7	50.0	–	2.10	1.15	0.98
0.2		0.21	24.4	12.4	11.8	39.4	10.6	2.07	1.05	1.0
0.4		0.39	24.8	12.7	12.0	30.3	19.7	2.07	1.06	1.0
0.6		0.60	25.2	12.2	12.0	19.9	30.1	2.10	1.02	1.04
0.8		0.80	25.2	12.6	12.1	10.0	40.0	2.08	1.04	1.02
1		1	25.6	12.5	11.9	–	50.0	2.15	1.05	1.04
0	500	0	24.9	13.0	12.6	50.0	–	1.98	1.03	0.97
0.05		0.07	25.1	13.8	11.6	46.6	3.4	2.16	1.19	0.95
0.1		0.12	25.5	13.2	11.7	44.0	6.0	2.18	1.13	1.02
0.15		0.23	25.3	13.2	11.7	38.6	11.3	2.16	1.13	1.02

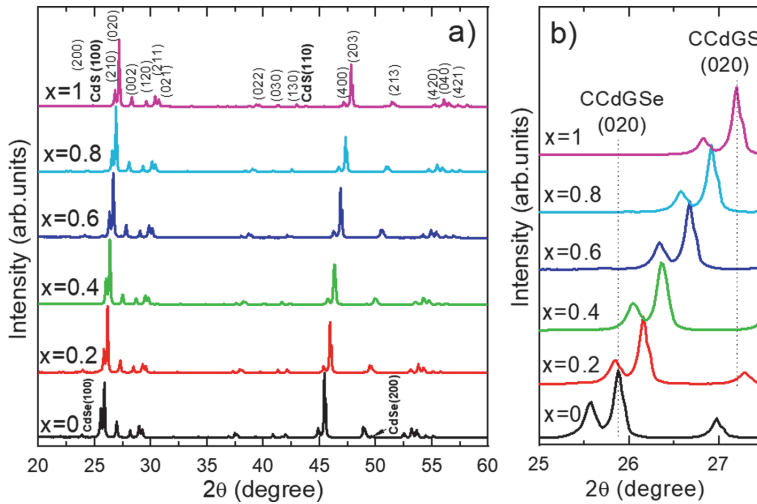


Fig. 2. a) XRD patterns of microcrystalline powders of  $\text{Cu}_2\text{CdGe}(\text{S}, \text{Se})_4$  solid solutions synthesized at 700 °C; b) magnified view of (020) diffraction peak.

structure ( $I-42m$ ) with lattice parameters presented in Table 2.  $\text{Cu}_2\text{CdGe}(\text{S}_x\text{Se}_{1-x})_4$  powder with  $x = 0.15$  contains about 79% of  $\text{Cu}_2\text{CdGe}(\text{S}_x\text{Se}_{1-x})_4$  with an orthorhombic structure ( $Pmn2_1$ ) with lattice parameters  $a = 7.994 \text{ \AA}$ ,  $b = 6.809 \text{ \AA}$ ,  $c = 6.534 \text{ \AA}$ , and about 18% of  $\text{Cu}_2\text{CdGe}(\text{S}_x\text{Se}_{1-x})_4$  with a tetragonal structure ( $I-42m$ ) with lattice parameters  $a = b = 5.697 \text{ \AA}$ ,  $c = 10.943 \text{ \AA}$ .  $\text{Cu}_2\text{CdGe}(\text{S}_x\text{Se}_{1-x})_4$  solid solutions with  $x = 0.2$  crystallize in the orthorhombic structure regardless of the synthesis temperature.

The substitution of Se with the smaller S atoms leads to the contraction of the unit cell (see Table 2). Since not only the size but also the electronic structures of S and Se are different, in addition to the change of the lattice parameters, changes in electronic structure are also expected.

### 3.3. Raman analysis of $\text{Cu}_2\text{CdGe}(\text{S}_x\text{Se}_{1-x})_4$ microcrystalline powders

The dependence of the Raman spectra on the anion composition of

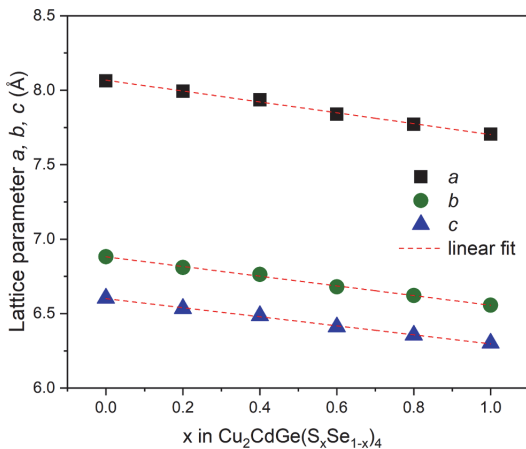


Fig. 3. Lattice parameters  $a$ ,  $b$  and  $c$  as a function of S content in the orthorhombic  $\text{Cu}_2\text{CdGe}(\text{S}_x\text{Se}_{1-x})_4$  solid solutions synthesized at 700 °C.

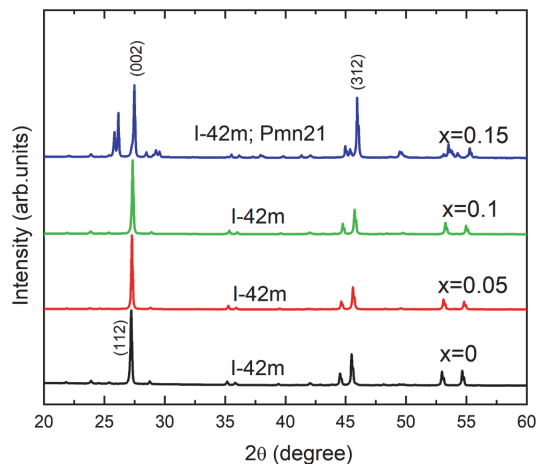


Fig. 4. XRD patterns of monograin powders of  $\text{Cu}_2\text{CdGe}(\text{S}_x\text{Se}_{1-x})_4$  solid solutions synthesized at 500 °C.

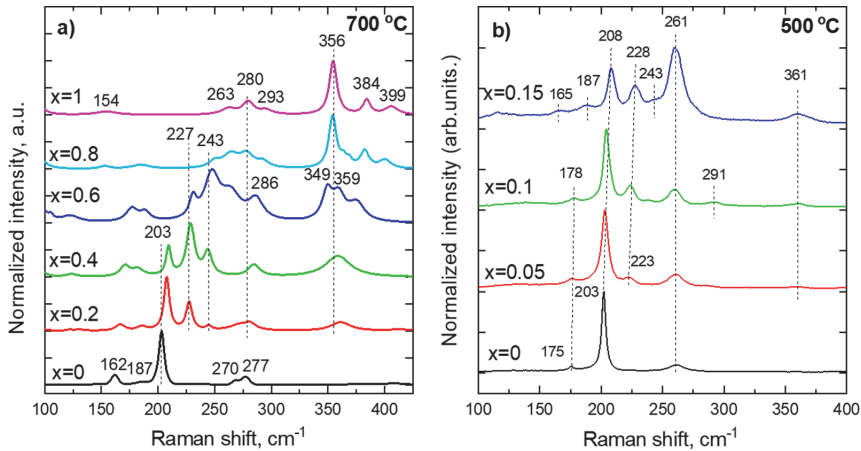


Fig. 5. Room-temperature Raman spectra of  $\text{Cu}_2\text{CdGe}(\text{S}_x\text{Se}_{1-x})_4$  solid solutions synthesized a) at 700 °C and b) at 500 °C.

the orthorhombic structured  $\text{Cu}_2\text{CdGe}(\text{S}_x\text{Se}_{1-x})_4$  solid solutions is presented in Fig. 5a. Fig. 5b shows the Raman spectra of  $\text{Cu}_2\text{CdGe}(\text{S}_x\text{Se}_{1-x})_4$  solid solutions with tetragonal structure. The  $A_1$  Raman peak of pure  $\text{CCdGSe}$  is at  $203 \text{ cm}^{-1}$  and it is not depending on the crystal structure. The additional characteristic Raman modes for orthorhombic  $\text{CCdGSe}$  were detected at  $162, 185, 270$  and  $277 \text{ cm}^{-1}$  (Kauk-Kuusik et al., 2018).  $\text{CCdGSe}$  with tetragonal structure has additional characteristic Raman modes at  $175$  and  $261 \text{ cm}^{-1}$  (Kauk-Kuusik et al., 2018).

The main Raman mode  $A_1$  for pure  $\text{CCdGS}$  is at  $356 \text{ cm}^{-1}$  (Krustok

et al., 2020). Other Raman peaks of  $\text{CCdGS}$  were detected at  $154, 263, 280, 293, 337, 384$  and  $388 \text{ cm}^{-1}$ , which are in good correlation with previously reported vibrational modes in  $\text{CCdGS}$  (Krustok et al., 2020; Litvinchuk et al., 2014).

The spectra of  $\text{Cu}_2\text{CdGe}(\text{S}_x\text{Se}_{1-x})_4$  solid solutions with S composition values ( $x = 0.2, 0.4, 0.6$  and  $0.8$ ) indicated the peaks of two  $A_1$  mode because of the co-existence of S and Se atoms in powders.

The spectra of  $\text{Cu}_2\text{CdGe}(\text{S}_x\text{Se}_{1-x})_4$  solid solutions with low S composition values ( $x = 0.05, 0.1$  and  $0.15$ ) showed clear shift of  $A_1$  mode toward the high frequency region (from  $203$  to  $208 \text{ cm}^{-1}$ ) to being proportional to the increasing of S composition (Fig. 5b). Additional peaks at  $223$  and  $361 \text{ cm}^{-1}$  were detected already for  $\text{Cu}_2\text{CdGe}$

Table 2  
The lattice parameters of the  $\text{Cu}_2\text{CdGe}(\text{S}_x\text{Se}_{1-x})_4$  solid solutions.

x in $\text{Cu}_2\text{CdGe}(\text{S}_x\text{Se}_{1-x})_4$	$T_{\text{synth}}$ , °C	a, Å	b, Å	c, Å	$V$ , Å <sup>3</sup>	Space group
0	700	8.064	6.882	6.604	366.47	$Pmn2_1$
0.2		7.994	6.810	6.534	355.77	$Pmn2_1$
0.4		7.935	6.762	6.486	348.06	$Pmn2_1$
0.6		7.839	6.680	6.410	335.67	$Pmn2_1$
0.8		7.772	6.622	6.355	327.07	$Pmn2_1$
1		7.705	6.556	6.301	318.33	$Pmn2_1$
0	500	5.747	5.747	11.051	365.08	$I-42m$
0.05		5.739	5.739	11.033	363.38	$I-42m$
0.1		5.721	5.721	10.994	359.81	$I-42m$
0.15		5.697	5.697	10.943	355.17	$I-42m$
		7.994	6.809	6.534	355.72	$Pmn2_1$
					(18%)	
					355.72	
					(79%)	

Table 3  
Summary of device parameters for the best performing  $\text{Cu}_2\text{CdGe}(\text{S}_x\text{Se}_{1-x})_4$  MGL solar cells depending on Se replacement with S in absorber materials.

x = [S]/([S] + [Se]) in precursors	$V_{oc}$ (mV)	FF (%)	$J_{sc}$ (mA/cm <sup>2</sup> )	Eff. (%) (active area)	$E_g^*$ (eV)
0	429	48.2	24.9	5.2	1.27
0.2	724	46.9	18.8	6.4	1.45
0.4	564	42.9	16.8	4.0	1.61
0.6	542	46.3	6.7	1.7	1.75
0.8	823	34.4	8.5	2.4	1.88
1	712	34.8	5.7	1.5	2.04

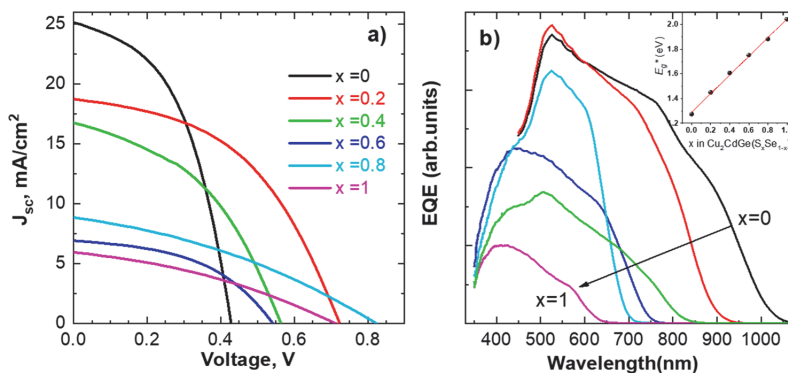


Fig. 6. a) J-V curves and b) EQE curves of  $\text{Cu}_2\text{CdGe}(\text{S}_x\text{Se}_{1-x})_4$  device with different S/Se ratios.



(S<sub>x</sub>Se<sub>1-x</sub>)<sub>4</sub> solid solutions with  $x = 0.05$ . The Raman mode at  $223\text{ cm}^{-1}$  shifted to the high frequency at  $228\text{ cm}^{-1}$ . The same peak exists in orthorhombic structured Cu<sub>2</sub>CdGe(S<sub>x</sub>Se<sub>1-x</sub>)<sub>4</sub> solid solutions.

#### 3.4. Cu<sub>2</sub>CdGe(S<sub>x</sub>Se<sub>1-x</sub>)<sub>4</sub> monograin layer solar cell performances

All orthorhombic structured Cu<sub>2</sub>CdGe(S<sub>x</sub>Se<sub>1-x</sub>)<sub>4</sub> powders with different S/Se ratio were used as absorber materials in the monograin layer solar cell structures. Photovoltaic properties of the monograin layer solar cells were characterized by  $J$ - $V$  measurements (Fig. 6a). The open circuit voltage ( $V_{OC}$ ) of Cu<sub>2</sub>CdGe(S<sub>x</sub>Se<sub>1-x</sub>)<sub>4</sub> monograin layer solar cells increased with increasing the sulfur content in the Cu<sub>2</sub>CdGe(S<sub>x</sub>Se<sub>1-x</sub>)<sub>4</sub> powders. An increase of the open circuit voltage values indicates to the widening of the band gap of Cu<sub>2</sub>CdGe(S<sub>x</sub>Se<sub>1-x</sub>)<sub>4</sub> with increase in S concentration. Although the values of  $V_{OC}$  are not increasing as expected due to increased band gap values. There are several reasons why real values are not achieved: either the recombination in the bulk increases with a higher S/Se ratio or the band alignment with the CdS buffer becomes worse, increasing detrimental interface recombination. The short circuit current density ( $J_{SC}$ ) of Cu<sub>2</sub>CdGe(S<sub>x</sub>Se<sub>1-x</sub>)<sub>4</sub> MGL solar cells decreased from  $24.9\text{ mA/cm}^2$  ( $x = 0$ ) to  $5.7\text{ mA/cm}^2$  ( $x = 1$ ), going from low to high S-content. As confirmed by EQE measurements, the increased S-content results in an increase of the band gap; thus the  $J_{SC}$  decrease is the result of less absorption. The Cu<sub>2</sub>CdGe(S<sub>x</sub>Se<sub>1-x</sub>)<sub>4</sub> solid solution with  $x = 0.2$  gave the best solar cell with parameters:  $V_{OC} = 724\text{ mV}$ ,  $J_{SC} = 18.8\text{ mA/cm}^2$ ,  $FF = 46.9\%$ ,  $\eta = 6.4\%$  (active area) (Table. 3).

The preparation of monograin layer solar cells contain many steps, which need to be optimized for each composition of Cu<sub>2</sub>CdGe(S<sub>x</sub>Se<sub>1-x</sub>)<sub>4</sub> absorber material- chemical etching and post-annealing of absorber material, selection of buffer layer etc. Therefore, all these steps need further study to improve the performance of Cu<sub>2</sub>CdGe(S<sub>x</sub>Se<sub>1-x</sub>)<sub>4</sub> solar cells with different S/Se ratio.

The external quantum efficiency (EQE) spectrum was used to study the spectral response of the Cu<sub>2</sub>CdGe(S<sub>x</sub>Se<sub>1-x</sub>)<sub>4</sub> monograin layer solar cells. Fig. 6b shows the EQE spectra of Cu<sub>2</sub>CdGe(S<sub>x</sub>Se<sub>1-x</sub>)<sub>4</sub> monograin solar cells. The absorption edge shifts to shorter wavelengths and the change of spectral response in the short wavelengths is visible with increase in S content in the absorber material. The effective band gap ( $E_g^*$ ) of Cu<sub>2</sub>CdGe(S<sub>x</sub>Se<sub>1-x</sub>)<sub>4</sub> solid solutions was evaluated from the linear segment of the low-energy side of the construction (EQE)<sup>\*</sup> vs. E curves. Inset graph in Fig. 6 shows the  $E_g^*$  values of Cu<sub>2</sub>CdGe(S<sub>x</sub>Se<sub>1-x</sub>)<sub>4</sub> solid solutions depending on the ratios of S/Se. An increase of  $E_g^*$  from 1.27 eV to 2.04 eV by increasing S content in Cu<sub>2</sub>CdGe(S<sub>x</sub>Se<sub>1-x</sub>)<sub>4</sub> microcrystalline powder materials was observed (Table 3).

#### 4. Conclusions

A continuous Cu<sub>2</sub>CdGe(S<sub>x</sub>Se<sub>1-x</sub>)<sub>4</sub> solid solution series of microcrystalline powders have been synthesized by molten salt method for different photovoltaic applications. Structural study by Raman and X-ray diffraction showed that all Cu<sub>2</sub>CdGe(S<sub>x</sub>Se<sub>1-x</sub>)<sub>4</sub> solid solutions synthesized at  $700\text{ }^\circ\text{C}$  crystallize in orthorhombic structure and solid solutions synthesized at  $500\text{ }^\circ\text{C}$  have only tetragonal structure in the range  $x = 0$  to  $x = 0.1$ . Cu<sub>2</sub>CdGe(S<sub>x</sub>Se<sub>1-x</sub>)<sub>4</sub> solid solutions with  $x = 0.15$  synthesized at  $500\text{ }^\circ\text{C}$  contain mixture of orthorhombic and tetragonal phases. Lattice parameters decrease linearly by increasing the S- content in the Cu<sub>2</sub>CdGe(S<sub>x</sub>Se<sub>1-x</sub>)<sub>4</sub> solid solutions. The median crystal size decreased with the increasing S content in the Cu<sub>2</sub>CdGe(S<sub>x</sub>Se<sub>1-x</sub>)<sub>4</sub> powders almost two times.

The increasing sulfur content in the orthorhombic Cu<sub>2</sub>CdGe(S<sub>x</sub>Se<sub>1-x</sub>)<sub>4</sub> solid solutions of microcrystalline powders led to an increase in the effective band gap energy from 1.27 eV to 2.04 eV. Therefore Cu<sub>2</sub>CdGe(S<sub>x</sub>Se<sub>1-x</sub>)<sub>4</sub> solid solutions with  $x = 0-0.2$  could be used as absorber materials for single junction solar cells and compounds with  $x > 0.2$  could be used as top cell absorber materials in a tandem solar cell structure due to too wide band gap ( $E_g > 1.6\text{ eV}$ ).

The highest power conversion efficiency of 6.4% for monograin layer solar cells have been achieved by Cu<sub>2</sub>CdGe(S<sub>x</sub>Se<sub>1-x</sub>)<sub>4</sub> solid solution with  $x = 0.2$  showing the parameters:  $V_{OC} = 724\text{ mV}$ ,  $J_{SC} = 18.8\text{ mA/cm}^2$  and  $FF = 46.9\%$ .

#### Declaration of Competing Interest

The authors declare that they have no known competing financial interests or personal relationships that could have appeared to influence the work reported in this paper.

#### Acknowledgments

This work was supported by the institutional research funding IUT19-28 of the Estonian Ministry of Education and Research and by the European Union through the European Regional Development Fund, Project TK141. This research has been funded by the EU Horizon 2020 Project CUSTOM-ART, Grant No. 952982. The authors thank Dr. Mati Danilson for assistance with EQE measurements. M. Grossberg is thankful to the L'Oréal Baltic for Women in Science Programme.

#### References

- Denton, A.R., Ashcroft, N.W., 1991. Vegard's law. *Phys. Rev. A* 43, 3161–3164. <https://doi.org/10.1103/PhysRevA.43.3161>.
- Grossberg, M., Raadik, T., Krustok, J., Kauk-Kuusik, M., Timmo, K., Kaupmees, R., Mikli, V., Mere, A., 2018. Optical and structural properties of orthorhombic and tetragonal polymorphs of Cu<sub>2</sub>CdGeSe<sub>4</sub>. *Thin Solid Films*. <https://doi.org/10.1016/j.tsf.2018.09.031>.
- Gulay, L.D., Romanyuk, Y.E., Parasyuk, O.V., 2002. Crystal structures of low- and high-temperature modifications of Cu<sub>2</sub>CdGeSe<sub>4</sub>. *J. Alloy. Compd.* [https://doi.org/10.1016/S0925-8388\(02\)00790-9](https://doi.org/10.1016/S0925-8388(02)00790-9).
- Huang, S., Zai, J., Ma, D., He, Q., Liu, Y., Qiao, Q., Qian, X., 2016. Colloidal synthesis of wurtzite-stannite Cu<sub>2</sub>CdGeS<sub>4</sub> nanocrystals with high catalytic activity toward iodine redox couples in dye-sensitized solar cells. *Chem. Commun.* <https://doi.org/10.1039/c6cc05163d>.
- Kauk-Kuusik, M., Li, X., Pilvet, M., Timmo, K., Grossberg, M., Raadik, T., Danilson, M., Mikli, V., Altsaar, M., Krustok, J., Raudoja, J., 2018. Study of Cu<sub>2</sub>CdGeSe<sub>4</sub> monograin powders synthesized by molten salt method for photovoltaic applications. *Thin Solid Films* 666, 15–19. <https://doi.org/10.1016/j.tsf.2018.09.025>.
- Krustok, J., Raadik, T., Li, X., Kauk-Kuusik, M., Timmo, K., Oueslati, S., Grossberg, M., 2020. Study of point defects in wide-bandgap Cu<sub>2</sub>CdGeS<sub>4</sub> microcrystals by temperature and laser power dependent photoluminescence spectroscopy. *J. Phys. D Appl. Phys.* <https://doi.org/10.1088/1361-6463/ab83c1>.
- Li, X., Pilvet, M., Timmo, K., Grossberg, M., Danilson, M., Mikli, V., Kauk-Kuusik, M., 2020. Effect of absorber surface modification on the optoelectronic properties of Cu<sub>2</sub>CdGeSe<sub>4</sub> solar cells. *Thin Solid Films*. <https://doi.org/10.1016/j.tsf.2020.137822>.
- Li, X., Zhuang, D., Zhang, N., Zhao, M., Yu, X., Liu, P., Wei, Y., Ren, G., 2019. Achieving 11.95% efficient Cu<sub>2</sub>ZnSnSe<sub>4</sub> solar cells fabricated by sputtering a Cu-Zn-Sn-Se quaternary compound target with a selenization process. *J. Mater. Chem. A*. <https://doi.org/10.1039/c9ta00385a>.
- Lide, D.R., 2003. CRC Handbook of Chemistry and Physics, 84th ed., *Handbook of Chemistry and Physics*.
- Litvinchuk, A.P., Dzhan, V.M., Yuhymchuk, V.O., Valakh, M.Y., Babichuk, I.S., Parasyuk, O.V., Piskach, L.V., Gordan, O.D., Zahn, D.R.T., 2014. Electronic structure, optical properties, and lattice dynamics of orthorhombic Cu<sub>2</sub>CdGeS<sub>4</sub> and Cu<sub>2</sub>CdSi<sub>4</sub> semiconductors. *Phys. Rev. B - Condens. Matter Mater. Phys.* <https://doi.org/10.1103/PhysRevB.90.165201>.
- Liu, F.S., Zheng, J.X., Huang, M.J., He, L.P., Ao, W.Q., Pan, F., Li, J.Q., 2014. Enhanced thermoelectric performance of Cu<sub>2</sub>CdSnSe<sub>4</sub> by Mn doping: Experimental and first principles studies. *Sci. Rep.* <https://doi.org/10.1038/srep05774>.
- Marushko, L.P., Piskach, L.V., Parasyuk, O.V., Oleksyuk, I.D., Volkov, S.V., Pekhnyo, V. I., 2009. The reciprocal system Cu<sub>2</sub>GeS<sub>3</sub> + 3CdSe ⇌ Cu<sub>2</sub>GeSe<sub>3</sub> + 3CdS. *J. Alloy. Compd.* <https://doi.org/10.1016/j.jallcom.2008.05.073>.
- Mellikow, E., Altsaar, M., Kauk-Kuusik, M., Timmo, K., Meissner, D., Grossberg, M., Krustok, J., Volobujeva, O., 2015. Growth of CZTS-Based Monograins and Their Application to Membrane Solar Cells. In: *Copper Zinc Tin Sulfide-Based Thin-Film Solar Cells*. John Wiley & Sons Ltd, Chichester, UK, pp. 289–309. <https://doi.org/10.1002/9781118437865.ch13>.
- Neubauer, C., Babatas, E., Meissner, D., 2017. Investigation of rough surfaces on Cu<sub>2</sub>ZnSn(S<sub>x</sub>Se<sub>1-x</sub>)<sub>4</sub> monograin layers using light beam induced current measurements. *Appl. Surf. Sci.* 423, 465–468. <https://doi.org/10.1016/j.apsusc.2017.06.111>.
- Sharif, M.H., Enkhbat, T., Enkhbayar, E., Kim, J., 2020. Control of defect states of kesterite solar cell to achieve over 11% power conversion efficiency. *acsam.0c01141 ACS Appl. Energy Mater.* <https://doi.org/10.1021/acsam.0c01141>.

- Son, D.H., Kim, Y.I., Kim, S.H., Nam, D., Cheong, H., Kang, J.K., Yang, K.J., Kim, D.H., 2019. Effects of S and Se contents on the physical and photovoltaic properties of  $\text{Cu}_2\text{ZnSn}(\text{S}_x\text{Se}_{1-x})_4$  thin films: Achieving a PCE of 9.47%. *J. Mater. Chem. A*. <https://doi.org/10.1039/c9ta08319g>.
- Timmo, K., Kauk-Kuusik, M., Altosaar, M., Raudoja, J., Raadik, T., Grossberg, M., Varema, T., Pilvet, M., Leinemann, I., Volobujeva, O., Mellikov, E., 2013. Novel  $\text{Cu}_2\text{CdSnS}_4$  and  $\text{Cu}_2\text{ZnGeSe}_4$  absorber materials for monograin layer solar cell application. 28<sup>th</sup> Eur. Photovolt. Sol. Energy Conf. Exhib. 2385–2388 <https://doi.org/10.4229/28thEUPVSEC2013-3BV.6.14>.
- Timmo, K., Altosaar, M., Pilvet, M., Mikli, V., Grossberg, M., Danilson, M., Raadik, T., Josepson, R., Krustok, J., Kauk-Kuusik, M., 2019. The effect of Ag alloying of  $\text{Cu}_2(\text{Zn}, \text{Cd})\text{Sn}_4$  on the monograin powder properties and solar cell performance. *J. Mater. Chem. A*. <https://doi.org/10.1039/c9ta07768e>.
- Wang, W., Winkler, M.T., Gunawan, O., Gokmen, T., Todorov, T.K., Zhu, Y., Mitzi, D.B., 2014. Device Characteristics of CZTSSe Thin-Film Solar Cells with 12.6% Efficiency. *Adv. Energy Mater.* 4, 1301465. <https://doi.org/10.1002/aenm.201301465>.
- Yan, C., Huang, J., Sun, K., Johnston, S., Zhang, Y., Sun, H., Pu, A., He, M., Liu, F., Eder, K., Yang, L., Cairney, J.M., Ekins-Daukes, N.J., Hameiri, Z., Stride, J.A., Chen, S., Green, M.A., Hao, X., 2018.  $\text{Cu}_2\text{ZnSnS}_4$  solar cells with over 10% power conversion efficiency enabled by heterojunction heat treatment. *Nat. Energy* 3, 764–772. <https://doi.org/10.1038/s41560-018-0206-0>.



**Publication IV**

J. Krustok, R. Kaupmees, **X. Li**, M. Kauk-Kuusik, and M. Grossberg. "Detailed photoluminescence study of  $\text{Cu}_2\text{Ge}(\text{SSe})_3$  microcrystals", *AIP Advances* 11, 085105 2021.  
<https://doi.org/10.1063/5.0053928>





# Detailed photoluminescence study of $\text{Cu}_2\text{Ge}(\text{SSe})_3$ microcrystals

Cite as: AIP Advances 11, 085105 (2021); doi: 10.1063/5.0053928

Submitted: 15 April 2021 • Accepted: 22 July 2021 •

Published Online: 3 August 2021



J. Krustok,<sup>1,2,a)</sup> R. Kaupmees,<sup>2</sup> X. Li,<sup>2</sup> M. Kauk-Kuusik,<sup>2</sup> and M. Grossberg<sup>2</sup>

## AFFILIATIONS

<sup>1</sup>Division of Physics, Tallinn University of Technology, Ehitajate Tee 5, 19086 Tallinn, Estonia

<sup>2</sup>Department of Materials and Environmental Technology, Tallinn University of Technology, Ehitajate Tee 5, 19086 Tallinn, Estonia

<sup>a)</sup>Author to whom correspondence should be addressed: [juri.krustok@taltech.ee](mailto:juri.krustok@taltech.ee)

## ABSTRACT

We present a detailed temperature and laser power dependent photoluminescence (PL) study of  $\text{Cu}_2\text{Ge}(\text{S}_{0.4}\text{Se}_{0.6})_3$  microcrystals. At  $T = 20$  K, two relatively narrow PL peaks were detected at about 1.16 eV (peak No. 1) and 1.12 eV (peak No. 2) and a weak, broad PL band was detected at about 0.82 eV (peak No. 3). The temperature and laser power dependencies indicate that at  $T = 20$  K, the properties of PL peak Nos. 1 and 2 can be explained by the distant donor–acceptor (DA) pair model where a donor defect has a depth of  $E_D \approx 20$  meV and  $E_D \approx 60$  meV for peak Nos. 1 and 2, respectively. The depth of acceptor defects was 57 and 76 meV for peak Nos. 1 and 2, respectively. At around  $T = 90$  K, the DA pair recombination of peak No. 1 gradually starts to transform into the conduction band–acceptor recombination, but peak No. 2 shows a DA pair recombination even at room temperature. The estimated bandgap energy of this compound at room temperature was  $E_g = 1.225$  eV.

© 2021 Author(s). All article content, except where otherwise noted, is licensed under a Creative Commons Attribution (CC BY) license (<http://creativecommons.org/licenses/by/4.0/>). <https://doi.org/10.1063/5.0053928>

$\text{I}_2\text{--IV--VI}_3$  compounds  $\text{Cu}_2\text{MS}_3$  ( $M = \text{Sn}$  and  $\text{Ge}$ ) have recently received increasing attention as candidates for the absorber layer of thin-film solar cells. Among them,  $\text{Cu}_2\text{GeS}_3$  (CGS) and  $\text{Cu}_2\text{GeSe}_3$  have direct bandgap energies of 1.65 and 0.82 eV, respectively.<sup>1–3</sup> Unfortunately, the bandgap energy of both compounds is far from ideal for single junction solar cells, and therefore, solid solutions  $\text{Cu}_2\text{Sn}_{1-x}\text{Ge}_x\text{S}_3$  have been used in order to reduce the bandgap energy of CGS. The record efficiency of these solar cells is 6.73%.<sup>4</sup> The cation substitution mainly affects the position of the conduction band edge. An alternative approach involves substitution of S by Se and thus shifting the energy of the valence band edge in  $\text{Cu}_2\text{Ge}(\text{S}_x\text{Se}_{1-x})_3$  (CGSSe) solid solutions. Unfortunately, there is very little information about properties of CGSSe solid solutions and there are no attempts to prepare solar cells using these solid solutions. A recent study of CGSSe nanocrystals showed that there is nearly linear relationship between the bandgap energy and the Se content in the CGSSe solid solutions, and thereby, it is possible to tune the bandgap energy to the ideal range for solar light absorption.<sup>5</sup> However, the defect structure of CGSSe is still not studied, while the properties of  $\text{Cu}_2\text{GeS}_3$  and  $\text{Cu}_2\text{GeSe}_3$  compounds

are more or less known. The photoluminescence spectroscopy (PL) has been a main tool to study defects in many compounds. Therefore, in this paper, we will present a first and detailed PL study of  $\text{Cu}_2\text{Ge}(\text{S}_x\text{Se}_{1-x})_3$  microcrystals, where  $x = 0.4$ .

$\text{Cu}_2\text{Ge}(\text{S}_{0.4}\text{Se}_{0.6})_3$  microcrystalline powder was synthesized by the molten salt method. 5N purity Cu, Ge, S, and Se were used as precursors and LiI as a reaction medium. All chemicals with a chemical composition of 33.32 mol. % Cu, 16.67 mol. % Ge, 19.97 mol. % S, and 30.03 mol. % Se corresponding to the formula  $\text{Cu}_2\text{Ge}(\text{S}_{0.4}\text{Se}_{0.6})_3$  were mixed and ground in an agate mortar. These operations were carried out in a glove box under an argon atmosphere. The mixture was put into the carbon coated quartz ampoule and sealed under a vacuum of  $3 \times 10^{-2}$  Torr. The powder synthesis was carried out at 700 °C in a closed quartz ampoule. The heating rate was maintained at 0.5 °C/min up to the requisite synthesis temperature and held for 100 h. Finally, the obtained product was cooled to room temperature in air and then washed with deionized water to release the powder crystals from the LiI salt. Before PL measurements, the powder crystal surfaces were cleaned from residues chemically with 1 wt. % Br-MeOH solution followed by 10 wt. % KCN and

isothermally annealed at 300 °C for 35 min. The shape and surface morphology of the synthesized microcrystals were studied with a high-resolution scanning electron microscope (SEM), Zeiss MERLIN. The average size of our microcrystals was around 80  $\mu\text{m}$ ; see Fig. 1(a).

The elemental composition of microcrystals was determined by Energy Dispersive X-ray (EDX) spectroscopy. Bulk composition of micro-crystalline powder was measured from polished crystals. According to EDX results, the average composition of synthesized microcrystals was  $\text{Cu}_{2.01}\text{Ge}_{0.99}(\text{S}_{0.4}\text{Se}_{0.6})_3$ .

The crystal structure of the studied  $\text{Cu}_2\text{Ge}(\text{S}_{0.4}\text{Se}_{0.6})_3$  microcrystals was determined by x-ray diffraction (XRD) using a Rigaku Ultima IV diffractometer operating with the silicon strip detector D/tex Ultra. XRD analysis showed an orthorhombic crystal structure with the space group *Imm2*. No other phases were detected. Unfortunately, there are no XRD data for the  $\text{Cu}_2\text{Ge}(\text{S}_{0.4}\text{Se}_{0.6})_3$  compound, but the closest match is the  $\text{Cu}_2\text{Ge}(\text{S}_{0.2}\text{Se}_{0.8})_3$  compound (ICDD PDF-2-2013, 00-059-0291). Figure 1(b) shows that due to different S/Se ratios in our crystals, all XRD peaks are slightly shifted toward higher angle values, but the overall coincidence is quite good. The lattice constants were determined using the Rietveld refinement procedure by Rigaku PDXL version 1.4.0.3 software. The obtained lattice parameters were  $a = 11.626$  Å,  $b = 3.883$  Å, and  $c = 5.376$  Å. We also expect that a small amount of Li is present in our crystals, and therefore, it could have a slight effect on lattice constants of our microcrystals.

Raman measurements were carried out using a Horiba LabRAM HR800 micro-Raman system equipped with a cooled multichannel CCD detection system in the backscattering configuration with a spectral resolution better than  $1\text{ cm}^{-1}$ . A YAG:Nd laser (wavelength  $\lambda = 532$  nm) was used for excitation. The laser spot size was about  $2\ \mu\text{m}$  in diameter. Figure 1(c) presents the deconvoluted Raman spectra of  $\text{Cu}_2\text{Ge}(\text{S}_{0.4}\text{Se}_{0.6})_3$  microcrystals fitted using a Lorentzian function to resolve the peaks. As with all solid solutions, the Raman spectrum includes the contribution of both sulfide and selenide. The most intense Raman peaks in  $\text{Cu}_2\text{GeS}_3$  are at 189 and 266  $\text{cm}^{-1}$ ,<sup>6</sup> while in  $\text{Cu}_2\text{GeS}_3$ , similar peaks can be found at 339 and 396  $\text{cm}^{-1}$ .<sup>1,7,8</sup> In solid solutions, all sulfide related peaks tend to shift toward smaller wavenumbers and the relative intensity of these peaks decreases and selenide related peaks will shift

toward higher wavenumbers and their intensity decreases. Almost all Raman modes of solid solutions follow the two-mode behavior as in other sulfide–selenide solid solutions and become wider.<sup>9,10</sup> In our solid solution, the selenide related peaks dominate at around  $200\text{ cm}^{-1}$  and sulfide related peaks around  $380\text{ cm}^{-1}$  are quite weak. All detected Raman peaks belong to our solid solution, and no other phases are present.

A 0.64 m focal length single grating ( $600\text{ mm}^{-1}$ ) monochromator and the 442 nm line of a He–Cd laser with different powers were used for PL measurements. For PL signal detection, a Hamamatsu InGaAs photomultiplier tube (PMT) was used. A closed-cycle helium cryostat was employed to measure temperature dependencies of the PL spectra at temperatures from 20 to 300 K. The laser spot size for these measurements was  $200\ \mu\text{m}$  in diameter.

The low temperature PL spectrum of CGSSe shows three bands, No. 1 at 1.16 eV, No. 2 at 1.12 eV, and a wide and weak No. 3 band at 0.82 eV; see Fig. 2(a). Unfortunately, this band was too weak for further analysis, but the presence of this rather deep band proves that quite deep defect levels are also present in CGSSe. Band Nos. 1 and 2 were fitted using an asymmetric double sigmoidal fitting function because both bands had slightly asymmetric shape; see Fig. 2(b). The full-width at half-maximum (FWHM) of band No. 1 was around 30 meV, while band No. 2 was significantly wider with a FWHM of  $\approx 55$  meV. A very similar double band arrangement of low temperature PL spectra was discovered also in CGS<sup>1</sup> and in CGSe.<sup>2</sup> On increasing the temperature, both bands show a small shift toward higher energy and a drastic change in shape at  $T = 40\text{--}90$  K; see Fig. 2(a). This blueshift at a low temperature is typical for donor–acceptor (DA) pairs where the low temperature DA emission is replaced by conduction band–acceptor (c–A) recombination due to ionization of shallow donor levels of the DA pair.<sup>11–13</sup> However, band No. 2 seems to be less affected. Therefore, it is possible that band No. 2 is related to deeper donor (and acceptor) levels and the DA recombination is not changed to c–A recombination in the measured temperature range, but we only observe a redistribution of recombination from closer DA pairs to more distant ones. At  $T = 40\text{--}80$  K, the FWHM of peak No. 1 shows an abrupt increase indicating the presence of both DA pair and c–A PL peaks; see Fig. 3(a).

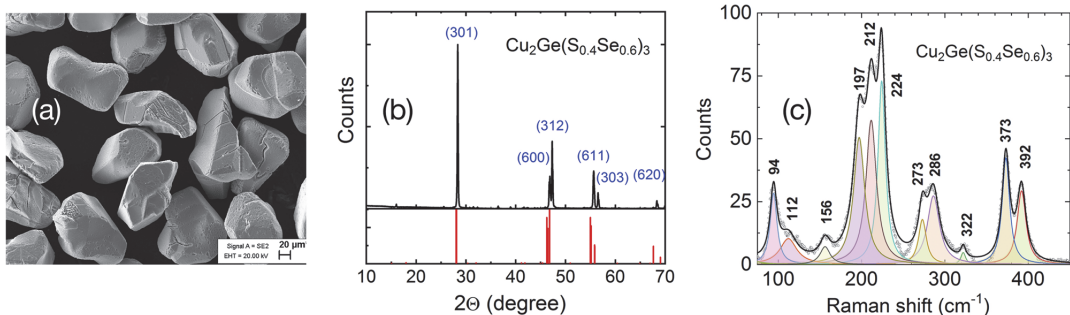


**FIG. 1.** (a) SEM image of CGSSe microcrystals. (b) Measured XRD pattern of  $\text{Cu}_2\text{Ge}(\text{S}_{0.4}\text{Se}_{0.6})_3$  microcrystals and a theoretical pattern of the  $\text{Cu}_2\text{Ge}(\text{S}_{0.2}\text{Se}_{0.8})_3$  compound (ICDD PDF-2-2013, 00-059-0291) (red lines). (c) Raman spectra of the CGSSe solid solution together with fitting results using a Lorentzian line shape.

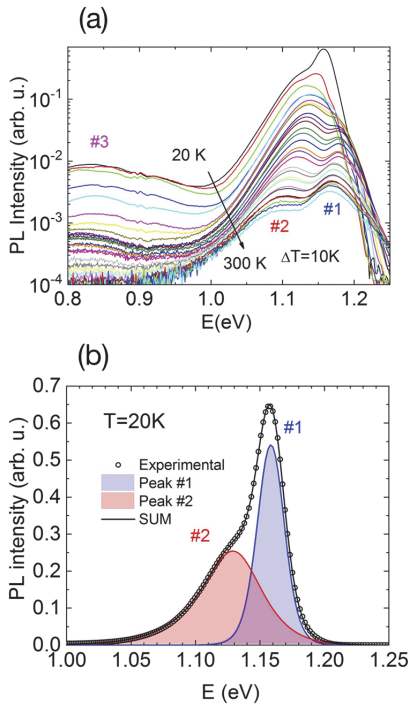


FIG. 2. (a) Temperature dependence of the PL spectrum and (b) example of PL fitting using an asymmetric double sigmoidal function at  $T = 20$  K.

The temperature dependence of the peak position obtained from the fittings of the PL spectra is plotted in Fig. 3(a). Experimental data points of peak No. 1 at  $T = 100$ – $300$  K were fitted with O'Donnell's expression<sup>14</sup>

$$E_{\max}(T) = E_{\max}(0) - S\langle E_{ph} \rangle \left[ \coth(\langle E_{ph} \rangle / 2kT) - 1 \right], \quad (1)$$

where  $E_{\max}(0)$  is the peak position at  $T = 0$  K,  $S$  is a dimensionless coupling constant, and  $\langle E_{ph} \rangle$  represents an average phonon energy. The obtained phonon energy of 54 meV corresponds to  $436 \text{ cm}^{-1}$ , and it is located at slightly higher energy than the highest detected Raman modes. All parameters of this fitting are given in Fig. 3(a). Assuming that peak No. 1 at this temperature range is related to c-A recombination and the peak shift with temperature is explained by the temperature dependence of  $E_g$ , we can estimate also the temperature dependence of  $E_g$  if we know the depth of the acceptor level. Peak No. 2 however shows more rapid shift with increasing temperature. It is known that the PL peak energy for every single DA pair recombination is expressed as

$$E_i(r) = E_g - (E_D + E_A) + \frac{e^2}{\epsilon r_i}, \quad (2)$$

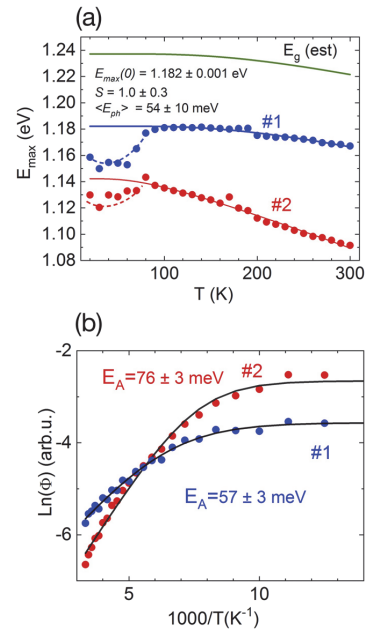


FIG. 3. (a) Temperature dependence of peak positions for peak Nos. 1 and 2 together with an estimated value of  $E_g$ . Fitting of peak No. 1 using Eq. (1) is given as a blue line; fitting parameters are given. The red line for peak No. 2 is a guide to the eye. (b) Arrhenius plot of integral intensity for both peaks together with the fitting result obtained using Eq. (3).

where  $E_g$ ,  $E_D$ , and  $E_A$  are the bandgap energy and the donor and acceptor ionization energies, respectively;  $r_i$  is the distance between the donor and acceptor defects; and  $\epsilon$  is the static dielectric constant.<sup>15</sup> This means that the FWHM of peak No. 2 is wider because of wider distribution of DA pair distances. At higher temperatures, defects from the closest DA pairs will be ionized and the distribution will shift toward more distant pairs having smaller peak position energy. Therefore, the peak position shift of peak No. 2 is a combined effect of the DA pair distribution shift and the  $E_g$  shift.

The thermal activation energies for the bands obtained from the Arrhenius plot [Fig. 3(b)] where the dependence of  $\ln \Phi(T)$  vs  $1000/T$  was fitted by using a theoretical expression for discrete energy levels,<sup>16</sup>

$$\Phi(T) = \Phi_0 \left[ 1 + A_1 T^{3/2} + A_2 T^{3/2} \exp(-E_A/kT) \right], \quad (3)$$

where  $\Phi$  is the integrated intensity of the PL band,  $A_1$  and  $A_2$  are the process rate parameters, and  $E_A$  is the thermal activation energy. Fitting results are presented in Fig. 3(b). The thermal activation energy of peak No. 1 represents the depth of the acceptor level  $E_A = 57 \pm 3$  meV. By using this acceptor defect depth value, we were able to estimate the temperature dependence of  $E_g$ ; see Fig. 3(a). The temperature dependence of the bandgap energy of CGSs crystals is rather small, and a very small shift of  $E_g$  was also detected in CGS and

CGSe crystals.<sup>1,2,17,18</sup> As was predicted, the activation energy for peak No. 2 is higher and, consequently, peak No. 2 is related to deeper defects.

Next, the temperature dependence of the full-width at half-maximum was fitted using the relation proposed by Rudin and Reinecke<sup>19</sup> given as

$$FWHM(T) = W_0 + \beta T + W_1 / [\exp(E_{ph}/kT) - 1], \quad (4)$$

where  $W_0$  is the width at  $T = 0$  K also including inhomogeneous broadening,  $\beta$  is a coefficient for the interaction of excitons with acoustic phonons, the last term represents the interaction with optical phonons, and  $E_{ph}$  is the phonon energy. The interaction with acoustic phonons was neglected because it is usually very small. The fitting result is presented in Fig. 4(a) for both bands. Obtained phonon modes 16 and 24 meV correspond to Raman modes related to CGSe ( $129$  and  $194 \text{ cm}^{-1}$ , respectively).

By increasing the laser power, the shape of the PL spectra did not show any dramatic changes, i.e., the integrated intensity  $\Phi$  of all peaks increases almost linearly with laser power [see Fig. 4(b)] and the experimental data can be fitted by the simple power law of the form  $\Phi \propto L^m$ , where  $\Phi$  is the PL integrated intensity,  $L$  is the excitation laser power, and  $m$  is a dimensionless exponent. It is well

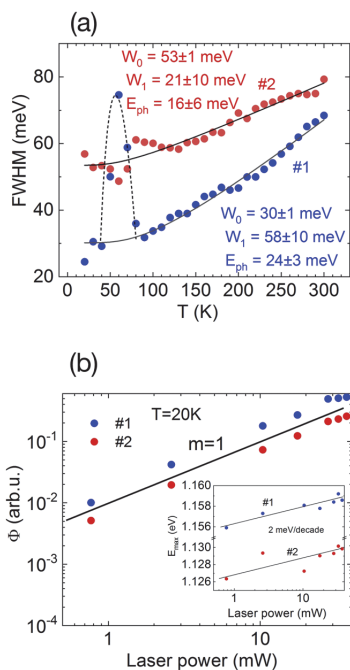


**FIG. 4.** (a) The temperature dependence of FWHM for both bands and fitting result (lines) and fitting parameters obtained using Eq. (4). (b) Laser power dependence of integral intensity for both bands; the inset shows the peak position shift with laser power.

known that for an excitation laser photon with an energy exceeding the bandgap energy, the coefficient  $m$  is generally  $1 < m < 2$  for the free- and bound-exciton emission and  $m \leq 1$  for free-to-bound and donor-acceptor pair recombinations.<sup>20</sup> Thus, the obtained value of  $m \approx 1$  for both bands is a sign that all measured PL bands are related to defects and do not have an excitonic nature. At the same time, both PL bands show a certain blueshift with laser power; see the inset in Fig. 4(b). The blueshift is typical for donor-acceptor (DA) pairs with different distances between donor and acceptor defects in the crystal lattice.<sup>21–23</sup> The rate of this blueshift is usually higher for DA pairs with shorter distances. Accordingly, PL band Nos. 1 and 2 with a blueshift of  $2 \text{ meV/decade}$  of laser power must be related to quite shallow defects. We assume that all the donor and/or acceptor levels observed are native and due to deviations in composition from the ideal stoichiometry. The shallowest acceptor level with  $E_A = 57 \text{ meV}$  is very close to the  $V_{Cu}$  level observed in CGSe crystals by PL and electrical measurements (about  $50\text{--}65 \text{ meV}$ ).<sup>2,24</sup> Remarkably lower activation energies were measured in CGS crystals,<sup>1</sup> and it seems that sulfur has an effect of reducing the activation energy of acceptor defects. At the same time, the deeper acceptor level in CGSe crystals is believed to be related to the selenium interstitial defect with an activation energy of  $E_A = 120 \text{ meV}$ .<sup>24</sup> Our measurements show

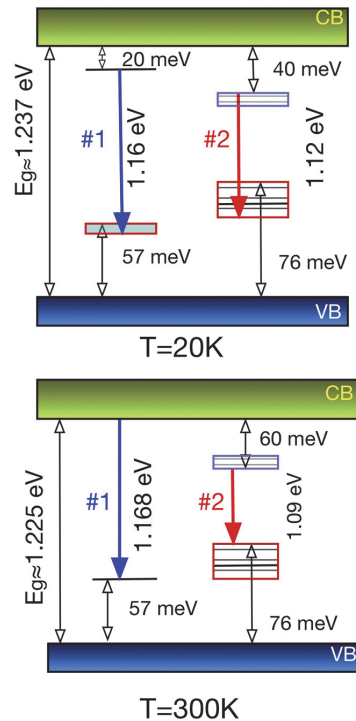


**FIG. 5.** Energy band diagram of the CGSse solid solution, illustrating the recombination processes at  $T = 20$  and at  $T = 300 \text{ K}$ . Distribution of DA pair energy levels is shown as blue and red boxes.

an activation energy of  $E_A = 76$  meV. This level can be related to the S/Se interstitial defect or to the antisite  $\text{Cu}_{\text{Ge}}$  defect.<sup>2</sup> We also have two shallow donor levels ( $E_D \approx 20$  and  $60$  meV) in our sample. The most probable donor defect could be the  $\text{Ge}_{\text{Cu}}$  antisite defect, but the origin of donor defects is not clear at the moment and further studies are needed.

In conclusion, we present a recombination model for the  $\text{Cu}_2\text{Ge}(\text{S}_{0.4}\text{Se}_{0.6})_3$  microcrystals; see Fig. 5. At low temperatures, the DA pair recombination is dominating for both PL peaks. At temperatures  $T > 90$  K, the DA pair recombination is gradually transformed into c-A recombination for peak No. 1, but peak No. 2 shows a DA pair recombination even at room temperature. The distribution of DA pair energy levels for peak No. 2 is wider due to shorter distances between donor and acceptor defects. According to this model, the estimated bandgap energy  $E_g$  at room temperature is about  $1.225$  eV, and this value is very close to the bandgap energy of  $\text{Cu}(\text{In,Ga})\text{Se}_2$  absorbers in record breaking thin-film solar cells.<sup>25</sup>

This work was supported by the European Regional Development Fund (Project No. TK141) and by the Estonian Research Council (Project No. PRG1023). M.G. acknowledges the L'Oréal Baltic For Women in Science Program. Dr. V. Mikli is thanked for his help with EDX measurements.

## DATA AVAILABILITY

The data that support the findings of this study are available from the corresponding author upon reasonable request.

## REFERENCES

- <sup>1</sup>N. Aihara, Y. Matsumoto, and K. Tanaka, *Phys. Status Solidi* **254**, 1700118 (2017).
- <sup>2</sup>G. Marcano, G. S. Pérez, and C. Rincón, *Phys. Status Solidi B* **254**, 1700332 (2017).
- <sup>3</sup>H. Araki, K. Chino, K. Kimura, N. Aihara, K. Jimbo, and H. Katagiri, *Jpn. J. Appl. Phys., Part 1* **53**, 05FW10 (2014).
- <sup>4</sup>M. Umehara, S. Tajima, Y. Aoki, Y. Takeda, and T. Motohiro, *Appl. Phys. Express* **9**, 072301 (2016).
- <sup>5</sup>C. Yang, B. Zhou, S. Miao, C. Yang, B. Cai, W.-H. Zhang, and X. Xu, *J. Am. Chem. Soc.* **135**, 5958 (2013).
- <sup>6</sup>G. Marcano, C. Rincón, G. Marín, G. E. Delgado, A. J. Mora, J. L. Herrera-Pérez, J. G. Mendoza-Alvarez, and P. Rodríguez, *Solid State Commun.* **146**, 65 (2008).
- <sup>7</sup>Y. Matsumoto, N. Aihara, N. Saito, and K. Tanaka, *Mater. Lett.* **194**, 16 (2017).
- <sup>8</sup>Y. Kim and I.-H. Choi, *J. Alloys Compd.* **770**, 959 (2019).
- <sup>9</sup>M. Grossberg, J. Krustok, J. Raudojka, K. Timmo, M. Altsaar, and T. Raadik, *Thin Solid Films* **519**, 7403 (2011).
- <sup>10</sup>R. Bacewicz, W. Gebicki, and J. Filipowicz, *J. Phys.: Condens. Matter* **6**, L777 (1994).
- <sup>11</sup>L. Bai, N. C. Giles, P. G. Schunemann, T. M. Pollak, K. Nagashio, and R. S. Feigelson, *J. Appl. Phys.* **95**, 4840 (2004).
- <sup>12</sup>M. V. Yakushev, I. Forbes, A. V. Mudryi, M. Grossberg, J. Krustok, N. S. Beattie, M. Moynihan, A. Rockett, and R. W. Martin, *Thin Solid Films* **582**, 154 (2015).
- <sup>13</sup>J. Krustok, T. Raadik, R. Kaupmees, F. Ghisani, K. Timmo, M. Altsaar, V. Mikli, and M. Grossberg, *J. Phys. D.: Appl. Phys.* **54**, 105102 (2021).
- <sup>14</sup>K. P. O'Donnell and X. Chen, *Appl. Phys. Lett.* **58**, 2924 (1991).
- <sup>15</sup>D. G. Thomas, M. Gershenson, and F. A. Trumbore, *Phys. Rev.* **133**, A269 (1964).
- <sup>16</sup>J. Krustok, H. Collan, and K. Hjelt, *J. Appl. Phys.* **81**, 1442 (1997).
- <sup>17</sup>B. K. Sarkar, A. S. Verma, and P. S. Deviprasad, *Physica B* **406**, 2847 (2011).
- <sup>18</sup>G. Marcano and L. Nieves, *J. Appl. Phys.* **87**, 1284 (2000).
- <sup>19</sup>S. Rudin and T. L. Reinecke, *Phys. Rev. B* **41**, 3017 (1990).
- <sup>20</sup>T. Schmidt, K. Lischka, and W. Zulehner, *Phys. Rev. B* **45**, 8989 (1992).
- <sup>21</sup>N. Aihara, K. Tanaka, H. Uchiki, A. Kanai, and H. Araki, *Appl. Phys. Lett.* **107**, 032101 (2015).
- <sup>22</sup>C. Spindler, D. Regesch, and S. Siebentritt, *Appl. Phys. Lett.* **109**, 032105 (2016).
- <sup>23</sup>N. Shrestha, C. R. Grice, E. Bastola, G. K. Liyanage, A. B. Phillips, M. J. Heben, Y. Yan, and R. J. Ellingson, *MRS Adv.* **3**, 3293 (2018).
- <sup>24</sup>G. Marcano, D. B. Bracho, C. Rincón, G. S. Pérez, and L. Nieves, *J. Appl. Phys.* **88**, 822 (2000).
- <sup>25</sup>L. M. Mansfield, R. L. Garris, K. D. Counts, J. R. Sites, C. P. Thompson, W. N. Shafarman, and K. Ramanathan, *IEEE J. Photovoltaics* **7**, 286 (2017).



**Publication V**

X. Li, K. Timmo, M. Grossberg, M. Pilvet, R. Kaupmees, J. Krustok, K. Muska, V. Mikli, M. Kauk-Kuusik. "Study of the structure and optoelectronic properties of  $\text{Cu}_2\text{Ge}(\text{Se}_x\text{S}_{1-x})_3$  microcrystalline powders", *Thin Solid Films* 742, 139053, 2022.

<https://doi.org/10.1016/j.tsf.2021.139053>







## Study of the structure and optoelectronic properties of $\text{Cu}_2\text{Ge}(\text{Se}_x\text{S}_{1-x})_3$ microcrystalline powders

X. Li<sup>\*</sup>, K. Timmo, M. Grossberg, M. Pilvet, R. Kaupmees, J. Krustok, K. Muska, V. Mikli, M. Kauk-Kuusik

Department of Materials and Environmental Technology, Tallinn University of Technology, Ehitajate tee 5, Tallinn 19086, Estonia

### ARTICLE INFO

#### Keywords:

Copper germanium sulfoselenide  
Crystal structure  
Photoluminescence  
Raman spectroscopy  
Solar cell

### ABSTRACT

In this study, the  $\text{Cu}_2\text{Ge}(\text{Se}_x\text{S}_{1-x})_3$  ( $x = 0, 0.2, 0.4, 0.6, 0.8, 1$ ) microcrystalline powders were synthesized from elemental precursors in the liquid phase of lithium iodide (LiI) flux material in evacuated quartz ampoules. The crystal structure and lattice parameters of the  $\text{Cu}_2\text{Ge}(\text{Se}_x\text{S}_{1-x})_3$  (CGSSe) were determined by X-ray diffraction measurement. Results showed the crystal structure of CGSSe transfers from monoclinic to orthorhombic with increasing the Se content in the powders, which occurs between  $0.2 < x < 0.4$ . Raman spectroscopy showed that all sulfide related peaks in the solid solutions tend to shift toward smaller wavenumbers and the relative intensity of these peaks was decreasing and selenide related peaks shifted toward higher wavenumbers and decreased. Radiative recombination processes in CGSSe microcrystalline powders were studied by using photoluminescence spectroscopy (PL). All spectra of CGSSe were composed of two asymmetric PL peaks. Peak positions of these bands (#1 and #2) as a function of Se/S concentration show nearly linear dependence with a slope about  $-0.8$  eV. Almost the same slope was detected for band gap values ( $E_g$ ) determined from room temperature external quantum efficiency measurements. Therefore, the peak position shift with  $x$  is related to  $E_g$  shift for both PL peaks. Both peaks are related to donor-acceptor pair recombination.

A best performing solar cell was fabricated by using  $\text{Cu}_2\text{Ge}(\text{Se}_x\text{S}_{1-x})_3$   $x = 0.6$  powder crystals as absorber material, exhibiting an open-circuit voltage of 537 mV, current density of  $15.8 \text{ mA/cm}^2$ , fill factor of 37.2% and a conversion efficiency of 3.16%.

### 1. Introduction

Economic development and the general growth in energy consumption have led to an increased demand for environmentally friendly energy production at lower cost. For these opportunities are sought in the renewable energy sector. New technologies for energy production should provide clean, low cost, environmentally friendly solutions with versatile applications, making solar energy the best solution today. The wide range of multinary compounds have been proposed as emerging inorganic absorber materials for thin film solar cell. Among them, researchers' interest in  $\text{Cu}_2\text{-IV-VI}_3$  (IV = Ge, Sn; VI = S, Se) ternary compounds and their solid solutions are also growing. For example,  $\text{Cu}_2\text{SnS}_3$  and  $\text{Cu}_2(\text{Sn,Ge})\text{S}_3$  based solar cells have shown efficiencies 5.1% [1] and 6.73% [2], respectively. Additionally, there are ternary compounds like  $\text{Cu}_2\text{GeS}_3$  (CGS) and  $\text{Cu}_2\text{GeSe}_3$  (CGSe), which are not extensively investigated as absorber materials for solar cell application.

Germanium is a scarce but not an extremely rare element in the crust of the Earth for example equaling in abundance to molybdenum and exceeding the elements cadmium and antimony. Previously mentioned elements are also widely used in semiconductor industry. CGS and CGSe have many promising properties for photoabsorber material, such as  $p$ -type conductivity, high absorption coefficient ( $10^4 \text{ cm}^{-1}$ ) and a direct band gap energy [3,4]. Unfortunately, pure sulfide compound has slightly higher bandgap (1.5–1.6 eV) [5,6] and selenide compound have slightly lower (0.78 eV) [7,8] bandgap values reported than it should be for single junction solar cells. Therefore, solid solutions  $\text{Cu}_2\text{Ge}(\text{Se}_x\text{S}_{1-x})_3$  need to be investigated in order to modify the bandgap energy and find the optimal S/Se ratio for absorber material.

According to several studies,  $\text{Cu}_2\text{GeS}_3$  exist in different crystal structures, such as orthorhombic, cubic and monoclinic structure, that varies with the synthesis temperature [6,9,10]. Single crystals of CGS grown by chemical vapor deposition method at  $620 \text{ }^\circ\text{C}$  showed

<sup>\*</sup> Corresponding author.

E-mail address: [xiaofeng.li@taltech.ee](mailto:xiaofeng.li@taltech.ee) (X. Li).

monoclinic crystal structure [9]. Thin films produced by Cu layer annealing in GeS/S vapor at 480 °C showed cubic crystal structure and transition to monoclinic polymorph was observed between 480 and 500 °C [6]. Colloidal nanocrystals (NCs) produced by a hot-injection method showed cubic structure for CGS and by adding Se into the compound, the orthorhombic structure was observed [11]. Although, some researchers have found that CGSe compound crystallize in the monoclinic structure [3,7], mostly it has been observed that pure CGSe crystallize in an orthorhombic structure [3,12,13].

There are only few papers about the defect structure of  $\text{Cu}_2\text{GeS}_3$ ,  $\text{Cu}_2\text{GeSe}_3$  and their solid solutions. Robert et al. [6] reported photoluminescence (PL) studies of the monoclinic  $\text{Cu}_2\text{GeS}_3$ . One PL band with a peak maximum at 1.57 eV was detected, they assigned it to the band to band transition. In the study [12], for  $\text{Cu}_2\text{GeSe}_3$  compound was detected three PL bands with peaks positions at 0.637 and 0.753 eV which were assigned to free-to-bound recombination from the conduction band to acceptor states and peak position at 0.727 eV was assigned to recombination of an exciton bound to an ionized acceptor. Recently, our group published detailed PL study of  $\text{Cu}_2\text{Ge}(\text{Se}_{0.4}\text{S}_{0.6})_3$  microcrystals [14]. At LT (low temperature) = 20 K, the donor acceptor pair recombination is dominating for both PL peaks, 1.16 eV and 1.12 eV respectively.

There are only few studies presenting the results about  $\text{Cu}_2\text{GeS}_3$ ,  $\text{Cu}_2\text{GeSe}_3$  or their solid solution based solar cell [6]. The best power conversion efficiency of 2.67% for  $\text{Cu}_2\text{GeS}_3$  thin film solar cell was achieved by combustion method [4]. In the study [11], the efficiency of 0.2% was presented for solar cells based on  $\text{Cu}_2\text{Ge}(\text{Se}_{0.33}\text{S}_{0.67})_3$  colloidal NCs.

In the present study,  $\text{Cu}_2\text{Ge}(\text{Se}_x\text{S}_{1-x})_3$  ( $x = 0 - 1$ ) high quality microcrystalline powders were synthesized by the molten salt synthesis-growth method with the aim to study structural, compositional and optical properties. The photovoltaic applicability of all  $\text{Cu}_2\text{Ge}(\text{Se}_x\text{S}_{1-x})_3$  ( $x = 0 - 1$ ) was evaluated by fabricating the monograin layer solar cells.

## 2. Experimental details

The ternary  $\text{Cu}_2\text{Ge}(\text{Se}_x\text{S}_{1-x})_3$  ( $x = 0, 0.2, 0.4, 0.6, 0.8, 1$ ) microcrystalline powders were synthesized from commercially available elements Cu powder (99.999%, Alfa Aesar), Ge powder (99.999%, Alfa Aesar), S powder (99.999%, Alfa Aesar) and Se powder (99.999%, Alfa Aesar) by molten salt method. The alkali salt LiI (99.8%, Alfa Aesar) was used as a molten salt medium (flux material). The used flux salt was added with the mass ratio of  $m_{\text{precursors}}/m_{\text{flux}}=1:1$ . The material mixtures were degassed, sealed into quartz ampoules, and then heated from room temperature (RT) to 700 °C at a rate  $\sim 0.5$  °C/min and maintained at 700 °C for 120 h. Ampoules were cooled down to RT in air, the salt was removed from solid powder particles by leaching with distilled  $\text{H}_2\text{O}$ . Then, the powder was dried in drying oven at 50 °C and sieved into narrow size fractions (38–112  $\mu\text{m}$ ) by sieving system Retsch AS 200.

The morphology of synthesized powder crystals was studied by high-resolution scanning electron microscope (HR-SEM Zeiss Merlin). The bulk composition of the synthesized powder crystals was analyzed by energy dispersive X-ray spectroscopy (EDX) by using the Bruker EDX-XFlash 6/30 detector with an accelerating voltage of 20 kV (the measurement error is about 0.5 at%). The crystal structure of studied  $\text{Cu}_2\text{Ge}(\text{Se}_x\text{S}_{1-x})_3$  microcrystalline powders was characterized by X-ray powder diffraction (XRD) by using a Rigaku Ultima IV diffractometer with monochromatic Cu K $\alpha$  radiation ( $\lambda = 1.5406$  Å) at 40 kV and 40 mA operating with the silicon strip detector D/teX Ultra. The phase analysis and lattice parameters calculations were made by using software on the Rigaku's system PDXL2. Phase composition of powders was analyzed by room temperature micro-Raman spectroscopy by using a Horiba Lab-RAM HR800 micro-Raman system equipped with a cooled multichannel CCD detection system in the backscattering configuration with a spectral resolution better than  $1\text{ cm}^{-1}$ . A YAG: Nd laser (wavelength  $\lambda = 532$  nm) was used for excitation. The laser spot size was about 2  $\mu\text{m}$  in diameter.

A 0.64 m focal length single grating (600  $\text{mm}^{-1}$ ) monochromator and the 442 nm line of a He-Cd laser with different power were used for the low temperature PL measurements. For PL signal detection a Hamamatsu InGaAs photomultiplier tube (PMT) or the cooled CCD detector were used. A closed-cycle helium cryostat was employed to measure the PL spectra at temperature  $T = 20$  K. The laser spot size for these measurements was 200  $\mu\text{m}$  in diameter.

The monograin layer solar cells were prepared from chemically and thermally treated powders. Chemical etching and post-annealing were done following the previously developed process in our laboratory [15, 16]. For chemical etching, bromine in methanol and KCN solutions were used, and annealing was done in closed quartz ampoules at 400 °C for 60 min. CdS buffer layer was deposited on the post-treated powder crystals by chemical bath deposition method by using vertical rotator in hot-air oven at 60 °C for 30 min. The 360 ° multi-functional vertical rotator provides compact and uniform CdS coverage on CGSs crystals. An alkali deposition solution contained 0.01 M cadmium iodide ( $\text{CdI}_2$ ) and 1 M thiourea ( $\text{SC}(\text{NH}_2)_2$ ), 2 M ammonia aqueous solution ( $\text{NH}_4\text{OH}$ ) was added to adjust the bath solution pH to 11.6 at room temperature. Monograin membranes were prepared by embedding the CdS covered crystals partway into low shrinkage epoxy resin layer on supporting foil. After curing of epoxy, the membranes were covered with transparent conductive oxide layer (i-ZnO and ZnO:Al) by radio-frequency magnetron sputtering. Finally, back contacts and front collector were made by conductive graphite paste and Ag-paste respectively.

The solar cells were characterized by measuring the current versus voltage ( $J$ - $V$ ) characteristics with a Keithley 2400 source meter under standard test conditions (AM 1.5, 100  $\text{mW cm}^{-2}$ ) using a Newport solar simulator. External quantum efficiency (EQE) measurements were performed in the spectral region of 350–1235 nm using a computer controlled SPM-2 prism monochromator. The generated photocurrent was detected at 0 V bias voltage at RT by using a 250 W halogen lamp.

## 3. Results and discussion

Fig. 1 shows the SEM images of  $\text{Cu}_2\text{Ge}(\text{Se}_x\text{S}_{1-x})_3$  powder crystals (with fraction size 63–75  $\mu\text{m}$ ) synthesized in LiI flux. All formed powders consist of non-aggregated, well-formed single crystals with round edges independent of the S/Se ratio. The median grain size of the powders increased with increasing the selenium content in the  $\text{Cu}_2\text{Ge}(\text{Se}_x\text{S}_{1-x})_3$  powders. This is also common in quaternary systems, where S/Se in varied [15].

EDX analysis were carried out to confirm the bulk composition of solid solutions. Compositional analysis of bulk was made from polished individual crystals by selecting 8–10 grains for EDX analysis and then average composition is calculated. Table 1 shows the average bulk composition of the  $\text{Cu}_2\text{Ge}(\text{Se}_x\text{S}_{1-x})_3$  microcrystalline powders. It was found that bulk composition of all powders was slightly Cu-rich and Ge-poor ( $[\text{Cu}]/[\text{Ge}] > 2$ ), the ratio of  $[\text{Se}]/([\text{S}] + [\text{Se}])$  in synthesized  $\text{Cu}_2\text{Ge}(\text{Se}_x\text{S}_{1-x})_3$  solid solutions followed nicely the input composition. The ratio of  $([\text{S}] + [\text{Se}])/([\text{Cu}] + [\text{Ge}])$  was approximately 1.0 regardless of the S/Se ratio in material.

Fig. 2a shows the XRD patterns and Fig. 2c shows corresponding lattice parameters of  $\text{Cu}_2\text{Ge}(\text{Se}_x\text{S}_{1-x})_3$  microcrystalline powders. The major diffraction peaks for pure  $\text{Cu}_2\text{GeS}_3$  correspond to monoclinic phase (space group Cc) (ICDD (PDF-2 01-088-0827) and for pure  $\text{Cu}_2\text{GeSe}_3$ , the characteristic peaks correspond to orthorhombic phase (space group  $Im\bar{m}2$ ) (PDF-2 01-076-7578). The crystal structure of  $\text{Cu}_2\text{Ge}(\text{Se}_x\text{S}_{1-x})_3$  transfer from monoclinic to orthorhombic between  $x = 0.2$  to  $x = 0.4$  because the  $\text{Cu}_2\text{Ge}(\text{Se}_x\text{S}_{1-x})_3$  ( $x = 0.2$ ) showed monoclinic structure, but further addition of Se in the  $\text{Cu}_2\text{Ge}(\text{Se}_x\text{S}_{1-x})_3$  ( $x = 0.4$ ) showed already orthorhombic structure. The position of most intensive diffraction peak shifts from 27.8 deg (for  $\text{Cu}_2\text{GeSe}_3$ ) to 29.2 deg (for  $\text{Cu}_2\text{GeS}_3$ ) as shown in enlarged view in Fig. 2b.

Using the X-ray diffraction patterns, the values of lattice parameters ( $a$ ,  $b$  and  $c$ ) for all powders were calculated and presented in Table 2 and

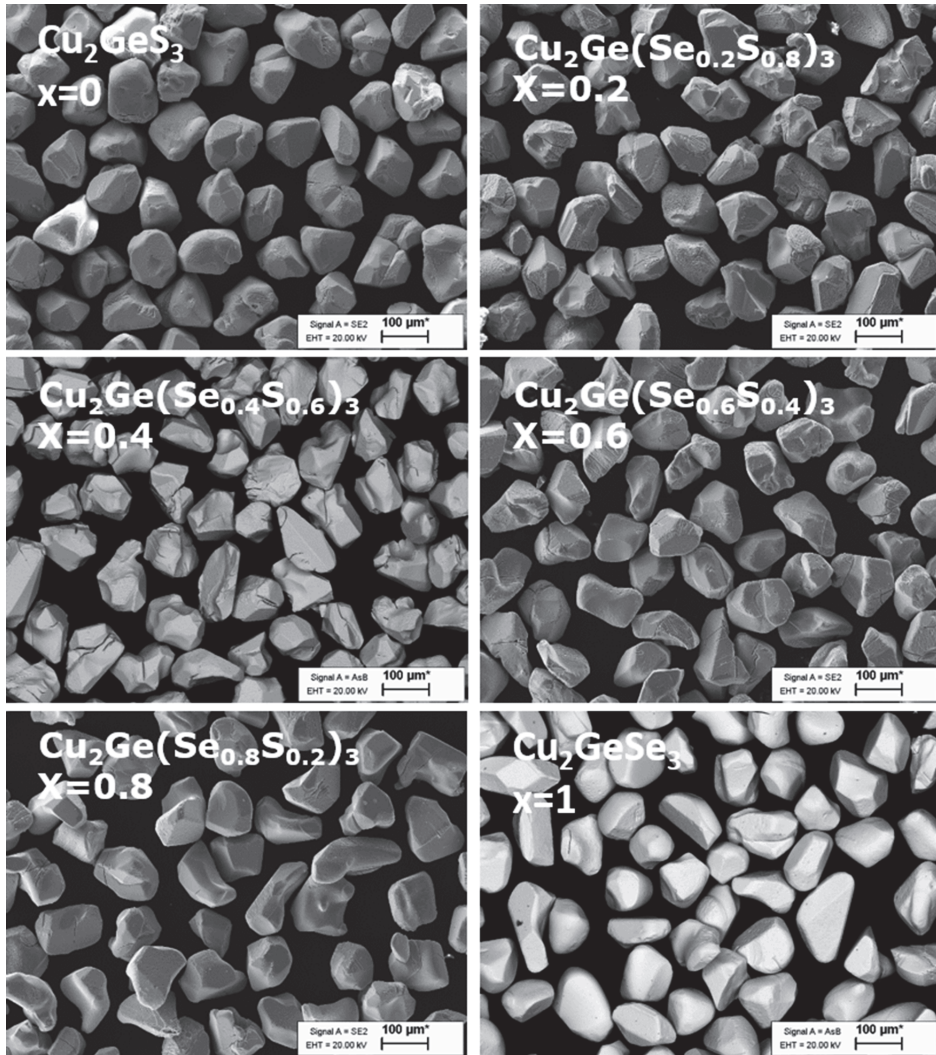


Fig. 1. SEM images of  $\text{Cu}_2\text{Ge}(\text{Se}_x\text{S}_{1-x})_3$  ( $x = 0, 0.2, 0.4, 0.6, 0.8, 1$ ) microcrystalline powders.

Table 1

Bulk composition of  $\text{Cu}_2\text{Ge}(\text{Se}_x\text{S}_{1-x})_3$  ( $x = 0, 0.2, 0.4, 0.6, 0.8, 1$ ) microcrystalline powders by EDX.

x	Bulk composition of powder crystals by EDX (at%) error~ 0.5 at %				Compositional ratios		
	Cu	Ge	S	Se	[Se]/([S]+[Se])	[Cu]/[Ge]	([S]+[Se])/([Cu]+[Ge])
0.0	33.62	16.28	50.10	–	0.00	2.06	1.00
0.2	33.75	16.51	40.21	9.53	0.19	2.04	0.99
0.4	33.48	16.49	30.01	20.02	0.40	2.03	1.00
0.6	33.48	16.57	19.99	29.96	0.60	2.01	1.00
0.8	33.55	16.24	10.08	40.13	0.80	2.06	1.01
1.0	33.73	16.25	–	50.02	1.00	2.07	1.00

Fig. 2c. Monoclinic  $\text{Cu}_2\text{GeS}_3$  had lattice parameters  $a = 6.439 \text{ \AA}$ ,  $b = 11.316 \text{ \AA}$  and  $c = 6.416 \text{ \AA}$ . Small amount of Se in the  $\text{Cu}_2\text{Ge}(\text{Se}_x\text{S}_{1-x})_3$  ( $x = 0.2$ ) increased all the lattice parameters. Additional S replacement by Se in  $\text{Cu}_2\text{Ge}(\text{Se}_x\text{S}_{1-x})_3$  ( $x = 0.4 - 1$ ) changed the crystal structure from monoclinic to orthorhombic together with enlargement in the lattice parameter values ( $a$  from  $11.541 \text{ \AA}$  to  $11.863 \text{ \AA}$ ;  $b$  from  $3.839 \text{ \AA}$  to  $3.954 \text{ \AA}$  and  $c$  from  $5.326 \text{ \AA}$  to  $5.485 \text{ \AA}$ ). This phenomenon is observed upon replacement of sulfur with selenium due to the smaller atom radius of S compared to Se.

Fig. 3 shows the Raman spectra obtained for  $\text{Cu}_2\text{Ge}(\text{Se}_x\text{S}_{1-x})_3$  solid solutions with different  $x$  value. The pure  $\text{Cu}_2\text{GeS}_3$  crystals show main Raman mode frequencies at  $337$  and  $390 \text{ cm}^{-1}$  and minor peaks at  $241$ ,  $268$ ,  $313$  and  $418 \text{ cm}^{-1}$ . All these peaks are assigned to monoclinic CGS phase and are in good correlation to single crystal study [9]. Pure  $\text{Cu}_2\text{GeSe}_3$  powder crystals showed main Raman peak at  $191 \text{ cm}^{-1}$  and the additional Raman modes were detected at  $184$ ,  $220$ ,  $268$  and  $296 \text{ cm}^{-1}$ . All these peaks are assigned to orthorhombic  $\text{Cu}_2\text{GeSe}_3$  phase

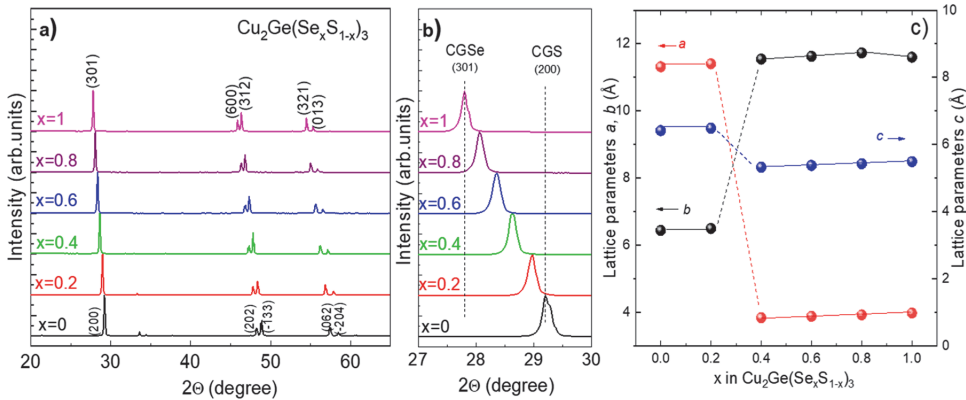


Fig. 2. (a) XRD patterns of  $\text{Cu}_2\text{Ge}(\text{Se}_x\text{S}_{1-x})_3$  solid solutions ( $x = 0, 0.2, 0.4, 0.6, 0.8, 1$ ), b) enlarged XRD patterns to view the shift of main peak position and c) lattice parameters.

Table 2

Lattice parameters of  $\text{Cu}_2\text{Ge}(\text{Se}_x\text{S}_{1-x})_3$  ( $x = 0, 0.2, 0.4, 0.6, 0.8, 1$ ) microcrystalline powders.

x	a, Å	b, Å	c, Å	V, Å <sup>3</sup>	Space group
0.0	6.439	11.316	6.416	443.97	Cc [No. 9]-monoclinic
0.2	6.497	11.402	6.486	456.31	Cc [No. 9]-monoclinic
0.4	11.541	3.839	5.326	236.32	Imm2 [No. 44]-orthorhombic
0.6	11.626	3.883	5.376	242.70	Imm2 [No. 44]-orthorhombic
0.8	11.729	3.925	5.428	249.90	Imm2 [No. 44]-orthorhombic
1.0	11.863	3.954	5.485	257.28	Imm2 [No. 44]-orthorhombic

[17]. In the solid solutions, all sulfide related peaks tend to shift toward smaller wavenumbers and the relative intensity of these peaks is decreasing and selenide related peaks will shift toward higher

wavenumbers. As the x value in the  $\text{Cu}_2\text{Ge}(\text{Se}_x\text{S}_{1-x})_3$  solid solutions increases, the Raman spectra of  $\text{Cu}_2\text{Ge}(\text{Se}_x\text{S}_{1-x})_3$  exhibit the two-mode characteristic due to the coexistence of S and Se atoms in powders. This trend is correlated with the increasing structural disorder due to the random distribution of S and Se atoms in the lattice that leads to fluctuations in the masses and force constants in the neighborhood [18]. All peaks belong to the  $\text{Cu}_2\text{Ge}(\text{Se}_x\text{S}_{1-x})_3$  solid solutions, no other phases were detected.

Fig. 4a shows the normalized photoluminescence spectra of the  $\text{Cu}_2\text{Ge}(\text{Se}_x\text{S}_{1-x})_3$  solid solutions with different Se/S concentration ratios measured at  $T = 20$  K. All spectra are composed of 2 asymmetric PL peaks. Spectral fitting results with a split-Pearson VII function are shown as colored bands. Peak positions of these bands (#1 and #2) as a function of Se/S concentration show nearly linear dependence with a slope about  $-0.8$  eV. Almost the same slope can be detected for  $E_g$  values

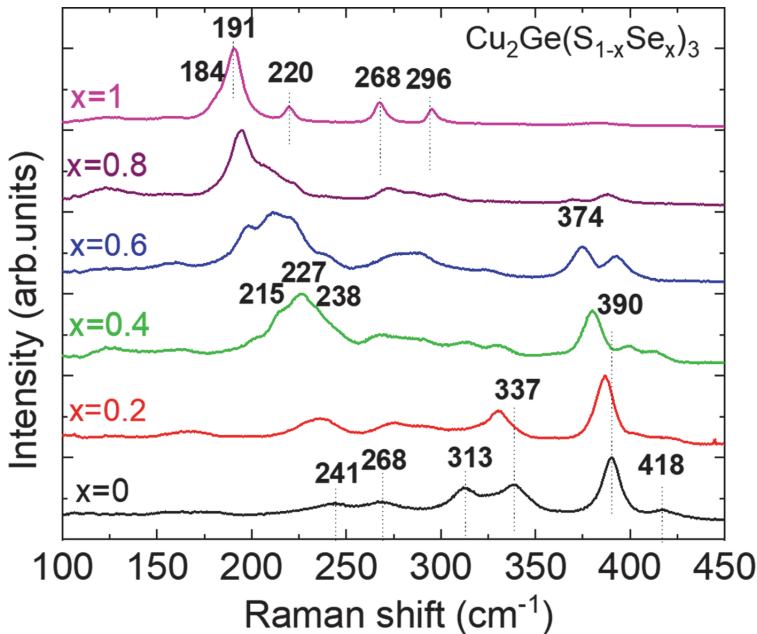


Fig. 3. Room-temperature Raman spectra of  $\text{Cu}_2\text{Ge}(\text{Se}_x\text{S}_{1-x})_3$  ( $x = 0, 0.2, 0.4, 0.6, 0.8, 1$ ) microcrystalline powders.



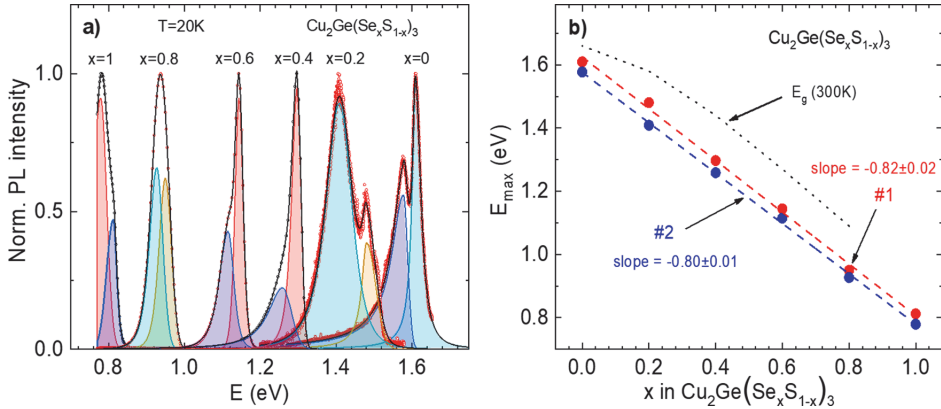


Fig. 4. (a) Normalized low temperature photoluminescence spectra of  $\text{Cu}_2\text{Ge}(\text{Se}_x\text{S}_{1-x})_3$  solid solutions with different S/Se ratios with fitting using an asymmetric double sigmoidal function, (b) Peak positions of two PL bands as a function of  $x$ . Results of linear fitting are shown as dashed lines. Room temperature bandgap energy  $E_g$  determined from EQE measurements is given as a dotted line.

determined from room temperature EQE measurements, see Fig 4b. Therefore, the peak position shift with  $x$  is related to  $E_g$  shift for both PL peaks. The average separation between peak #1 and #2 is around 40 meV. A detailed study of these peaks for  $x = 0.6$  was published in [14]. It was shown that both peaks are related to donor-acceptor pair recombination and therefore it is quite likely that the same model holds for the whole range of  $x$  values.

The applicability of the  $\text{Cu}_2\text{Ge}(\text{Se}_x\text{S}_{1-x})_3$  powders as absorber materials were tested in monograin layer solar cell structure. Fig. 5a shows illuminated  $J$ - $V$  characteristics and Fig. 5b shows corresponding EQE curves for all studied  $\text{Cu}_2\text{Ge}(\text{Se}_x\text{S}_{1-x})_3$  based devices. The basic characteristics of solar cells and band gap energy values are presented in Table 3.  $\text{Cu}_2\text{GeSe}_3$  based solar cell characteristics were excluded because devices did not show any photoresponse.

Open circuit voltage ( $V_{oc}$ ) of monograin layer solar cells increased from 372 mV to 537 mV by increasing the selenium content in the  $\text{Cu}_2\text{Ge}(\text{Se}_x\text{S}_{1-x})_3$  from  $x = 0$  to  $x = 0.6$ . Also, current density ( $J_{sc}$ ) values increased from 5.9  $\text{mA}/\text{cm}^2$  to 16.5  $\text{mA}/\text{cm}^2$ . The monograin layer solar cell with the highest conversion efficiency ( $\eta$ ) in this study, which was fabricated from  $\text{Cu}_2\text{Ge}(\text{Se}_x\text{S}_{1-x})_3$  ( $x = 0.6$ ), demonstrated  $V_{oc} = 537$  mV,  $J_{sc} = 15.8$   $\text{mA}/\text{cm}^2$ ,  $FF = 37.2\%$ , and  $\eta = 3.16\%$ . According to external

Table 3

Summary of the main characteristics of  $\text{Cu}_2\text{Ge}(\text{Se}_x\text{S}_{1-x})_3$  monograin layer solar cells depending on S replacement with Se in absorber materials.

$x$	$V_{oc}$ , mV	$FF$ , %	$J_{sc}$ , $\text{mA}/\text{cm}^2$	$\eta$ , %	$E_g^*$ , eV
0.0	372	39.9	5.9	1.16	1.65
0.2	270	38.1	5.3	0.72	1.57
0.4	415	42.2	16.5	2.90	1.43
0.6	537	37.2	15.8	3.16	1.26
0.8	239	30.6	7.3	0.54	1.07
1	91	25.4	0.7	0.02	-

quantum efficiency (EQE) spectra in Fig. 5b, with the increasing the selenium content in monograin powders, it is obvious to see that the absorption edge shifts to longer wavelengths and the change of spectral response in the long wavelengths. The effective band gap ( $E_g^*$ ) of  $\text{Cu}_2\text{Ge}(\text{Se}_x\text{S}_{1-x})_3$  solid solutions was evaluated from the linear segment of the low-energy side of the construction (EQE)<sup>2</sup> vs. E curves (inset graph in Fig. 5b). An decrease of  $E_g^*$  from 1.65 eV to 1.07 eV by increasing Se content in  $\text{Cu}_2\text{Ge}(\text{Se}_x\text{S}_{1-x})_3$  ( $x = 0-0.8$ ) powder materials was observed (Table 3).

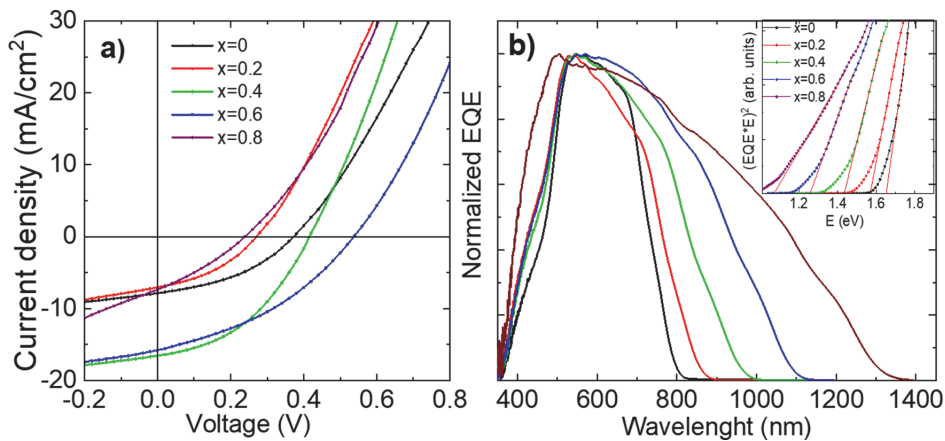


Fig. 5. (a) Light  $J$ - $V$  characteristics and (b) EQE of  $\text{Cu}_2\text{Ge}(\text{Se}_x\text{S}_{1-x})_3$  ( $x = 0, 0.2, 0.4, 0.6, 0.8, 1$ ) monograin layer solar cells. Inset graph shows bandgap extraction by plotting  $[(EQE \cdot E)^2]$  vs. E.

Results showed that  $\text{Cu}_2\text{Ge}(\text{Se}_x\text{S}_{1-x})_3$  ( $x = 0.4 - 0.6$ ) materials have potential as absorber materials in solar cells. Monograin layer solar cells preparation process contain many technological steps which need to be optimized for example optimization of absorber materials composition, selection of buffer layer etc. Therefore, further research is needed to improve the performance of  $\text{Cu}_2\text{Ge}(\text{Se}_x\text{S}_{1-x})_3$  solar cells.

#### 4. Conclusion

$\text{Cu}_2\text{Ge}(\text{Se}_x\text{S}_{1-x})_3$  ( $0 \leq x \leq 1$ ) microcrystalline powders were successfully synthesized in LiI flux by molten salt synthesis-growth method. The compositional analysis by EDX indicated that changing the S/Se ratio in  $\text{Cu}_2\text{Ge}(\text{Se}_x\text{S}_{1-x})_3$ , complete series of solid solutions is formed. All synthesized powders were slightly Cu-rich and Ge-poor. All synthesized powders  $\text{Cu}_2\text{Ge}(\text{Se}_x\text{S}_{1-x})_3$  consisted of well-formed crystals independent of the S/Se ratio. Structural studies by X-ray diffraction showed that  $\text{Cu}_2\text{GeSe}_3$  crystallize in monoclinic and  $\text{Cu}_2\text{GeSe}_3$  crystallize in orthorhombic structure. The crystal structure of  $\text{Cu}_2\text{Ge}(\text{Se}_x\text{S}_{1-x})_3$  transfer from monoclinic to orthorhombic was detected between  $x = 0.2$  to  $x = 0.4$ . Raman and PL studies also confirmed that full series of  $\text{Cu}_2\text{Ge}(\text{Se}_x\text{S}_{1-x})_3$  is formed. Raman modes of solid solutions followed the bimodal behavior. PL spectra of CGSs were composed of two asymmetric PL peaks. Peak positions of these bands as a function of Se/S concentration show nearly linear dependence with a slope about  $-0.8$  eV. Almost the same slope was detected for band gap values determined from room temperature EQE measurements. Therefore, the peak position shift with  $x$  is related to  $E_g$  shift for both PL peaks. Both peaks are related to donor-acceptor pair recombination.

Most promising compounds for solar cell application are  $\text{Cu}_2\text{Ge}(\text{Se}_x\text{S}_{1-x})_3$  solid solutions with  $x = 0.4 - 0.6$ . A best performing solar cell was fabricated by using  $\text{Cu}_2\text{Ge}(\text{Se}_x\text{S}_{1-x})_3$   $x = 0.6$  powder crystals as absorber material, exhibiting an open-circuit voltage of 537 mV, current density of  $15.8 \text{ mA/cm}^2$ , fill factor of 37.2% and a conversion efficiency of 3.16%.

#### CRedit authorship contribution statement

**X. Li:** Investigation, Validation, Writing – original draft. **K. Timmo:** Supervision, Writing – review & editing. **M. Grossberg:** Writing – review & editing, Funding acquisition. **M. Pilvet:** Investigation. **R. Kaupmees:** Investigation. **J. Krustok:** Investigation, Writing – review & editing. **K. Muska:** Investigation. **V. Mikli:** Investigation, Writing – review & editing. **M. Kauk-Kuusik:** Conceptualization, Supervision, Writing – review & editing, Project administration.

#### Declaration of Competing Interest

The authors declare that they have no known competing financial interests or personal relationships that could have appeared to influence the work reported in this paper.

#### Acknowledgments

This study was funded by the Estonian Research Council project PRG1023, by ERDF project “Center of nanomaterials technologies and

research (NAMUR+)” (2014–2020.4.01.16–0123), by the European Regional Development Fund “Estonian Center of Excellence project TK141”.

#### References

- [1] A. Kanai, M. Sugiyama, Na induction effects for J–V properties of  $\text{Cu}_2\text{SnS}_3$  (CTS) solar cells and fabrication of a CTS solar cell over-5.2% efficiency, *Sol. Energy Mater. Sol. Cells* 231 (2021), 111315, <https://doi.org/10.1016/j.solmat.2021.111315>.
- [2] M. Umehara, S. Tajima, Y. Aoki, Y. Takeda, T. Motohiro,  $\text{Cu}_2\text{Sn}_{1-x}\text{Ge}_x\text{S}_3$  solar cells fabricated with a graded bandgap structure, *Appl. Phys. Express* 9 (2016), 072301, <https://doi.org/10.7567/APEX.9.072301>.
- [3] A. Dugarte-Dugarte, N. Ramirez Pineda, L. Nieves, J.A. Henao, G. de Delgado, J. M. Delgado, The crystal structure of  $\text{Cu}_2\text{GeSe}_3$  and the structure-types of the  $\text{I}_2\text{-VI}_3$  family of semiconducting compounds, *Acta Crystallogr. Sect. B* 77 (2021) 158–167, <https://doi.org/10.1107/S2052520620016571>.
- [4] X. Jin, L. Zhang, G. Jiang, W. Liu, C. Zhu, High open-circuit voltage of ternary  $\text{Cu}_2\text{GeSe}_3$  thin film solar cells from combustion synthesized Cu-Ge alloy, *Sol. Energy Mater. Sol. Cells* (2017), <https://doi.org/10.1016/j.solmat.2016.11.001>.
- [5] H. Araki, K. Chino, K. Kimura, N. Aihara, K. Jimbo, H. Katagiri, Fabrication of  $\text{Cu}_2\text{GeSe}_3$ -based thin film solar cells by sulfurization of Cu/Ge stacked precursors, *Jpn. J. Appl. Phys.* 53 (2014), <https://doi.org/10.7567/JJAP.53.05FW10>, 05FW10.
- [6] E.V.C. Robert, J. de Wild, D. Colombara, P.J. Dale, M.J. Heben, M.M. Al-Jassim, Crystallographic and optoelectronic properties of the novel thin film absorber  $\text{Cu}_2\text{GeSe}_3$ , in: *Proceedings of the Thin Films Solar Energy Technology VIII*, 2016, 993607, <https://doi.org/10.1117/12.2236621>.
- [7] M. Morihama, T. Maeda, I. Yamauchi, T. Wada, Crystallographic and optical properties of narrow band gap  $\text{Cu}_2\text{GeSe}_3$  and  $\text{Cu}_2(\text{Sn}_{1-x}\text{Ge}_x)\text{Se}_3$  solid solution, *Jpn. J. Appl. Phys.* 53 (2014), <https://doi.org/10.7567/jjap.53.05fw06>, 05FW06.
- [8] G. Marcano, R. Márquez, Variable-range hopping conductivity and magnetoresistance in p-type  $\text{Cu}_2\text{GeSe}_3$ , *J. Phys. Chem. Solids* 64 (2003) 1725–1727, [https://doi.org/10.1016/S0022-3697\(03\)00195-1](https://doi.org/10.1016/S0022-3697(03)00195-1).
- [9] Y. Matsumoto, N. Aihara, N. Saito, K. Tanaka, Growth of  $\text{Cu}_2\text{GeSe}_3$  bulk single crystals by chemical vapor transport with iodine, *Mater. Lett.* 194 (2017) 16–19, <https://doi.org/10.1016/j.matlet.2017.02.009>.
- [10] P. Ramasamy, J. Kim, Wurtzite  $\text{Cu}_2\text{GeSe}_3$  nanocrystals: phase- and shape-controlled colloidal synthesis, *Chem. Asian J.* (2015), <https://doi.org/10.1002/asia.201500199>.
- [11] C. Yang, B. Zhou, S. Miao, C. Yang, B. Cai, W.H. Zhang, X. Xu,  $\text{Cu}_2\text{Ge}(\text{S}_{3-x}\text{Se}_x)$  colloidal nanocrystals: synthesis, characterization, and composition-dependent band gap engineering, *J. Am. Chem. Soc.* 135 (2013) 5958–5961, <https://doi.org/10.1021/ja400452t>.
- [12] G. Marcano, G.S. Pérez, C. Rincón, Photoluminescence spectra of  $\text{Cu}_2\text{GeSe}_3$  orthorhombic semiconductor compound, *Phys. Status Solidi* 254 (2017), 1700332, <https://doi.org/10.1002/pssb.201700332>.
- [13] D.S. Premkumar, R. Chetty, P. Malar, R.C. Mallik, High temperature XRD of  $\text{Cu}_2\text{GeSe}_3$ , *AIP Conf. Proc.* 1665 (2015), 120020, <https://doi.org/10.1063/1.4918127>.
- [14] J. Krustok, R. Kaupmees, X. Li, M. Kauk-Kuusik, M. Grossberg, Detailed photoluminescence study of  $\text{Cu}_2\text{Ge}(\text{SSe})_3$  microcrystals, *AIP Adv.* 11 (2021) 85105, <https://doi.org/10.1063/5.0053928>.
- [15] X. Li, M. Pilvet, K. Timmo, M. Grossberg, V. Mikli, M. Kauk-Kuusik, The effect of S/Se ratio on the properties of  $\text{Cu}_2\text{CdGe}(\text{S}_x\text{Se}_{3-x})_4$  microcrystalline powders for photovoltaic applications, *Sol. Energy* (2020), <https://doi.org/10.1016/j.solener.2020.09.045>.
- [16] X. Li, M. Pilvet, K. Timmo, M. Grossberg, M. Danilov, V. Mikli, M. Kauk-Kuusik, Effect of absorber surface modification on the optoelectronic properties of  $\text{Cu}_2\text{CdGeSe}_4$  solar cells, *Thin Solid Films* (2020), <https://doi.org/10.1016/j.tsf.2020.137822>.
- [17] G. Marcano, C. Rincón, G. Marín, G.E. Delgado, A.J. Mora, J.L. Herrera-Pérez, J. G. Mendoza-Alvarez, P. Rodríguez, Raman scattering and X-ray diffraction study in  $\text{Cu}_2\text{GeSe}_3$ , *Solid State Commun.* 146 (2008) 65–68, <https://doi.org/10.1016/j.ssc.2008.01.018>.
- [18] M. Grossberg, J. Krustok, J. Raudoja, K. Timmo, M. Altosaar, T. Raadik, Photoluminescence and Raman study of  $\text{Cu}_2\text{ZnSn}(\text{Se}_x\text{S}_{1-x})_4$  monograins for photovoltaic applications, *Thin Solid Films* 519 (2011) 7403–7406, <https://doi.org/10.1016/j.tsf.2010.12.099>.

## Curriculum vitae

### Personal data

Name: Xiaofeng Li  
Date of birth: 27.09.1993  
Place of birth: China  
Citizenship: Chinese

### Contact data

E-mail: [xiaofeng.li@taltech.ee](mailto:xiaofeng.li@taltech.ee)

### Education

2018–2022 Tallinn University of Technology, PhD  
2016–2018 Tallinn University of Technology, MSc (*cum laude*)  
2012–2016 Shanghai Dianji University, BSc (*cum laude*)  
2008–2012 Shenqiu No.1 High School, secondary education

### Language competence

Chinese Native  
English Fluent

### Participation in conferences

2021 European Materials Research Society Spring Virtual Meeting, 2021. Poster Presentation.  
2018-2022 Graduate School of Functional Materials and Technologies (GSFMT), Scientific Conference, Tallinn University of Technology and Tartu University, Estonia. Oral and poster presentations.  
2020 11<sup>th</sup> Kesterite+ online workshop. Poster presentation.  
2019 10<sup>th</sup> Kesterite+ workshop, Uppsala, Sweden. Poster presentation.  
2019 European Materials Research Society Spring Meeting, Nice, France. Poster Presentation.

### Professional employment

2018–2022 Laboratory of Photovoltaic Materials, Tallinn University of Technology,  
Early stage researcher

### Defended dissertations

2018 Study of  $\text{Cu}_2\text{CdGeSe}_4$  monograin powders for photovoltaic applications.  
Supervisor: Senior researcher Marit Kauk-Kuusik, PhD

### Supervised dissertations

2021 Sharath Chandra Pottabathini, Master's Degree, "Phase evolution of  $\text{Cu}_2\text{CdGeSe}_4$  monograin powders during the synthesis process in different flux materials", supervisors: Marit Kauk-Kuusik; Xiaofeng Li, Tallinn University of Technology, Department of Materials and Environmental Technology.



## Research project

PRG1023 “Sustainable, cost-efficient, flexible, lightweight and semi-transparent multinary chalcogenide based solar cells for building integrated photovoltaics”.

## List of publications

1. **X. Li**, M. Pilvet, K. Timmo, M. Grossberg, R. Kaupmees, J. Krustok, K. Muska, V. Mikli, M. Kauk-Kuusik, “*Study of the structure and optoelectronic properties of  $Cu_2Ge(Se_xS_{1-x})_3$  microcrystalline powders*”, *Thin Solid Films* 742 (2022) 139053. <https://doi.org/10.1016/j.tsf.2021.139053>
2. J. Krustok, R. Kaupmees, **X. Li**, M. Kauk-Kuusik, and M. Grossberg. “*Detailed photoluminescence study of  $Cu_2Ge(S,Se)_3$  microcrystals*”, *AIP Advances* 11 (2021) 085105. <https://doi.org/10.1063/5.0053928>
3. **X. Li**, M. Pilvet, K. Timmo, M. Grossberg, V. Mikli, M. Kauk-Kuusik, “*The effect of S/Se ratio on the properties of  $Cu_2CdGe(S_xSe_{1-x})_4$  microcrystalline powders for photovoltaic applications*”, *Solar Energy* 209 (2020) 646–652. <https://doi.org/10.1016/j.solener.2020.09.045>
4. **X. Li**, M. Pilvet, K. Timmo, M. Grossberg, M. Danilson, V. Mikli, M. Kauk-Kuusik. “*Effect of absorber surface modification on the optoelectronic properties of  $Cu_2CdGeSe_4$  solar cells*”, *Thin Solid Films* 697 (2020) 137822. <https://doi.org/10.1016/j.tsf.2020.137822>
5. J. Krustok, T. Raadik, **X. Li**, M. Kauk-Kuusik, K. Timmo, S. Oueslati, M. Grossberg. “*Study of point defects in wide-bandgap  $Cu_2CdGeS_4$  microcrystals by temperature and laser power dependent photoluminescence spectroscopy*”, *J. Phys. D: Appl. Phys.* 53 (2020) 275102. <https://doi.org/10.1088/1361-6463/ab83c1>
6. M. Kauk-Kuusik, **X. Li**, M. Pilvet, K. Timmo, M. Danilson, V. Mikli, R. Kaupmees, M. Grossberg. “*Nano-scale sulfurization of the  $Cu_2ZnSnSe_4$  crystal surface for photovoltaic applications*”. *Journal of Materials Chemistry A* 7 (2019) 24884–24890. <https://doi.org/10.1039/C9TA08020A>
7. M. Kauk-Kuusik, **X. Li**, M. Pilvet, K. Timmo, M. Grossberg, T. Raadik, M. Danilson, V. Mikli, M. Altosaar, J. Krustok, J. Raudoja. “*Study of  $Cu_2CdGeSe_4$  monograin powders synthesized by molten salt method for photovoltaic applications*”, *Thin Solid Films* 666 (2018) 15–19. <https://doi.org/10.1016/j.tsf.2018.09.025>

## Elulookirjeldus

### Isikuandmed

Nimi: Xiaofeng Li  
Sünniaeg: 27.09.1993  
Sünnikoht: Hiina  
Kodakondsus: Hiinlane

### Kontaktandmed

E-post: [xiaofeng.li@taltech.ee](mailto:xiaofeng.li@taltech.ee)

### Hariduskäik

2018–2022 Tallinna Tehnikaülikool, PhD  
2016–2018 Tallinna Tehnikaülikool, MSc (*cum laude*)  
2012–2016 Shanghai Dianji Ülikool, BSc (*cum laude*)  
2008–2012 Shenqiu No.1 High School, Keskhariidus

### Keelteoskus

Hiina keel Emakeel  
Inglise keel Kõrgtase

### Osalemine konverentsidel

2021 Euroopa Materjaliuuringute Seltsi kevadine virtuaalkonverents. Posterettekanne.  
2018-2022 Funktsionaalsete materjalide ja tehnoloogiate doktorikool (FMTDK), Tallinna Tehnikaülikool ja Tartu Ülikool, Eesti. Suulised ja posterettekanded.  
2020 11. Euroopa kesteriitide+ virtuaalne töötuba. Posterettekanne.  
2019 10. Euroopa kesteriitide+ töötuba, Uppsala Ülikool, Uppsala, Rootsi. Posterettekanne.  
2019 Euroopa Materjaliuuringute Seltsi kevadine konverents ja näitus, Nice, Prantsusmaa. Posterettekanne.

### Teenistuskäik

2018–2022 Päikeseenergeetika materjalide teaduslabor, Tallinna Tehnikaülikool, doktorant-nooremteadur

### Kaitstud väitekirjad

2018 “Cu<sub>2</sub>CdGeSe<sub>4</sub> monoterapulbrite uurimine päikeseplatareide rakendusteks”, magistritöö  
Juhendaja: vanemteadur Dr. Marit Kauk-Kuusik

### Juhendatud väitekirjad

2021 Sharath Chandra Pottabathini, magistrikraad, “Cu<sub>2</sub>CdGeSe<sub>4</sub> faasi kujunemine monoterapulbri sünteesi protsessis erinevates sulandajates”, Juhendajad: Marit Kauk-Kuusik; Xiaofeng Li.  
Tallinna Tehnikaülikool, Materjali- ja keskkonnatehnoloogia instituut.

## Teadusprojektid

PRG1023 "Mitmik-kalkogeniididel põhinevad jätkusuutlikud, kuluefektiivsed, kerged, painduvad ja poolläbipaistvad ehitisintegreeritavad päikesepatareid".

## Teaduspublikatsioonid

1. **X. Li**, M. Pilvet, K. Timmo, M. Grossberg, R. Kaupmees, J. Krustok, K. Muska, V. Mikli, M. Kauk-Kuusik, "Study of the structure and optoelectronic properties of  $Cu_2Ge(Se_xS_{1-x})_3$  microcrystalline powders", *Thin Solid Films* 742 (2022) 139053. <https://doi.org/10.1016/j.tsf.2021.139053>
2. J. Krustok, R. Kaupmees, **X. Li**, M. Kauk-Kuusik, and M. Grossberg. "Detailed photoluminescence study of  $Cu_2Ge(S,Se)_3$  microcrystals", *AIP Advances* 11 (2021) 085105. <https://doi.org/10.1063/5.0053928>
3. **X. Li**, M. Pilvet, K. Timmo, M. Grossberg, V. Mikli, M. Kauk-Kuusik, "The effect of S/Se ratio on the properties of  $Cu_2CdGe(S_xSe_{1-x})_4$  microcrystalline powders for photovoltaic applications", *Solar Energy* 209 (2020) 646–652. <https://doi.org/10.1016/j.solener.2020.09.045>
4. **X. Li**, M. Pilvet, K. Timmo, M. Grossberg, M. Danilson, V. Mikli, M. Kauk-Kuusik. "Effect of absorber surface modification on the optoelectronic properties of  $Cu_2CdGeSe_4$  solar cells", *Thin Solid Films* 697 (2020) 137822. <https://doi.org/10.1016/j.tsf.2020.137822>
5. J. Krustok, T. Raadik, **X. Li**, M. Kauk-Kuusik, K. Timmo, S. Oueslati, M. Grossberg. "Study of point defects in wide-bandgap  $Cu_2CdGeS_4$  microcrystals by temperature and laser power dependent photoluminescence spectroscopy", *J. Phys. D: Appl. Phys.* 53 (2020) 275102. <https://doi.org/10.1088/1361-6463/ab83c1>
6. M. Kauk-Kuusik, **X. Li**, M. Pilvet, K. Timmo, M. Danilson, V. Mikli, R. Kaupmees, M. Grossberg. "Nano-scale sulfurization of the  $Cu_2ZnSnSe_4$  crystal surface for photovoltaic applications". *Journal of Materials Chemistry A* 7 (2019) 24884–24890. <https://doi.org/10.1039/C9TA08020A>
7. M. Kauk-Kuusik, **X. Li**, M. Pilvet, K. Timmo, M. Grossberg, T. Raadik, M. Danilson, V. Mikli, M. Altosaar, J. Krustok, J. Raudoja. "Study of  $Cu_2CdGeSe_4$  monograin powders synthesized by molten salt method for photovoltaic applications", *Thin Solid Films* 666 (2018) 15–19. <https://doi.org/10.1016/j.tsf.2018.09.025>

ISSN 2585-6901 (PDF)  
ISBN 978-9949-83-820-2 (PDF)